ABSTRACT

Title of Dissertation: QUANTITATIVE PHENOTYPING OF BRAIN ENDOTHELIAL CELL-CELL JUNCTIONS FOR PHYSIOLOGICAL AND PATHOPHYSIOLOGICAL APPLICATIONS

Kelsey M. Gray, Doctor of Philosophy, 2019

Dissertation directed by: Assistant Professor, Kimberly M. Stroka, Fischell Department of Bioengineering

The integrity of endothelial cell-cell junctions is required for the maintenance of normal physiological processes. The expression of junctional proteins is particularly important in the endothelial cells of the blood-brain barrier (BBB), the cellular unit that protects the brain via regulated transport between the peripheral blood and the central nervous system. Dysfunction of the BBB is linked with decreased junctional protein localization and is implicated in several diseases including Alzheimer's disease and multiple sclerosis. On the other hand, the tight junctions of the BBB impede the delivery of medications targeting the brain. Therefore, understanding the key players driving junction stability could hold significant promise for therapeutic discovery and drug delivery applications. Despite this, the mechanisms underlying junction disruption aren't fully understood. While several studies have linked different junction protein patterns with altered barrier function, the quantification of this parameter remains

limited due to the lack of efficient measurement techniques. Here, we aimed to investigate the influence of junction phenotype on brain endothelial barrier properties. To accomplish this, we developed the Junction Analyzer Program (JAnaP) to semi-automatically calculate edge-localization protein phenotypes.

Application of the JAnaP to measure the junctional proteins VE-cadherin and ZO-1 in different physiological and pathophysiological conditions revealed that discontinuous junctions contribute more to barrier permeability compared to continuous, linear junctions. Continuous junctions were also increased in endothelial cells with decreased contractility, mediated biochemically or by lowered subendothelial matrix stiffness. Finally, breast cancer cell secreted factors increased immature adherens junctions, likely through VEGF signaling, but minimally affected tight junction presentation. Thus far, the development and application of the JAnaP has revealed insights into the effects of junction patterns on barrier function, the mechanobiology of endothelial cells, and the response of brain endothelial cells to biochemical cues involved in breast cancer metastasis. Understanding the conditions driving altered junction presentation, and the resultant effects on barrier integrity, could lead to the development of therapeutics capable of traversing the BBB for delivery to the brain or for diseases associated with BBB dysfunction. Future use of this program holds significant potential for physiological and pathophysiological study in various endothelial and epithelial cell systems.

QUANTITATIVE PHENOTYPING OF BRAIN ENDOTHELIAL CELL-CELL JUNCTIONS FOR PHYSIOLOGICAL AND PATHOPHYSIOLOGICAL APPLICATIONS

by

Kelsey M. Gray

Dissertation submitted to the Faculty of the Graduate School of the
University of Maryland, College Park, in partial fulfillment
of the requirements for the degree of
Doctor of Philosophy
2019

Advisory Committee:
Assistant Professor Kimberly M. Stroka, Chair
Professor John P. Fisher
Associate Professor Steven Jay
Professor Wolfgang Losert
Professor Gregory F. Payne

Personal Acknowledgements

There are several individuals I would like to thank for their guidance and support during my time at the University of Maryland. Their help, both personally and professionally, made this dissertation possible and I am forever grateful for their encouragement.

First, I would like to thank my advisor, Dr. Kimberly M. Stroka. Her persistent positive outlook is truly an inspiration. I am extremely grateful for her constant advice and support of my personal and professional goals and am very thankful to have her as a mentor and role model. Also, thank you to Kim for regularly boosting the lab mood with trips to the UMD creamery, especially with "scientists-in-training"!

Next, I would like to thank my lab-mates. First, Marina Pranda who was the only other graduate student at the start of the lab. Her consistent willingness to lend a helping hand and her attention to detail is always an inspiration. Thank you, Marina, for your continued encouragement throughout our Stroka Lab journey. I would also like to thank Mary Doolin, for endless technical and emotional support, and for showcasing the ability to be a productive scientist while emphasizing work-life balance. Additionally, I would like to thank Rebecca Moriarty, for her constant positivity and uplifting spirit, and for many board game adventures. Finally, I would like to thank Ariana DeCastro for her "team player" attitude exemplified by her immediate contribution to the blood-brain barrier project upon joining the lab. I am very grateful to have worked with and been influenced by the smart, impressive women of the Stroka Lab!

I would also like to acknowledge several peers with whom I have enjoyed working with on collaborative projects. Thank you to Christina Conrad, Collin Inglut, Divya Patel, and Jinyang Li – I have learned a lot from working with each of you!

I would also like to thank several faculty members who have served as additional mentors during my time at UMD. First, thank you to Dr. Gregory Payne. Since my time as an undergraduate researcher, he has been a constant source of support, both scientifically and professionally. I have learned so much from his guidance and I am extremely grateful for his almost 10 years of mentorship. Next, I would like to thank Dr. Steven Jay for his influence as a great teacher and mentor, emphasizing the "big picture" applications of scientific research. I would also like to thank Dr. Christopher Jewell. My rotation in his lab significantly influenced my approach to science, fellowship application writing, and graduate school in general. Finally, I would like to thank Dr. Helim Aranda-Espinoza, for helpful scientific discussions, his encouragement to join the Graduate Studies Committee, and for his mentorship and guidance regarding future career and life endeavors.

Thank you, also, to the members of the Fischell Department of Bioengineering staff, for their day-to-day help with graduate school requirements and activities. I would especially like to thank Bill Churma, Kishwar Kabiruddin, Karen Lasher, Debbie Thompson, and Theresa Moore, for making my time at UMD, especially during my time in BGSS, such a positive experience.

I would also like to acknowledge several friends for their continued support and reassurance. Thank you to Poonam Sharma, Leo Torres, George Banis, Krystina Hess,

Michelle Bookstaver, and Anjana Jeyaram, for keeping things fun and also in perspective.

My family also deserves a huge thank you for their love and support during my career as an academic, and in all things in life. Thank you to my amazing parents, Chris and Steve, my brother Collin, my Grandma Lois, and my Aunt Sherrie, for always cheering me on but reminding me to stay grounded. I would also like to acknowledge my soon-to-be parent and sibling in-laws, Jared, Michelle, David, Emily, and Jordan, for their unwavering encouragement.

Finally, I owe a HUGE thank you to my best friend and fiancé, Mike. His endless love, patience, support, and encouragement have kept me motivated and balanced, through the ups and downs of graduate school. Thank you, Michael!

Scientific Acknowledgements

I would like to thank the following people for their guidance and support in the completion of this dissertation:

- My advisor, Dr. Kimberly Stroka, for all of the help and feedback regarding experimentation, interpretation, and presentation of results.
- My committee members for their time and their feedback during my proposal examination and dissertation defense:
    - Professor John P. Fisher
    - Associate Professor Steven Jay
    - Professor Wolfgang Losert
    - Professor Gregory F. Payne

Chapter 4:

- Kyle Thomas at Yellow Basket, LLC (kyle@yellowbasket.io) for software development support.

Chapter 5:

- Jae W. Jung (Stroka Lab) for performing JAnaP analysis, collecting TEER measurements, and aiding in local permeability analysis.
- Collin Inglut (Huang Lab) for performing Transwell permeability experiments

Chapter 6:

- Dakota B. Katz (Stroka Lab) for her work on the immunostaining and polyacrylamide gel protocols. Also, for her work on the blebbistatin experiments.

- Erica G. Brown (Stroka Lab) for her work on the monolayer coverage quantification, calyculin experiments, and waypointing images for JAnaP analysis.
- Dr. Rachel L Manthe (Muro Lab) for valuable conversation regarding HBMEC cell culture at the start of the Stroka Lab.

Chapter 7:

- Marina A. Pranda (Stroka Lab) for all tumor cell experiments on HA/Gtn films (Figure 7.1 and 7.2) and incorporation into HBMECs (Figure 7.8).
- Ariana J. DeCastro and Greg M. Dawson (Stroka Lab) for their help to Marina in analyzing tumor cell migration and morphology.
- Jae W. Jung (Stroka Lab) for performing JAnaP analysis.
- Note, several sections in this chapter were co-written by Marina A. Pranda and Kelsey M. Gray.

Chapter 9:

- Jae W. Jung (Stroka Lab) for performing JAnaP analysis for the preliminary dynamic junction studies (Figure 9.1).
- Dr. William Luscinskas (Harvard Medical School) for providing the VE-cadherin-GFP adenovirus used in the preliminary dynamic junction studies (Figure 9.1).
- Collin Inglut (Huang Lab) for performing the photodynamic therapy treatments (and permeability studies, data not shown) (Figure 9.2).

Appendix A:

- Kyle Thomas at Yellow Basket, LLC (kyle@yellowbasket.io) for software development support.

I would also like to thank my funding sources for their support:

- Fischell Department of Bioengineering
    - Fischell Fellowship in Biomedical Engineering
    - Dean's Fellowship
    - Merit Scholarship
- A. James Clark School of Engineering
    - Future Faculty Program
- University of Maryland Graduate School
    - Dr. Mabel S. Spencer Award for Excellence in Graduate Achievement
    - 3-Minute Thesis Award
    - Jacob K. Goldhaber Travel Award
    - International Conference Student Support Award
- Biomedical Engineering Society
    - Biomedical Engineering Society Career Development Award
    - Cellular and Molecular Bioengineering Shooting Star Award
    - Biomedical Engineering Society Student Travel Award
    - Cellular and Molecular Bioengineering Student Travel Award
- University of Maryland, College Park
- Burroughs Wellcome Career Award at the Scientific Interface to advisor, Dr. Kimberly Stroka

Table of Contents

† These chapters were taken or adapted from K.M. Gray's previously published manuscripts, with permission from the publishers. Specific citations are included in footnotes at the beginning of each chapter.

List of Tables

List of Figures

List of Abbreviations

AJs – adherens junctions

BBB – blood-brain barrier

BM – basement membrane

BMECs – brain microvascular endothelial cells

cAMP – cyclic adenosine monophosphate

CN – collagen I

CIV – collagen type IV

CPT-cAMP - 8-(4-chlorophenylthio) adenosine-3',5'-cyclic monophosphate sodium salt

ECs – endothelial cells

ECM – extracellular matrix

FBN – fibronectin

F:C:L – fibronectin: collagen IV: laminin

HA – hyaluronic acid

HA/Gtn – hyaluronic acid / gelatin mixture

HBMECs – human brain microvascular endothelial cells

HUVECs - human umbilical vein endothelial cells

JAIL - junction-associated intermittent lamellipodia

JAM – junction adhesion molecule

JAnaP – Junction Analyzer Program

LN - laminin

MFDs - microfluidic devices

PA – polyacrylamide

PR – permeated region

ROCK – Rho-associated kinase

RO-20-1724 - 4-(3-butoxy-4-methoxybenzyl) imidazolidin-2-one

TCM – tumor conditioned medium

TEER – Trans-endothelial electrical resistance

TJs – tight junctions

TGF-β – transforming growth factor- β

VE-cadherin – vascular endothelial cadherin

VEGF – vascular endothelial growth factor

ZO-1 – zonula occluden-1

Chapter 1 - Introduction

The blood-brain barrier (BBB) is the cellular unit that modulates transport between the circulatory and central nervous systems, thereby maintaining homeostasis of the brain microenvironment [1]. One role of the BBB is to protect the central nervous system from potentially toxic substances circulating in the blood. As a result, it also serves as a barrier for most therapeutic delivery into the brain. On the other hand, breakdown of this barrier is implicated in several neurological and neurodegenerative diseases, including cancer metastasis, Alzheimer's disease, Parkinson's disease, multiple sclerosis, and stroke [2–4]. The mechanisms of BBB breakdown, however, remain elusive. BBB disruption is reportedly associated with two phenomenon: (1) increased permeability (of proteins and molecules) and (2) massive cellular infiltration across the barrier [5]. In multiple sclerosis, for example, clinical symptoms have been found to correlate with a loss of junctional proteins at the BBB and an increase in adhesion molecules (e.g. ICAM-1, VCAM-1) on the surface of brain endothelial cells leading to elevated immune cell trafficking in the brain [5]. Still, in most diseases it remains unknown at which stage of progression (early versus late) the dysfunction occurs, which is critical for the development of therapeutics to prevent disease initiation or progression.

The World Health Organization predicts that by 2040, neurodegenerative diseases will become the second leading cause of death, exceeding cancer [6]. Current therapeutics for many of these disorders strictly target symptom management, rather than serving as corrective measures. As such, significant focus in the field has shifted towards the development of *in vitro* BBB models to study the physiology and

pathophysiology of this barrier and its related diseases to enable (1) more efficient development of barrier-penetrating therapeutics, and (2) mechanistic study of BBB dysfunction to identify targets for therapeutics development.

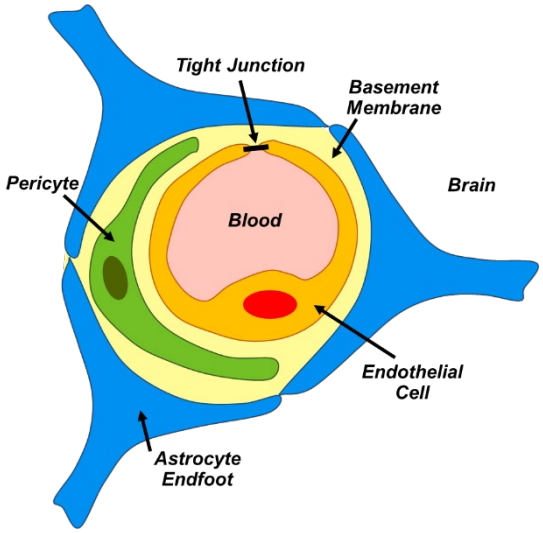

Figure 1.1. Schematic of the Blood-Brain Barrier. Cerebral endothelial cells wrap around and form tight junctions with themselves to create the microvasculature of the brain. Pericytes and astrocytes within the brain microenvironment wrap around and support the capillaries, which are enclosed by the basement membrane or basal lamina.

The BBB is composed of brain microvascular endothelial cells (BMECs), which sit upon a basement membrane primarily consisting of laminin, collagen type IV, and fibronectin (Figure 1.1, recreated based on [7]) [8]. This unit is reinforced by physical and biochemical interactions with neural cells such as astrocytes and pericytes, further enhancing the selectively permeable barrier properties [9,10]. BMECs express tight junction proteins (e.g., occludins, claudins), which anchor to actin cytoskeleton via zonula occludens (e.g., ZO-1) (Figure 1.2) [11–13]. The tight junctions work cooperatively with adherens junctions (e.g. vascular endothelial cadherin, VE-cadherin) to organize and stabilize the cell monolayer and regulate junctional tension [14]. The integrity of these junctions is required for the maintenance of normal

physiological processes. Therefore, understanding the key players driving junction stability could hold significant promise for therapeutic discovery.

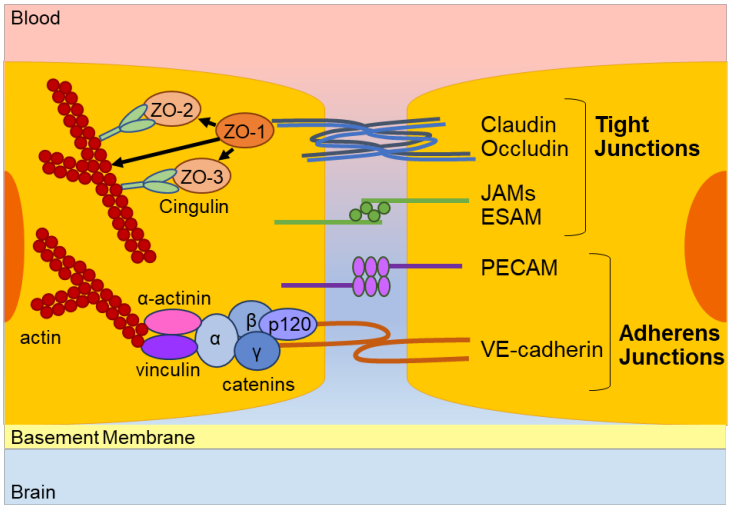

Figure 1.2. Schematic of the Cell-Cell Junctions in the BBB. Simplified and incomplete schematic presenting the components of the tight and adherens junctions. Claudins and occludin form the tight junctions, in addition to the junctional adhesion molecules (JAMs) and the endothelial selective adhesion molecule (ESAM). The most important adherens junction protein in endothelial cells is vascular endothelial cadherin (VE-cadherin), but, the platelet–endothelial cell adhesion molecule (PECAM) is also present. Several first-order adaptor proteins interact with the junctions within the cytoplasm, including zonula occludens 1, 2, and 3, (ZO-1,2,3), p120, and β- and γ-catenin. These can bind to other proteins such as cingulin, α-catenin, vinculin, and α-actinin, which bind to actin cytoskeleton, or directly interact with actin themselves (e.g., ZO-1).

Despite this, the mechanisms underlying junction disruption aren't fully understood. This is largely due to the lack of efficient techniques to quantify the junctional proteins as they are presented at the cell edge. Importantly, previous studies have linked the edge-presentation of VE-cadherin with junction and barrier maturity. Specifically, linear VE-cadherin structures parallel to the cell boundary are considered to be stable and mature, while immature junctions take the form of discontinuous focal adherens presenting a punctate or serrated morphology [15]. Therefore, a useful parameter in evaluating monolayer integrity is the amount of mature (i.e., continuous

or linear) versus immature (i.e., discontinuous) junctions localized at the cell perimeter. Quantification of this parameter, however, remains cumbersome since most current methods rely on manual, tedious measurement techniques. Here, we aimed to address this gap by developing the Junction Analyzer Program (JAnaP), a semi-automated program capable of measuring the percent of a cell perimeter covered by continuous and discontinuous junction, or no junction, as well as other characteristic junction parameters.

The overall objective of this dissertation was to investigate cell-cell junction phenotypes and their effects on endothelial barrier properties. We accomplished this by developing the JAnaP to quantify junction presentation, then applied this tool to understand the junctional changes involved in BMEC physiology and pathophysiology (Figure 1.3). In Chapter 4, the establishment of standardized junction phenotypes is discussed, as well as the development and validation of the JAnaP to semi-automate the analysis and quantification of these junction presentations. In Chapter 5, the influence of basic culture parameters (e.g., culture time and substrate protein) on junction phenotype is investigated, as well as how junction patterns contribute to the permeability of the endothelial barrier. In Chapter 6, the effects of cell contractility and substrate stiffness on junction presentation are presented, and finally, in Chapter 7, the effects of breast cancer cell secreted factors on junctions in the context of breast cancer metastasis to the brain is investigated.

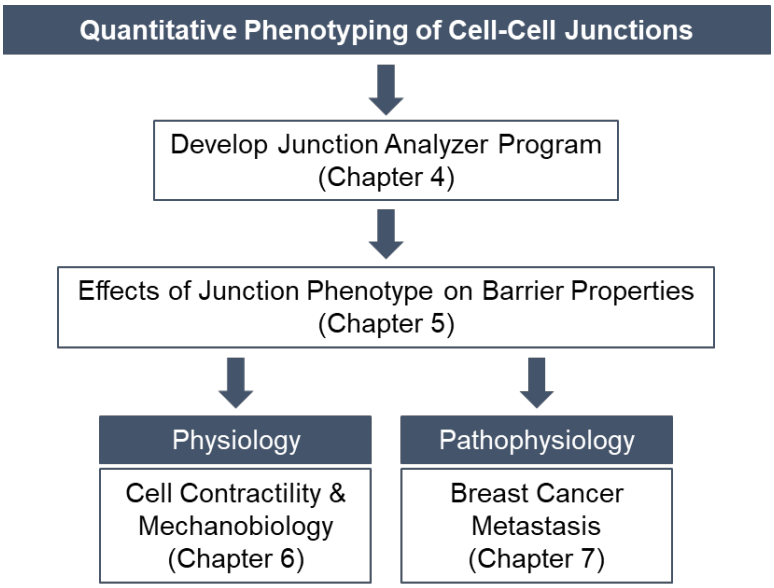

Figure 1.3. Dissertation Overview.

Chapter 2 - Background

2.1 Endothelial Cells and Cell-Cell Junctions

2.1.1 Vasculature

The vascular system provides the perfusion of nutrient-containing blood throughout the body, with blood vessels serving as the connection between all tissues and organs. Blood vessels are composed of endothelial cells (ECs) which line the inner surface and sit upon a basement membrane comprised of extracellular matrix (ECM) proteins (e.g. collagen type-IV, laminin, fibronectin, perlecan, agrin). The vasculature operates with selective permeability to mediate the transfer of ions, molecules, cells, and other materials from the luminal space to the adjacent tissues, and vice versa. It acts as a key regulator of immune responses and wound healing processes, and is implicated in the progression of several diseases [16]. Thus, there is significant motivation for the study of the vasculature and EC function.

Vasculature is primarily categorized into arteries, veins, and capillaries (Figure 2.1, from [17]). Arteries are thick-walled conduits that carry oxygenated blood away from the heart in a pulsatile manner. They contain long and narrow ECs that align in the direction of flow [18]. Veins are thin-walled conduits that carry de-oxygenated blood back to the heart, contain valves, and are not pulsatile [18]. They contain shorter and wider ECs that do not align in the direction of flow. Capillaries are thin, small vessels (less than 10 μm in diameter) with slow blood flow and are responsible for most of the diffusive exchange between the blood and the surrounding tissues. ECs also line the vessels of the lymphatic system, which is coupled to the vascular system, and is

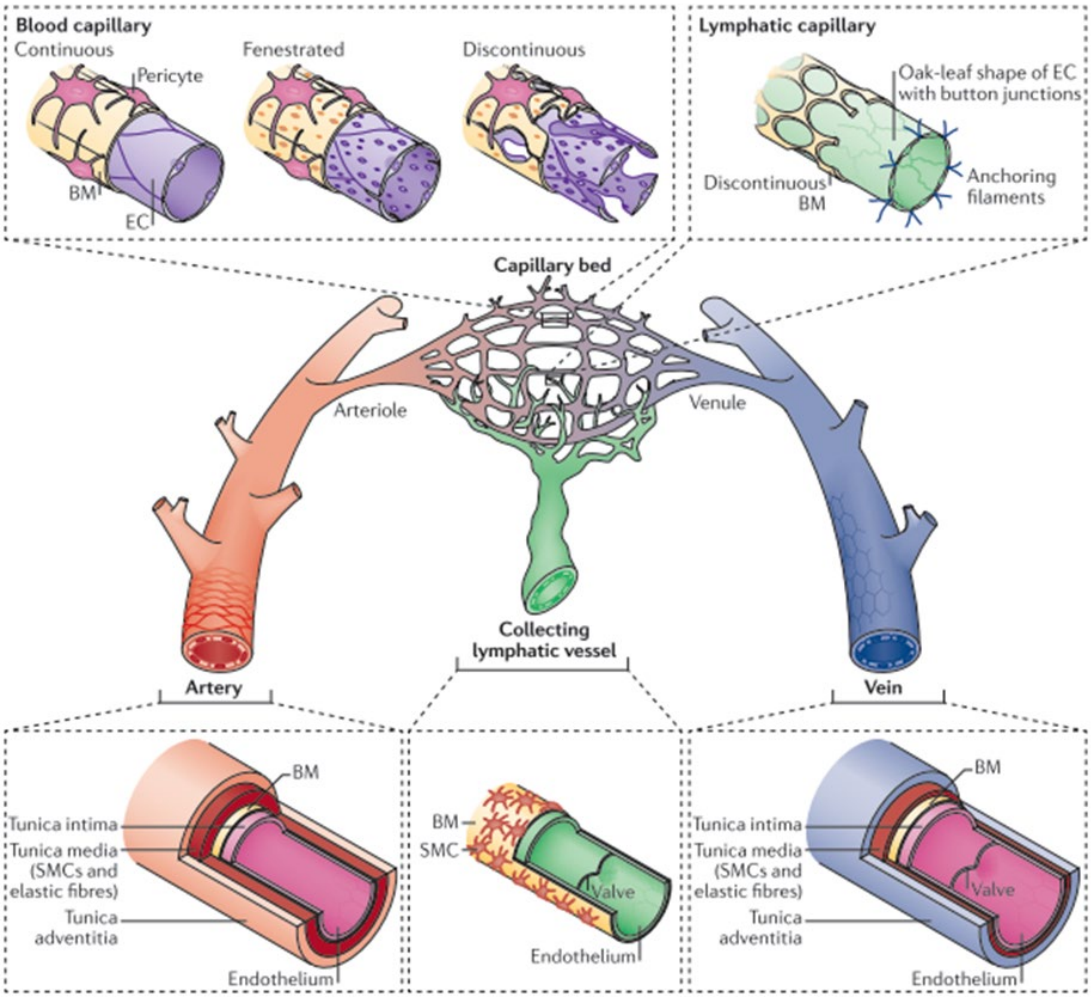

Figure 2.1. Organization of the Vasculature. The vasculature is organized into hierarchical networks of arteries (red), veins (blue) and interconnected capillaries, as well as lymphatic capillaries and collecting vessels (green) that drain fluid into the venous circulation. Arterioles, capillaries and venules constitute the microvasculature, the site where most intercellular communication occurs. Large arteries and veins are characterized by a continuous lining of ECs, basement membrane (BM) and layers of smooth muscle cells (SMCs). Blood capillary ECs can be continuous, fenestrated or discontinuous, and they have varying extents of BM and pericyte coverage. Lymphatic capillaries consist of oak-leaf-shaped ECs with specialized button-like junctions and anchoring filaments that pull the ECs apart and allow the entry of fluid under conditions of high interstitial pressure. Collecting lymphatic vessels have a sparse SMC coverage and luminal values that help with pumping and that prevent the backflow of lymph, respectively. The anatomy of capillary vessels is shown at the top of the figure and larger vessels are shown at the bottom. The tunica adventitia is the outer connective tissue covering of the vessel. *Reprinted from Potente, M. & Mäkinen, T. Vascular heterogeneity and specialization in development and disease. Nat. Rev. Mol. Cell Biol. 18: 477–494, 2017 with permission from Spring Nature.*

comprised of lymphatic vessels, lymph nodes, and lymphoid organs [17]. Lymphatic vessels are also organized in a hierarchical manner, comprised of lymphatic capillaries, pre-collecting vessels and collecting vessels. Excess interstitial fluid is removed by the lymphatic capillaries, which also provide an entry site for immune cells residing in the tissue to enter the lymphatic system. Collecting vessels, on the other hand, are dedicated to the transport of fluid and lymph into ducts that ultimately return to the vascular system. The endothelial cells lining each of these vascular and lymph categories have different phenotypes and contain different protein and trafficking structures to reflect their respective function and surrounding mechanical environment.

Endothelia are categorized as continuous or discontinuous, depending on the gaps and transport properties associated with the respective vascular bed. Continuous endothelium is further categorized as non-fenestrated or fenestrated, where increased filtration or transendothelial transport is observed [19]. The arteries, veins and capillaries of the heart, skin, lung and brain are non-fenestrated continuous endothelium, while the capillaries of, for example, the exocrine and endocrine glands, are categorized as continuous fenestrated endothelium. Fenestrae are transcellular pores, approximately 70 nm in diameter, that span the thickness of the EC and are typically covered by a 5 nm non-membranous diaphragm [19]. Discontinuous endothelium, on the other hand, contains much larger fenestrae, approximately 100 to 200 nm in diameter, and are not covered by a diaphragm. This endothelial category comprises the liver and some sinusoidal vascular beds. These differences in endothelial barrier structure translate to different transport and permeability properties. It is generally accepted that the paracellular route is used for passive transport of fluids and

small solutes, while transcellular shuttling via membrane-bound vesicles is used to move macromolecules across EC barriers. Basal permeability is therefore governed by the presence or absence of fenestrae, the activity of the transcytotic machinery, and the properties of the junctional adhesion proteins mediating EC-to-EC interaction [19]. For the purposes of this dissertation, the focus will be specifically on cell-cell adhesions.

Endothelial cell-cell adhesions include tight junctions (TJs), adherens junctions (AJs), gap junctions, and other adhesion molecules (e.g. PECAM-1) [20]. Tight and adherens junctions are involved in cell-to-cell contact, while gap junctions regulate the flow of water, ions, and small molecules between adjacent ECs [21]. Junction complexes are formed at sites of cell-to-cell contact by transmembrane proteins that form homophilic dimerized structures with the identical protein on neighboring cells. These proteins also link to various intracellular components, which tether to the cytoskeleton [22]. The integrity of these protein complexes is critical for vascular function since they play a key role in regulating cell behavior in both quiescent and activated (e.g., inflammation, angiogenesis) states, [21] influencing cell proliferation and apoptosis, the ability of cells to sense their positions, cell migration, cell polarity, and tubular structure formation [23]. Vascular dysfunction, including systemic loss of junctional integrity, is associated with several diseases including cancer, stroke, atherosclerosis, diabetes, hypertension, inflammation, ischemia, [20] Ebola hemorrhagic fever, [24] and bacterial sepsis [25,26]. Together, this emphasizes the role of junctional proteins in both physiology and pathology [27]. Since the focus of this dissertation is on cell-to-cell junctions, the discussion will primarily concentrate on TJs and AJs versus other junction types within the vasculature.

2.1.2 Endothelial Adherens Junctions

AJs are responsible for the initiation, maturation, and maintenance of cell-to-cell contacts [23]. They are primarily composed of cadherins, a family of calcium-dependent proteins. Included in this protein family is epithelial cadherin (E-cadherin), placental cadherin (P-cadherin), and heart cadherin (H-cadherin, or T-cadherin). Neuronal cells predominately express neural cadherin (N-cadherin), though N-cadherin is expressed in several cell types, including ECs and epithelial cells during epithelial-mesenchymal transition [28,29]. VE-cadherin, also known as CD144, is uniformly expressed in ECs, while N-cadherin is more diffuse throughout the cell membrane. The two cadherins share the greatest homology in the cytoplasmic domains, containing the binding domains for intracellular transcription factors like β-catenin and p120 [28]. β-catenin or γ-catenin (plakoglobin) connect the cadherins to the actin cytoskeleton, while p120 prevents endocytosis of the cadherins to maintain protein levels and mediate adhesion strength. These junctions therefore act as signal transducers through this tethering and retention of transcription factors, limiting their translocation to the nucleus, or by directly engaging signaling proteins or growth factor receptors [30].

Both VE-cadherin and N-cadherin are important for inhibiting cell proliferation and apoptosis [31], but the differences in the extracellular domains contribute to differences in protein function, especially during angiogenesis. Specifically, VE-cadherin is thought to mediate homotypic cell-cell adhesions between ECs, while N-cadherin facilitates heterotypic interactions between ECs and vascular support cells (i.e. vascular smooth muscle cells or pericytes) [28]. Therefore, N-cadherin is up-regulated with barrier disruption and is needed for the maturation of newly forming

blood vessels, while VE-cadherin is increased with barrier maturation, accompanied by a down-regulation of N-cadherin. As such, AJs are important during development and angiogenesis, whereas TJs form later, requiring AJs for organization.

In addition to β-catenin and γ-catenin, AJs also bind to α-catenin which tethers to zonula occluden-1 (ZO-1). ZO-1, along with homologous proteins ZO-2/-3, belong to the membrane-associated guanylate kinase homologs (MAGUKs), which express a PDZ-binding domain responsible for the anchoring of transmembrane proteins to cortical actin [21]. There are two splicing variants of ZO-1, an α+ isoform which contains an 80-amino-acid α-domain, and an α- isoform that does not contain the α-domain. While epithelial cells express the α+ isoform, the α- isoform is restricted to ECs. During early stages of junction formation, ZO-1 localizes to AJs. As junctions become more stabilized, the ZO-1 subsequently moves away to interact with TJs. In addition to actin and other transmembrane junctional proteins, ZO-1 is known to independently bind ZO-2 and ZO-3, as well as to various signaling molecules and transcription factors [32].

VE-cadherin can regulate the permeability of EC barriers in several ways. One mechanism increasing permeability is the internalization of VE-cadherin via clathrin-dependent endocytosis. While this process is inhibited by the cytosolic binding of p120 to VE-cadherin, increased internalization can occur by the activation of the small GTPase Rac via non-receptor tyrosine kinase protein, src [23]. Src can phosphorylate VE-cadherin, leading to the recruitment of components that drive VE-cadherin endocytosis. Notably, Rac can also be activated by VE-cadherin clustering, which can inhibit Rho and decrease permeability via decreased cellular contraction [33]. EC

contractility is also modulated by various stimuli (e.g. histamine, thrombin), which can phosphorylate myosin light chain and activate p21-activated kinase (PAK), driving increased contraction and resultant increases in permeability [34]. This mechanism of contraction-induced permeability is the result of centripetal contraction of the actomyosin ring exerting a pulling force on the junctional complexes (including TJs), since the junction proteins link to the actin cytoskeleton via actin-associated proteins such as ZO-1 [35]. Finally, VE-cadherin can also be cleaved via enzymatic proteolysis to increase permeability [12]. This mechanism is especially important when considering the disruption of junctions for the transmigration of other cells such as leukocytes and tumor cells, which can secrete these enzymes to promote extravasation and vascular leakiness [23].

VE-cadherin can also play a significant role in EC migration, proliferation and apoptosis. The inhibition of cell apoptosis is influenced by the interaction of p85, a component of the phosphatidylinositol 3-kinses (PI3K), to the VE-cadherin/catenin complex. Decreased VE-cadherin is associated with increased susceptibility of ECs to pro-apoptotic stimuli, since VE-cadherin clustering activates PI3K and Akt phosphorylation, which inhibits apoptosis. VE-cadherin also effects EC response to vascular endothelial growth factor (VEGF), influencing cell proliferation [36]. Association of VEGF-receptor 2 (VEGFR2) to the VE-cadherin/catenin complex contributes to density-dependent growth inhibition. VEGF induces clathrin-dependent internalization of VEFR2 where it activates mitogen-activated protein kinase (MAPK) and cell proliferation. This internalization process occurs more rapidly in the absence of VE-cadherin. Therefore, VE-cadherin inhibits VEGFR2 internalization, thereby

reducing VEGR2-signaling and limiting cell proliferation. Furthermore, the expression of VE-cadherin positively correlates with the activity of transforming growth factor-β (TGF-β), whose signaling influences anti-proliferation and anti-migratory responses in ECs [23]. Therefore, VE-cadherin influences EC stabilization by VEGFR2 inhibition and TGF-β activation, inhibiting cell growth and motility in mature EC barriers.

2.1.3 Endothelial Tight Junctions

TJs regulate the paracellular flow of ions and solutes, and limit the diffusion of lipids and proteins between the apical and basal sides of the cell [23]. As such, they are sometimes referred to as the "fence" proteins of the cell-to-cell junctional complexes. They are typically located in the apical region of the intracellular cleft, and play an important role in establishing apical-basal polarity within the cell barrier [30]. TJs develop after AJ maturation, requiring AJ formation for structural organization. TJs are primarily composed of transmembrane proteins including occludin, claudins, and JAMs. Similar to AJs, these TJ proteins link to several intracellular components such as ZO-1/-2/-3 and cingulin [21]. TJs complexes are associated with several signal transduction molecules (e.g. G-proteins, protein kinases) and other molecules, and therefore play a role in the regulation of EC growth and survival.

The claudin protein family comprises more than 20 members, approximately 22 kDa in size [32]. These proteins span the cell membrane four times, giving rise to two extracellular loops known to contribute to the para-cellular permeability. While the claudin family comprises several members, claudin-5 is specific to ECs [37]. Evidence in the literature suggests that expression of this protein is controlled by VE-cadherin, [38] and as such, their functions are highly interdependent. Claudins have been shown

to regulate size and charge selectivity. For example, in the brain, claudin-5 has been shown to regulate the flow of small molecules (less than 800 Da) [37]. Furthermore, mutations in different claudins to alter their charge has been associated with changes in their permeability to different anions and cations, indicating their role as electrostatic barriers in the endothelium [39]. Intracellularly, claudins can directly bind the three ZO molecules, generating a link between the TJ protein and the actin cytoskeleton [32].

Occludin was the first transmembrane member of the TJ architecture to be identified [32]. It is approximately 65 kDa in size and spans the cell membrane four times, generating two extracellular loops with both termini located intracellularly. This protein is associated with cellular adhesion and its variable expression along the vascular tree correlates with the permeability of the tissue. It is thought to contribute to the passage of non-electrolyte solutes across the barrier, as well as the fence function of the TJ complex. Like claudin, it too directly binds the three ZO-1 molecules intracellularly, linking to the actin cytoskeleton [32].

The JAM family is composed of at least five members including JAM-A (or JAM-1), JAM- B, JAM-C, JAM-4, JAM-L, and the coxsackie adenovirus receptor (CAR) [20]. JAM-A, JAM-B and ESAM, another protein that has many similarities to the JAMs, closely associate with TJs in ECs. These proteins contain PDZ domains responsible for anchoring the junction complexes to the actin cytoskeleton and also associate with components such as ZO-1 [23]. JAMs and CAR influence EC cell-cell interaction, mediate leukocyte transmigration, establish and maintain cell polarity, and regulate permeability [20,40].

The role of TJs in barrier permeability has been vastly studied. It is important to note, however, that the signaling pathways involved with TJs have been most extensively studied in epithelial cells, along with brain microvascular endothelial cells, likely due to the overexpression of these protein complexes in BMECs. Nevertheless, the most closely studied regulator of TJs and their role in EC barrier permeability is protein kinase C (PKC), the activation of which favors the assembly of nascent or growing TJs but weakens the barrier function of mature TJ complexes [38]. For instance, compounds that stimulate PKC generally induce the recruitment of ZO-1 [41] and occludin [42] in epithelial cells during junction assembly, but have been shown to disrupt TJs and increase paracellular permeability when applied to mature BMEC monolayers [43]. Activation of PKC has also been shown to decrease permeability by decreasing cell contractility via myosin light chain kinase inhibition [44]. Other kinases, such as tyrosine kinase and extracellularly regulated kinase 1 and 2 (ERK1/ERK2) are also known to exert different effects on TJs. For example, inhibitors of tyrosine kinase have been shown to prevent reassembly of disrupted TJs, [45] while inhibitors of tyrosine phosphatase decreased barrier function when applied to established barriers [46]. Stimulation of the ERK1/ERK2 pathways by hydrogen peroxide was shown to increase permeability by rearranging occludin localization and altering its association with ZO-1, while inhibition of this pathway blocked these changes in response to hydrogen peroxide treatment [47].

Heterotrimeric G-proteins, which signal through cyclic nucleotides (e.g., cyclic adenosine monophosphate, cAMP; cyclic guanosine monophosphate, cGMP), have been shown to associate with ZO-1 [38]. As such, enhanced barrier function, including

improved TJ structure, has been observed with cAMP elevation both BMECs and *in vitro* BBB models [48–50]. In contrast, elevated cGMP is evidenced to increase paracellular permeability, decreasing barrier function [51]. cGMP production is likely in response to nitric oxide, the signaling of which influences barrier permeability, since a nitric oxide donor is reported to enhance permeability while a nitric oxide inhibitor inhibits VEGF-induced permeability [52].

In addition to PKC and heterotrimeric G proteins, GTPases of the Rho family have also been shown to influence TJs and barrier function. Importantly, these effects require a delicate balance, since TJs have been shown to be sensitive to both excessive and insufficient levels of GTPase activity [38]. Notably, one effector of this activity is Rho-associated kinase (ROCK), which regulates paracellular permeability by myosin-mediated cellular contractility [53,54]. Together these examples demonstrate the numerous mechanisms by which TJs influence EC stability and barrier properties and illustrate the overlap between TJ and AJ function.

2.1.4 Junction Function and Vascular Beds

Many of the AJ and TJ proteins described above are universally found along the vascular tree. For example, VE-cadherin and claudin-5 are present in most blood vessels and in confluent EC in culture [21]. It is important to note that junction organization and distribution between vessels *in vivo* and *in vitro* is comparable in most vessel types [21]. The structure and composition of some junctional complexes, however, vary based on the vascular bed to which it belongs, driven by organ-specific requirements [20] (Figure 2.2, from [21]).

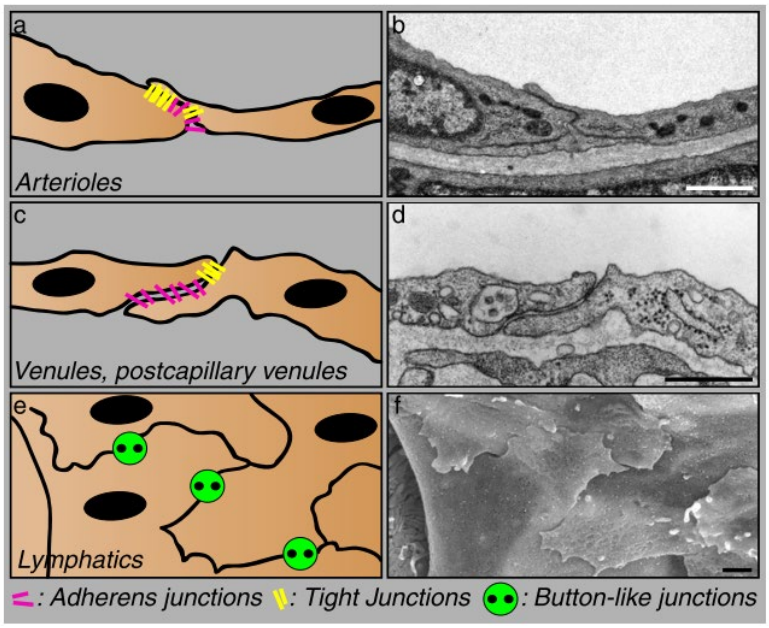

Figure 2.2. Example of Junctional Differences Between Vascular Beds. Representation of three types of endothelial junctions (*left*) and the corresponding electron micrographs (*right*). In small arterioles (a,b), EC junctions are tight, probably being formed by TJs intermingled with AJs to limit exchange between blood and tissues. In venules (c,d) junctions are formed by AJs, and small areas of TJs are frequently concentrated at the apical side of the intercellular cleft. In initial lymphatics (e,f), in which intercellular junctions control entry (intravasation) and drainage of fluid and cells from tissues, junctions are permeable, and endothelial borders have discontinuous button-like junctions with intermingled flaps resembling valve-like structures. AJ and TJ proteins are concentrated at the buttons and allow the flaps to open freely without disrupting overall vascular organization. The most distal collecting lymphatic vessels have continuous zipper-like junctions similar to those of blood vessels (not shown). In addition to AJ and TJ proteins, other junctional adhesive proteins and intracellular partners are present at endothelial junctions but, for simplicity, are not reported here. (scale bars = 1 μm) *Reprinted from Dejana, et al., Organization and signaling of endothelial cell-to-cell junctions in various regions of the blood and lymphatic vascular trees. Cell Tissue Res. 335: 17–25, 2009 with permission from Spring Nature.*

The endothelium of large arteries display strong junctions since they experience high rates of pulsatile blood flow [19]. ECs of the microvasculature, however, display varying junction structure. Arterioles typically display the tightest junctions, then capillaries, and then venules display junctions “loosest” in nature, likely resulting from the need of this vessel type to mediate increased transport of immune cells and plasma constituents in response to inflammatory signaling. The microvasculature of the brain,

however, is extremely unique (Figure 2.3, from [5]). Here, TJs are overexpressed for tighter regulation of permeability between the blood and the central nervous system. In areas where a more dynamic exchange between blood and tissue is required (e.g., in post capillary venules), the junctions are structured to allow for more leakage [21]. Another unique junction structure is found in lymphatic vessels, since they require a high volume of solute and leukocyte passage. To allow for this, the lymphatic ECs contain intermingled "flaps" and "buttons". The "button-like" regions contain concentrated TJs and AJs, while the "flap regions" contain PECAM, known to promote leukocyte trafficking. This allows the "flaps" to open without disruption of the junctional structures [55]. Notably, as lymphatic vessels become more distal, the junctions begin to resemble the blood vessel endothelium with more continuous "zipper-like" junctions.

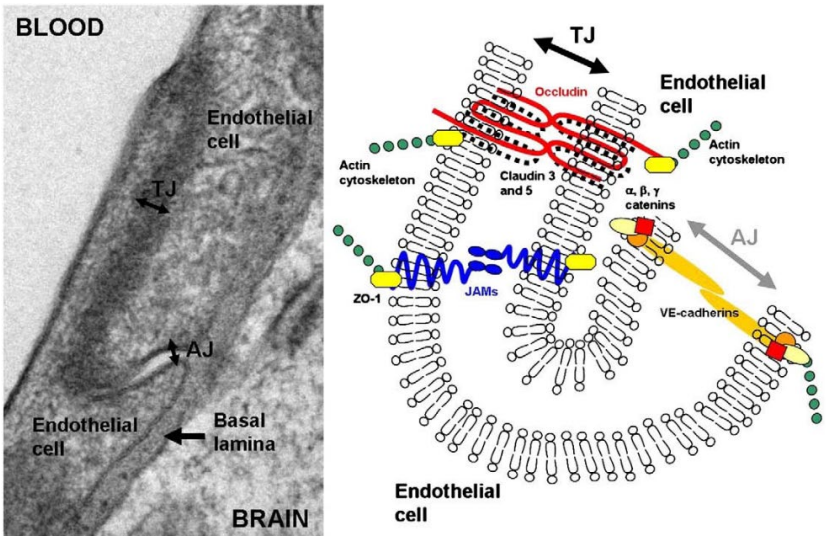

Figure 2.3. Image of BBB Junctions. Left: Electron microscopy of rat brain section showing a tight junction (TJ) between two cerebral endothelial cells. Right: Schematic view of cerebral TJ. Cerebral endothelial cells have close intercellular contacts due to the presence of TJs constituted by transmembrane proteins: occludin, claudins (claudin-3 and -5) associated with actin cytoskeleton via cytosolic proteins, such as the ZO family. Peripherally to TJs are localized JAMs and proteins of Adherens Junctions (AJs), such as VE-cadherin which is also associated with actin cytoskeleton via catenins. *Reprinted from Weiss, N., et al., The blood-brain barrier in brain homeostasis and neurological diseases. Biochim. Biophys. Acta - Biomembr. 1788: 842–857, 2009 with permission from Elsevier.*

2.1.5 Relevance to Dissertation

The focus of this dissertation is on the microvasculature of the brain. Disruption of the BBB, and specifically, alterations in junctional protein expressed within the endothelium, is implicated in many neurogenerative diseases [2]. As such, understanding the mechanisms driving these dysfunctional states could lead to therapeutic discovery for these otherwise often untreatable ailments. On the other hand, because the junctions of this barrier are overexpressed to tightly regulate permeability, most brain-targeted therapeutics are unable to penetrate the intact brain capillaries. This simultaneously drives the need to understand how to modulate junction presentation to circumvent this, to inform new treatment delivery methods.

Here, VE-cadherin, ZO-1, and to some extent, claudin-5, have been the focus of study. Many of the current techniques to study cell-cell junctions rely on the measurement of "bulk" barrier properties, rather than the junction proteins at the individual cell level *in situ*. The following section will discuss these current techniques in detail and discuss the limitations we sought to address by developing the JAnaP. While our focus here is on those specific proteins in BMECs, we believe that the developed tool is relevant to other junctional proteins and ECs from other vascular beds.

In addition to JAnaP development, we utilized the tool to gain new understanding about junctional proteins in BMECs. Throughout the dissertation, the use of agents known to elevate cAMP have been used, since these agents are known to increase junctional architecture and barrier properties (section 2.1.3). This provided a method of validating the JAnaP and studying the effects of elevated cAMP in various

biochemical and mechanical contexts. In chapter 6, we investigate the role of contractility in ZO-1 junctional presentation. While it is widely accepted that cell contractility can influence barrier properties (section 2.1.2 and 2.1.3), we explicitly investigate its role in ZO-1 junction localization and phenotype, and the modulation of this response by mechanotransduction. Finally, in chapter 7, we study the role of breast cancer secreted factors, and VEGF (section 2.1.3), on BMEC junction presentation.

2.2 Barrier Assessment and Junction Phenotyping

2.2.1 Evaluating Barrier Integrity

The current experimental tools for monitoring the dynamics of endothelial systems has been recently reviewed [56]. The two most closely studied parameters, include: 1) Permeability – which measures the permeability of molecular probes, and 2) Trans-endothelial electrical resistance (TEER) – which measured the permeability of small inorganic ions. The "gold standard" methods for measuring these parameters typically involve ECs grown on highly porous membranes that separate two fluid-filled compartments, commonly known as a Transwell insert or a Boyden chamber (Figure 2.4) [56]. Both methods, as well as their pros and cons, are discussed below.

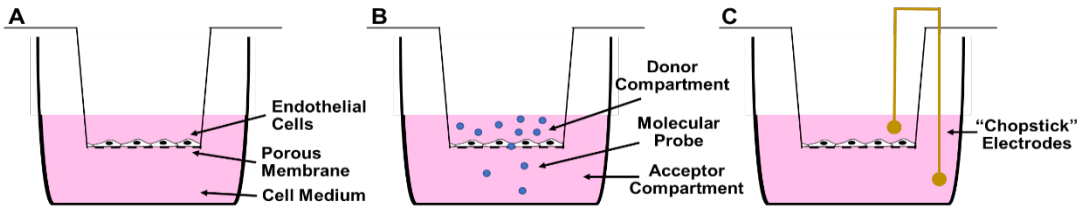

Figure 2.4. Transwell Assay for Permeability and TEER. Schematic of a Transwell insert depicting ECs grown on a permeable membrane separating two fluid-filled compartments (A). Permeability assay applying a molecular probe of known concentration to the top "donor" compartment then measuring the concentration of the probe in the "acceptor" compartment after a specific time has passed (B). TEER assay using "chopstick" electrodes to measure the resistance across the EC monolayer (C).

2.2.1.A Permeability Coefficient of Molecular Probes

To measure the permeability of molecular probes, Transwell assays are typically used (Figure 2.4.B) [56]. This setup requires that any solute transfer from one compartment to the other must cross the cell layer. Typically, a highly water-soluble, non-membrane permeable molecular probe that is not actively transported by the cells (e.g., dextran) is then placed into the "donor" compartment and the concentration of the probe in the other "acceptor" compartment is subsequently sampled. The probes are often radio- or fluorescently-labeled for ease of sample measurement [57]. This data enables the calculation of the permeability coefficient of that system, which is dependent on the functional properties of the ECs and is specific for the given probe. As such, use of probes of different molecular weight and charge can provide different insights into the size- and charge-dependent transport properties of the EC barrier. Notably, the size and permeability of the porous membrane itself (although typically negligible) must be considered [56].

While this assay can provide useful information about the cell-cell junctions, and a global reading of the overall barrier properties, it is easily compromised by defects in the monolayer. Small disruptions in the barrier can serve as short-cuts for the probes and significantly increase the overall permeability result. Additionally, this low-throughput assay requires an accumulation time prior to measurement, prohibiting real-time measurements of the barrier status and junction integrity [56]. Furthermore, this setup does not allow for the incorporation of mechanical cues, such as shear stress, which have been shown to influence EC function (discussed more in Chapter 3) [58]. Moreover, this assay only provides information about the "bulk" properties of the

monolayer, and does not provide measurement of any local parameters, thereby neglecting information about single-cell heterogeneities. Despite these limitations, this assay remains a popular technique to assess barrier integrity *in vitro* due to its ease of experimental use and co-culture capabilities.

To address some of the drawbacks associated with the traditional Transwell setup, several techniques have been developed. A common approach to enable real-time analysis, and the induction of shear stress, is to use microfluidic-based systems. One such example of this uses integrated microfluidic and laser technologies to establish a method with automated and time-resolved measurements of permeability coefficients [59]. To do this, ECs were seeded on a porous membrane separating two levels of a microfluidic channel. Laser-induced fluorescence (LIF) was used to detect fluorescently tagged bovine serum albumin as it permeated across the cell layer, enabling high-throughput and shear-based permeability studies. Expansion of this technology has the potential for pharmacological applications, given the *in vivo*-like drug screening approach, and could be coupled with additional parameter measurements for basic mechanistic studies.

To incorporate spatial resolution of barrier permeability, other approaches have been developed. One of the first techniques reported utilized ECs grown on a permeable membrane exposed to inhomogeneous flow fields. The membrane was then placed upon an agarose gel and 70 kDa FITC-dextran was allowed to diffuse across the monolayer, where it accumulated in the underlying gel matrix [60]. The membrane with the cells was then removed, leaving the gel containing dextran entrapped at the sites of permeation. The gel was subsequently cut into pieces with marked position relative to

the flow field and the fluorescence was measured to provide an indication of permeability relative to flow. While this setup provided enough resolution to show differences in EC permeability with differing flow regimes, the overall lateral resolution remained low due to diffusion of the dextran in the agarose gel away from the permeation site and well beyond the single-cell scale [56].

The development of an assay incorporating cells onto macroporous silicon chips further improved lateral resolution capabilities [61]. Notably, this system was reported for use with epithelial cell cultures but commented on its suitability for EC cultures. The silicon chip contained an array of densely populated and highly ordered pores of sub-cellular size (approximately 1 μm in diameter, located every 4 μm), open only towards the cell monolayers (approximately 10 μm deep). These pores enabled the collection and retention of the permeability marker at the site of permeation, the amount and location of which was quantifiable by confocal microscopy. Simultaneous immunostaining of cells enabled the visualization of cellular characteristics in conjunction with permeability analysis. This technique enables measurement of sub-cellular permeability, since it can discriminate between sites of transcellular permeation and paracellular diffusion. Development of the "XPerT" assay, however, further improved lateral resolution [62]. This assay made use of the biotin-avidin complex to decrease lateral diffusion away from the permeation site. For this method, gelatin was doped with biotin and used as the EC substrate. The permeating probe, FITC-labeled avidin, was then applied and subsequently immobilized to the biotin at sites of permeation, conserving the permeation route for subsequent analysis via microscopy. This technique was used in conjunction with EC immunostaining to correlate

permeability with various EC parameters (e.g., junction architecture). The lateral resolution of this system was controlled by the biotin-density of the gelatin substrate. The disadvantage of this method, however, is the restriction to avidin (or streptavidin) as the permeation probe, which limits systematic studies investigating the effects of probe size, charge, etc.

A completely different approach for the measurement of local permeability has also been reported, making use of scanning electro-chemical microscopy (SECM) to measure the transfer of a redox-active molecule across the cell barrier [63]. For this technique, a redox molecule is applied to the sample and a small working electrode, roughly hundreds of nanometers in size, applies a constant potential as it scans across the system. At the tip, a measurable current is generated by the oxidation/reduction reactions occurring in proportion to the local concentration of the redox-active species. To measure permeability using this setup, ECs are grown on a permeable membrane and the abluminal chamber is doped with the redox-species. This compound can then permeate across the cell barrier as the luminal EC surface is continuously scanned by the electrode, generating a "permeability map" based on the measured redox current at every pixel. This system is advantageous because it can differentiate between trans- and paracellular transport routes and can provide lateral resolution on the order of hundreds of nanometers. One disadvantage, however, is the length of time for data collection since one sample can take several minutes to be scanned. Additionally, the molecular probe is limited to electrochemically active molecules capable of redox-activity at potentials safe for cell viability and function. As such, the temporal resolution for this method remains limited. The potential to use this technique in

parallel with other imaging modes, however, could enable exciting parameter analysis for EC function.

2.2.1.B Trans-Endothelial Electrical Resistance (TEER)

For TEER, ECs are also plated on a porous membrane and placed between two fluid compartments, each containing an Ag/AgCl electrode to use direct current (DC, I) for measuring the voltage drop (V) across the barrier (Figure 2.4.C). Using Ohm's Law (V=IR), the resistance can be calculated to represent the ionic permeability (when corrected for the resistance contribution of the empty filter and the area of the membrane). One popular setup is the commercially available chopstick system, which allows the user to place the electrode pair into each compartment of a Transwell insert and simply record the resistance readout. While TEER is beneficial because it is non-invasive and can be performed in real time with high time resolution, there are several limitations to this method [56]. First, it is a global measurement, like the molecular probe permeability assay, such that any defect within the monolayer can create a short-cut to current flow and significantly decrease resistance measurements. Another challenge is that it requires a homogeneous electrical field throughout measurement, a requirement that even commercially available systems do not always meet [56]. With point-based electrode setups, like the chopstick system, the current often only flows through an unknown portion of the cell monolayer but is still corrected by the size of the entire area. This leads to an overestimation of the barrier tightness and is especially important when membranes with larger surface areas are used. Moreover, TEER results are often challenging to interpret, since the resultant resistance is a measure of several

contributors, not just junction protein expression. Nevertheless, TEER remains a commonly used tool for understanding ECs function and barrier properties.

To address some of the limitations to TEER measurements, the field has moved towards impedance spectroscopy (IS, or electrochemical IS, EIS) which instead uses alternating current (AC). In this approach, a sinusoidal voltage is applied, and the resulting steady-state current is measured. The relationship between these values can be described by the amplitude ratio of the voltage and current, and the phase shift between them. These are then fit to an equivalent circuit model (i.e. sequences of capacitors and resistors) and used to deduce information about the system. This technique allows one to distinguish between the resistance of the medium and the TEER across the cell-cell junctions, preventing the need for blank measurements of the empty setup. A benefit of this type of measurement is the ability to use coplanar gold-film electrodes, which allows the system to remain closed during measurement [64]. The electrodes are very thin (approximately 50-100 nm) so they remain transparent, enabling parallelization with microscopic methods. Importantly, the fabrication techniques of these micro-electrodes remain feasible, with the ability to generate small electrodes down to the single cell scale. One advantage to this type of electrode-chip is the spatial resolution associated with each electrode-pair, providing insight into the distribution of parameters rather than the average over the entire cell population. In some cases, electrodes have been integrated into the wells of 384-well devices, also enabling high-throughput readout capabilities.

An even further extension of local resistance measurements with lateral resolution is referred to as conductance or voltage scanning [65]. For this technique, a

uniform clamp current is established across an entire monolayer, while the potential is measured locally at the cell surface by a scanning electrode to generate a “resistance map” of the sample. This allows for recognition of local defects and can distinguish between, and separately quantify, the para- and trans-cellular current pathways, enabling the specific study of cell-cell-junction changes. Unfortunately, similar timing limitations exist as the SECM method described above.

Notably, one thing to consider when comparing the Transwell insert method versus the gold-film electrode-chips, is the difference in substrate permeability [56]. The electrodes serve as an impermeable surface, such that cells are only exposed to nutrients on the apical side, compared to the membranes, where both the apical and basal sides of the cells are exposed. On one hand, this makes the insert a more biomimetic system. On the other hand, it should be considered that most routine cell culture is still performed on impermeable surfaces, such as petri dishes and culture flasks. Therefore, while the insert acts as a more biologically relevant surface for transport purposes, one could argue for the use of ECIS and electrode-surfaces when performing structure-function studies and functional barrier analysis relative to the other substrates used for cell culture.

Another consideration is that while TEER can reflect the junctional tightness of ECs, alterations in cell morphology, without changes to the junctional structure, can also change the output values [56]. The amount of current following through the paracellular pathway will depend on the specific resistance of that pathway and the amount of available pathway [66]. One factor influencing the amount of pathway is the cell shape and size, with smaller and more circular cells providing more length of

paracellular pathway, increasing the number of regions available for current to pass. Accordingly, TEER will be higher larger cells when the resistance per length of junction is the same. For cells of the same size, however, elongated cells will likely have lower TEER values, attributed to the higher perimeter to surface area ratio compared to more circular cells. Indeed, shear-stress-induced elongation of ECs has been associated with decreased TEER values without changes to cell-cell integrity or junctional architecture [67]. Importantly, this relationship is consistent for all parameters describing paracellular barrier function, motivating the study of cell-cell junctions and paracellular transport properties in conjunction with cell morphology.

2.2.2 Junction Phenotype

Tight and adherens proteins present themselves in several patterns when localized at the cell-cell junctions. These diverse patterns have been described in many EC types in the literature, resulting primarily from visualization via immunostaining techniques. While the names for categorical phenotyping differs slightly between reports, the two overarching patterns that consistently emerge are the continuous, "linear-like" junctions, and the discontinuous, "interrupted" junctions. These discontinuous (or "zigzag" [68]) junctions are separated by regions where no apparent junction is localized to the cell edge, where the image intensity is equivalent to the cytoplasmic background, representing a "free cell border" [69]. Continuous lines of adherens junctions are considered characteristic of *in vivo* vessels [70]. *In vitro*, these types of junctions are also found in highly confluent cultures, [71] and after stimulation with biochemical agents, such as hydrocortisone [72], or mechanical cues, such as shear stress [67] and biomimetic substrate stiffness [15]. Interrupted junctions, on the other

hand, are characteristic of subconfluent cultures, in migrating ECs (e.g., during wound healing) and in response to inflammatory mediators (e.g., TNF-α) [24,68,73]. For VE-cadherin, these are the sites of junction remodeling and are termed focal adherens junctions, molecularly identified by the association of vinculin at their attachment point to radial actin bundles [54]. In each case where discontinuous junctions are observed, the mechanism for cellular response involves changes in cell shape, increased motility, and the transition of actin from junction-associated filaments to stress fiber formation [71,74].

Alterations in actin fibers have been directly linked with VE-cadherin presentation, where linear VE-cadherin is observed in cells with low tension and active Rac, whereas discontinuous focal adherens junctions are observed in cells experiencing high tension and active Rho [75]. Immature junctions are presented as punctate regions or have a serrated morphology approximately perpendicular to the cell edge. As junctions mature, they become larger and form more linear structures parallel to the cell boundary [15]. Functionally, linear junctions are associated with decreased permeability, [76] whereas junction disassembly and increased permeability have been linked with increased transmigration of leukocytes and breast cancer cells through BMECs, resulting from increased contractility via the Rho/ROCK signaling pathway [77]. In this specific example, linear patterns of tight junctions were present at the cell-cell border of BMECs, but shifted to a “discontinuous, segmented and dotted” phenotype within 8 hours of co-culture with a human small cell lung cancer cell line [77]. Similarly, treatment of human umbilical vein ECs (HUVECs) with endothelial hormones (e.g., TNF-α, VEGF) shifted VE-cadherin junctions from “linear

stable/mature" junctions to "perpendicularly orientated remodeling cell-cell junctions", mediated through a Rho/ROCK-actomyosin contractility mechanism [54]. Interestingly, though, others have reported that increases in permeability resulting from TNF-α are the result of decreased occludin and re-distributed ZO-1, rather than the contractile mechanisms mediated by Rho/ROCK, since inhibition of this pathway but not MLCK prevented the effects of TNF-α [73].

In one example, a model of brain injury (via cell stretching) showed redistributed ZO-1 into a punctate pattern at the cell edge with diffuse presentation across the cell body in BMECs [78]. In another example, the pattern of claudin and occludin were described "frayed" in iPSC-derived BMECs, a presentation that shifted to "continuous" upon treatment with retinoic acid, known to improve BBB properties in various BMEC types [79].

Another group described VE-cadherin junctions as displaying linear, reticular, interrupted and plaque morphologies (Figure 2.5, from [69]). The dynamics of these adherens junction clusters are thought to be regulated by fusion and fission [67]. Nascent cell junctions are mediated by actin-drive lamellipodia which bring adjacent cells together to promote adhesion receptor binding and cell adhesion complex formation [80]. The lamellipodia then transition to filopodia which generates highly dynamic and discontinuous adherens junction patterning in growing cell cultures. Time-lapse imaging has shown consistent transitions between discontinuous and continuous patterning, though these transitions decreased with increasing cell density, as the continuous phenotype became more persistent [71]. The mechanism of gap closure has recently been discovered, reportedly governed by VE-cadherin–mediated

cell adhesion and ARP2/3-controlled and actin-driven junction-associated intermittent lamellipodia (JAIL) formation [69]. JAIL are small plasma membrane protrusions that exist between VE-cadherin junctions to form new adhesion plaques that then become incorporated into junctions [71]. More JAIL is observed in regions of discontinuous junction while continuous junctions reduce their size. This process constitutively remodels VE-cadherin patterns and maintains the integrity EC junctions.

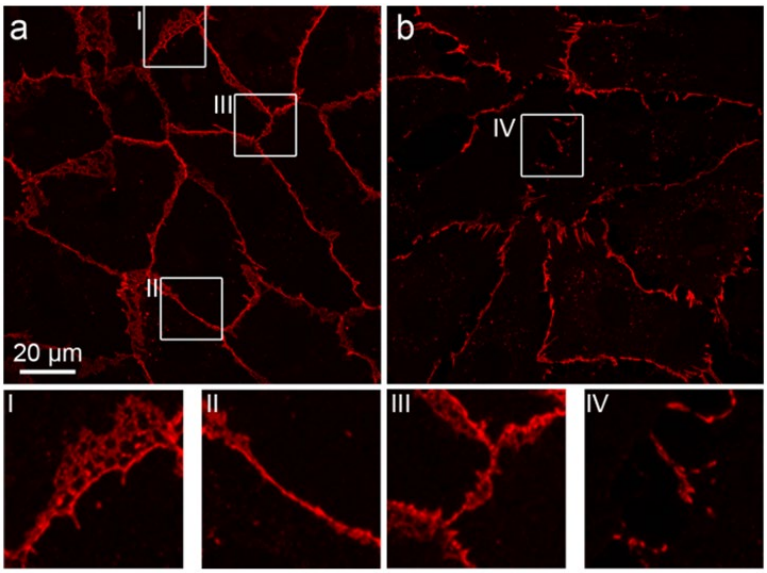

Figure 2.5. Demonstration of VE-cadherin structures in HUVEC cultures. (a) Confluent and (b) subconfluent HUVEC cultures are labeled with antibodies against human VE-cadherin. Confluent cells display mostly reticular (cropped area I) or linear (cropped area II). Plaque-like structures are seen in both confluent and subconfluent conditions (here shown in confluent cells). (cropped area III) structures along the junctions. In contrast, in subconfluent cultures, VE-cadherin appears overall interrupted (cropped area IV). This diversity in VE-cadherin appearances is a challenging task for image analyses. *Reprinted from Seebach, et al., "The CellBorderTracker, a novel tool to quantitatively analyze spatiotemporal endothelial junction dynamics at the subcellular level." Histochem. Cell Biol. 144: 517–532, 2015 with permission from Spring Nature.*

2.2.3 Current Methods to Quantify Junction Phenotypes

Despite the plethora of evidence regarding junction phenotypes, only a handful of methods have been described for the quantification of these parameters. One example of a method for junction quantification simply counted the occurrence of each

individual junction to report the discrete number of tight junctions localized to the cell border [81]. Another approach commonly used is to measure the pixel intensity of the junctional protein compared to the brightness of the cytosolic-background to gauge the relative expression in various experimental conditions [71,82]. As described by Fan et al., this method calculates the corrected cell membrane intensity for each junctional protein by subtracting the average noise intensity for multiple random regions for each image from the raw intensity profile of the entire cell junction [82]. In this example, they went on to perform subsequent analysis such as the "staining percentage" which calculated the percent of pixels with positive intensity values localized around the cell boarder. Additionally, this group reported the count and area of gaps in the junctional staining, as manually traced in ImageJ, which they reported as the number and percentage per area. While these methods provide insight into how frequently junctions are present, and the relative comparisons between experimental conditions, they do not provide any information about junction morphology.

One approach to quantify junction characteristics is to measure the width of the junctions (or junction gaps) around the cell edge by drawing a line across the junction, perpendicular to the cell perimeter [53,54,83,84]. The intensity profile of the line is then fit to a Gaussian (or two-gaussian, in the case of junction gaps) curve. The width measurement is then determined as some parameter of the Gaussian fit, such as the full-width-at-half-max (FWHM) [85] or the width of the fit 20% above background pixel intensity [84]. One disadvantage to this approach is that it only provides measurements at discrete locations, selected by the user. As such, it does not calculate the width throughout the entirety of the cell and can therefore be skewed by the regions selected

for measurement. Another approach to measure junction size was described by Ting, et al., who developed a custom-written MATLAB code to measure pixel intensity along the cell borders [86]. To do this, disconnected regions between adherens junctions were joined via pixel dilation and the boundaries were isolated from the background by subtracting the pixels below 30% of the maximum intensity. The cell boundaries were then defined using the watershed algorithm and a ribbon of interest was identified around the boundaries with a width of 10 pixels. Within this ribbon, the total pixel intensity was calculated, then divided by the total ribbon length and the number of cells to generate the amount of junctional protein per length per cell. Notably, this measurement was reported as a ratio relative to the control value rather than per cell quantified output. For both examples, the phenotypic detail on a per cell basis is limited.

To instead measure "how linear" a junction is, one group reported the calculation of the "junctional linearity index" [87]. This parameter is calculated by dividing the length between two vertices or cell junction points, as measured using the Straight-line tool in ImageJ, by the length of the junction, as measured using the Freehand-tool. An index value of 1 indicates a perfectly straight junction, while lower values indicate a more tortuous phenotype. This clarifies the shape of continuous junctions that span the full length between cell vertices, however, it does not provide information on any discontinuities present at the cell borders.

To measure the extent of junction coverage, the calculation of the "area fraction index" has been reported [88,89]. For this, images are corrected for background signal using ImageJ and a threshold value is applied to the gray scale intensity profile to isolate junctions. The images are then converted to binary and outlined using the

ImageJ outline filter to determine the perimeter of junction staining. The total perimeter is then normalized by the square root of the cell number within the image, and the value is typically normalized to the value of the control condition. For this parameter, an index of 1 represents fully continuous junctions while decreased values indicate more discontinuous or non-existent junctions. While this method provides a useful tool to gauge overall junction coverage, it only provides relative measures and calculates results on a per image basis. This inherently provides an average measurement of the monolayer, without providing details about cell-cell variability.

The measurement of phenotypic detail on a per cell basis has been reported as a purely manual technique [15]. In one example, the fraction of cells expressing a "frayed" junction phenotype, defined by any cell-cell contact point with discontinuous junction, was calculated by manually counting the number of cells presenting this pattern [79]. In another example, the percent of the cell perimeter covered by linear junctions was calculated by tracing regions of linear VE-cadherin, identified by the eye of the user, in ImageJ. The values were then summed and compared to the whole cell perimeter to provide a fraction of linear versus non-linear coverage. While this method provides more details about cell-to-cell variations in linear junction presentation, it neglects the presentation of any other junction phenotype. Admittedly, the same approach could be used to trace the regions of discontinuous junctions and calculate a comparable parameter but given that this method is completely manual in nature, that would be an extremely tedious and time-consuming task.

To prevent the need for completely manual border tracing, some automated approached have been developed. One of the first developments was the "live wire"

method which enabled semi-automated boundary extraction [90]. This method used a segmentation algorithm to convert an image into a weighted graph that assigns a cost value to each pixel based on features typically associated with an object edge (e.g., high-intensity gradients). Using a mouse click to seed a point near the object boundary, the algorithm can compute the path between that and the next point following the minimal cost pixels, thereby reflecting part of the object boundary. Subsequent seeding points allows for complete boundary tracing. This approach is more efficient and enables high reproducibility and accuracy compared to a solely manual process [69]. However, while this method allows for semi-automated boundary identification, it is not tailored to cells or their junctions, and as such, requires adaptation to quantify edge-localized protein phenotypes.

One benefit of the live wire method is that the point seeding enables the control and monitoring of segmentation by the user. This level of interaction, though, is not ideal for more automated image processing, especially for cellular networks, where weak gradients are often present. To build on this limitation, the CellBorderTracker (CBT) was developed [69]. This package enables dynamic tracing of cell junctions within a time-lapse sequence. While this is generally automated, it does require an interactive cell boarder extraction step where seed points are generated to identify the cell boarders in the first image of every sequence. This program can output the protein distribution patterns and junction dynamics, including gap formations, as well as cell shape changes and migration velocities, over time. This program holds significant potential for efficient analysis of junction dynamics. It is not clear, however, on what

basis the data is provided (i.e., per cell or per image) and to what level of detail the protein distribution patterns are reported.

Overall, the current methods in the field suggest a desire to quantify junction localization and a need to characterize phenotypic parameters *in situ*. The current approaches enable one to gauge junctional protein characteristics, though not without significant limitation. An improved technique combining several of the parameters described above, calculated in an efficient manner, could provide significant insight into the function of junction phenotypes and the response in physiological and pathophysiological applications.

2.2.4 Relevance to Dissertation

Phenotypic differences in junction presentation are apparent in the literature and significant evidence suggests that these differences relate to various stages of junction maturity, thereby influencing EC function. Importantly, these diverse patterns of junction proteins are widely heterogenous even within one single cell, thus significant non-uniformities are present in any one given monolayer [69]. As such, it seems clear that better standardization and quantification of these parameters is needed to collectively understand the mechanisms driving these alterations and how they influence the barrier-specific properties of the endothelium. The current methods in the field for characterizing junctions *in situ*, however, are lacking phenotypic classification on a full-cell and per-cell basis. As such, we developed the JAnaP (Chapter 4) to quantify the percent of the cell edge presenting various junction phenotypes. To begin to understand the influence of junctional architecture on barrier properties, we then studied BMEC junction phenotype in conjunction with TEER, as well as local and

global permeability, as described above in section 2.2.1 (Chapter 5). Finally, we characterized junction presentation the BMECs in several contexts, as examples of applications for which junction phenotyping can be informative and useful (Chapters 6 and 7).

Chapter 3 - Vascular Endothelial Cell Mechanosensing: New Insights Gained from Biomimetic Microfluidic Models†

3.1 Introduction

In vivo, cells of the vascular system are subjected to various mechanical stimuli (Figure 3.1, citations refer to: [1]-[16], [2]-[91], [3]-[8], [4]-[92], [5]-[93]) and have demonstrated the ability to adapt their behavior via mechanotransduction. Mechanotransduction is the process by which cells convert biophysical or mechanical stimulation in the local cellular microenvironment into intracellular or biochemical signaling which regulates the cell response [94,95]. Recent advances in microfluidic and "on-chip" techniques (e.g. 3D printing) have provided the technology to study these alterations in cell behavior. Contrary to traditional *in vitro* cell culture, these microfluidic devices (MFDs) provide the opportunity to integrate multiple mechanical cues (e.g. shear stress, substrate stiffness) with *in situ* quantification capabilities (Figure 3.2). Additionally, they provide precise geometries towards physiological dimensions and length scales, allowing for decreased cell numbers and material quantity for synthesis and experimentation. Thus, they can be used to recapitulate the *in vivo* mechanical setting and systematically vary microenvironmental conditions, using minimal resources, for improved mechanobiological studies of the endothelium. MFD types and various design considerations have been recently reviewed in detail [96], and as such, will not be explicitly discussed here. In Table 3.1, we highlight unique features

† This chapter was adapted from K.M. Gray and K.M. Stroka "Vascular Endothelial Cell Mechanosensing: New Insights Gained from Biomimetic Microfluidic Models". *Seminars in Cell and Development Biology* 71, 106-117 (2017). Permission was not required by Elsevier to use this material in this dissertation.

of MFDs that have allowed for discovery of new biological information and mechanisms of mechanosensation, as we review here.

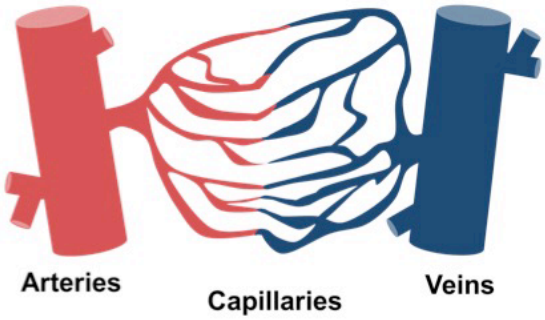

Type	Arteries	Capillaries	Veins
Vessel Diameter	0.02–10 mm [1]	5-8 μm [1]	0.03–12.5 mm [1]
Shear Stress	4–30 dyn/cm^2 [2] Pulsatile	10–20 dyn/ cm^2 [2]	1–4 dyn/ cm^2 [2]
ECM Stiffness	~2.7 kPa [3]**	d.n.a.	d.n.a.
Wall Composition	EC, VSMC, I/M/A [1]	EC, BM, ECM, Pericytes [1]	EC, VSMC, I/M/A [1]
Cyclic Strain	~7-11% [4]	~10% [5]	<10%

Figure 3.1. *In vivo* Data for Vascular Stimuli. The major types of vasculature in the body, and the types of biophysical cues they are exposed to in healthy microenvironments *in vivo*. Values collected from human samples, except **bovine samples. I–intima, M-media, A–adventitia, VSMC–vascular smooth muscle cells, d.n.a.-data not available.

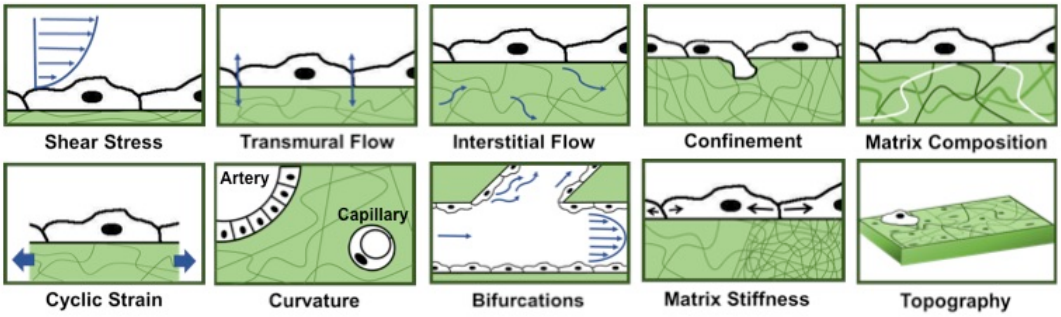

Figure 3.2. Mechanical Cues Presented to ECs. Biophysical stimuli that have been integrated in MFDs for *in vitro* mechanosensing experiments. Blue arrows represent direction of each mechanical stimulus (e.g., in case of shear stress, transmural flow, interstitial flow, cyclic strain, and bifurcations), while black arrows indicate contractile forces in endothelial cells (e.g, in case of matrix stiffness). These biophysical cues may be active (e.g., shear stress, transmural flow, interstitial flow, and cyclic strain), or passive (e.g., confinement, matrix composition, matrix stiffness, curvature, bifurcations, and topography). Wavy lines represent extracellular matrix and basement membrane components.

Adequate EC and vascular modelling provides for enhanced understanding of disease progression, design of cell separation [97] and drug delivery systems, and the development of biomaterials for tissue engineering applications (Figure 3.3 [98]). As such, several reviews have recently been published which nicely outline the advances in MFDs for mechanobiology and mechanotransduction [95,99,100]**.** These reviews broadly cover multiple cell and tissue types and discuss the suitability of the devices to mimic the physiologic environment. Other reviews describe the use of MFDs for specifically studying angiogenesis and the microvasculature [101–104], but focus on specific organ microvasculature or non-mechanosensing aspects of EC function. MFDs have been particularly useful in studying the role of EC mechanobiology in the transmigration of immune and/or tumor cells, and have been reviewed elsewhere [105–107]. Here, we will discuss the advances in knowledge about EC mechanosensing resulting from the design and application of biomimetic on-chip and microfluidic platforms. Specifically, we will focus on the novel reports within the last five years from using devices designed to study EC mechanobiology, rather than technical fabrication approaches or mechanosensitive properties learned using alternative techniques.

3.2 Shear Stress & Hydrodynamic Forces

When the heart beats, blood is pumped throughout the body due to cycles of contraction and relaxation of the ventricles and atria [108]. This flow results in shear stress experienced by ECs, the magnitude of which is dependent on many *in vivo* factors. As such, several on-chip systems, capable of a range of shear stresses, have been designed to study EC responses.

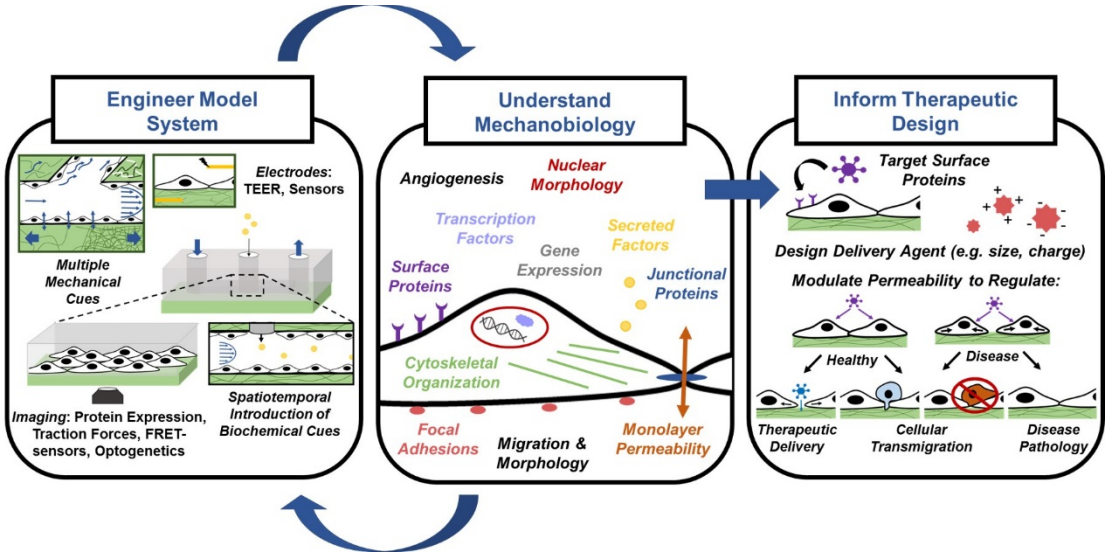

Figure 3.3. The Process of Designing MFDs to Study EC Mechanobiology. MFDs allow for unique capabilities in engineering a model system, including the incorporation of multiple mechanical cues, electrodes for sensing, imaging modalities, and spatiotemporal introduction of biochemical cues. These MFDs can be used to understand endothelial cell mechanobiology through exploration of the role of various proteins, pathways, processes, and ultimately functionality, in the cells. Revelation of new biological information could help re-engineer the model system to enhance physiological relevance or could help inform design of new therapeutics.

3.2.1 Elongation, Cytoskeletal Realignments, & Junctional Relocation

Numerous reports have shown that in straight vessels, ECs elongate and align in the direction of flow, and redistribute junctional proteins. These (and other) responses depend heavily on the magnitude [109–112], and the laminar (versus pulsatile) continuity [113], of the shear stress applied. This well-characterized shear-induced response has conveniently come to serve as a "proof-of-concept" feasibility check in many new device designs, particularly useful for organ-on-chip systems [108,114] (recently reviewed in [16,115–118]).

Mechanistically, the ability of cells to sense the direction and strength of shear stress is still largely unknown and has been suggested to occur via mechanisms involving the glycocalyx, PECAM-1, stretch-activated ion channels, receptor tyrosine

kinases, VE-cadherin, and VEGF-receptor. Recent work has also provided evidence that shear stress mechanotransduction can occur through the hydrodynamic drag applied to EC nuclei [119]**.** Tkachenko *et al.* showed that HUVECs developed spatial polarity of organelles at a rate proportional to the shear stress, with the golgi apparatus and microtubule organizing center biased to the upstream side of the nucleus, and that flow-induced polarization was resisted by the acto-myosin cytoskeleton. This result suggests that relocation of nuclei downstream of applied force prompts EC polarization.

Interestingly, flow-induced elongation reportedly depends on EC-type. HBMECs, for example, do not transition from a cobblestone morphology in response to shear (16 dyn/cm^2) [120]**.** In this study, actin fibers remained randomly oriented, and while junctional ZO-1 decreased, western blot analysis suggested increased ZO-1 (and beta-catenin) expression under shear stress. These results suggest an evolutionary advantage for ECs of the BBB to resist shear-induced shape alterations. This is particularly relevant, as MFDs have shown significant promise in BBB-on-chip applications, which has been thoroughly reviewed in [121,122]. This difference in response based on EC-type, however, should be thoroughly considered when planning MFD-based studies. Helms, et. al. nicely presented the detailed differences reported in the literature of the approximately thirty different EC types and co-cultures reported for *in vitro* BBB evaluation [121]. In general, we urge researchers to consider the EC source in combination with a physiologically-relevant shear stress for that type of micro- or macro-vessel. As shown in Table 1, the majority of MFDs in recent literature have incorporated HUVECs or bovine aortic endothelial cells (BAECs), both large artery

ECs, with only a few studies utilizing microvascular ECs. As the field moves forward, MFDs will be useful tools to study the effects of physiologically-relevant mechanical cues on a wide range of ECs from different tissue sources.

3.2.2 Calcium

Intercellular calcium serves as an important messenger that regulates an abundance of spatiotemporal cellular signals. As such, the calcium ion (Ca^{2+}) concentration within the cell is tightly controlled through various machineries (e.g. ion transporters, cytosolic calcium-binding proteins) [123]. Multiple calcium regulators have been implicated in mechanosensitive mechanisms, so several microfluidic approaches have been developed to study the response of intracellular Ca^{2+} to mechanical stimuli.

ECs are exposed to ATP contained in the blood. Both shear stress and ATP serve as regulators of EC function (e.g. proliferation, migration, apoptosis), and have been identified as regulators of dynamic Ca^{2+} signaling [124]. Their synergistic influence was recently studied using adhesive micropatterns to modulate the elongation and orientation of BAECs exposed to shear stress [125]. Flow induced retraction upstream of the cell, while lamellipodia formation was observed downstream. Ca^{2+} increase was reported in BAECs patterned orthogonal to flow; however, the direction of intracellular Ca^{2+} waves were more heavily influenced by cell polarization (versus flow direction). The group speculated that the orientation of Ca^{2+} waves is due to the organized actin filaments within the polarized cell, since waves are correlated with ATP release from caveolae-rich regions [126] associated with actin microfilaments [127,128]. Chen *et al.* reported a single peak Ca^{2+} response in HUVECs under steady shear, with a second dynamic response which occurred at the same frequency as a dynamic ATP signal

introduced to the system [124]. These results suggest that a combination of shear and ATP signals play a significant role in EC Ca^{2+} signal transduction induced by blood flow.

Several reports indicate that mechanotransduction involves mechanosensitive ion channels [129]. Transient receptor potential vanilloid 4 (TRPV4), for example, is a mechano-activated cation channel [130] that has been implicated as a signal transducer of shear stress. The effects of the TRPV4-selective agonist, GSK1016790A, in response to a range of shear stress (up to 63 dyn/cm^2) was recently reported [131]. A reduction in EC response time was observed with increasing shear stress, while increasing GSK1016790A at each shear stress level reduced the peak response time, suggesting that a shear stress-dependent sensitization exists for GSK1016790A-evoked Ca^{2+} signaling. In BAECs, increases in intracellular Ca^{2+} were proportional to shear stress magnitude, reportedly due to an influx of Ca^{2+} from the extracellular space rather than release from intracellular storage [129]. Activation of the TRPV4 channel was necessary for this flow-dependent response, as use of its antagonist, HC067047, reduced Ca^{2+} influx, thus supporting the possibility of a shear stress sensitization mechanism involved in TPRV4 function.

Interestingly, Compton *et al.* exposed HUVECs to hydrodynamic shear at the microscale via micro-bubble bursts termed “microtsunamis” [132]. While this is not a microfluidic approach, this technology provides for extremely high-throughput capabilities to determine the key regulators of mechanotransduction involved in Ca^{2+} signaling. Microtsunami-induced Ca^{2+} signaling was attenuated by dose-dependent inhibition of the inositol triphosphate receptor, suggesting Ca^{2+} release by the

endoplasmic reticulum via G-protein-coupled receptor signaling. Thus, there seem to be conflicting reports about whether the cell response relies on Ca^{2+} release from intracellular versus extracellular space. Together, these results support that mechanical stimuli play a role in EC Ca^{2+} signaling and suggest the importance of incorporating and controlling shear stress into experiments for mechanistic study.

3.2.3 Surface Proteins & mRNA

Shear stress has been shown to influence surface receptor expression and other signaling proteins in the endothelium. The role of mechanosensitive microRNAs in EC responses to shear stress and redox state was recently reviewed [133]. Here, we will outline the influences of shear stress on protein and mRNA expression as determined via MFDs. Notably, several groups have developed MFDs to simultaneously expose ECs to varying magnitudes of shear stress and biochemical cues, and evaluated the resultant expression of surface marker proteins and mRNAs (e.g. ICAM-1, VCAM-1, endothelial-to-mesenchymal transition markers), often in comparison to previous literature [134–136].

To investigate the effects of localized cytokine exposure, a model was developed to deliver TNF-α to the middle section of a blood vessel from the "tissue side" [137]. As expected, BAECs in the middle section (i.e. cytokine-activated) exposed to 12 dyn/cm^2 exhibited significant ICAM-1 increase. Interestingly, ICAM-1 expression was also increased downstream of activation (compared to upstream) even though the cells themselves were not activated, thus introducing the concept of spatial resolution in EC activation via cytokine signaling.

Vasculoprotection, via high laminar shear stress (HLSS), is reportedly modulated through Kruppel-like factor 2 (KLF2), a transcription factor involved in endothelial homeostasis via nitric oxide (NO) production [138]. Connexin37 (Cx37) is a gap junctional protein highly expressed in healthy endothelium, but not in regions of atherosclerosis [139]. Pfenniger *et al.* reported increased Cx37 and KLF2 expression after ECs were exposed to HLSS but found that KLF2 silencing significantly reduced Cx37 expression. This result suggests that Cx37 may be involved in the protective effects of HLSS, as increases in its expression, via KLF2 activation, provides for increased intercellular gap-junctional communication and EC synchronization. More recently, the modulation of aquaporin-1 (AQP1), a transmembrane NO-transporter, by HLSS-induced KLF2 expression and inflammatory stimuli was reported. Since inflammatory conditions decreased AQP1 expression, while atheroprotective KLF2 expression increased its expression, AQP1 is thought to be characteristic of non-inflamed vessels [138]. KLF2 was also found to play a role in lung injury, as its expression decreased in response to pathologic cyclic stretching and inflammation, and pulmonary vascular integrity became dysregulated when EC KLF2 was disrupted [140].

Effects of shear stress are also implicated in diabetes mellitus (DM). Using a model mimicking healthy and partially blocked vessels, increased rates of apoptosis were reported in HUVECs subjected to increased glucose concentrations and shear stress magnitudes [141]. Apoptotic rates were further increased after exposure to hyperglycemic plasma from DM patients. Interestingly, no change in apoptosis was observed between plasma samples from healthy and DM patients when tested under

static conditions, suggesting a flow-mediated mechanism involved in hyperglycemic-driven apoptosis.

Additionally, arterial hemodynamics are reported to play a role in atherosclerotic plaque formation [142]. Low shear stress (2 dyn/cm^2) resulted in TNF-α-induced upregulation of VCAM-1, a biomarker of atherogenesis, and IRF-1, a transcription factor involved in immune responses and inflammation, in human aortic ECs. To evaluate the effects of high-fat foods, ECs were exposed to triglyceride-rich lipoproteins, which augmented the response, indicating a synergistic effect. Intriguingly, IRF-1-silencing eradicated this effect on VCAM-1 expression, demonstrating that VCAM-1 production is IRF-1-dependent. Together, these results elucidate a mechanism that may contribute to spatial atherosusceptibility via hemodynamic- and high lipid blood content- regulated VCAM-1 expression.

3.2.4 Angiogenesis

Angiogenesis is the formation of new blood vessels derived from existing vasculature, requiring several aspects of EC function (e.g. migration, proliferation) [101]. It is driven by the need to supply surrounding tissues with oxygen and nutrients and is therefore essential to both normal development (which we will discuss), as well as many pathological processes, including cancer (which we do not focus on here). Several reports indicate that angiogenesis is heavily influenced by the dynamic mechanical environment experienced by ECs. This has motivated the design of MFDs to include hydrodynamic forces such as luminal- (over ECs), transmural- (through ECs), and interstitial- (through ECM) [143] flow to decode their effects on EC behavior in angiogenesis (see Figure 2). The study of mechanotransduction in angiogenesis

using traction force microscopy for was recently reviewed by Boldock *et al.* [144] so traction forces will not be discussed here. Notably, a sophisticated technique was recently reported to elucidate new characteristics of how stalk versus tip cells interact with the surrounding ECM for evaluation of mechanotransduction pathways involved in angiogenesis [145].

The effects of luminal versus transmural flow was investigated by Galie *et al.* [146]. Regardless of flow type and EC-junctional maturation, 10 dyn/cm^2 served as the threshold to induce sprout formation. Interestingly, matrix metalloproteinase 1 was found to be upregulated with flow, and its inhibition arrested flow-induced sprouting, demonstrating the role of matrix degradation in angiogenic progression. The direction of transendothelial flow (i.e. apical-to-basal, A-B, versus basal-to-apical, B-A) was also reported to affect angiogenesis [147]**.** Only B-A flow promoted capillary morphogenesis, increased VE-cadherin localization, and focal adhesion kinase phosphorylation; suggesting that the transition of ECs to a more invasive phenotype is mediated by a direction-dependent mechanism.

To study the effects of interstitial flow (IF), Kim *et al.* developed an MFD to evaluate angiogenic [148] and lymphangiogenic [149] sprouting of HUVECs (co-cultured with fibroblasts) in response to biochemical cues and IF. In both cases, sprout growth was significantly augmented in the direction opposite of flow, while sprouting was suppressed downstream. Collectively, these results implicate IF as a key mechanical regulator of tissue vascularization, the mechanism of which was recently investigated by Song *et al.* [150]. IF-induced EC sprouting was reported to occur in a RhoA-dependent manner, where RhoA modulated flow-induced filopodial extensions

by tip cells, but not VEGF gradients. Thus, RhoA-signaling is involved in mechano-driven neovascularization.

These studies highlight the importance of using on-chip systems to independently modulate flow-induced mechanical cues and biochemical signals to understand the mechanistic interplay involved in EC mechanosensing during angiogenesis.

3.3 Subendothelial Matrix Mechanics

In vitro cell culture requires functionalized surfaces (e.g. protein or bioactive hydrogel coatings) for cellular engagement and binding-ligands. The properties of these bioactive coatings reportedly affect EC behavior, since ligand composition and abundance present within the coating can alter cell-matrix interactions and affect the stiffness and topography of the underlying matrix. Several groups have worked to decouple the effects of these parameters to evaluate their individual roles in EC responses.

3.3.1 ECM Composition & Structure

In vivo, blood vessels interact with several ECM proteins (e.g. collagen type 1, laminin, fibronectin). The presence of these and other ECM proteins have been investigated to understand their role in EC behavior. Shamloo *et al.* reported that VEGF-induced angiogenic sprout paths were dependent on the density of the surrounding collagen/fibronectin matrix [151]. Relative to the VEGF-gradient, dense matrices induced parallel sprout formation, compared to less dense matrices where misaligned sprout formation initially occurred in response to less VEGF, but ultimately

reorganized parallel to the gradient. More recently, the group integrated computational methods and determined that a matrix of intermediate collagen density (1.2–1.9 mg/ml) is optimal to induce long, stable sprout formation [152]. Unstable sprouts were reported in low concentration collagen matrices (0.7 mg/ml) while high concentration collagen matrices (2.7 mg/ml) inhibited cell migration and sprout growth as a result of increased collagen fibril entanglements. Despite this report, other results suggest collagen crosslinking does not hinder vascular stability or function [153]. Chan *et al.* presented stable EC tube formation in both uncrosslinked and crosslinked gels in response to 10 dyn/cm^2. In fact, when tubes were subsequently exposed to decreased shear (~5 dyn/cm^2) they only remained stable in crosslinked gels, suggesting a potential advantage. In another study, optimal vasculogenesis was observed on 3.0 mg/ml collagen gels compared to lower concentrations, but pure fibrin matrices (2.5 mg/ml) improved mature network formation compared to collagen or collagen/fibrin combinations, and were suggested as the optimal scaffold for *in vitro* modelling [154]. HUVECs co-cultured with fibroblasts reportedly increased the number of branches, and decreased the average branch length and diameter, of angiogenic sprouts, with increasing fibrin concentration [155].

The effects of matrix properties have also been studied at the pericellular level using a magneto-microfluidic system [156]. Collagen fiber deformations were induced local to the site of magnetic beads embedded in the matrix, without altering the bulk material properties. Angiogenic activity of HMECs increased under magnetic force exposure, suggesting EC migration typically occurs in the direction with opposing force

gradients. This supports prior results of increased area and motility with increased matrix stiffness.

Overall these results encourage use of MFDs to probe fundamental aspects of matrix effects on angiogenesis, and EC behavior in general, and highlight the importance of gel concentration and composition, and the interplay between biophysical and biochemical factors, in promoting the maturation of microvascular networks. An important consideration moving forward is the possible turning over of exogenous ECM and replacement with endogenous ECM laid down by the ECs. While this effect is likely also at play in traditional assays, it may be even more pronounced in MFD studies, where cells may be cultured over longer time periods. Researchers should be aware of this potential effect and plan for evaluation of, or control of, ECM production by ECs within the MFDs.

3.3.2 Matrix Rigidity

Mounting evidence indicates that ECs are capable of mechanosensing matrix rigidity [76,157,158]. To independently study the effect of substrate stiffness on ECs, a new method to immobilize proteins on polyacrylamide hydrogels has been developed [159]. Micropatterns of fibronectin-coated rectangles were used to control the spreading and morphology of single HUVECs on different stiffness. Soft hydrogels (2.5 kPa) led to a lower actin fiber density, a rounded nucleus, and lower Young's modulus compared to HUVECs on stiffer hydrogels (25 kPa). The observed reorganization of actin suggests that internal tension is modulated by matrix stiffness, which regulates cell stiffness and nuclear remodeling.

The effects of matrix rigidity are particularly relevant in age-related arterial stiffening, which is implicated in the pathology of cardiovascular disease (reviewed in [160])**.** The combined effects of shear stress (12 dyn/cm^2) and vessel stiffening were recently investigated [161]. BAECs on "young" hydrogels (2.5 kPa) exhibited typical flow-induced EC elongation and increased junctional tightness, decreased RhoA activation, and increased NO production, relative to "old" hydrogels (10 kPa). This demonstrates that substrate stiffness and shear stress signaling are coupled, and that compliant matrices, mimicking young blood vessels, can induce a flow-activated atheroprotective phenotype.

Evidence of crosstalk between stiffness and shear stress signaling was also provided by Galie *et al.* who showed that the magnitude of shear stress required to induce an EC response was different depending on the underlying substrate rigidity [162]. Their studies indicated that the interplay is Rho/ROCK-mediated. Cell surface receptor CD44 is upstream of this pathway and is known to bind hyaluronan (HA), a glycosaminoglycan present in the EC glycocalyx. Under static conditions, HA degradation induced no change in cell morphology or response to TNF-α on stiff matrices, but prevented cell spreading on soft substrates. With shear stress, HA disruption eradicated the flow-induced NF-κB decrease observed in ECs on soft matrices. This suggests that HA plays a role in EC mechanosensing and the inflammatory response on soft matrices specifically.

Collectively, these results suggest that subendothelial matrix stiffness, independent of protein coating and cellular morphology, can modify the cytoskeleton, and impact the nucleus. Understanding the independent effects of stiffness, as well as combined

effects with shear stress, on EC function, might elucidate the mechanisms involved in response to vascular stiffening in aging and disease.

3.4 Topography

Protein fibers in the basement membrane (BM) present biophysical cues to cells in the form of topography. Surface topography of a physiologically relevant size-scale has been recapitulated in MFDs *in vitro* and has been shown to effect EC mechanobiology, particularly under simultaneous shear stress exposure.

To study the effect of topography on wound-healing, an MFD with 1 μm gratings was developed [163]**.** Increased HUVEC regeneration was observed in wounds perpendicular to flow, when cells were on gratings (versus flat surfaces) oriented parallel to flow. Shear stress (14 dyn/cm^2) and wounding activated junctional Src activity leading to phosphorylation of VE-cadherin, decreasing adhesion strength. Grated substrates, and Src-inhibition on flat surfaces, decreased phosphorylation, which enhanced wound healing, likely due to improved mechanical connection and junctional integrity, rendering improved collective coordination and motility. The device was later used to test the interplay of topography and flow [164]. Under supraphysiological shear stress (up to 100 dyn/cm^2), gratings induced polarization and ECs oriented themselves perpendicular to flow, leading them to withstand shear levels over 100% of those withstood on flat substrates. Topographical cues have also been found to dominate HUVEC migration on electrospun HA fibers under a VEGF gradient [165]. ECs were most persistent when fibers were aligned in the gradient direction, indicating a combinatorial effect of topographical and chemical cues. Meanwhile, no gradient effect was observed with a perpendicular fiber-gradient orientation. HUVEC

orientation and elongation is also reportedly affected by topographical cues provided from the apical versus the basal surface [166]. Delivery of apical flow (20 dyn/cm^2) combined with basal exposure to ridge/groove topography parallel to flow had synergistic effects, while perpendicular flow resulted in less alignment, and increased migration tortuosity.

In another approach, a synthetic ECM designed to mimic native structures was developed by depositing BM material, laminin, onto nanofibers of collagen I [167]. On COL1-only nanofibers, discontinuous VE-cadherin, and EC-detachment after 5 days, was observed. On BM-COL1 nanofibers, however, densely localized VE-cadherin was reported, and viable cell culture was maintained for several days. Evidence suggested that this improved attachment was due to integrin-α6, which has a high affinity to laminin and plays a role in "outside-in signaling". BM-COL1 fibers enhanced laminin-integrin-α6 binding and stabilized focal adhesion integrin clustering via connections with actin cytoskeleton and suppression of junctional diphosphorylated myosin light chain II.

Collectively, these results demonstrate the directional role of surface topography, and the apical versus basal application of, in guiding EC behavior. While simultaneous topographical and chemical signals may have combined effects, evidence suggests that topographical cues may be more influential.

3.5 Geometry

Similar to topographical cues that regulate cell phenotype, the slightly more macro-scale parameter of vessel geometry reportedly influences EC behavior. ECs migrate through confined environments during angiogenesis and form the walls of tubular- and

branch-shaped blood vessel structures of varying diameters (see Figure 2). MFDs provide the capability to study the independent role of each of these geometries as mechanical inputs to the endothelium.

3.5.1 Confinement

The study of cell behavior in constricted environments is particularly relevant to our understanding of the mechanisms of cell invasion, where cells must move through ECM proteins in 3D to invade other tissues. In this regard, MFDs serve as promising platforms that "provide well-controlled physical, chemical and confined environments to study cell phenotype and behavior", as noted by Spuul *et al.* who developed a device to study confinement of varying height [168]. No cells were observed in 1.28 μm fibronectin-coated slits. Interestingly, ECs exhibited cytoskeletal reorganization and podosome formation in 3.13 μm environments, and the fraction of podosome-forming cells decreased with increased slit height (up to 7.3 μm). Since ECs are typically devoid of podosomes, the experiments demonstrate that a confined cellular microenvironment can induce podosome formation.

3.5.2 Curvature

Vessel or fiber-like curvature has been shown to improve EC monolayer formation. As such, several groups have introduced this geometry into their MFDs. A methacrylated gelatin-alginate composite was engineered to construct double-layer hollow microfibers to simulate complex tissues such as the osteon [169]. The vascular vessel was mimicked via ECs, and osteoblast-like cells were seeded in the outer layer to act as bone. Similarly, a photolithography approach was reported for the continuous

synthesis of cell-laden multilayered microfibers for osteon-like fiber formation [170]. In both cases, the fiber geometry induced robust growth of the cells and enhanced vasculogenic and osteogenic expression.

The effects of curvature are reportedly dependent on EC-type. In contrast to peripheral ECs, HBMECs have been shown to resist elongation in response to curvature and shear stress [171]. HBMECs were seeded onto glass rods with diameters ranging 10–500 mm, spanning the range from brain capillaries to larger vessels. On 10 mm rods, only HBMECs wrapped around to form junctions with themselves. While HUVEC orientation, aspect ratio, and actin stress fiber distribution were extremely sensitive to vessel diameter and shear stress, HBMECs exhibited only weak dependencies. In both EC-types, actin fibers were noticeably aligned with the long-axis of the rod, suggesting that vessel shape may impact cytoskeleton organization.

Alternative to the standard vessel-like geometry, increased angiogenic sprouting was observed at the corners of a microchannel embedded in collagen I, independent of a biochemical gradient [172]**.** The authors speculated that the mechanism involved was mechanically-driven, where geometric asymmetry may lead to increased matrix stiffness via cell-mediated ECM alterations. This in turn, would elevate cell contractility thereby altering sprout localization. While square vessels are not physiologically relevant, branch points and tortuous, tumor-associated sprouts, represent irregular vascular shapes *in vivo,* where enhanced angiogenesis is observed. Since geometry and cell density were key, these results indicate that biophysical cues and/or autocrine signaling may supersede pro-angiogenic paracrine signaling within a given environment.

3.5.3 Bi-furcation Angles & Protrusions

Deviations from standard tubular-shaped vessels are present *in vivo* (e.g. bifurcations, aneurysms, stenosis), so a perfusable vasculature model was developed to recapitulate these structures [173]. Geometric alterations were shown to manifest as local changes in shear stress, which induces change in EC physiology (see section 2). Here, VCAM-1 expression correlated with shear stress variations due to vascular geometries. In particular, geometries mimicking stenosis decreased platelet adhesion while bifurcation-like geometries escalated adhesion of sickle cell disease erythrocytes. Similarly, an MFD was designed to mimic the flow conditions in a stenotic artery to study the effects of plaque geometries [174]. Again, geometric alterations induced alterations in shear stress magnitude, which here, was shown to play a role in the activity of von Willebrand Factor (vWF), a glycoprotein involved in platelet aggregation. Geometry-induced shear increase upregulated vWF secretion by ECs thereby promoting platelet aggregation and thrombus formation. These results implicate vWF as a shear-sensitive protein involved in regulating thrombogenesis via hydrodynamic force recognition in the local microenvironment.

Overall, these results demonstrate the importance of geometrical considerations in MFD design and highlight the capability of these systems to study EC mechanosensing of their geometrical environment.

3.6 Mechanical Strain

Within the body, ECs are routinely exposed to cyclic stretch resulting from blood pressure and flow and breathing motions. The effects of mechanical strain have been

investigated by integrating stretch capabilities into MFDs to characterize EC behavior [175].

For instance, a microfluidic flow-stretch chip to study shear stress (26 dyn/cm^2), cyclic stretch (5%, 1 Hz), and the combined effects on ECs was developed [176]. Increased HUVEC adhesion and spreading was observed in all conditions relative to static experiments. Stress fiber alignment was weakly induced by shear stress, but strongly organized parallel to flow with the addition of stretch, suggesting a synergistic effect. This synergy was further studied in MFDs which provided various orientations of biaxial strains and flow combinations [177]. Maximal HUVEC alignment was observed with increased ratios of maximum:minimum principal strain, typically aligning opposite of the maximum principal strain direction. Stretch-induced alignment and elongation was also observed in lymphatic ECs cycled between 0% and 10% strain at a 0.1 Hz frequency in a dielectric elastomer actuator based deformable bioreactor [178]. Furthermore, increased axisymmetric and nonuniform strains have been shown to increase inflammatory mRNAs and proteins (e.g. MCP-1, IL-8, IL-6, and ICAM-1) in a HUVEC cell line, providing insight into the inflammatory and mechanical mechanisms involved in vascular disease [179].

Mechanical strain is of particular interest for lung applications since cells in the lung experience breathing-induced cyclic mechanical strain in combination with flow within the lung alveoli. These strains were found to play a crucial role in barrier permeability [180] and vascular leakage in a lung alveolar-capillary interface device used to mimic complex disease pulmonary edema [181]. While cyclic strain alone had no detrimental effects on barrier permeability, its presence in combination with IL-2,

often prescribed to cancer patients, lead to a threefold increase in leakiness compared to IL-2 treatment alone. Subsequent evaluation of a TRPV4 ion channel inhibitor suggested its role as potential therapeutic, highlighting the importance of evaluating drug efficacy and toxicity in appropriate biomimetic models. These devices provide simple and useful tools for *in vitro* investigation of the mechanotransduction involved in healthy tissue and in disease progression, and suggest mechanical strain significantly affects EC behavior.

3.7 Microfluidic Platforms & Endothelial Cell Mechanosensing to Inform Therapeutic Applications

One of the major goals of *in vitro* EC culture, particularly in the form of biomimetic organ- or vessel- on-chip systems, is for use in drug scanning, toxicity testing, and drug evaluation. *In vitro*, drug delivery is reportedly affected by the shear stress, pressure, and geometric conditions exhibited in the testing device. This evidence motivates the design of new devices to vary these parameters to appropriately study drug delivery in conditions specific to each application. The incorporation of physiological shear rates and hydrostatic pressure levels have been shown to alter nanoparticle uptake, sedimentation onto cells, cytotoxicity, and EC surface protein expression, relative to static or non-physiological conditions in MFDs [182–184]. Larger bifurcation angles were also shown to increase adhesion of neutrophils and microparticles to ECs, with larger and more rigid particles adhering preferably to the cell-cell junctions [185].

MFDs have also been used to inform therapeutic design, providing the capabilities to investigate particle distribution and cellular uptake of delivery agents

with different properties. For instance, while low shear stress (0.5 dyn/cm^2) has been shown to maximize cationic micro-particle uptake; intracellular uptake of anionic particles seems unaffected by flow [186,187]. However, others have reported maximized uptake of negatively charged, nanoparticles with low shear [188].

These studies demonstrate the mechanotransduction involved in EC responses and highlight the importance of incorporating the *in vivo*-like mechanical properties relevant to each application in MFD design. Optimization of particle physical and chemical properties are required for improved cellular distribution and targeted delivery of parenteral drug delivery systems. Government agencies including the federal Defense Advanced Research Projects Agency (DARPA) and the National Institutes of Health (NIH) have developed several initiatives to further explore the potential of these organomimetic platforms. For example, the NIH has an ongoing program titled “Tissue Chip for Drug Screening” aimed at streamlining development to eliminate toxic drugs earlier in the process and improve the success rate of promising medications [189]. The Food and Drug Administration (FDA) has even developed partnerships to develop microsystems aimed at evaluating organ-response to possible chemical hazards present in foods, supplements, and cosmetics in a more efficient and precise manner than current technologies [190]. It seems clear, from our perspective, that the benefits of MFDs, and likely the biomimetic mechanical cues they impart, are widely recognized in the field and that the use of these devices for standardized testing lies ahead in the future.

3.8 Conclusion and Outlook

MFDs provide unparalleled tools for systematic incorporation of multiple mechanical cues, imaging modalities, electronics and sensors, as well as spatiotemporal introduction of biochemical cues into *in vitro* vascular models, in order to study cell mechanosensing capabilities. Indeed, mounting evidence demonstrates that the mechanical environment drastically alters EC signaling, protein and mRNA expression, cytoskeletal organization, morphology, migration, barrier function, and angiogenesis, and MFDs should continue to be used to study these functions. The ability of MFDs to incorporate shear stress on the microscale has tremendously impacted the progression of the mechanobiology field. In particular, the interplay of shear stress and other mechanical cues such as matrix stiffness, vessel geometry, topography, and mechanical strain, as well as biochemical cues, are illuminating interesting combinatorial effects. We expect that MFDs should continue to be developed and utilized to not only provide new correlative information, but also more detailed mechanistic insight into what mechanosensitive molecules are at play, and through which signaling pathways they act.

A major challenge lying ahead will be the determination of what should be considered "state of the art" for best mimicking the physiological properties of the vasculature. While many designs have been reported, the question still remains what success criteria should be required for device characterization and which mechanical stimuli are truly needed to most accurately recapitulate the *in vivo* cellular responses. Until then, the systematic evaluation of each stimulus should continue to be explored to deduce the mechanisms responsible for the specific changes in EC behaviors and

functions. We suggest that, at minimum, physiologically-relevant shear stress and matrix stiffness should be simultaneously included in vascular models moving forward, since these mechanical cues significantly alter not only cellular response and function, but also the activation of various mechanosensors. Furthermore, the MFD, and the EC type, must critically reflect the specific *in vivo* setting which the researcher is trying to explore. It is likely that these advances will be aided by the integration of, or augmentation with, additional quantification capabilities, such as embedded electrodes for trans-endothelial electrical resistance measurements or optogenetic techniques for biosensor and photo-control capabilities. Nevertheless, increased understanding of EC mechanosensing will likely lead to enhanced future therapeutic design, and it is expected that MFDs incorporating physiologically relevant biophysical and biochemical cues will find increased applications in drug scanning, toxicity testing, and drug evaluation.

Table 3.1. Summary of new fundamental information about EC response to various mechanical stimuli (alone or in combination, as noted in the first column) gained from MFDs, along with the extent to which mechanisms of mechanosensing are known. Unique features of MFDs that allowed for this new insight are also described in the second column. Composed by KM Stroka.

Mechanical stimulus	Unique MFD features	Cell type	New fundamental information	Biological mechanism
Shear stress [119]	Resistance channels	HUVECs	Elongation and alignment of cell body and actin cytoskeleton in direction of flow	Hydrodynamic drag on nucleus (Experimental)
Shear stress [119]	Resistance channels	HUVECs	Polarity - Gogli and MTOC upstream; nucleus downstream	Hydrodynamic drag on nucleus (Experimental)
Shear stress [124]	Y-shaped MFD	HUVECs	Dynamic Ca^{2+} signaling synchronizes with ATP signals	Correlative observation only
Shear stress [125]	Micropattern	BAECs	Elongation and orientation of cells; retraction upstream of cell; lamellipodia formation downstream	Correlative observation only
Shear stress [129]	Multiple shear stress magnitudes in one view field	BAECs	Increases in intracellular Ca^{2+} were proportional to shear stress magnitude	Ca^{2+} influx through TRPV4 (Experimental)

Shear stress [137]	Spatiotemporal introduction of biochemical cues	BAECs	Upstream vs. downstream biochemical signaling in response to TNF-alpha	Correlative observation only
Shear stress [141]	3 microchannel rows (for triplicate experiments), with 3 blood vessels each	HUVECs	Increased cell apoptosis with shear stress in combination with increased glucose	Correlative observation only
Shear stress [142]	Linear gradient of shear stress	HAECs	Shear stress mediated VCAM-1 expression in response to cytokine and dietary lipids	Interferon regulatory factor (IRF)-1-dependent transcription (Experimental)
Luminal vs. transmural flow [146]	Luminal or transmural flow	HUVECs	Sprout formation when shear stress threshold (luminal or transmural) is reached; MMP-1 upregulation with flow	MMP-1 dependent (Experimental)
Transmural flow [147]	2 channels connected by a region of 3D ECM	HUVECs and HDMECs	Basal to apical transmural flow promotes angiogenesis and de-localization of VE-cadherin from cell-cell adhesions, while apical to basal transmural flow does not	FAK/Src-mediated (Experimental)
Collagen/ fibronectin matrix density [151,152]	3D ECM containing a concentration gradient of soluble biochemical factors	HDMECs	Dense matrices required steeper VEGF gradient and higher VEGR concentration for proper sprouting polarization	Upregulation of VEGFR2 in stiffer matrices (Speculation)
Matrix stiffness and shear stress [162]	Varying shear stress in discrete steps and substrates with varying magnitudes of stiffness	BAECs	Shear stress-dependent effects of matrix stiffness on cell morphology	Rho/ROCK-mediated, possibly through shear-induced deformation of hyaluronan-containing glycocalyx and activation of CD44 (Experimental)
Topography and shear stress [163]	Topographic gratings	HUVECs	Gratings enhanced junctional integrity	Inhibition of Src-mediated VE-cadherin phosphorylation by topography (Experimental)
Topography and shear stress [164]	Topographic gratings perpendicular to flow	HUVECs	Cells oriented themselves along gratings, leading to ability to withstand increased shear stresses above physiological values	Correlative observation only
Topography [165]	Electrospun hyaluronic acid fibers	HUVECs	Cell migrational persistence when fibers aligned in direction of VEGF gradient	Correlative observation only
Topography [167]	3D ECM (collagen 1 + laminin) nanofibers	Bovine Brain ECs	Enhanced cell-cell attachment with laminin incorporation	Integrin-mediated (Experimental)
Confinement [168]	Confining slits	HMVECs	Cytoskeletal reorganization and podosome formation	Promoted by fibronectin (Experimental)

Curvature [169,170]	Double-layer hollow microfiber from composite material	HUVECs	Fiber geometry induced robust growth of the cells and enhanced vasculogenic and osteogenic expression	Correlative observation only
Curvature and shear stress [120,171]	Glass rods of varying diameter	HBMECs	Resistance to elongation in response to curvature and shear stress	Actin cytoskeleton orientation (Experimental)
Geometric asymmetry [172]	3D collagen-embedded microchannels and biochemical gradient	HUVECs	Increased angiogenic sprouting at microvessel corners	Cell density-dependent expression of pro-angiogenic factors or contractility-dependent (Speculation)
Mechanical strain and shear stress [176]	Shear stress and cyclic stretch	HUVECs	Stress fiber alignment most strongly oriented with combined mechanical cues	Correlative observation only
Mechanical strain and shear stress [177]	Shear stress and variously oriented anisotropic biaxial strains	HUVECs	Maximal cell alignment observed with increased ratios of maximum:minimum principal strain, typically aligning opposite of the maximum principal strain direction	Correlative observation only
Mechanical strain [179]	Axisymmetric and nonuniform strains	HUVECs	Increased axisymmetric and nonuniform strains promote inflammatory mRNAs and proteins (e.g. MCP-1, IL-8, IL-6, and ICAM-1)	Correlative observation only
Mechanical strain [180,181]	3D cyclic mechanical strain	Lung alveolar ECs	Mechanical strain, in combination with IL-2, increased EC barrier permeability	Correlative observation only

Chapter 4 - Junction Analyzer Program (JAnaP) Development†

4.1 Introduction

The integrity of cell-cell junctions is required for the maintenance of normal physiological processes. Indeed, disruption of these junctions in, for example, the brain endothelium, is linked with numerous neurodegenerative diseases including Alzheimer's disease and multiple sclerosis [2]. Therefore, understanding the key players driving junction stability could hold significant promise for therapeutic discovery. Furthermore, the ability to modulate junction integrity holds important potential for drug delivery purposes.

Despite this, the mechanisms underlying junction disruption aren't fully understood. This is largely due to the lack of appropriate BBB models and efficient techniques to quantify the junctional proteins as they are presented at the cell edge. Importantly, previous studies have linked edge-presentation of VE-cadherin with junction and barrier maturity. Specifically, linear VE-cadherin structures parallel to the cell boundary are considered to be stable and mature, while immature junctions take the form of discontinuous focal adherens presenting a punctate or serrated morphology [15]. Therefore, a useful parameter in evaluating monolayer integrity is the amount of mature (i.e., continuous or linear) versus immature (i.e., discontinuous) junctions localized at the cell perimeter. Quantification of this parameter, however, remains

---

† This chapter was adapted from K.M. Gray, D.B. Katz, E.G. Brown, K.M. Stroka. "Quantitative Phenotyping of Cell-Cell Junctions to Evaluate ZO-1 Presentation in Brain Endothelial Cells." *Annals of Biomedical Engineering* 47(7), 1675-1687 (2019). Permission was obtained from Springer Nature to use this material in this dissertation. Kyle Thomas (Yellow Basket, LLC) provided support for software development.

cumbersome due to a lack of efficient techniques for analysis. Here, we aimed to address this gap by developing the Junction Analyzer Program (JAnaP), a semi-automated program capable of measuring the percent of cell perimeters covered by continuous and discontinuous junction, or no junction.

4.2 Program Workflow

To quantitatively analyze cell-cell junction presentation, we developed a Python-based program to analyze immunofluorescent images of junctional protein. We integrated the ability to calculate junction data in conjunction with cell morphology to streamline the analysis processes. This program was originally developed and validated using images immunostained for ZO-1. Therefore, the example images provided in this section depict ZO-1 phenotyping, except in section 4.2.4, where the analysis of multiple proteins is discussed. The JAnaP source code, guided user interface, and detailed instructions have been made available on the Stroka Lab GitHub account (https://github.com/StrokaLab/JAnaP) for practitioners to download and use. The detailed user guide is attached in Appendix A.

4.2.1 Image Processing and Cell Waypointing

The first step when using the JAnaP is to load images of EC monolayer (ideally collected using a 60x objective) into the program. Figure 4.1.A presents one example image. Each image is then converted to grayscale using the formula for effective luminescence, $p_i = 0.2989*r + 0.5870*g + 0.1140*b$, where r=red, g=green, and b=blue. This algorithm converts the color value of each pixel to an intensity (p_i) between 0 (pure black) to 255 (pure white). Next, the images are inverted relative to

their maximum intensity values and a White Tophat filter is applied with a 5-pixel disk-shaped structuring element to correct for the non-uniform background noise. To avoid over-filtering, the original image is normalized to 10% of this modified image and added to the modified image to generate a "cost image" used to trace the cell perimeter. For perimeter tracing, the user marks the edges of each cell fully contained within the image with a small number (typically 5-10) of single-pixel dots (Figure 4.1.B). This process is termed "way-pointing" and is similar to the livewire method described in Chapter 2. As the user adds each waypoint on the original image, the program uses the cost image to generate a "minimum cost path segment" between each waypoint using the Scikit path-finding algorithm. This essentially generates the path between each waypoint based on the maximum intensity present in the original image (i.e. follows the perimeter based on junction presentation). Conveniently, each path segment is generated in real time, so the user can adjust the waypoints, if needed, to accurately capture the cell edge. Each path segment is subsequently stitched together to create a full loop or "path" around the cell edge (Figure 4.1.B). This waypoint process generates an ordered set of points that is specific to every cell, each identified by their center coordinates (Figure 4.1.C). Note that this process allows the user to select only the cells in which the junction detail is visible around the entire perimeter of the cell. As such, only cells that are fully attached to and spread out on the substrate should be analyzed, and any rounded or overexposed cells should be excluded.

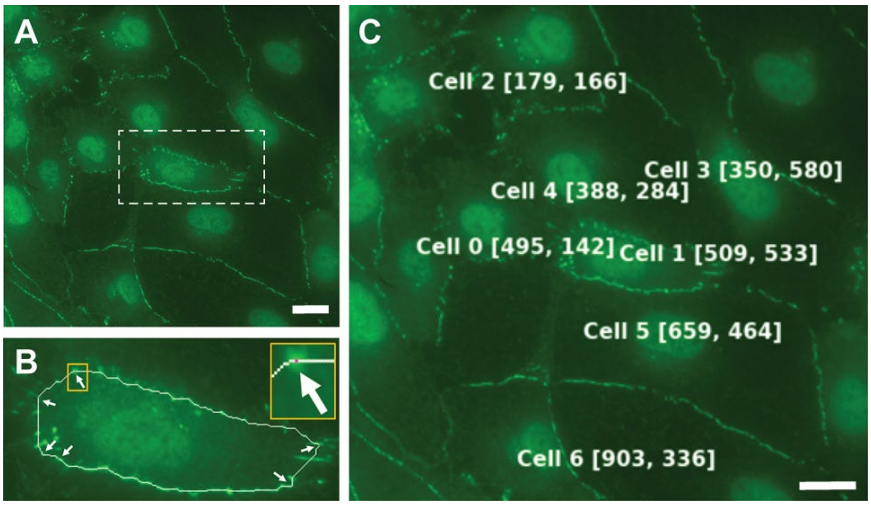

Figure 4.1. JAnaP Cell Identification. An example monolayer is presented in (A) with the cell of interest denoted in the white hashed box. (B) presents that cell after the waypointing process. The white arrows point to each waypoint seeded around the perimeter, with a zoomed-in clip in the top corner. The thin white line presents the perimeter traced by the program by connecting each waypoint (purple) using the A* search algorithm. The entire monolayer after the waypointing process is presented in (C) with the center coordinates of each waypointed cell denoted in white. (scale bars = 20 μm)

4.2.2 Cell Morphological Parameter Calculation

To calculate the cell shape parameters, the cell path generated in section 4.2.1 is used. A numpy array representing the polygon bounded by the path is generated using the scikit Python module. This binary two-dimensional array is used with the scikit measure module to calculate a more accurate measure of the cell perimeter by accounting for diagonal lengths across pixels, the value of which is then converted to μm-scale and used to calculate cell area (Figure 4.2.A). Cell circularity can then be calculated using the formula $4\pi(area)/perimeter^2$. Next, a convex hull is fit to the cell path using the Scipy library (Figure 4.2.B). The area of this hull is calculated via the Shoelace Method and used to calculate the cell solidity using the formula:

$(cell\ area)/(convex\ hull\ area)$. The cell presented in Figure 4.2 has a perimeter, area, circularity, and solidity of 132 μm, 771 μm^2, 0.55, and 0.93, respectively.

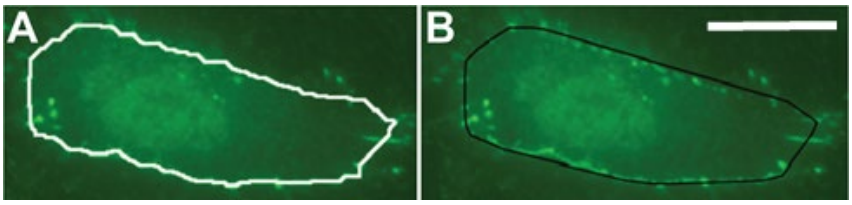

Figure 4.2. JAnaP Cell Shape Parameters. An example perimeter (white) generated by the JAnaP is presented in (A). This is used to calculate cell area and circularity. The generated convex hull (black) is presented in (B). This is used to calculate cell solidity. (scale bar = 20 μm, applies to A and B)

4.2.3 Junction Phenotyping

The junction phenotype categories are presented below in Figure 4.3. To quantify each junction into one of these categories, a threshold value is first identified to differentiate between regions with and without immunofluorescently tagged protein. The identification of this threshold value is described below in the validation section (Section 4.3.1). In this example, a threshold value of 15 was used. The JAnaP then compares the intensity of each pixel along the cell path to this threshold. Any pixel above this value is categorized as a "junction", while "no junction" is any pixel below this threshold. Figure 4.4.A presents the isolated junctions of the example cell after the threshold has been applied and Figure 4.4.B depicts the regions of the cell path designated to the "no junction" category.

To categorize the individual junction pieces, a feature mask is generated by creating a matrix equal to the image size. A "feature" is a contiguous region within the image (i.e., junction). Every feature is labeled by assigning each element of the matrix to a unique integer based on the feature it is a part via a fully connected structuring

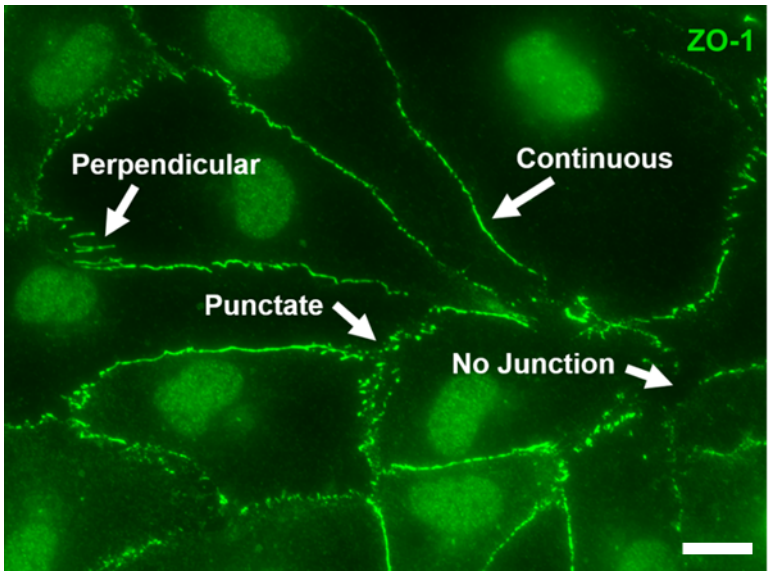

Figure 4.3 Junction Phenotypes. Examples of each junction presentation quantified by the JAnaP are indicated by the white arrows. (scale bar = 20 μm)

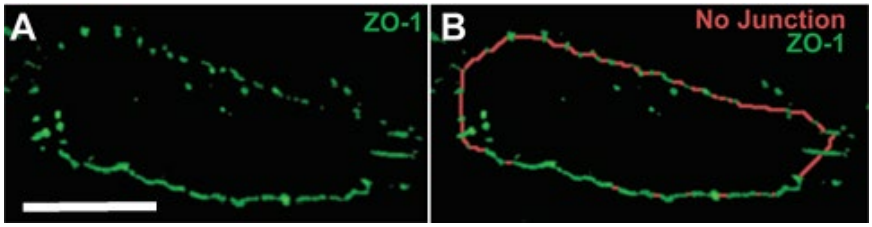

Figure 4.4. JAnaP Generated Images of Isolated junctions. (A) Presents ZO-1 junctions isolated by applying the threshold value (here 15) to the image in the JAnaP. (B) Presents the regions of the cell path classified as "no junction" (i.e. regions where there are no isolated ZO-1 junctions). (scale bar = 20 μm, applies to A and B)

element. This feature mask can then be filtered down to include only the features which lie on the perimeter of the cell of interest. Then, junctions can be categorized into continuous or discontinuous by measuring the length of the cell path that passes through the feature, termed "Path Length", and comparing it against a "Continuous Minimum Length", determined here to be 15 pixels (for a 1024-pixel x 1024-pixel image, ~2.7 μm). Determination of this value is described in the validation section (Section 4.3.2). If the Path Length is greater than the Minimum Length, that junction feature is considered continuous; otherwise, it is grouped as discontinuous (Figure 4.5). The

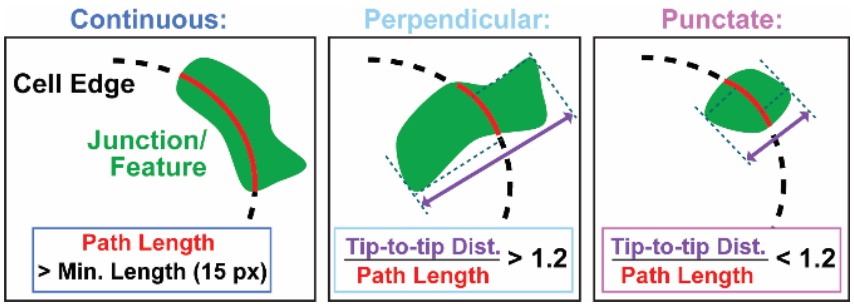

Figure 4.5 Criteria for Phenotype Categorization. The dotted black line represents the edge of the cell while the green represents a single junction. The path length (red) represents the distance that the feature coincides with the cell path. If this distance is greater than the minimum length (min. length), the junction is considered continuous. Otherwise, it is grouped as discontinuous. The tip-to-tip distance (Tip-to-tip Dist.) (purple) is calculated first by finding the locations of the junction piece that are furthest away from the cell path (in both directions). The sum of the perpendicular distances from those points to the cell path is designated as the Tip-to-tip Dist. Since the path length and tip-to-tip distance provides measures of junction length and width (or thickness), respectively, dividing the tip-to-tip distance by the path length provides a relative aspect ratio with respect to the cell path that can be used to categorize each (discontinuous) junction piece into punctate or perpendicular.

cumulative sum of the path length of all junctions divided by the entire cell perimeter provides the total ZO-1 coverage (i.e., overall edge-localization) for that cell. In Figure 4.4, 57.9% of the cell edge is covered by ZO-1 junction, while 42.1% has no junction localized at the perimeter. On the other hand, the cumulative sum of the path length of each junction type divided by the entire perimeter of the cell provides a measure of the fraction of the cell edge presenting each junction type. For the cell presented in this example, continuous junctions are expressed at 34.1% of the cell edge (Figure 4.6 – dark blue color), while 23.8% of the perimeter is covered by discontinuous junctions.

The discontinuous junctions can be further categorized into punctate or perpendicular, based on the "relative aspect ratio" of that feature. This is calculated by dividing the "tip-to-tip distance" (thickness measure) by the "Path Length" (Figure 4.5). A threshold value of 1.2 was determined (described in the validation section

(Section 4.3.3), such that any feature with a relative aspect ratio less than 1.2 would be categorized as punctate, while any larger ratio would render the feature perpendicular. For the cell in this example, 21.7% of the cell edge is covered by punctate junction while 2.1% is covered by perpendicular junction (Figure 4.6 – light blue and magenta colors).

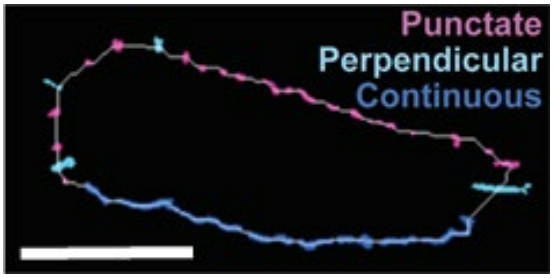

Figure 4.6 Example of JAnaP Categorized Junctions. The isolated junctions of the example cell have been classified as punctate (magenta), perpendicular (light blue), or continuous (blue) based on the categorization criteria outlined in Figure 4.5. (scale bar = 20 μm)

4.2.4 Multi-Protein Analysis

An additional capability of the JAnaP is to analyze more than one junction protein for the same cell. This requires that samples are immunostained for more than one protein, that sufficiently co-localize with one another, and that the images used capture each channel for the same location within the sample. This process allows the user to generate waypoints on one protein image, following the same steps as in Section 4.2.1. These waypoints are then projected onto the other channels, and the path between each waypoint is generated based on the intensities of the other channels. A threshold value is identified for each channel and the remainder of the analysis continues as previously described in sections 4.2.1 - 4.2.3. This eliminates the need to re-waypoint

(i.e., re-trace) cells for each immuno-stain, thus streamlining the analysis process. This capability was quantitatively validated as described in Section 4.3.4.

4.2.5 Quantification and Statistical Analysis

Throughout this dissertation, the analysis of the data generated using the JAnaP has been primarily on a per-cell basis (unless otherwise noted in the method section or figure caption), pooled together over three biological replicates or trials. This has been done to account for cell heterogeneities and allow for easy visualization (e.g., via dot plot) of the spread of the data. However, this also means that the total N value, or number of data analyzed, is relatively large in most cases. This could skew the statistical results, since the standard error of the mean (SEM, used here) is the standard deviation divided by the square root of N. Another approach could be to pool the average of each trial, creating an N value of three, representing the result of each biological replicate. While this could minimize any over-estimation of significant differences, and represent inter-trial differences, it could also diminish the heterogeneities present within each trial. As such, we have chosen to present pooled data here.

4.3 JAnaP Validation

4.3.1 Intensity Threshold Identification

The threshold value is used to isolate the junction pieces from the background noise within the uploaded immunostained images. This value is identified by the user for each set of images and is applied to all images within the specified image category.

Figure 4.7 presents an example process for identifying the threshold value for a set of images. The images in this figure are representative of cells within one image set and were selected to span the range of cells presenting bright, medium and dim junctions at their edge. The "original" images in the figure were filtered using a range of threshold values (5, 10, 15, 20, 25). The post-filtered images were then qualitatively compared to the original image to identify the threshold value that isolated the junctions to best reflect their presentation in the original image. The lower threshold values do not remove enough background for the bright cells, while the higher threshold values over-filtered the junctions in the dim cell. This narrowed the threshold to approximately 15. To probe the effects of smaller changes in threshold, we then compared the images filtered using threshold values ranging from 12 to 18. Only slight changes were observed within this range. This process identified 15 as the optimal threshold value for these and several other cells evaluated, leading to the use of 15 in this example.

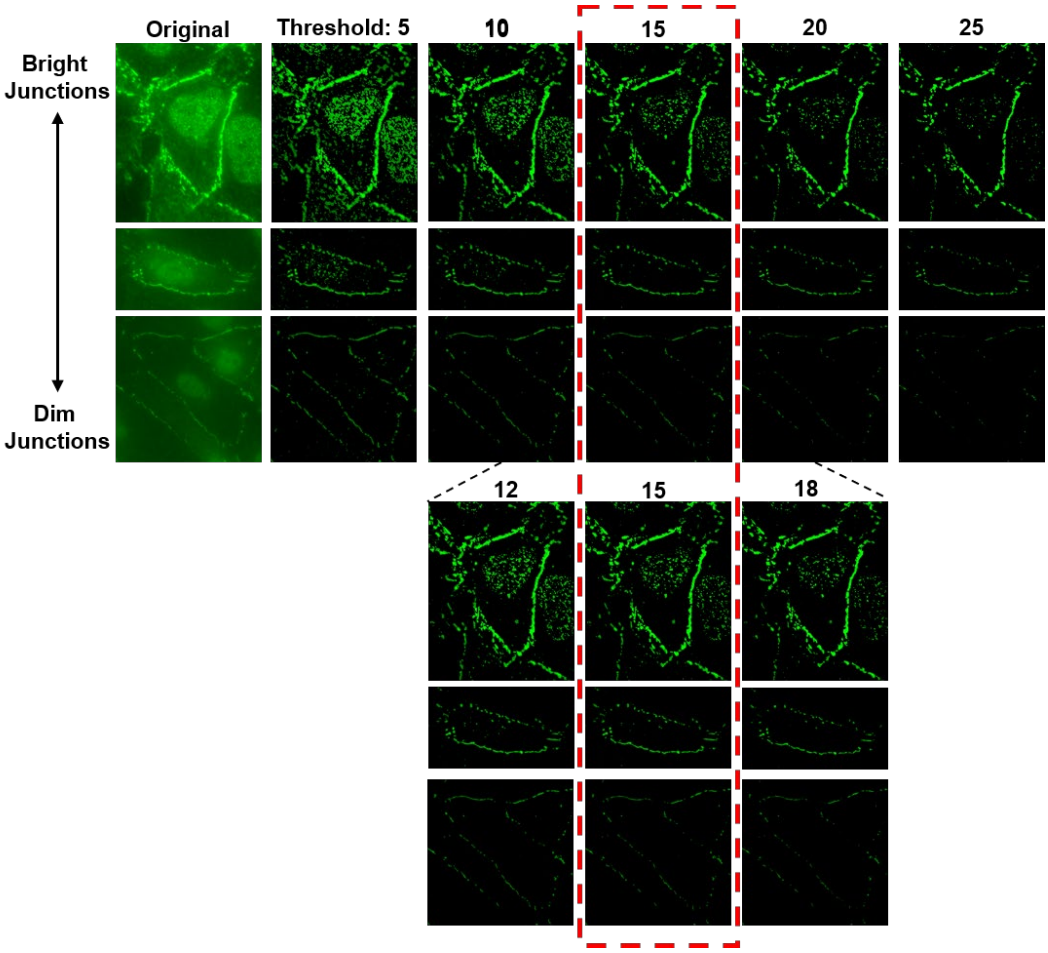

Figure 4.7 Intensity Threshold Identification. Post-filtered images of cells representing bright, medium, and dim junctions were compared at various thresholds to identify a value that adequately isolated the junctions for all cells. A value of 15 was identified for this image set.

4.3.2 Continuous Minimum Length Determination

The continuous minimum length (CML) is the value that determines whether junction features are categorized as continuous or discontinuous. The cell presented in Figure 4.8 represents one example used to determine the CML. Each junction was color-coded based on the category to which it was assigned when using the specified CML value (and a relative aspect ratio of 1.2). Each image was then reviewed to determine which CML value most accurately categorized the junction pieces as we

would have qualitatively categorized them. The arrows point to example junction pieces that are mis-categorized using the respective CML value. The white arrows present regions where the CML is too low and thus discontinuous junction pieces are coded as continuous, while the yellow arrows indicate junctions that are mis-coded as discontinuous because the CML threshold value is too high. This process identified 15 as the optimal CML value for this and several other cells evaluated, leading to the use of this value as the default value for the JAnaP.

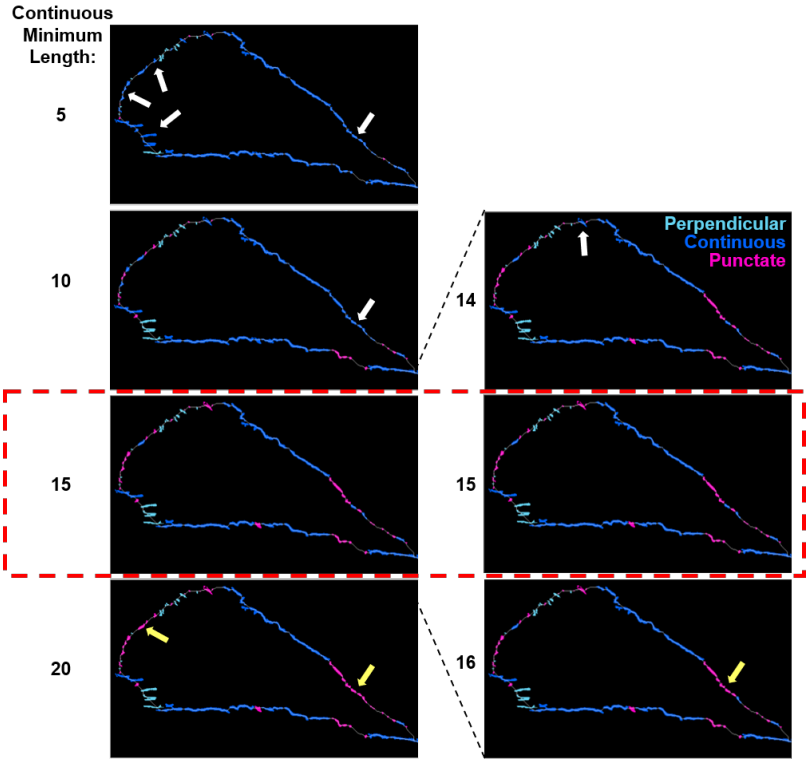

Figure 4.8 Continuous Minimum Length (CML) Threshold Determination. The threshold length for the categorization of continuous versus discontinuous junctions. White arrows indicate junctions that were incorrectly marked as continuous but should be discontinuous when the respective CML was set too low. Yellow arrows indicate regions that were incorrectly categorized as discontinuous but should be continuous due to the CML value being set too high.

4.3.3 Relative Aspect Ratio Determination

The relative aspect ratio (RAR) is the value that determines whether discontinuous junction features are categorized as punctate or perpendicular. The cell presented in Figure 3.9 represents two examples used to determine the RAR. Each junction was color-coded based on the category to which it was assigned when using the specified RAR value (and a CML value of 15). Each image was then reviewed to determine which RAR value most accurately categorized the junction pieces as we would have qualitatively categorized them. The arrows point to example junction pieces that are mis-categorized using the respective RAR value. The white arrows present regions where the RAR is too low and thus punctate junction pieces are coded as perpendicular, while the yellow arrows indicate junctions that are mis-coded as punctate because the RAR threshold value is too high. This process identified 1.2 as the optimal RAR value for this and several other cells evaluated, leading to the use of this value as the default value for the JAnaP.

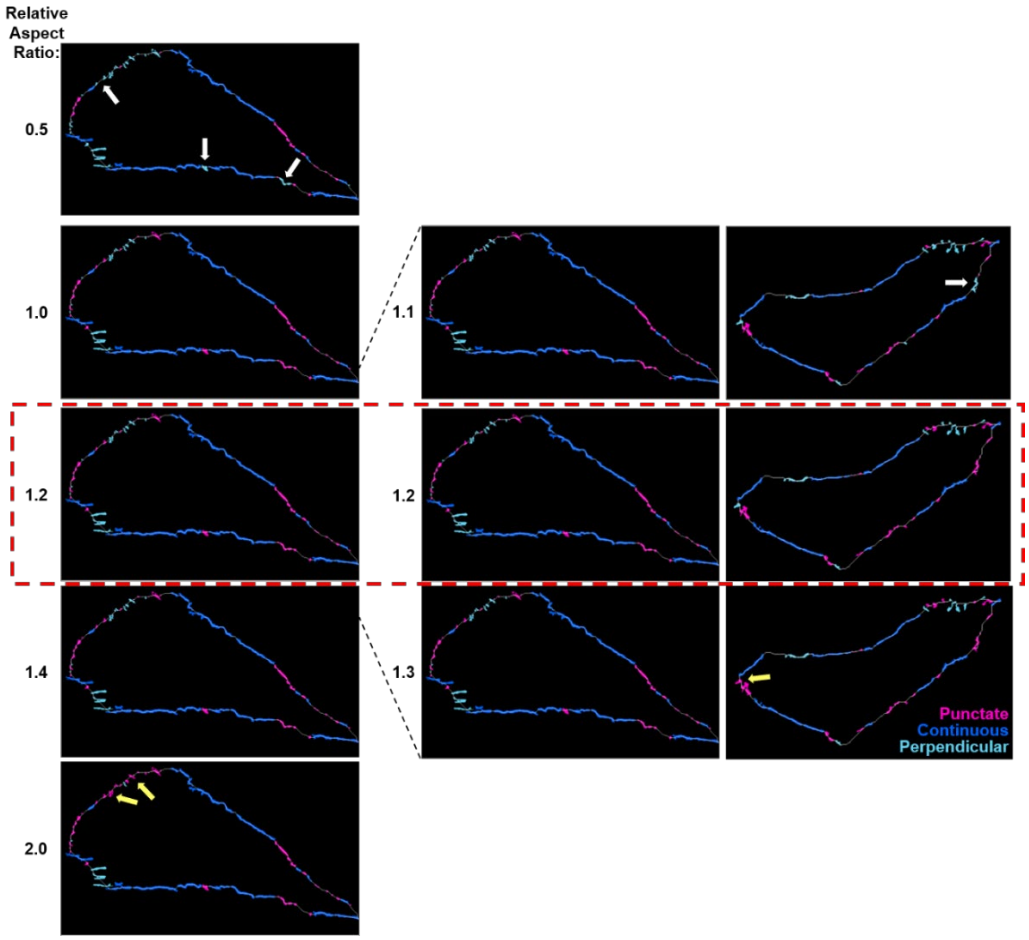

Figure 4.9 Relative Aspect Ratio (RAR) Threshold Determination. The threshold length for categorization of punctate versus perpendicular junctions. White arrows indicate junctions that were incorrectly marked as perpendicular but should be punctate when the respective RAR was set too low. Yellow arrows indicate regions that were incorrectly categorized as punctate but should be perpendicular due to the RAR value being too high.

4.3.4 Quantitative Validation of JAnaP Calculations

The JAnaP program was qualitatively and quantitatively validated by selecting 10 cells that included a mix of junction types and shape factors. The cells were traced in ImageJ and the shape descriptors were directly compared. The line tool was used to manually calculate the percentage of the cell perimeter covered by each junction type. The percent difference calculated between the JAnaP results and ImageJ calculations

were within 1% for cell area, 2% for perimeter and solidity, and 3% for circularity and all junction types (Table 4.1).

		Perimeter (px)	Area (px^2)	Solidity	Circularity	Total ZO-1 Coverage (%)	Contin-uous (%)	Punctate (%)	Perpend-icular (%)
JAnaP Results	Cell 1	1659.5	99100	0.855	0.452	74.95	57.24	14.76	2.96
	Cell 2	1095.1	51940	0.857	0.544	58.59	50.57	6.62	1.39
	Cell 3	1009.8	46006	0.966	0.567	51.43	25.20	24.81	1.42
	Cell 4	733.9	23990	0.935	0.560	57.86	34.06	21.71	2.09
	Cell 5	1664.2	80403	0.774	0.365	37.81	19.07	18.65	0.08
	Cell 6	903.1	44117	0.918	0.680	38.80	8.46	24.04	6.30
	Cell 7	1131.8	52482	0.895	0.515	57.97	42.52	12.58	2.87
	Cell 8	1858.2	179867	0.957	0.655	53.06	34.55	17.10	1.42
	Cell 9	2208.8	115117	0.708	0.296	48.09	27.63	17.25	3.21
	Cell 10	1243.2	74846	0.934	0.609	75.51	61.17	10.70	3.64
ImageJ Traced	Cell 1	1633.1	98489	0.874	0.464	75.56	57.80	14.71	3.05
	Cell 2	1106.6	52405	0.855	0.538	57.21	49.20	6.65	1.36
	Cell 3	1015.7	46465	0.963	0.566	51.63	25.79	24.39	1.44
	Cell 4	742.6	24322	0.932	0.554	58.89	35.14	21.65	2.09
	Cell 5	1657.7	79776	0.779	0.365	38.61	19.38	19.15	0.09
	Cell 6	898.0	43737	0.917	0.682	38.33	8.37	23.71	6.25
	Cell 7	1136.5	53021	0.894	0.516	58.30	42.49	12.97	2.83
	Cell 8	1857.5	179147	0.956	0.652	51.80	33.47	16.93	1.40
	Cell 9	2213.8	116168	0.709	0.298	48.15	27.51	17.48	3.16
	Cell 10	1230.9	74352	0.933	0.617	73.66	59.53	10.45	3.67
Percent Difference	Cell 1	2%	1%	-2%	-3%	-1%	-1%	0%	-3%
	Cell 2	-1%	-1%	0%	1%	2%	3%	0%	3%
	Cell 3	-1%	-1%	0%	0%	0%	-2%	2%	-2%
	Cell 4	-1%	-1%	0%	1%	-2%	-3%	0%	0%
	Cell 5	0%	1%	-1%	0%	-2%	-2%	-3%	-2%
	Cell 6	1%	1%	0%	0%	1%	1%	1%	1%
	Cell 7	0%	-1%	0%	0%	-1%	0%	-3%	1%
	Cell 8	0%	0%	0%	0%	2%	3%	1%	1%
	Cell 9	0%	-1%	0%	-1%	0%	0%	-1%	1%
	Cell 10	1%	1%	0%	-1%	2%	3%	2%	-1%

Table 4.1 JAnaP Validation via ImageJ Comparison.

4.3.5 Quantitative Validation of Multi-Protein Calculations

This capability was first tested on images co-stained for ZO-1 and VE-cadherin. The waypoints were generated on the ZO-1 image and were projected onto the VE-cadherin-tagged image. To validate this approach, cell morphology and junction coverage results were calculated based on waypoints generated on the same image and the image of the different stain, for both proteins. A threshold value of 15 was used to isolate ZO-1 junctions while a threshold of 5 was used to isolate VE-cadherin junctions.

Note that the cells used in the study are from section 5.3.2 below and were selected due to the variations observed in protein co-localization with some treatments (Figure 4.10).

For the shape factors (Figure 4.11), the values for each condition returned the same, non-significantly different result regardless of what image was used to calculate it. This means that waypointing a cell in ZO-1 to measure the cell in that image returned the same shape factor output when those waypoints were (1) projected on the VE-cadherin staining and used to re-trace the same cell, (2) generated on the same cell on the VE-cadherin staining and used to measure the cell in the VE-cadherin image, (3) generated on the same cell on the VE-cadherin image, projected onto the ZO-1 image, and used to re-trace the ZO-1-stained cell.

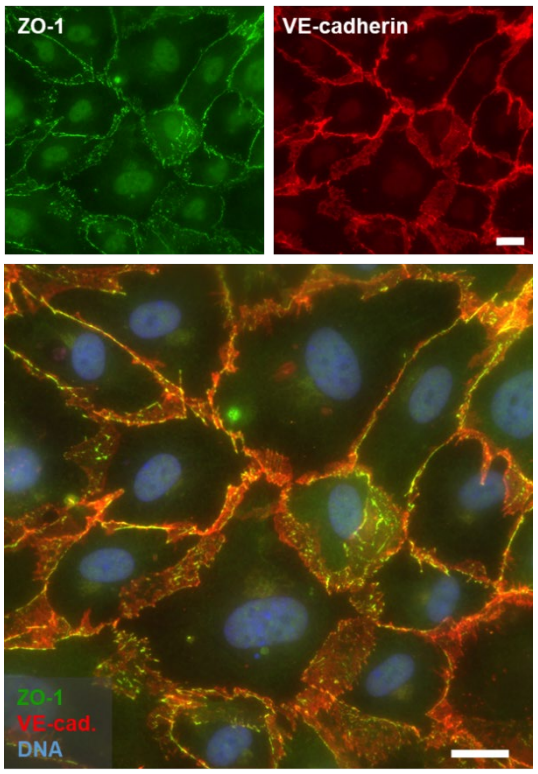

Figure 4.10 Immunostaining of Example Image in Multi-Protein Validation. Immunofluorescence image of HBMECs on fibronectin, cultured for 7 days with 3 days of cAMP treatment, stained for ZO-1 (green), VE-cadherin (red), and DNA (blue). (scale bars = 20 μm)

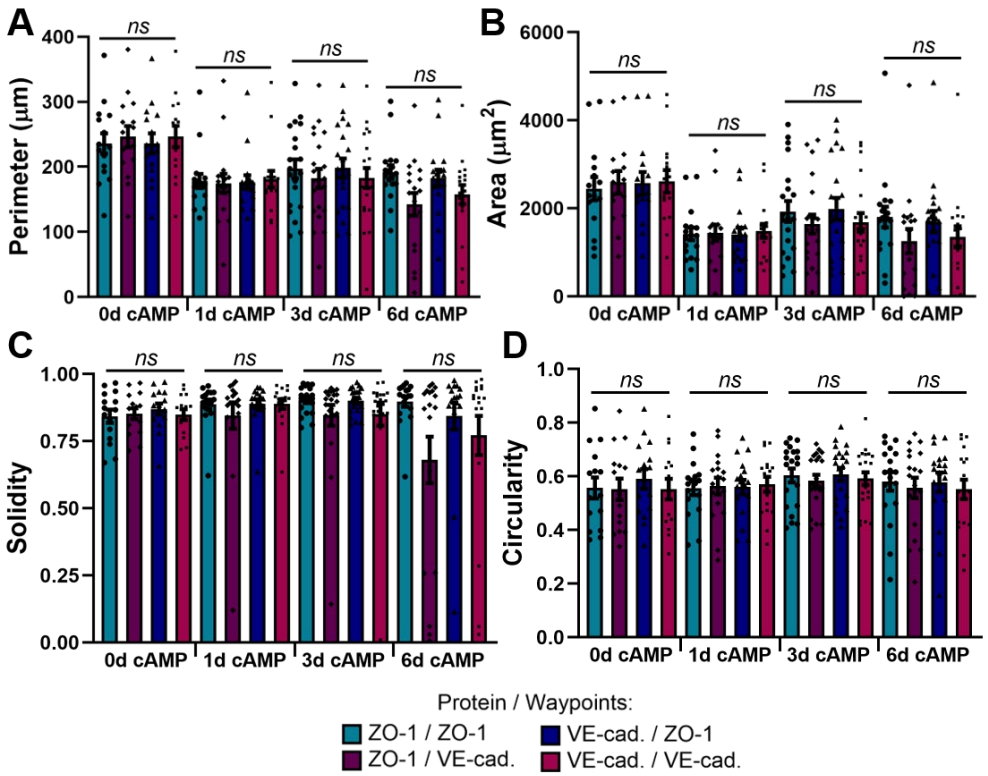

Figure 4.11 Shape Factor Calculations via Multi-Protein Method. Perimeter (A), Area (B), Solidity (C), and Circularity (D) of HBMECs cultured for 7 days with 0, 1, 3, or 6 days of cAMP treatment (see Chapter 5). Naming indicates the channel that the values were calculated for and / the channel the waypoints were generated in. Therefore, ZO-1 / ZO-1 and VE-cad / VE-cad indicate that the values were calculated using the same channel as the waypoint generation. ZO-1 / VE-cad indicates that the waypoints generated in the VE-cad channel were projected onto, and the cells were re-traced using, the ZO-1 image. VE-cad / ZO-1 indicates the opposite. $15 \leq N \leq 21$, where N is the number of cells. The Kruskal-Wallis test with Dunn's multiple comparison tests were used to calculate significant differences for each parameter, where ns = no statistical significance.

For the junction coverage (Figure 4.12), the values for each protein again returned the same, non-significantly different result regardless of what image was used to calculate it. For junction coverage, though, differences between ZO-1 and VE-cadherin would be expected. Therefore, this means that waypointing a cell in ZO-1 to measure the ZO-1 coverage returned the same coverage value when those waypoints

were generated for the same cell on the VE-cadherin image and projected onto the ZO-1 image, and vice versa for the VE-cadherin.

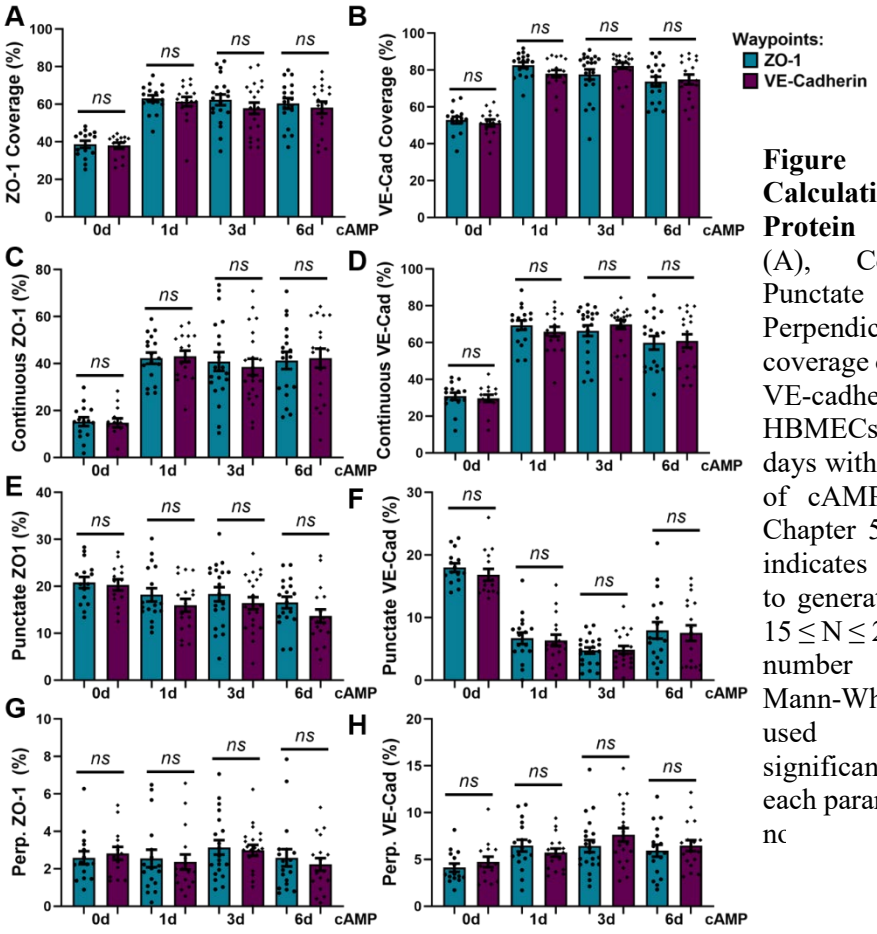

Figure 4.12 Junction Calculations via Multi-Protein Method. Total (A), Continuous (B), Punctate (C), and Perpendicular (D) coverage of ZO-1 (left) and VE-cadherin (right) in HBMECs cultured for 7 days with 0, 1, 3, or 6 days of cAMP treatment (see Chapter 5). Color coding indicates the channel used to generate the waypoints. $15 \leq N \leq 21$, where N is the number of cells. The Mann-Whitey test was used to calculate significant differences for each parameter, where ns = nc .

Together, these results indicate that (1) ZO-1 and VE-cadherin are sufficiently overlapped within the cell-edge, such that using the stain of either one was adequate to measure the shape based on the other, and (2) the method of projecting waypoints within the JAnaP to trace at least two proteins is sufficient for generating consistent cellular outlines and measured results. Importantly, this type of analysis should be performed for every set of proteins intended for use, at least visually or via the method performed here, to ensure that the co-localization of the two proteins is acceptable. If

the proteins are not sufficiently colocalized, the waypoints of one protein will be projected onto the other but may be inconsistently connected due to insufficient alignment with the second protein. If they appear too spread or the shape factors are different depending on which protein was used to generate the waypoints, then each protein image should be traced individually.

4.4 Discussion

The expression of EC junctional proteins plays a vital role in the physiology and pathophysiology of vascular barriers [191]. However, the ability to quantitatively measure the protein presentations as localized in a cellular monolayer has been significantly lacking in the field, limiting analysis of how various parameters involved with homeostasis or pathology influence junctional expression. Here, we developed a program that calculates edge-localized junction presentations in conjunction with cell morphological parameters. The program provides a streamlined analysis process in a semi-automated fashion, since the user only needs to identify the perimeter of each cell via waypointing and the remainder of the calculations are performed automatically. This helps to minimize human error beyond that which exists when identifying the cell perimeter, though, use of the Scikit path-finding algorithm further helps to minimize human error during this step. Note that this program is limited by image and microscope resolution; however, this same limitation exists in current manual analysis techniques. While others have manually calculated the percent of the cell perimeter covered by linear junctions,[15] to our knowledge, this is the first program that allows for a streamlined and automated approach to this otherwise tedious task. Additional reports of junction quantification includes the number [81] and width [83,160] of tight

junctions around the cell edge. Although not explicitly presented here, the JAnaP also measures these parameters in its overall calculations. Importantly, this program could theoretically be expanded to study virtually any cellular system in which immunofluorescent staining or fluorescent protein-tagging of cell-cell junctional proteins is feasible. Indeed, the program could also prove useful for analyzing dynamics of cell-cell junction presentation in real-time in response to drug treatments, mimicked disease conditions, or other relevant processes using fluorescently-tagged junctional proteins and live cell imaging.

The JAnaP has important implications in the field of biomedical engineering and can serve as a tool to gain fundamental biological information about cell-cell junctions, as well as to help inform therapeutic strategies that require knowledge of drug transport mechanisms across vascular barriers. In particular, the JAnaP generates quantitative data that can undergo statistical analysis on cell-cell junctions, rather than relying on a person's subjective interpretation of qualitative images. For example, the JAnaP could provide quantitative measures of continuous, punctate, and perpendicular tight junction protein alterations in ECs in response to interactions with tumor or immune cells,[77,192,193] inflammatory cytokines,[68] ischemia,[194] VEGF or thrombin treatment,[54,195] or even in response to mechanical injury such as traumatic brain injury [78,196]. Additionally, it could be used to quantify the extent of barrier opening when investigating new techniques for therapeutic delivery via BBB-penetration (e.g., ultrasound,[197–199] photodynamic therapy,[200] photothermal therapy [201]).

Chapter 5 - Junction Phenotypes and Barrier Integrity

5.1 Introduction

As described in Chapter 2, cell-cell junctions, especially within the blood-brain barrier, are extremely important for maintaining normal physiological processes. They regulate numerous cell functions (e.g., migration, proliferation) and paracellular transport across the barrier, such that decreased junctional protein is associated with dysregulated transport and leaky vasculature. Despite the important role of cell-cell junctions and the BBB, the mechanisms involved in barrier formation and disruption aren't fully understood. Furthermore, the specific influence of different junction presentations on BBB properties remains largely understudied. One reason for this lack of quantification was the lack of efficient quantification methods to assess junction phenotype. The development of the JAnaP (Chapter 4) has since addressed this gap, enabling quantitative phenotyping of junction presentation *in situ*.

One difficulty in studying the BBB *in vitro*, is the challenge associated with recapitulating the *in vivo* BMEC properties, [202] such as the overexpression of the tightly structured network of cell-cell junctions. To address this, however, many approaches have been reported for various brain EC types. One technique to improve tight junction formation and barrier properties, evidenced by junction immunostaining, Transwell permeability studies, and TEER, is the co-culturing of ECs with neural cells (e.g., astrocytes) or their conditioned medium [203,204]. This not only improved BBB properties, but also provided insights into the roles of biochemical and physical contacts of BMECs with other cells present in the *in vivo* microenvironment. Another

biomimetic approach has been the use different matrix proteins that (at least partially) recapitulate the *in vivo* basement membrane or the brain microenvironment. The basement membrane is known to have an important role in maintaining vascular function [205]. As such, is it unsurprising that constituents of this matrix (i.e., fibronectin, collagen type IV, and laminin; or combinations of the three) are reported to elevate TEER values relative to type I collagen in porcine brain capillary ECs, [206] and promote adhesion and spreading of iPSC-derived brain ECs [83]. Additionally, hyaluronic acid is a primary component of the brain microenvironment, [8] and has been shown to induce tube formation in a mouse-derived brain capillary EC line [207]. A mixture of hyaluronic acid and gelatin is reported to improve cell spreading of endothelial progenitor cells and HUVECs [208] and has been used for *in vitro* models of the BBB [209,210].

Another approach towards improving brain EC phenotype is the activation of cyclic 3'-5'-adenosine monophosphate (cAMP)-dependent protein kinase (PKA) via cAMP, dexamethasone or hydrocortisone, which is linked with improved barrier function [49,72,211]. Specifically, 8-(4-chlorophenylthio) adenosine-3',5'-cyclic monophosphate sodium salt (CPT-cAMP) and 4-(3-butoxy-4-methoxybenzyl) imidazolidin-2-one (RO-20-1724) have been shown to decrease permeability and increase tight junctions in various EC types [48,212]. These supplements: (1) inhibit myosin light chain phosphorylation which decreases EC contraction, and (2) activate Rac1 to increase cortical actin stabilization and decrease actin stress fiber formation; both of which lead to improved endothelial barrier function [213]. Furthermore, barrier

confluency and maturity are also reported to influence junction presentation within the endothelium [15,71].

Using the JAnaP to quantify junction presentation, we aimed to understand the influence of each junction phenotype in terms of contribution to overall barrier properties, such as permeability and barrier tightness (measured by TEER). To do this, we investigated what *in vitro* factors most influence junction presentation in HBMECs, then systematically varied those parameters to vary junction phenotype. Specifically, we studied substrate protein coating, culture time, and treatment with cAMP supplements to identify conditions driving altered states of junction presentation. We then aimed to correlate these junction phenotypes with measures of barrier integrity.

5.2 Materials and Methods

5.2.1 Cell Culture

Ethics approval for all studies were obtained from the University of Maryland, Institutional Biosafety Committee (Protocol Number ESSR #15-06). HBMECs were purchased from Cell Systems and cultured as previously described [214].

5.2.2 Substrate Coating and Experimental Conditions

On Day 0, glass bottom 24-well plates (Greiner Bio-One, 662892) were coated with 100 µg/ml collagen I (CN) (Sigma Aldrich, C3867), 100 µg/ml fibronectin (FBN) (Sigma Aldrich, F2006), 100 µg/ml collagen IV (CIV) (Sigma Aldrich, C6745), 100 µg/ml fibronectin: 100 µg/ml collagen IV: 2 µg/cm^2 laminin (FCL), or 0.4% thiol-modified hyaluronan: 0.4% thiol-modified gelatin (HA/Gtn) (ESI-BIO, GS313) for 30

min at 37 °C, or 2 μg/cm^2 laminin (LN) (Sigma Aldrich, L4544) for 60 min at 37 °C. All constituents were resuspended per the manufacturer's instructions, then diluted to the respective concentration in PBS (+/+ $Ca^{2+/}Mg^{2+}$). After coating the surface, the excess solutions were removed, the wells were rinsed with 37 °C PBS (+/+), 500 μl of warm HBMEC medium was added to each well, and the plate was incubated at 37 °C until HBMEC seeding (5E4 cells/cm^2, 9.5E4 cells/well) (approximately 20 minutes). After the cells were seeded, 500 μl of warm medium was additionally added to each well, and the cells were cultured for 2, 4, or 7 days, with varying treatments with cAMP supplements. These "supplements" include 250 μM 8-CPT-cAMP (Abcam, ab120424) and 17.5 μM RO-20-1724 (Tocris Bioscience, 0415), which are routinely used in EC culture to improve junction localization barrier properties [215–219]. A summary of the culture conditions is presented in Figure 5.1. For all experiments, the medium was changed the day after cell seeding on Day 1, to "control" HBMEC medium or medium containing cAMP supplements. For 2-day experiments, the samples were fixed and stained on the subsequent day (Day 2), generating a sample with no cAMP treatment (2D/0d cAMP) or 1 day of cAMP treatment (2D/1d cAMP). For 4-day experiments, the medium was again changed two days later on Day 3, maintaining the cAMP supplements in the 4D/3d cAMP sample, adding the supplements to the 4D/1d cAMP sample, and maintaining no supplement in the 4D/0d cAMP sample. Those samples were then fixed the next day, on Day 4. For 7-day experiments, the medium was changed to add or maintain the respective supplement treatments on Day 3, Day 4, and Day 6. Those samples were then fixed the next day, on Day 7, to generate samples cultured for 7 days with 6 days of cAMP treatment (7D/6d cAMP), 3 days of cAMP

treatment (7D/3d cAMP), 1 day of cAMP treatment (7D/1d cAMP), or no cAMP treatment (7D/0d cAMP). Three biological replicates were performed for each experiment.

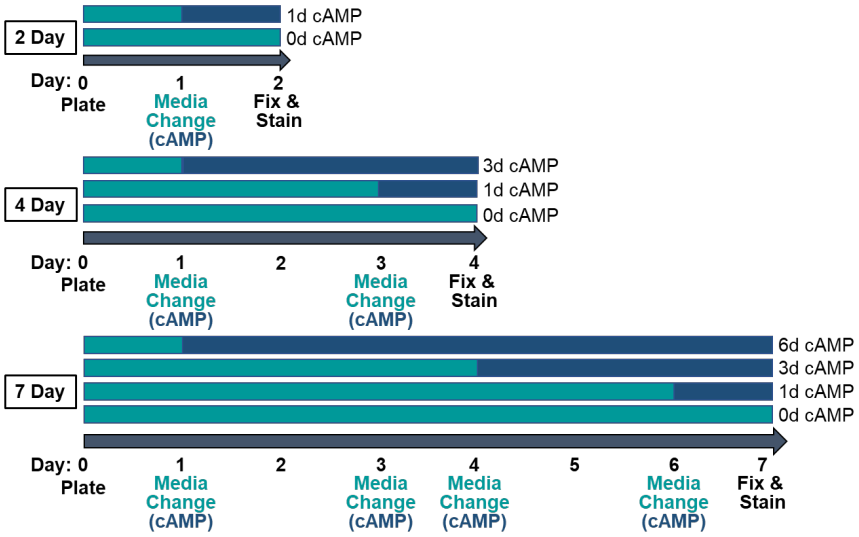

Figure 5.1 Cell Culture Conditions and Treatments.

5.2.3 Immunostaining

HBMECs were rinsed with 37 °C PBS (+/+) and fixed with 1% formaldehyde (ThermoFisher Scientific, BP531) for 20 minutes. Note that all steps were performed under gentle rocking. Samples were then washed three times, 5 minutes each, with room temperature PBS (+/+), then permeabilized for 5 minutes with 0.25% TritonX-100 (Sigma-Aldrich). The washing steps were repeated, then the samples were blocked for 1 hour at room temperature with 2% goat serum (Abcam). Primary antibodies against ZO-1 (rabbit polyclonal IgG, ThermoFisher Scientific, 61-7300, 1:500 dilution) and VE-cadherin (mouse monoclonal IgG, Santa Cruz, sc-9989, 1:50 dilution) in 2% goat serum were added to the cells overnight at 4°C. The next day, the wash and blocking steps were repeated, then secondary antibodies goat anti-rabbit Alexa Fluor 488 (Abcam, ab150077, 1:100 dilution) and goat anti-mouse Alexa Fluor 568

(ThermoFisher Scientific, A-11004, 1:100 dilution), plus 1:2500 Hoechst (ThermoFisher Scientific, H3570), were added to the cells in PBS (+/+) for 1 hour at room temperature. The wash steps were again repeat prior to imaging. For claudin-5 staining (rabbit polyclonal IgG, Abcam, ab15106, 1:200 dilution), cells were instead fixed with 100% ice cold methanol (Sigma Aldrich) for 10 minutes and blocked with 2% goat serum containing 0.3% TritonX-100 for 1 hour at room temperature.

5.2.4 Junction Analysis

This analysis was performed by Jae W. Jung (Stroka Lab).

Junction presentation was quantified using the Junction Analyzer Program (JAnaP) previously described (Chapter 4, [215]). Briefly, the complete cells within each image were traced via "waypoints". For ZO-1 and VE-cadherin quantification, this was performed on the images from the green fluorescent channel (i.e. ZO-1 immunostaining), and the waypoints were projected onto the red fluorescent channel (i.e. VE-cadherin immunostaining). For claudin-5 quantification, the cells were traced using the red fluorescent channel (i.e. VE-cadherin immunostaining) and the waypoints were projected onto the green fluorescent channel (i.e. claudin-5 immunostaining), for improved cell-edge visualization. Threshold values of 15, 5, and 5, were applied to isolate the ZO-1, VE-cadherin, and claudin-5 junctions, respectively. The cell morphological parameters (e.g., area, solidity, circularity) were then calculated, as well as the percent of the cell edge presenting continuous, punctate, or perpendicular junction. The junction types were classified based on the length of the junction piece that coincides with the cell path (> 15 pixels for continuous junction) and the relative

aspect ratio with respect to the cell path (> 1.2 for perpendicular junction, otherwise punctate).

5.2.5 Transwell Permeability Assay

Permeability measurement performed by Collin Inglut (Huang Lab).

The Transwell permeability assay was performed per the 2-day treatment condition (Figure 1). On day 0, HBMECs were seeded (5E4 cells/cm^2, 1.6E4 cells/well) into Transwell inserts (Falcon, 24 well format, 1.0 µm pore size) that had been coated with 100 µg/ml FBN for 30 minutes at 37 °C. The next day (day 1), the medium was changed to control medium (no supplements) or cAMP-medium. On day 2, solutions of 1 mg/ml FITC-Dextran (70 kDa, Sigma-Aldrich) were prepared in the respective medium formulations. Each Transwell was moved to a new well containing 800 µl of fresh medium (containing the respective cAMP treatment) and the top well medium was replaced with 400 µl of the dextran-medium. After 30 minutes at 37 °C, medium was collected, and the fluorescence was measured using a BioTek Synergy Neo2 plate reader (Excitation/Emission: 492/518 nm, Gain: 65). A standard curve was used to calculate the mass of dextran within the sample and the apparent permeability coefficient (P_app) was calculated as previously described by Tominaga et. al, [220].

$$P\_app = (VA \cdot [C_{abluminal}]) \cdot A^{-1} \cdot [C_{luminal}]^{-1} \cdot t^{-1} \; [=] \; cm/s$$

$VA = volume\ of\ abluminal\ chamber$ (0.8 cm^3)

$A = membrane\ surface\ area$ (0.33 cm^2)

$[C_{abluminal}] = abluminal\ dextran\ concentration$ (µ$g\ ml^{-1}$)

$[C_{luminal}] = intial\ luminal\ dextran\ concentration$ (1000 µ$g\ ml^{-1}$)

$t = time\ of\ experiment$ (1800 s)

Transwells were subsequently fixed and stained as described in the "Immunostaining" section above. The membranes were then removed from the inserts using an X-acto knife and sandwiched between two coverslips, luminal-side down. The membranes were then imaged, and the junctions were quantified, as described above. Three biological replicates were performed for this experiment.

5.2.6 Local Permeability Assay

To visualize areas of monolayer leakiness and correlate them with junction phenotype, we adapted the XPerT permeability assay developed by Dubrovskyi et al. [62]. Here, however, FBN was biotinylated (b-FBN) using EZ-Link NHS-LC-LC-Biotin (ThermoFisher Scientific, 21343) according to the manufacturer's instructions (instead of gelatin described in [62]). b-FBN was then adsorbed onto glass bottom 24-well plates overnight at 4 °C. Excess protein was then removed, the wells were rinsed with PBS (+/+), and 500 µl of warm HBMEC medium was added to each well. The plate was incubated at 37 °C until HBMEC seeding (5E4 cells/cm^2, 9.5E4 cells/well) (approximately 20 minutes). After the cells were seeded, 500 µl of warm medium was additionally added to each well, and the cells were cultured per the 2-day experiment in Figure 5.1. Prior to fixing, however, the samples were treated with 50 µg/ml FITC-avidin (ThermoFisher Scientific, A821) for 3 min. This resulted in immobilized FITC-avidin bound to the underlying b-FBN at permeable sites of the monolayer. The samples were then fixed and stained for ZO-1 and VE-cadherin per the "Immunostaining" section above, but each protein was immunostained separately and goat anti-rabbit Alexa Fluor 568 (ThermoFisher Scientific, A-11011) was used as the secondary antibody for ZO-1. This allowed visualization of permeable regions in green,

due to the immobilized FITC-avidin, and phenotyping of red junctions, via immunostaining. Three biological replicates were performed for each ZO-1 and VE-cadherin.

5.2.7 Local Permeability Analysis

To analyze the results of the local permeability assay, two primary steps were performed. An example monolayer image is presented in Figure 5.2.A to depict each step. First, image processing of the green-channel images of the bound FITC-avidin was performed in ImageJ (Figure 5.2.B). To do this, each image was converted to 8-bit and a threshold was applied to create a binary image showing the presence or absence of a permeated region (PR) (Figure 5.2.C). The second step was to process the red-channel junctional protein images (Figure 5.2.D) using the JAnaP. This analysis differed from other JAnaP processing described in section 5.2.4, since every single cell border was waypointed, regardless of whether the entire cell was present in the image. The Jupyter Notebook was then used to generate several images of the categorized junctions, in some cases, overlaying them onto the PR threshold images (Figure 5.2.E-L). For the quantification of this assay, several parameters were studied, as outlined below.

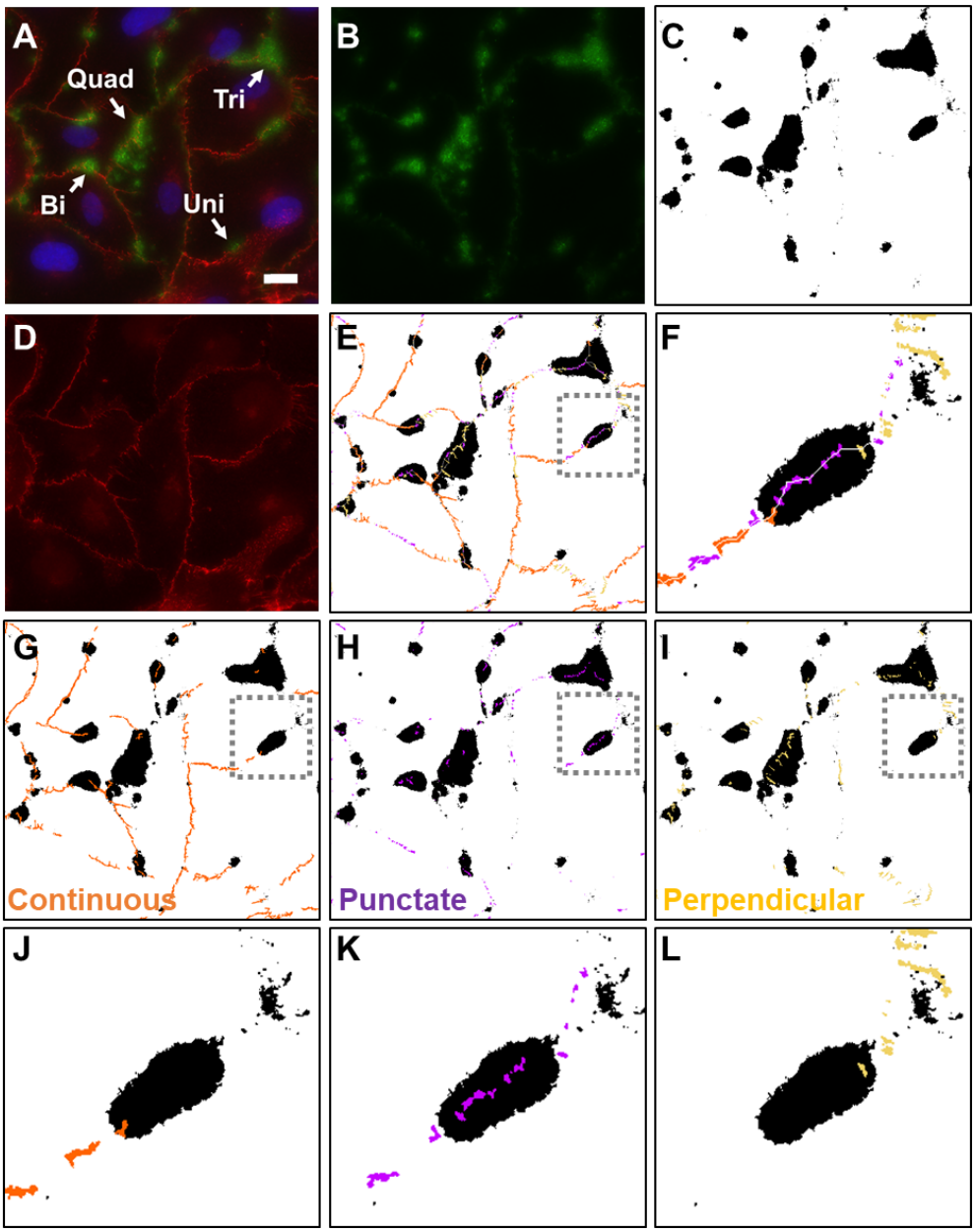

Figure 5.2 Local Permeability Analysis – Image Processing. Composite image of VE-cadherin (red) and FITC-avidin (green), labeled to identify examples of the PR categories (A). Images of bound FITC-avidin (B) are processed in ImageJ to generate 8-bit binary images of PRs (C). The raw junctional protein images (D) are processed in the JAnaP to generate images of categorized junctions, which can be overlaid onto the PR images (E) and separated into images depicting only junctions of a specific category (J-L). Cropped images depicting the regions in the gray-dotted box for (E, G-I) are presented in (F, J-L), respectively. (scale bar = 20 μm, applies to A-E, G-I)

5.2.7.A PR Categorization

PRs were categorized as Uni, Bi, Tri, Quad, or Multi, depending on the number of cells the PR was associated with (1, 2, 3, 4, 5+, respectively). Figure 5.2.A presents an example of most categories. To quantify PR area, the Analyze Particles function in ImageJ function was used on the PR threshold images (Figure 5.2.C). Images showing the cell edges on top of the PRs (Figure 5.2.E) were used to manually identify the number of cells that each PR was adjacent to. Five images from each of the 2-3 trials were measured, and the average count of each PR category per image was calculated. The PR area measurements were averaged over all PRs within the respective category. While this was performed for the PR images associated with both the VE-cadherin- and ZO-1-stained images, only the VE-cadherin-associated results are presented here. Note that the ZO-1-associated images showed similar trends.

5.2.7.B Junction analysis along PR length

To calculate the percent and count of junctions along the cell perimeters coinciding with PRs, images like Figure 5.3.A were used. These overlapped images were manually traced in ImageJ using the segmented line tool. Importantly, only PRs greater than 400 pixels^2 were included in this analysis. For each blot (Figure 5.3.B), the length of the cell path(s) overlapping the PR was manually traced to calculate the PR length (Figure 5.3.C). Then, the number and length of each junction type was subsequently summed (Figure 5.3.D-F). The difference was taken to be the length of the no junction regions. The summed length of each junction type divided by the PR length was taken to be the % Junction Along the PR Path. For the continuous versus discontinuous analysis, the punctate and perpendicular values were subsequently added

together as the measures of discontinuous junctions. Three images from the 2-3 trials were measured, with the values calculated on a per PR basis.

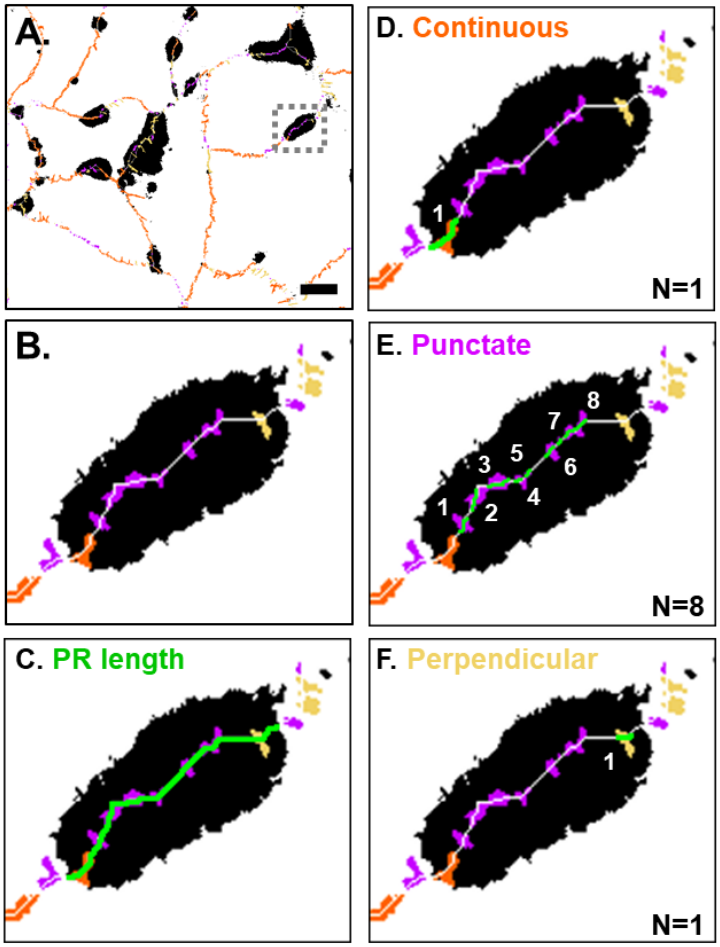

Figure 5.3 Junction Analysis Along PR Length. Junction categorization and cell paths overlaid onto PR threshold image (A). Gray-dotted box indicates blot cropped for this example (B). Tracing the length of the cell path that corresponds to the length of the PR (green) provides the PR length (C). Tracing the length of each junction type (green) provides the count and length of continuous (D), punctate (E), and perpendicular (F) junctions along the PR length. The numbers indicate a distinct junction piece. (scale bar = 20 µm, applies to A)

5.2.7.C Co-localization Analysis

For the co-localization analysis, the Jupyter Notebook was used to generate junction-categorized images that presented all the junctions for each category within a given image, on a black background without the cell path (Figure 5.4.top row). These images were uploaded into ImageJ, converted to 8-bit, and a threshold was applied to isolate the junctions. A selection was then created to measure the total area of each junction type present within the image (A_total). Next, the PR threshold images (Figure

5.2.C) were again uploaded into ImageJ. A selection was created to isolate the PRs and was used as a mask applied to each junction image (Figure 5.4.middle row). The junctions present outside of the masked PR region were removed, leaving only the junction pieces corresponding to the PRs remaining (Figure 5.4.bottom row). Another selection was created to measure the area of each junction type that corresponded with PRs in the image (A_PR). The % Co-localization was taken as (A_PR/A_total)*100 for each junction type.

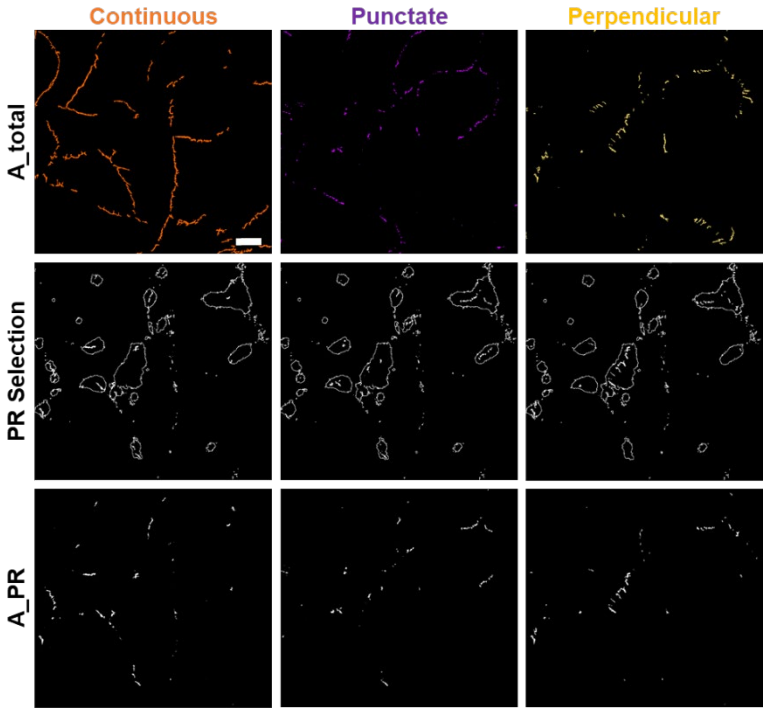

Figure 5.4 Co-localization Analysis. Isolated junctions used to calculate the total junction area (A_total) for each junction type (top row). A "selection" of the corresponding PR threshold image was used to create a mask applied to each junction type (middle row) and remove all junctions that did not colocalize with a PR. Area measurement of remaining junctions (bottom row) provided the PR colocalized junction area (A_PR).

5.2.8 Trans-Endothelial Electrical Resistance (TEER) Assay

TEER measurement performed by Jae Jung (Stroka Lab).

For the TEER assay, cells were cultured on Transwell inserts (24-well) with a 0.4 µm pore size (Falcon, 353047) according to the 4 Day schedule (Figure 5.1). On day 0, the inserts were coated with 100 µg/ml FBN and incubated for 1 hour at 37 °C.

Excess solution was then removed, and the inserts were rinsed with warm PBS (+/+). The top and bottom chambers of the system were then respectively filled with 100 µl and 800 µl of warm HBMEC medium and placed in the incubator during cell splitting. HBMECs were then plated at $5x10^4$ cells/cm^2 and the volume of the top chamber was then brought to 200 µl. The controls for this experiment were a blank insert and an insert with just the FBN coating for each condition. Starting on Day 1, resistance measurements were performed using an $EVOM^2$ meter and performed every day for the duration of the experiment. Electrodes were rinsed in warm PBS (+/+) then HBMEC medium prior to measurement of each sample. On days on which a media change occurred, the TEER measurement was performed prior to the media change. After collecting the measurement on Day 4, the inserts were rinsed with warm PBS and fixed as described in section 5.2.3. Prior to imaging, the membranes were removed from the insert, inverted, and sandwiched between two glass coverslips with PBS. Junction analysis was then performed on the images as described in section 5.2.4.

5.2.9 Microscopy

All samples were imaged using a 60x oil objective on an inverted IX83 Olympus microscope and Olympus cellSens Software. For fixed-cell epifluorescence microscopy, images were simultaneously collected using the red, green, and blue filters. Images within the manuscript have been enhanced via ImageJ for improved visualization. For live-cell imaging, the imaging chamber was maintained at 37°C, 50% humidity, and 5% CO_2. Images were collected every 5-10 minutes, then then image sequences were analyzed for junction presentation as described in the "Junction Analysis" section above.

5.2.10 Statistical Analysis

All statistical analysis and graph generation was performed using GraphPad Prism 8. For each data set, a D'Agostino-Pearson normality test was used to identity the normality of the data. If the data was normal, a one-way ANOVA with a Tukey's multiple comparison post-hoc test was performed. More frequently, the data was non-normal, in which case the non-parametric Kurskal-Wallis ANOVA with Dunn's multiple comparison post-hoc testing was performed instead. For instances where only two groups were compared, a Mann-Whitney test was used. A linear regression was used to compare the junction presentation with global permeability and a two-way ANOVA was used to compare the experimental versus the control group for each set in the TEER study. No statistical significance (ns) was determined using $p > 0.05$, and statistical significance was indicated as * $p \leq 0.05$, ** $p \leq 0.01$, *** $p \leq 0.001$, **** $p \leq 0.0001$. Errors bars represent standard error of the mean. All data represents pooled values from three independent trials unless otherwise noted in the figure captions.

5.3 Results

5.3.1 cAMP supplements increase continuous ZO-1 and VE-cadherin junctions, independently of substrate coating

Figure 5.5 respectively presents HBMECs cultured for 2 days with and without cAMP supplements on six different matrix constituents. Only minor differences in cell and junction morphology were apparent between each substrate coating. While no significant differences in cell area, solidity, or circularity were observed (Figure 5.6), CIV and LN generally induced lower junctional protein localization (Figure 5.7 and

Table 5.1). The addition of cAMP supplements generally decreased cell area but had only minor effects on cell circularity and solidity (Figure 5.6). On the other hand, cAMP supplements consistently improved barrier architecture, as expected. Significant increases in continuous junction were observed for every condition for both ZO-1 and VE-cadherin (Figure 5.7), with the greatest presentation observed on FBN (though, F:C:L and HA:G induced similar coverage). While only minor changes in punctate and perpendicular ZO-1 were observed, cAMP supplements significantly decreased punctate VE-cadherin and increased perpendicular VE-cadherin.

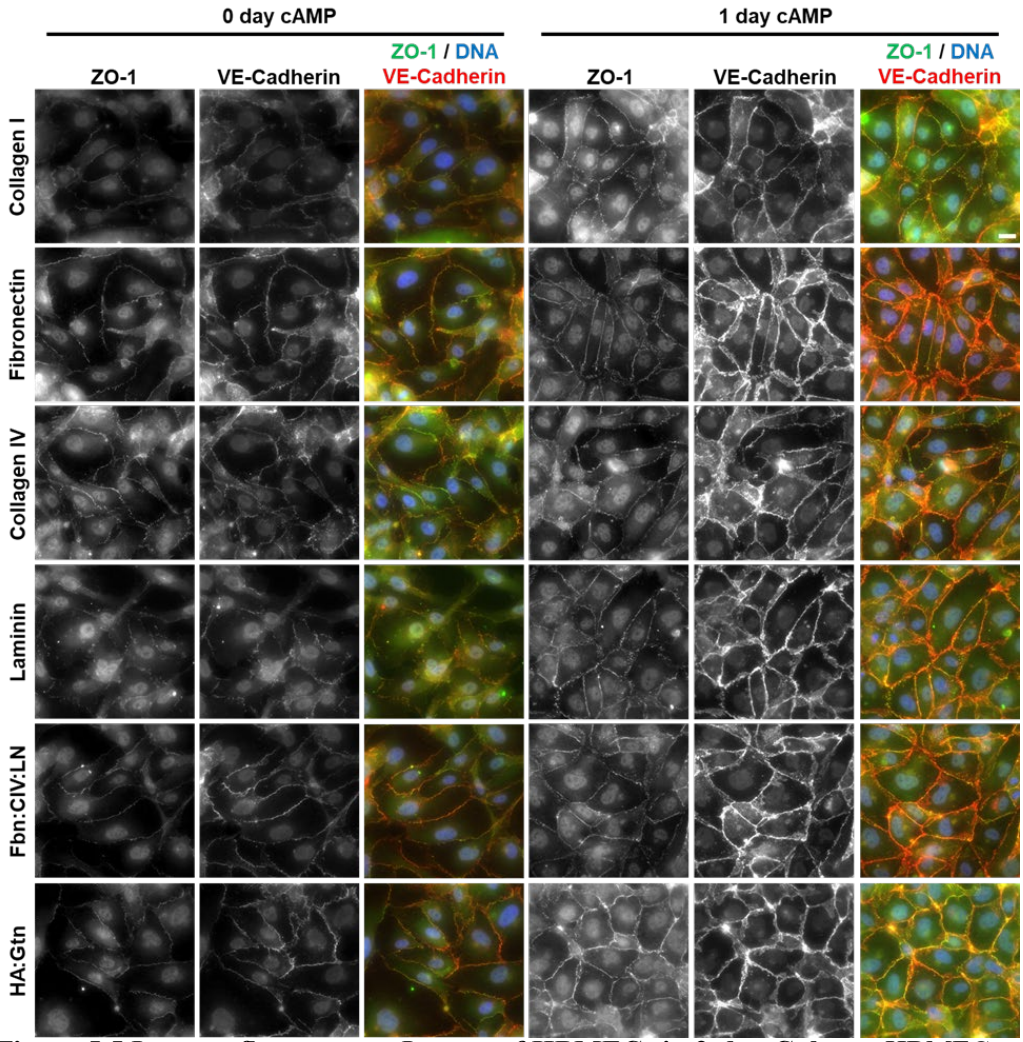

Figure 5.5 Immunofluorescence Images of HBMECs in 2-day Culture. HBMECs on 6 substrate coatings, cultured for 2 days with and without cAMP treatment, stained for ZO-1 (green), VE-cadherin (red), and DNA (blue). (scale bar = 20 μm)

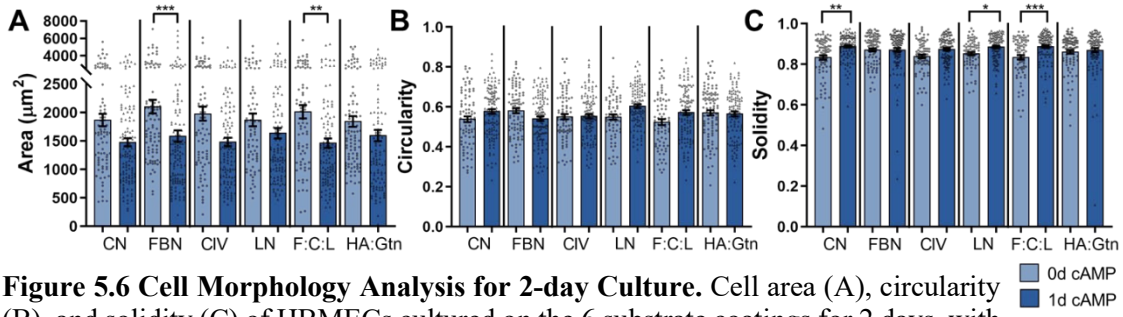

Figure 5.6 Cell Morphology Analysis for 2-day Culture. Cell area (A), circularity (B), and solidity (C) of HBMECs cultured on the 6 substrate coatings for 2 days, with and without 1d cAMP treatment. $72 \leq N \leq 125$, where N is the number of cells. The Kruskal-Wallis test was used to calculate significant differences for each parameter, where * $p < 0.05$, ** $p < 0.01$, and *** $p < 0.001$.

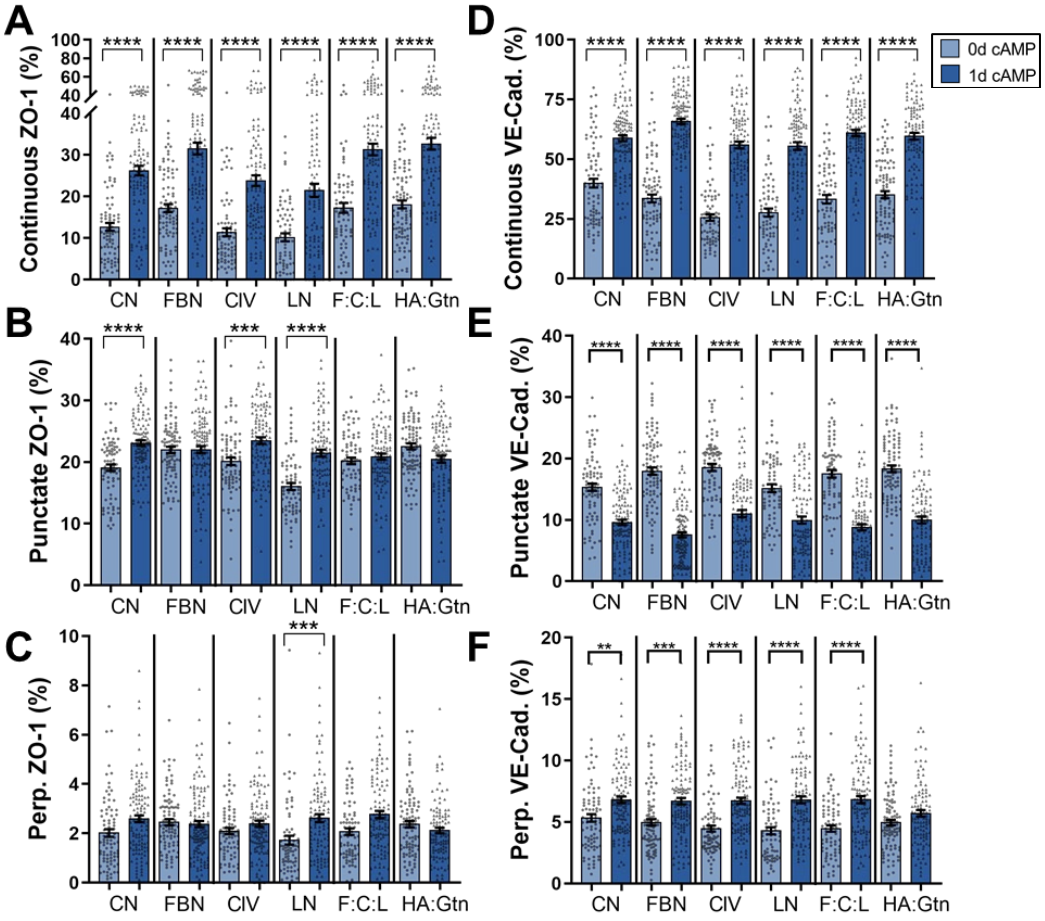

Figure 5.7 Junction Phenotype Analysis for 2-day Culture. Edge presentation of continuous (A, D), punctate (B, E), and perpendicular (C, F) junctions for ZO-1 and VE-cadherin, respectively. $72 \leq N \leq 125$, where N is the number of cells. The Kruskal-Wallis test with a Dunn's multiple comparison test was used to calculate significant differences for each parameter, where * $p < 0.05$, ** $p < 0.01$, *** $p < 0.001$, and **** $p < 0.0001$. See Table 5.1 for statistical analysis.

ZO-1 Coverage

Comparisons	0cAMP	1cAMP
CIV vs CN	ns	ns
CIV vs FBN	*	*
CIV vs FCL	ns	ns
CIV vs GG	**	ns
CIV vs LN	ns	ns
CN vs FBN	*	ns
CN vs FCL	ns	ns
CN vs GG	**	ns
CN vs LN	ns	*
FBN vs FCL	ns	ns
FBN vs GG	ns	ns
FBN vs LN	****	****
FCL vs GG	ns	ns
FCL vs LN	**	****
GG vs LN	****	****

ZO-1 Continuous

Comparisons	0cAMP	1cAMP
CIV vs CN	ns	ns
CIV vs FBN	*	*
CIV vs FCL	ns	*
CIV vs GG	**	**
CIV vs LN	ns	ns
CN vs FBN	ns	ns
CN vs FCL	ns	ns
CN vs GG	ns	ns
CN vs LN	ns	*
FBN vs FCL	ns	ns
FBN vs GG	ns	ns
FBN vs LN	**	****
FCL vs GG	ns	ns
FCL vs LN	*	****
GG vs LN	***	****

VE-Cad Coverage

Comparisons	0cAMP	1cAMP
CIV vs CN	**	ns
CIV vs FBN	**	ns
CIV vs FCL	ns	ns
CIV vs GG	ns	ns
CIV vs LN	ns	ns
CN vs FBN	ns	ns
CN vs FCL	ns	ns
CN vs GG	ns	ns
CN vs LN	***	ns
FBN vs FCL	ns	ns
FBN vs GG	ns	ns
FBN vs LN	ns	***
FCL vs GG	ns	ns
FCL vs LN	ns	ns
GG vs LN	*	ns

VE-Cad Continuous

Comparisons	0cAMP	1cAMP
CIV vs CN	**	ns
CIV vs FBN	ns	**
CIV vs FCL	ns	ns
CIV vs GG	ns	ns
CIV vs LN	ns	ns
CN vs FBN	ns	ns
CN vs FCL	ns	ns
CN vs GG	ns	ns
CN vs LN	*	ns
FBN vs FCL	ns	ns
FBN vs GG	ns	ns
FBN vs LN	ns	**
FCL vs GG	ns	ns
FCL vs LN	ns	ns
GG vs LN	ns	ns

ZO-1 Punctate

Comparisons	0cAMP	1cAMP
CIV vs CN	ns	ns
CIV vs FBN	ns	ns
CIV vs FCL	ns	*
CIV vs GG	ns	*
CIV vs LN	**	ns
CN vs FBN	ns	ns
CN vs FCL	ns	ns
CN vs GG	**	ns
CN vs LN	ns	ns
FBN vs FCL	ns	ns
FBN vs GG	ns	ns
FBN vs LN	****	ns
FCL vs GG	ns	ns
FCL vs LN	**	ns
GG vs LN	ns	****

ZO-1 Perpendicular

Comparisons	0cAMP	1cAMP
CIV vs CN	ns	ns
CIV vs FBN	ns	ns
CIV vs FCL	ns	ns
CIV vs GG	ns	ns
CIV vs LN	ns	ns
CN vs FBN	ns	ns
CN vs FCL	ns	ns
CN vs GG	ns	ns
CN vs LN	ns	ns
FBN vs FCL	ns	ns
FBN vs GG	ns	ns
FBN vs LN	***	ns
FCL vs GG	ns	ns
FCL vs LN	ns	ns
GG vs LN	**	ns

VE-Cad Punctate

Comparisons	0cAMP	1cAMP
CIV vs CN	ns	ns
CIV vs FBN	ns	**
CIV vs FCL	ns	ns
CIV vs GG	ns	ns
CIV vs LN	ns	ns
CN vs FBN	ns	ns
CN vs FCL	ns	ns
CN vs GG	ns	ns
CN vs LN	ns	ns
FBN vs FCL	ns	ns
FBN vs GG	ns	ns
FBN vs LN	ns	ns
FCL vs GG	ns	ns
FCL vs LN	ns	ns
GG vs LN	ns	ns

VE-Cad Perpendicular

Comparisons	0cAMP	1cAMP
CIV vs CN	ns	ns
CIV vs FBN	ns	ns
CIV vs FCL	ns	ns
CIV vs GG	ns	ns
CIV vs LN	ns	ns
CN vs FBN	ns	ns
CN vs FCL	ns	ns
CN vs GG	ns	ns
CN vs LN	ns	ns
FBN vs FCL	ns	ns
FBN vs GG	ns	ns
FBN vs LN	ns	ns
FCL vs GG	ns	ns
FCL vs LN	ns	ns
GG vs LN	ns	ns

Table 5.1 Statistical Significance for Junction Phenotype Analysis for 2-day Culture. The comparison between each substrate protein with and without cAMP is presented, as calculated using the Kruskal-Wallis test with a Dunn's multiple comparison test. A red box marked with "ns" signifies no significant difference. A green box signifies a significant difference, where * $p < 0.05$, ** $p < 0.01$, *** $p < 0.001$, and **** $p < 0.0001$. Data corresponds to Figure 5.8.

5.3.2 Extending cell culture requires increased cAMP treatment for similar junction coverage

While treatment with cAMP supplements led to increased junction coverage for both ZO-1 and VE-cadherin, the total percentage of junction presented at the cell edge (calculated by adding the junction presentation of each junction type) remained less than full coverage. We therefore investigated the effects of extended cell culture and cAMP treatment time to probe the ability of these parameters to further increase

junction coverage. Since we observed minimal differences between substrate protein coatings, we investigated these effects only on FBN.

First, we studied the effects of extending the time in cell culture to 4 days. Figure 5.8 respectively presents HBMECs cultured for this length of time with 0, 1, or 3 days of cAMP supplements. No change in cell area, circularity, or solidity, were observed with cAMP treatment, though the cells were smaller compared to those cultured for 2 days, except for 4D/3d cAMP groups where increased area was observed. Increased cAMP treatment increased both continuous and perpendicular ZO-1 and VE-cadherin. The greatest continuous junction presentation was observed with 3d cAMP, which covered approximately 38% and 61% of the cell edge for ZO-1 and VE-cadherin, respectively. These coverage values were similar to those observed in HBMECs cultured for 2 days with 1d cAMP, suggesting increased culture time required increased cAMP treatment to reach comparable junction presentation.

Punctate junctions, on the other hand, displayed different responses for ZO-1 versus VE-cadherin. While no chance in punctate ZO-1 was observed, punctate VE-cadherin decreased with increased cAMP treatment.

Next, we studied the effects of extending cell culture to 7 days with 0, 1, 3, or 6 days of cAMP treatment on FBN (Figure 5.9). While 1d cAMP treatment decreased cell area, increased cAMP treatment beyond 1d increased area, with the largest cells observed with 6d cAMP. Notably, the cell area with 7-day culture was comparable to the size of cells cultured for 2 days, versus 4-day culture where smaller cells were observed. Continuous ZO-1 increased with increased cAMP treatment up to 3d, while continuous VE-cadherin increased with 1d of cAMP treatment and maintained this

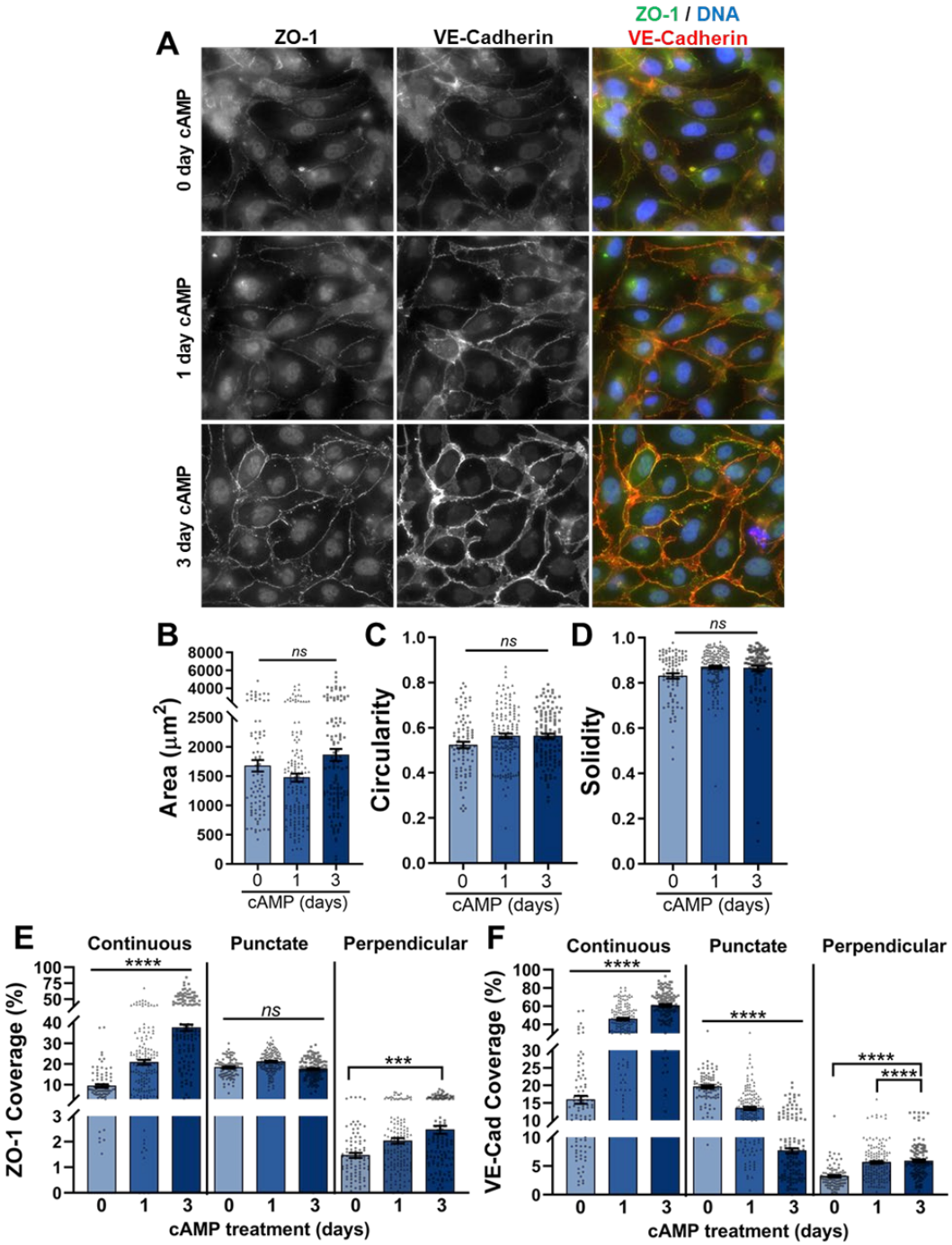

Figure 5.8 4-day HBMEC Culture. (A) Immunofluorescence images of HBMECs on FBN, cultured for 4 days with 0, 1, or 3 days of cAMP treatment. Stained for ZO-1 (green), VE-cadherin (red), and DNA (blue). (scale bar = 20 μm) (B) Cell area, (C) circularity, and (D) solidity. Edge presentation of continuous, punctate, and perpendicular junctions for (E) ZO-1 and (F) VE-cadherin. $87 \leq N \leq 145$, where N is the number of cells. The Kruskal-Wallis test with a Dunn's multiple comparison test was used to calculate significant differences for each parameter, where ns = $p > 0.05$, *** $p < 0.001$, and **** $p < 0.0001$.

level of presentation with 3d treatment. For both junction proteins, however, 6d of cAMP treatment led to a significant decrease in continuous junction presentation, comparable to 1d treatment. While no change in perpendicular junctions was observed punctate ZO-1 increased with 1d cAMP treatment, and punctate VE-cadherin decreased with increased cAMP treatment up to 3d, then spiked up with 6d cAMP treatment.

Cumulatively, the greatest total protein coverage observed during 7-day culture was with 3d cAMP treatment, with approximately 54% of the cell edge covered by ZO-1 and 76% by VE-cadherin. These values were comparable to the total coverage observed during 4-day culture with 3d cAMP treatment, and 2-day culture with 1d cAMP treatment . This suggests that increased cAMP treatment is needed to maintain ZO-1 and to a lesser extent, VE-cadherin, with increased culture time. Importantly, there seems to be a limit to this trend since a decrease in continuous ZO-1 (and a spike in punctate VE-cadherin) was observed with 6d cAMP treatment. Furthermore, these studies suggest that FBN is a suitable matrix to induce varied presentation of ZO-1 and VE-cadherin in HBMECs with varied cAMP treatment.

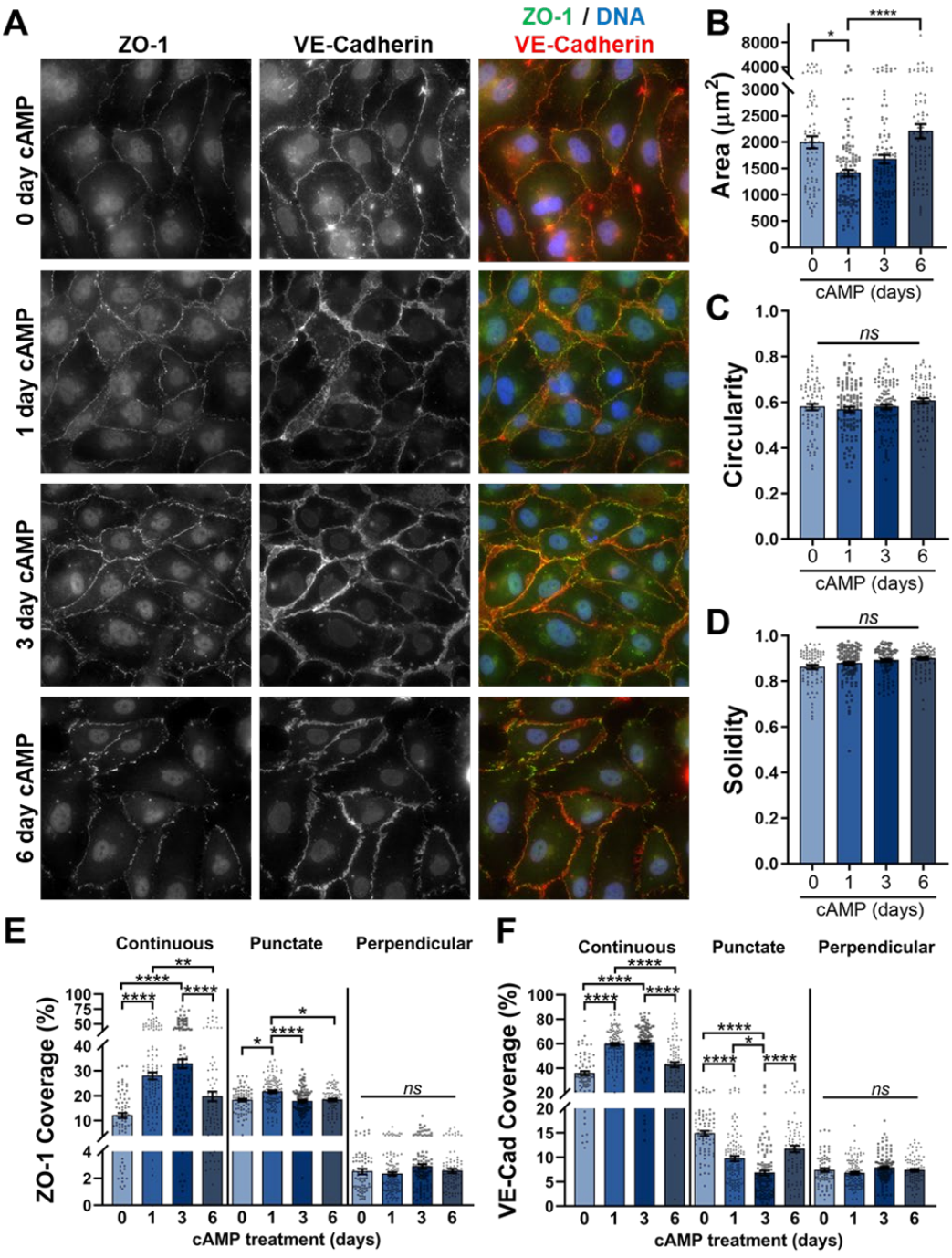

Figure 5.9 7-day HBMEC Culture. (A) Immunofluorescence images of HBMECs on FBN, cultured for 7 days with 0, 1, 3, or 6 days of cAMP treatment. Stained for ZO-1 (green), VE-cadherin (red), and DNA (blue). (scale bar = 20 μm) (B) Cell area, (C) circularity, and (D) solidity. Edge presentation of continuous, punctate, and perpendicular junctions for (E) ZO-1 and (F) VE-cadherin. $74 \leq N \leq 115$, where N is the number of cells. The Kruskal-Wallis test with a Dunn's multiple comparison test was used to calculate significant differences for each parameter, where ns = $p > 0.05$, * $p < 0.05$, ** $p < 0.01$, *** $p < 0.001$, and **** $p < 0.0001$.

5.3.3 Increased culture time increases continuous claudin-5 junctions

Since TJs are known to assemble after AJs, we next investigated the effects of increased cell culture and cAMP treatment time on the phenotypic presentation of TJ protein claudin-5 on FBN coating. First, we cultured HBMECs for 4 days with 0d, 1d, or 3d cAMP, where we qualitatively saw increased edge-localization with cAMP treatment (Figure 5.10.A). Figure 5.10.B presents the quantified junction analysis, supporting this observation, showing that continuous and perpendicular claudin increased with cAMP treatment, independent of 1d or 3d treatment length, while punctate claudin remained unchanged.

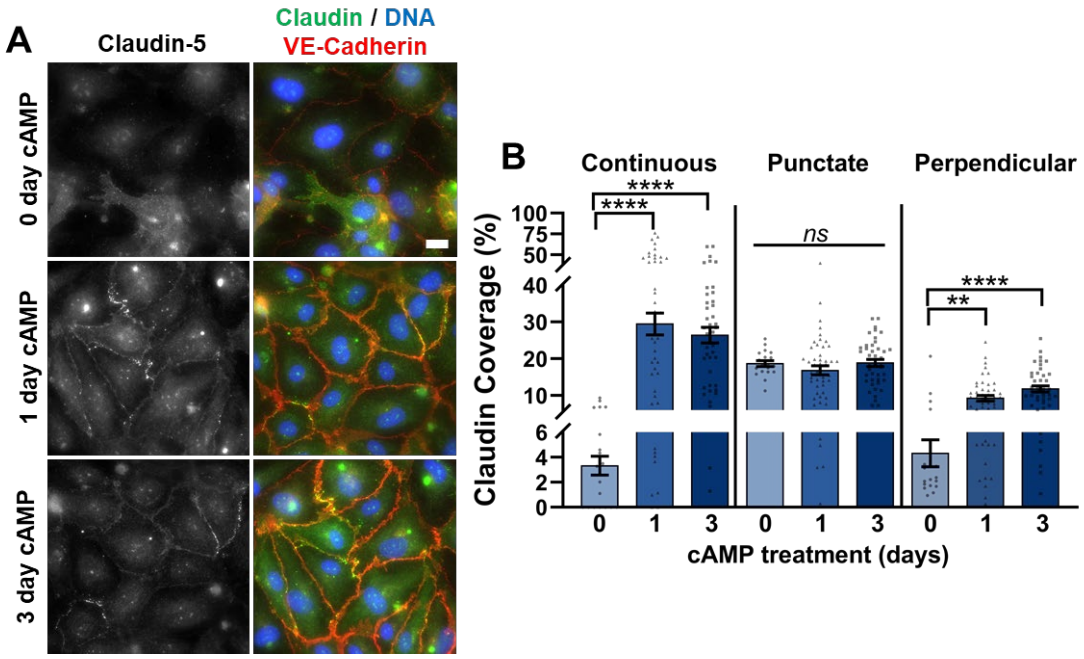

Figure 5.10 Claudin-5 Phenotype Analysis for 4-day Culture. (A) Immuno-fluorescence images of HBMECs on FBN, cultured for 4 days with 0d, 1d, or 3d cAMP treatment, stained for Claudin-5 (green), VE-cadherin (red), and DNA (blue). (scale bar = 20 μm)**.** (B) Edge presentation of continuous, punctate, and perpendicular claudin. $19 \leq N \leq 47$, where N is the number of cells. The Kruskal-Wallis test with a Dunn's multiple comparison test was used to calculate significant differences for each parameter, where ns = no statistical significance, ** $p < 0.01$ and **** $p < 0.0001$.

Next, we extended the culture time to 7 days, and observed minimal claudin presentation with 6d cAMP treatment, in line with our observations for ZO-1 and VE-cadherin (Figure 5.11). Maximal continuous claudin was found to be approximately 35% with 1d cAMP, higher than the approximate 30% observed with 1d cAMP treatment during 4-day culture. Punctate claudin, however, was unchanged with cAMP treatment and was presented at comparable levels to those found during 4-day culture. With cAMP treatment, perpendicular claudin was found at similar levels between 4-day and 7-day culture, though 6d cAMP treatment significantly decreased presentation to the approximate levels of 4-day culture with 0d cAMP.

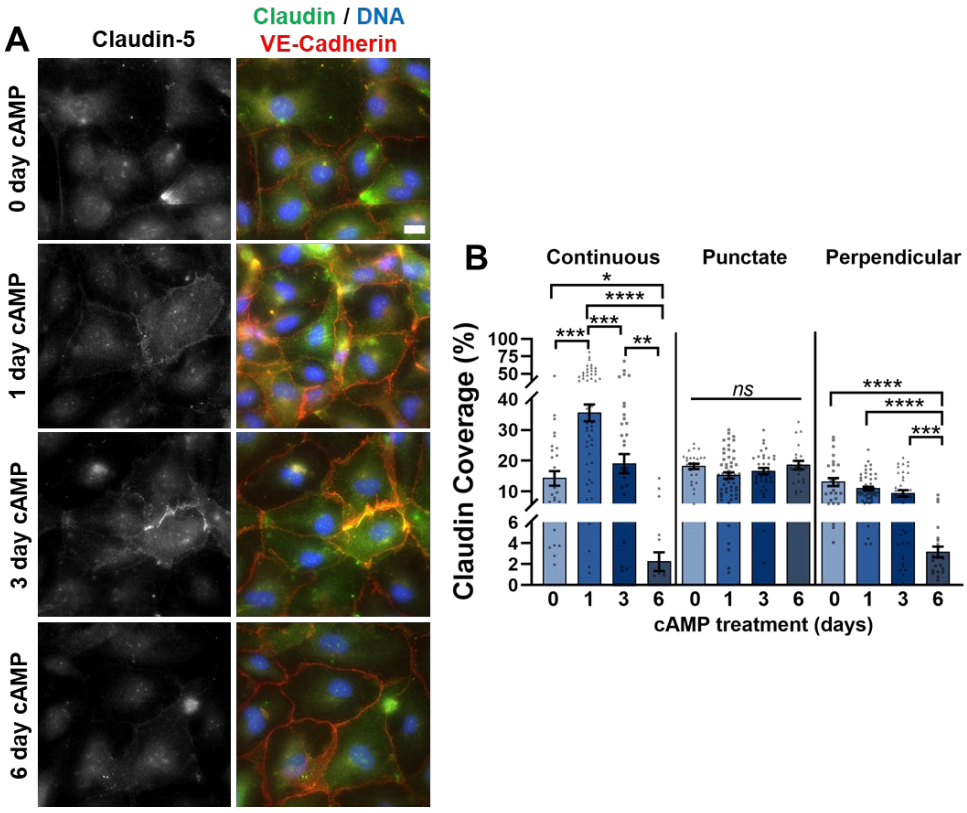

Figure 5.11 Claudin-5 Phenotype Analysis for 7-day Culture. (A) Immunofluorescence images of HBMECs on FBN, cultured for 7 days with 0d, 1d, 3d, or 6d cAMP treatment, stained for Claudin-5 (green), VE-cadherin (red), and DNA (blue). (scale bar = 20 μm)**.** (B) Edge presentation of continuous, punctate, and perpendicular claudin. $21 \leq N \leq 52$, where N is the number of cells. The Kruskal-Wallis test with a Dunn's multiple comparison test was used to calculate significant differences for each parameter, where ns = no statistical significance, * $p < 0.05$, ** $p < 0.01$, *** $p < 0.001$, and **** $p < 0.0001$.

5.3.4 Transwell TEER and permeability assays are insufficient for correlative assessment of junction phenotype and barrier properties

In the literature, continuous, linear adherens junctions are indicative of stable, mature EC barriers, while immature junctions are presented as punctate or perpendicular regions of junction [15]. As such, discontinuous junctions are typically linked with decreased barrier function, such as increased permeability [76]. Since the conditions tested here generated varied presentations of continuous and discontinuous tight and adherens junctions, we aimed to use these treatments to gain an understanding of the influence of junction phenotype on barrier properties (e.g., TEER, permeability) using traditional measurement techniques (e.g., Transwell assays) .

First, we performed a permeability assay by culturing HBMECs for 2 days on FBN-coated Transwell inserts, comparing the effects of 0d and 1d cAMP treatment on the permeability of 70 kDa FITC-dextran. Since 1d cAMP treatment significantly increased junction coverage in section 5.3.1, we expected decreased permeability with

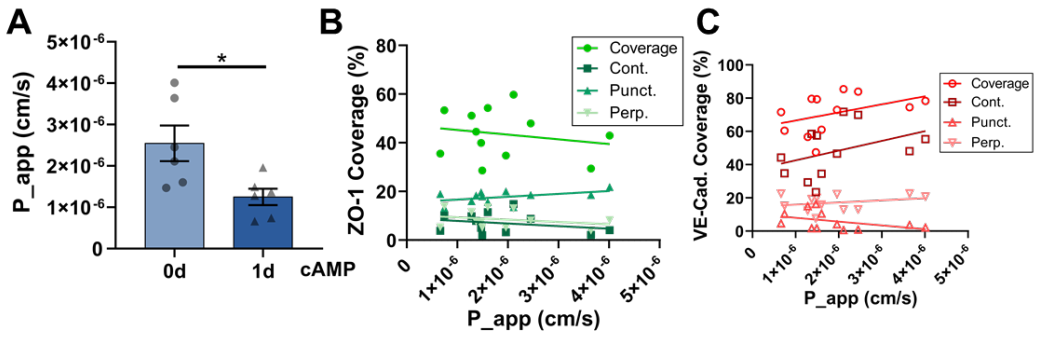

Figure 5.12 Transwell Permeability Analysis. Apparent permeability coefficient (P_app) of HBMECs cultured for 2 days with 0d or 1d cAMP treatment. N = 6, where N is the number of inserts measured over 3 trials. Significant difference of * $p < 0.05$ as determined using a Mann-Whitney statistical test. Correlation of each junction type for ZO-1 (B) and VE-cadherin (C) coverage with P_app, where a linear regression rendered the slope of all relationships non-significantly non-zero. N = 12, where N is the number of inserts pooled between the 0d and 1d cAMP conditions. Data collection for (A) was performed by Collin Inglut (Huang Lab).

1d treatment. Indeed, the apparent permeability coefficient (P_app) decreased with 1d cAMP, as presented in Figure 5.12.A. To correlate these permeability values with junction presentation, the inserts were fixed, immunostained for ZO-1 and VE-cadherin, and imaged for cell and junction morphology analysis using the JAnaP. The P_app values for each sample were then plotted against the junction coverage values (Figure 5.12.B,C). Surprisingly, no significant correlation was found between junction coverage and permeability, which could suggest that ZO-1 and VE-cadherin phenotype does not influence permeability. This result is very unlikely given the literary evidence suggesting otherwise [34,81,221–223]. It is important to note, though, that these reports are qualitatively correlative between immunostaining and permeability measurement, and not a quantitative correlation between permeability and junction presentation. Based on our results in section 5.3.1 and Figure 5.12.A, we could draw a similar conclusion that increased continuous junctions is linked with decreased permeability. This conclusion, however, assumes that the junction presentation of the cells within the two different experimental setups in consistent.

To probe the validity of this assumption, we investigated the cell and junction characteristics on the Transwell inserts to compare them against the results from section 5.3.1 when the cells were cultured on glass bottom plates (Figure 5.13). While cAMP decreased cell area from approximately 2000 μm^2 to 1500 μm^2 on glass (Figure 5.6), cells on the inserts were approximately 1700 μm^2 in area and remained unchanged with cAMP treatment. In both cases, circularity and solidity were consistent with and without cAMP. While the treatment increased continuous junctions in both cases, the resultant increase in overall coverage of continuous junctions was less on the inserts

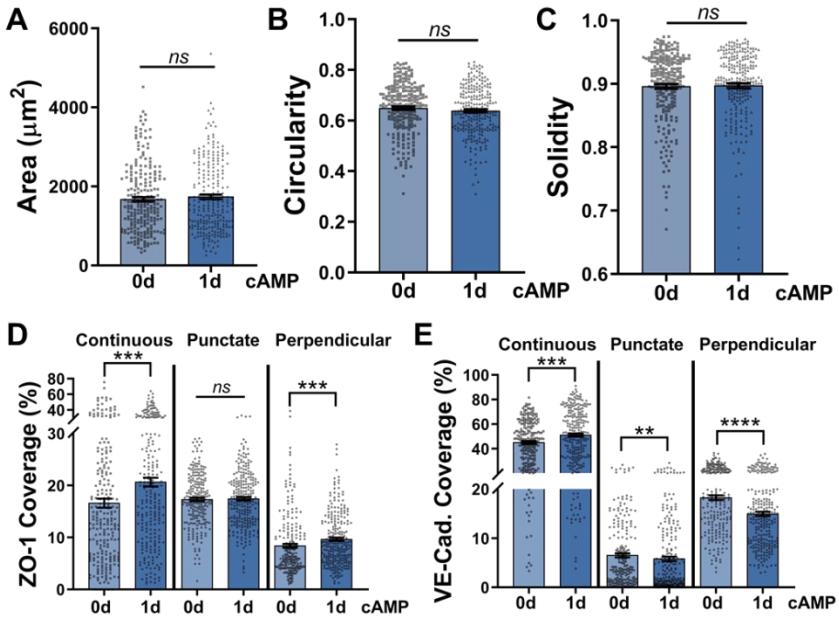

Figure 5.13 Cell Morphology and Junction Phenotyping from Transwell Permeability Assay. Cell area (A), circularity (B), and solidity (C) of HBMECs cultured on Transwell inserts coated with FBN, cultured for 2 days, with 0d or 1d cAMP treatment. Edge presentation of continuous, punctate, and perpendicular junctions for ZO-1 (D) and VE-cadherin (E). The Mann-Whitney test was used to calculate significant differences for each parameter, where ns = no significance, * $p < 0.05$, ** $p < 0.01$, *** $p < 0.001$ and **** $p < 0.0001$. For (A-E), $53 \leq N \leq 72$, where N is the number of cells.

compared to glass. For example, continuous ZO-1 and VE-cadherin respectively reached approximately 20% and 51% on the inserts, compared to the approximate 32% and 66% coverage values observed on glass. These different trends for cell area and junction presentation with cAMP treatment suggest that the assay (e.g., treatment with FITC-Dextran, or cAMP supplements to both the apical and basal side), or the different mechanical environments (i.e., stiff glass versus softer membrane), could be altering the cells and/or their response to cAMP treatment. This could potentially explain the lack of correlation observed between junction phenotype and permeability, since one possibility is that the magnitude of change of each junction type did not vary enough to influence permeability. This would mean that significantly more (or less) junction

presentation would be required to alter the overall permeability of the barrier. Furthermore, the monolayer may not be homogenous throughout the entire insert. Any gaps or regions of heterogeneity could lead to increased permeability, significantly skewing the P_app results since it is a "bulk" measurement of the entire barrier.

We next measured TEER to probe barrier integrity as a function of junction phenotype. The 4-day culture protocol (Figure 5.1) on FBN with 0d, 1d, and 3d cAMP treatment was selected to provide more sequential values of total junction coverage. The resistance measurements were performed on each day and the adjusted results are presented in Figure 5.14. We observed the expected outcome: increased TEER with increased cAMP treatment, though the changes were minor and insignificant.

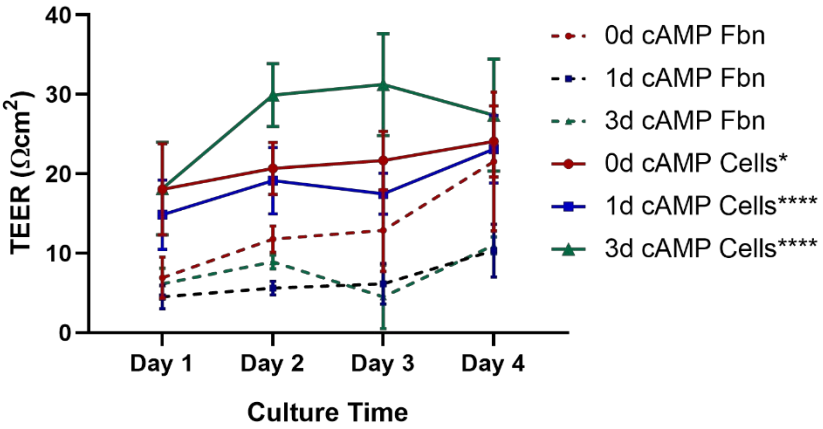

Figure 5.14 TEER Assay. Resistance measurements of HBMECs cultured on FBN-coated Transwell inserts for 4 days with 0d, 1d, or 3d cAMP treatment. Control measurements without cells are also presented. N = 3, where N= number of trials. A two-way ANOVA indicated significant differences for each condition versus their FBN-only control , presented in the figure legend, where * $p < 0.05$ and **** $p < 0.0001$. Data collection for this assay was performed by Jae W. Jung (Stroka Lab).

To examine the monolayer characteristics, the samples were again fixed and immunostained after the TEER measurement on the fourth day (Figure 5.15). Cell morphology and junction presentation were then characterized using the JAnaP (Figure 5.16) and plotted against the TEER values for correlative analysis (Figure 5.17). Like

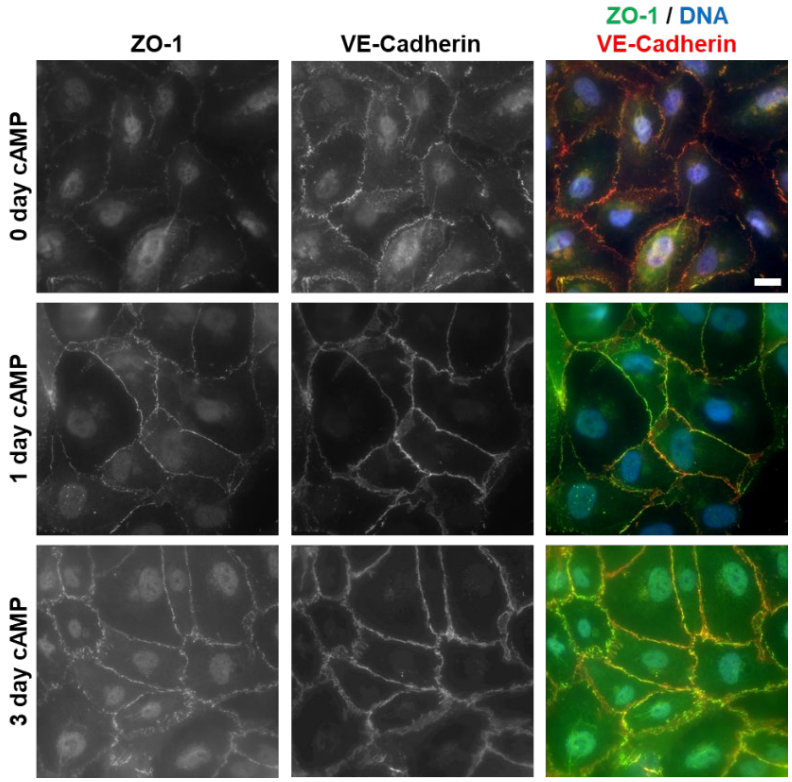

Figure 5.15 Transwell Images from TEER Assay. Immunofluorescence images of HBMECs on Transwell inserts coated with FBN, cultured for 4 days, with 0d, 1d, and 3d cAMP treatment. Stained for ZO-1 (green), VE-cadherin (red), and DNA (blue). (scale bar = 20 μm)

permeability, no correlations between junction presentation and resistance measurements were observed, which was not surprising since the TEER values themselves were insignificant between each condition. While the trends with cAMP treatment for area, circularity, and solidity were generally consistent with the previous findings in section 5.3.2, the cells were larger on the inserts compared to the glass-bottom plates (Figure 5.6). In line with the observations from the permeability assay, the junction presentations of both ZO-1 and VE-cadherin were different on the inserts compared to glass and did not respond to cAMP treatment in the same manner. While continuous ZO-1 on FBN-coated glass increased from approximately 10% to 20% to 40% with cAMP treatment of 0d, 1d, and 3d, respectively, the presentation on FBN-coated inserts increased to approximately 35% with 1d and 3d cAMP from approximately 20% with 0d cAMP treatment. Similarly, while continuous VE-cadherin

increased from approximately 15% to 45% to 60% on FBN-coated glass with 0d, 1d, and 3d cAMP, respectively, the presentation on FBN-coated inserts increased to approximately 58% with 1d and 3d cAMP from approximately 50% with 0d cAMP treatment. This decreased response to cAMP in the Transwell system could explain the lack of significant difference in TEER values between each day, since the range of changes in junction might not be large enough to induce significant differences in resistance. The generally low values, however, suggest that small defects or heterogeneities in the monolayers may have been present, generating "shortcuts to current flow", drastically decreasing the resistance measurement [56]. According to Wegener, et al., even just missing one in a hundred cells within a monolayer can decrease the TEER value by 50 $\Omega \cdot cm^2$ [56].

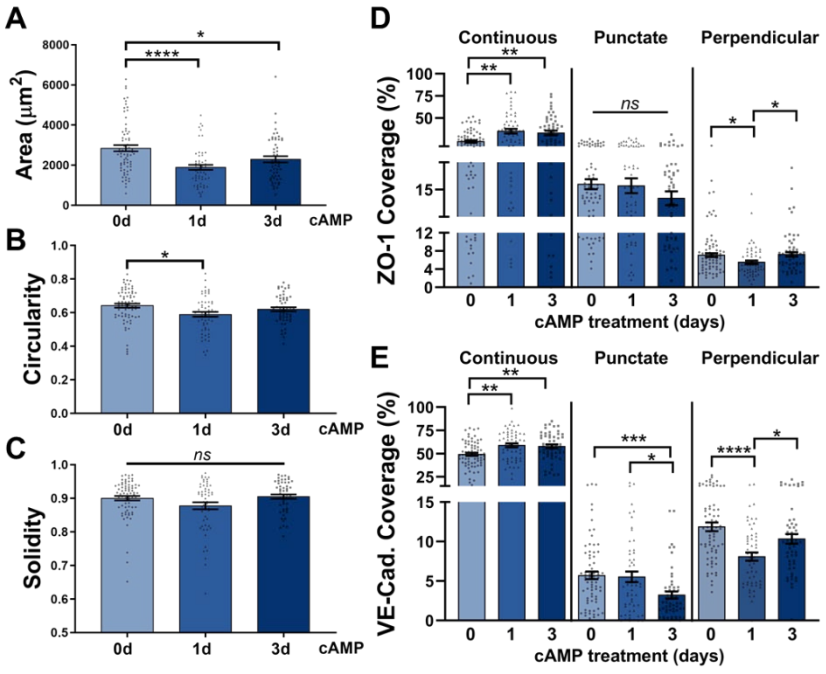

Figure 5.16 Cell Morphology and Junction Phenotyping from TEER Assay. Cell area (A), circularity (B), and solidity (C) of HBMECs cultured on Transwell inserts coated with FBN, cultured for 4 days, with 0d, 1d, and 3d cAMP treatment. Edge presentation of continuous, punctate, and perpendicular junctions for ZO-1 (D) and VE-cadherin (E). $53 \leq N \leq 72$, where N is the number of cells. The Kruskal-Wallis test with a Dunn's multiple comparison test was used to calculate significant differences for each parameter, where * $p < 0.05$, ** $p < 0.01$, *** $p < 0.001$ and **** $p < 0.0001$.

Overall, this motivated the use of a more localized assay to understand the effects of junction phenotype on local barrier function. Specifically, the ability to correlate local junction presentation with local barrier properties *in situ* was needed to mechanistically study the role of junction phenotyping.

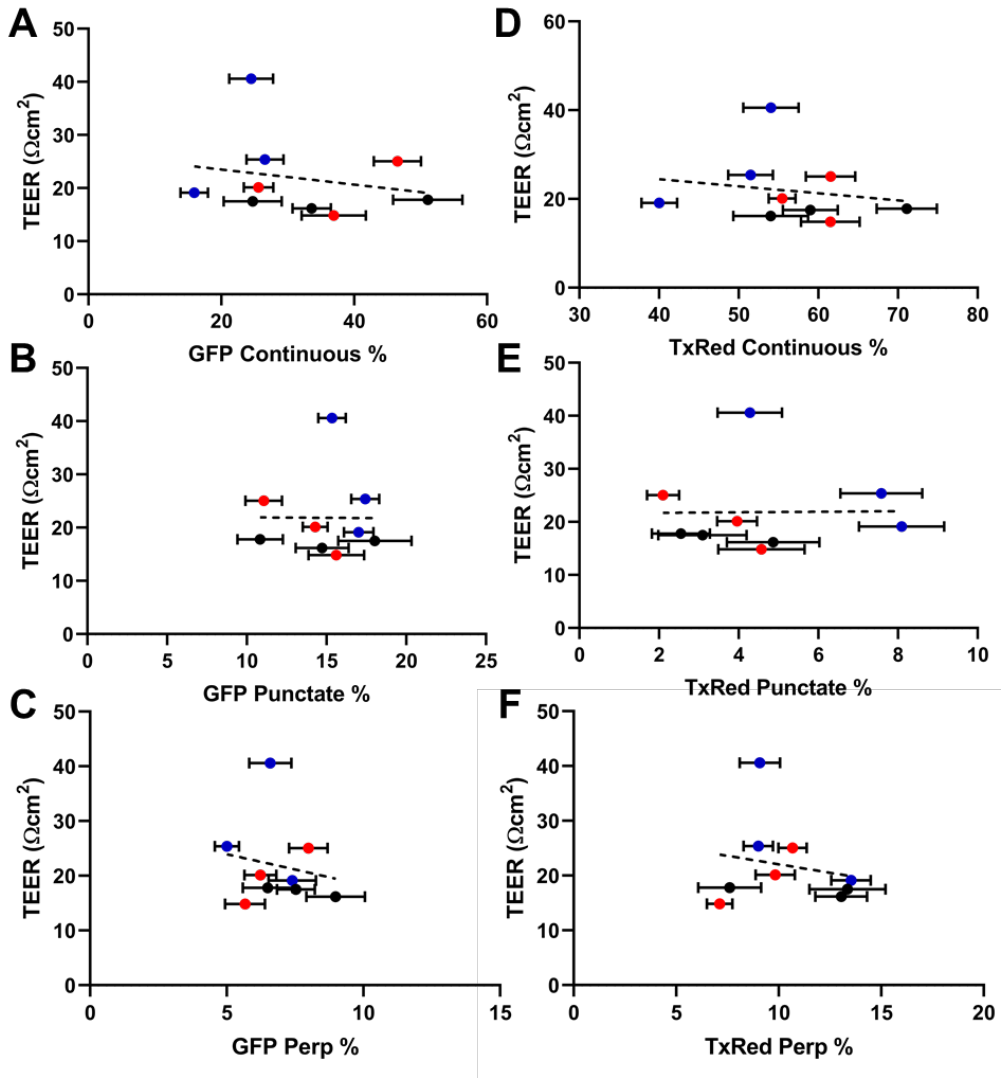

Figure 5.17 Junction Phenotype and TEER Correlation. Correlation of each junction type for ZO-1 (A-C) and VE-cadherin (D-F) coverage with TEER, where a linear regression rendered the slope of all relationships non-significantly non-zero. N = 9, where N is the number of inserts pooled between the 0d, 1d, and 3d cAMP conditions.

5.3.5 Local permeability assay reveals correlation between discontinuous junctions and barrier penetration

To circumvent the challenges faced in the Transwell permeability and TEER assays, we adapted the XPerT assay [62] to detect regions of local monolayer permeability *in situ*. This technique enables visualization of barrier permeation via FITC-avidin-binding to biotinylated-FBN, in parallel with junction immunostaining. Here, we used this assay in conjunction with the JAnaP to quantitatively study junction phenotype and site-specific barrier permeability. Figure 5.18 presents representative images of VE-cadherin (A-B) and ZO-1 (C-D) in HBMECs cultured for 2 days with no cAMP treatment.

To start, we characterized the permeated regions (PR) of the monolayers, indicated by substrate-bound green fluorescence, since the number of cells corresponding to PRs was not always consistent. We therefore categorized each PR based on the number of cells with which it correlated (i.e., Uni, Bi, Tri, Quad, or Multi). To quantify each of these instances, we averaged the number of times each category was present within each image (Figure 5.19.A). Bi-cellular PRs were the most consistent PR, with about 16 bi-cellular PRs per image. Larger PRs such as Quad or Multi were much less common, occurring less than or equal to one time per image. Size analysis indicated that PR area significantly increased with each additional cell contact, such that Uni PRs were smallest and Multi PRs were much larger (Figure 5.19.B).

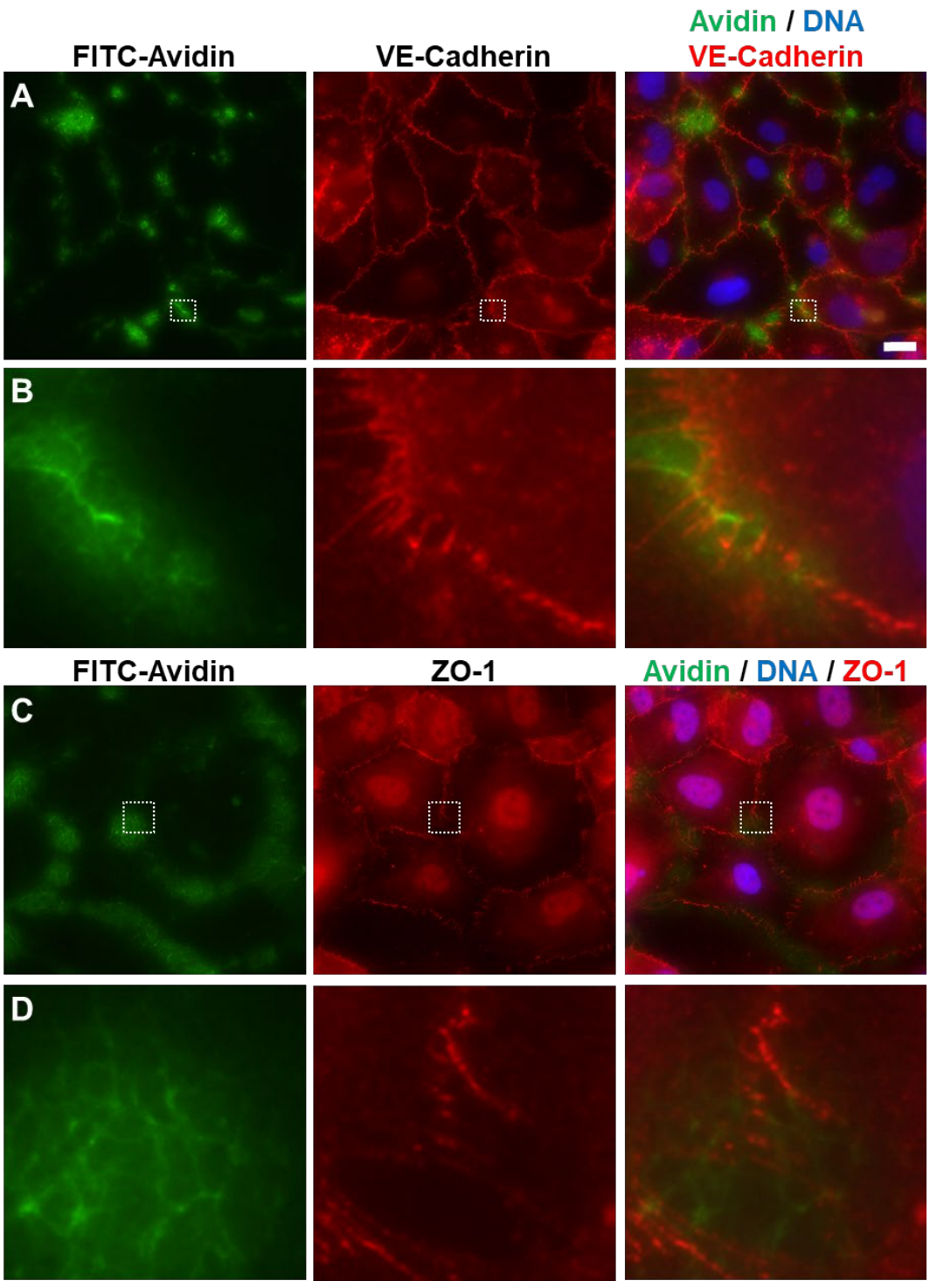

Figure 5.18 Local Permeability Assay. Immunofluorescence images of HBMECs cultured for 2 days on B-FBN without cAMP, treated with FITC-avidin (green), then stained for VE-cadherin (row A, red), ZO-1 (row C, red), and DNA (blue). Rows B and C provide a zoomed-in view of the region outlined in the white-dotted box in the respective images. (scale bar = 20 μm, applies to rows A and C)

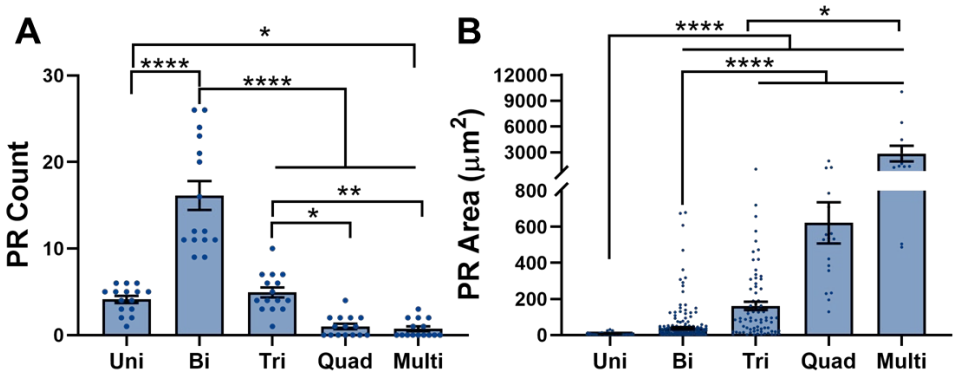

Figure 5.19 Permeated Region Analysis. The average number of each PR type per image is presented in (A) while the average size of each PR type is presented in (B). N = 15 for (A) where N is the number of images. $11 \leq N \leq 247$ for (B) where N is the number of PRs. The Kruskal-Wallis test with a Dunn's multiple comparison test was used to calculate significant differences for each parameter, where * $p < 0.05$, ** $p < 0.01$, and **** $p < 0.0001$.

Next, we investigated the types of junctions present around the PRs. Here, we combined perpendicular and punctate junctions as discontinuous junctions. Qualitatively, we observed PRs primarily in regions of no junction or discontinuous junctions. To quantify this observation, we traced the length of each junction type present along the cell path overlapping each PR (Figure 5.20). The total junction count and coverage fraction was dominated by regions of no junction for both VE-cadherin and ZO-1. This suggests that in regions where FITC-avidin penetrated the barrier, the cell edge was most commonly covered by regions of "no junction". For VE-cadherin, continuous and discontinuous junctions covered the same fraction of the PR, though the fraction of no junction was significantly greater. For ZO-1, however, continuous junction covered significantly less than either discontinuous or no junction. To gauge how frequently each junction type corresponded with a PR, we calculated the percent co-localization for each image (Figure 5.20.E-F). Interestingly, the co-localization was rather consistent between the VE-cadherin and ZO-1, with about 15% of the continuous

junctions and about 30% of the discontinuous junctions co-localizing with the PRs. Together this suggests that while discontinuous junctions are more likely to associate with a PR, the presence of either junction does not necessarily indicate a permeable region of the monolayer.

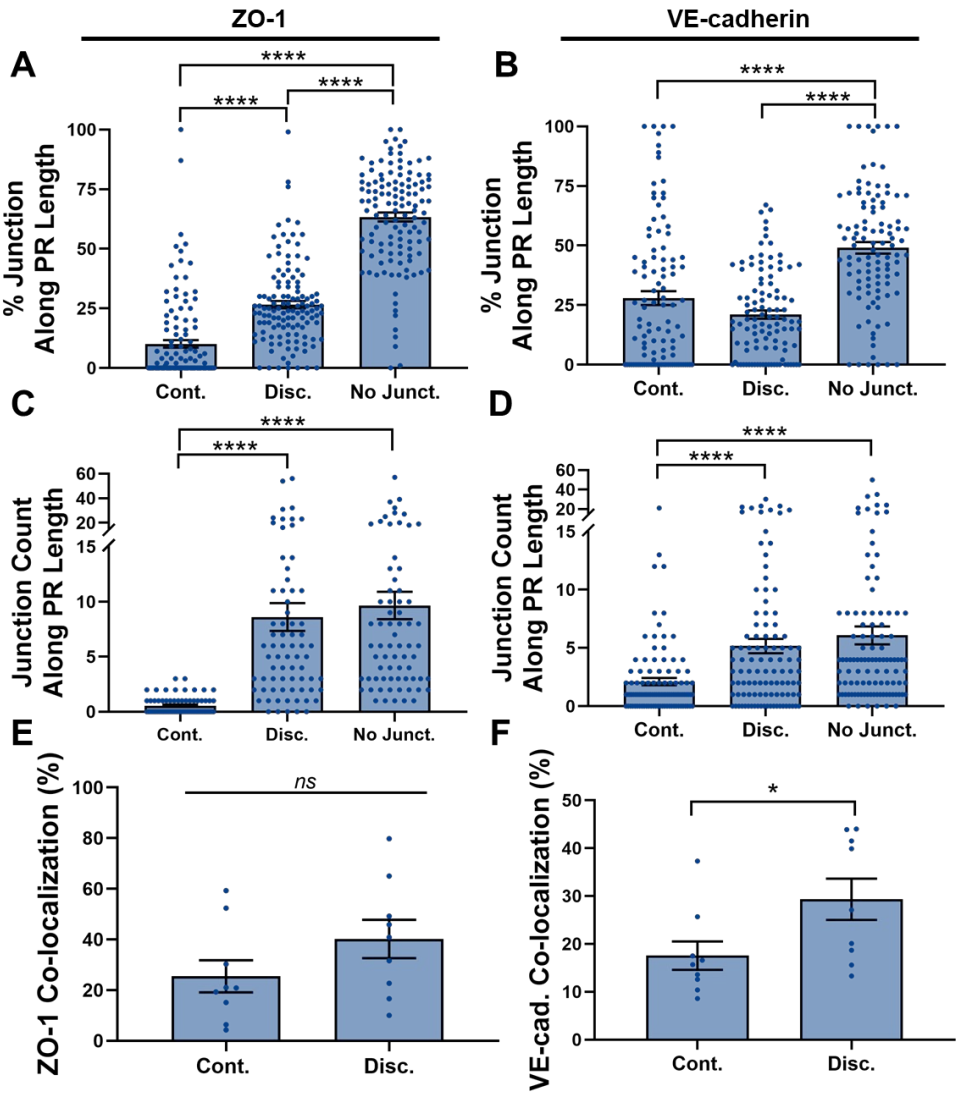

Figure 5.20 Co-localization Analysis – Continuous vs. Discontinuous. Count (A-B) and percentage (C-D) of ZO-1 and VE-cadherin junctions along the cell edges co-localized with PRs. N = 126 for ZO-1 and 105 for VE-cadherin, where N is the number of PRs. The percent of co-localization of each junction type with PRs in each image is presented in (E) for ZO-1 and (F) for VE-cadherin. N = 9, where N is the number of images. The Kruskal-Wallis test with a Dunn's multiple comparison test was used to calculate significant differences for (A-D) and a Mann-Whitney test was used for (E-F), where ns = no statistical significance, * $p < 0.05$, ** $p < 0.01$, *** $p < 0.001$, and **** $p < 0.0001$.

Despite this, we were curious if the amount of any one junction type (or no junction region) would instead correlate with "how permeable" the permeable regions were. We measured the extent of permeability as the area of the PR and investigated the correlation between PR area and junction presentation (Figure 5.21). Note that these graphs have excluded 2-3 very large Multi PRs that were likely affected by more than just the local junction presentation of these proteins. Since the fraction of no junction regions dominated the PR length for both VE-cadherin and ZO-1, the magnitude of this line is greater than either continuous or discontinuous. For VE-cadherin, there was no statistically significant correlation between percent junction and PR area. For ZO-1, however, discontinuous junction showed a significant correlation ($p < 0.05$), though the R^2 value was low ($R^2 = 0.039$). Analysis of the junction counts, however, showed significant trends for almost every condition. Since the junctions are inherently categorized by size, looking at the number of junctions considers the smaller sizes of discontinuous junctions relative to continuous, that could inadvertently be skewing the percentage results. For both VE-cadherin and ZO-1, all junction types presented a significant correlation ($p < 0.0001$), with discontinuous and no junctions showing a much greater positive correlation compared with continuous junction. Together this suggests that the size of the PR, or how permeable the barrier is as permeable region, is influenced by the presentation of discontinuous junction and no junction, with continuous junctions playing less of a role.

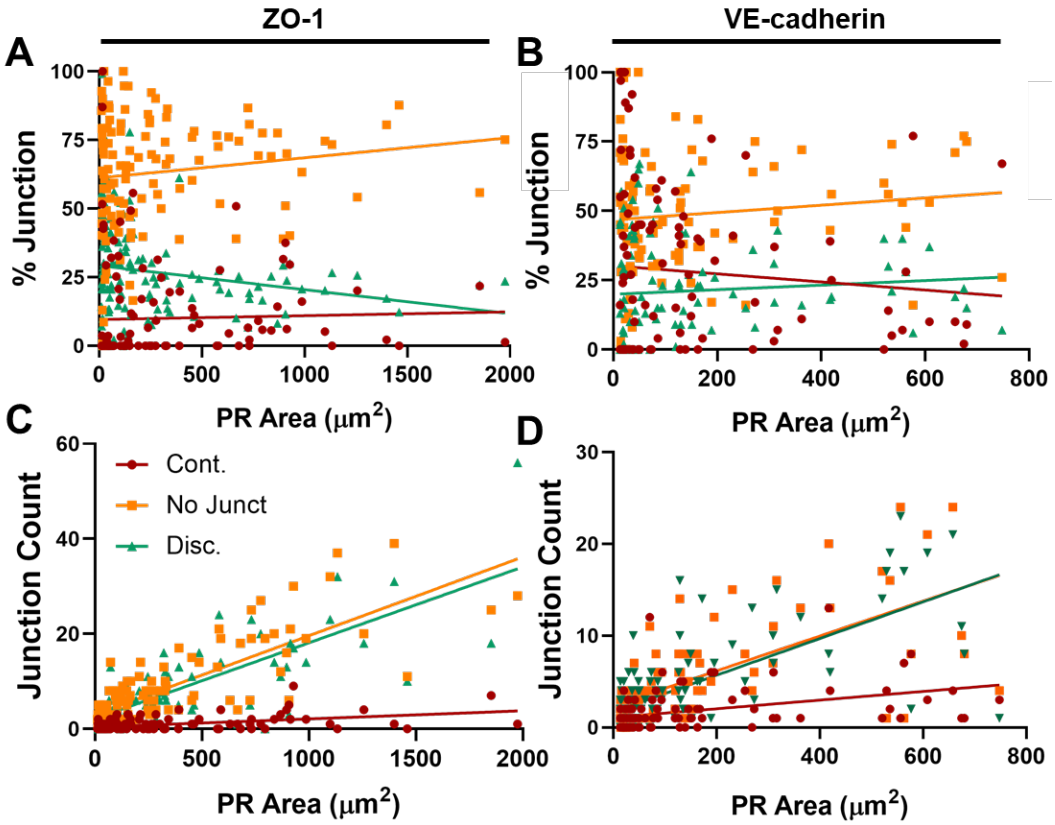

Figure 5.21 Junction Presentation and PR Area – Continuous vs. Discontinuous. The correlation between PR area and the percent (A,B) and count (C,D) each continuous (Cont.), discontinuous (Disc.), and no junction (No Junct.) the cell edge co-localized with the PR for ZO-1 and VE-cadherin. All results were fit using a linear regression. N = 126 for ZO-1 and 105 for VE-cadherin, where N is the number of PRs. The Cont., Disc., and No Junct. R^2 values are as follows: 0.001, 0.039, 0.019 for (A), 0.008, 0.009, 0.007 for (B), 0.213, 0.617, 0.662 for (C), and 0.143, 0.451, 0.493 for (D)..

5.4 Discussion

While the influence of junction protein localization and presentation at the cell-cell borders of ECs on barrier properties has been significantly investigated, these studies have been performed in a primarily qualitative manner and lacked the quantification of junction phenotype. Development of the JAnaP (Chapter 4) has enabled the quantitative analysis of cell-cell junctions *in situ,* thereby permitting the study of junction phenotype on EC barrier properties in a calculated manner. In this

study, we varied cell culture parameters to understand their influence on junction presentation, then used them to probe the effects on barrier permeability.

Despite the different properties of the matrix proteins studied here, [205,224] use of different substrate coatings seemed to have little effect on cell and junction phenotype of HBMECs. CN, Fbn, F:C:L, and HA/Gtn, all induced similar levels of total junction coverage, though CIV and LN induced less junction localization in some cases. This result that LN induced a less optimal BBB phenotype was not surprising, since previous reports with iPSC-derived brain ECs reported the lowest TEER values and occludin expression on LN compared to other proteins, including several that were studied here [205]. This study also reported the greatest TEER values on FBN, supporting our result that, while marginal, FBN induced the greatest junction protein coverage [205].

The addition of cAMP supplements was found to have the greatest effect in junction presentation, increasing continuous junctions in almost every case. This was not surprising given the significant evidence that these supplements improve barrier phenotype in ECs [48,212]. Of specific relevance, one study reported increased TEER and localization of ZO-1 and VE-cadherin, showing a more linear morphology (assessed qualitatively) in HUVECs treated with the same concentrations of cAMP supplements for 1 day, supporting our results in this study [217]. Interestingly, increasing culture time did not increase junction coverage, and required more cAMP treatment to reach similar presentation values observed in shorter experiments. This was surprising, since barrier maturity is thought to correlate with a more continuous, linear junction phenotype, but here required additional biochemical signaling. Notably,

we did see presentation of claudin-5, which peaked with increased culture time, as expected, since TJs are known to form after AJs, requiring their structure for organization [23]. Interestingly, claudin responded differently to cAMP treatment time compared to VE-cadherin and ZO-1, possibly indicating different mechanisms regulating tight and adherens junction proteins.

To correlate barrier properties, we performed TEER and permeability measurements. As expected, our permeability coefficient decreased with cAMP treatment, to a similar value reported for the B.end3 brain EC cell line in comparable conditions with 70 kDa Dextran (approximately 1E-06 cm/s) [225]. The TEER measurements were on par with literature values, on the order of 10-30 $\Omega \cdot cm^2$ for static monoculture of B.end3 cells, [225] primary rat brain ECs, [226] purified murine brain ECs, [227] as well as for HBMECs [218]. The resultant trends, however, were not expected, since no significant differences were observed with cAMP treatment. Furthermore, neither TEER nor permeability showed a correlation with junction coverage. While this was surprising, it was likely due to heterogeneities in the cell barrier skewing the readouts, or insufficient differences in junction coverage to generate measurable differences. Notably, continuous junction coverage alone spanned a range of about 20-30%, suggesting that more extreme coverage values such as less than 10% or greater than 60% might be required to affect the output measurements. Notably, other reports that qualitatively associate changes in junction phenotype and localization with barrier measurement often use treatments such as inflammatory cytokines (e.g., TNF-α) which could be altering other cell features that drive the changes in TEER rather than just phenotypic changes in junction presentation [68].

Another important influence likely driving the unexpected results, are the differences in cellular response due to the different experimental setups (i.e., glass versus insert, apical versus basal nutrient accessibility). Often in literature, the immunofluorescent staining of cells is performed, the TEER or permeability measurement is performed separately, and the two results are then correlated to infer function. We've shown here that cells can respond differently in the different systems and as such, caution should be taken when comparing cellular responses. These results motivated the use of a local assay to measure site-specific permeability in a single system that enables direct correlative measures. Since ECs can sense and respond to their microenvironment, EC phenotypes are known to display spatial heterogeneity, further supporting the use of local studies to gain mechanistic insights into EC function [23]. Importantly, though, global assays still provide valuable understanding, since assessment of whole barrier function is important in, for example, *in vitro* modelling for the study of drug delivery systems.

The local permeability studies showed that permeated regions were most affected by the number of discontinuous and no junction regions of coverage, showing a positive correlation with PR area. It's important to note that this assay is only measuring permeability of FITC-avidin and as such, could return different results for the permeability of molecules of different size or charge; or for different cell types transmigrating across the barrier. Use of the JAnaP with other local permeability assays for different molecules [61] or live cell imaging for cell transmigration [228,229] could therefore provide additional insights into the effects of junctional phenotypes. This is especially of interest to further study the differences in function between punctate and

perpendicular junctions, since the two were combined in this analysis. Also of note, is that these studies were performed in static culture, despite the evidence that suggests the significant influences of mechanical cues in EC function [230]. Therefore, performing these correlative local permeability or TEER studies in a system that enables the incorporation of biomimetic microenvironmental cues (e.g., shear stress [205], substrate stiffness [15]) to probe the interplay of these parameters on a local scale is an important future application. Notably, in Chapter 6 we investigate the effect of substrate stiffness on ZO-1 localization and phenotype in HBMECs.

Overall, this study highlights the capabilities of combining junction phenotyping and assessment of barrier function for the mechanistic study of the BBB, and possibly other EC and epithelial barriers. Together, these data suggest that increased continuous junction presentation is associated with a less permeable barrier, with increased gaps or discontinuous junctions indicating increased permeability. Understanding what conditions influence junction presentations and how that affects barrier properties, could lead to therapeutic development for diseases associated with BBB dysfunction or delivery mechanisms capable of traversing healthy barrier systems.

5.5 Conclusion

In summary, we investigated the influence of cell culture parameters such as matrix protein coating, culture time, and cAMP treatment, and used the JAnaP to quantify their role in cell and junction morphology. While protein coating seemed to have little effect on these parameters, cAMP treatment significantly increased continuous junction presentation. Total cell culture time did not increase junction

presentation, but instead required increased cAMP treatment for protein coverage comparable to shorter culture time. No correlation between junction presentation and barrier permeability was found when comparing junction phenotype to Transwell-based TEER and permeability experiments, motivating the use of an assay that could instead capture cell-to-cell inhomogeneities rather than a "bulk" barrier measurement. A local permeability assay identified that barrier permeability most closely correlates with the number of gaps with no junction coverage, and by extension, the number of discontinuous junctions, present at the cell edge. Together this promotes the use of local quantification techniques to quantitatively study barrier function in conjunction with junction phenotype to understand the mechanisms at play in functional and dysfunctional barrier systems.

Chapter 6 - Role of Contractility in ZO-1 Presentation†

6.1 Introduction

In this chapter, we used the JAnaP to quantify the effect of cell contractility on ZO-1 presentation in HBMECs. Cell contractility and actin fiber formation have been directly linked with adherens junction presentation in several EC types, including BMECs [15]. Furthermore, this has been correlated with barrier permeability, where increased contractility drives junction disassembly, leading to vascular leakage [53] and increased transmigration of immune and cancer cells [77]. Additionally, we and others have previously shown that peripheral EC tension and adherens junction presentation can be modulated by altering the subendothelial matrix stiffness, a phenomenon driven by myosin II-mediated contractility [15,76,157,231,232]. Specifically, stable, linear adherens junctions are observed in cells on soft substrates,[15] or in cells with low tension and active Rac,[75] while discontinuous junctions and increased permeability are observed in cells on stiff substrates, [76] or in cells experiencing high tension and active Rho [75]. The link between myosin II-mediated contractility and vascular barrier properties (e.g., cell-cell junctions, permeability) has been recently reviewed [233,234]. The effects of cell contractility, and specifically its modulation via substrate stiffness, on BMEC barriers and ZO-1 junction formation, however, remains relatively understudied. The effects of matrix

† This chapter was adapted from K.M. Gray, D.B. Katz, E.G. Brown, K.M. Stroka. "Quantitative Phenotyping of Cell-Cell Junctions to Evaluate ZO-1 Presentation in Brain Endothelial Cells." *Annals of Biomedical Engineering* 47(7), 1675-1687 (2019). Permission was obtained from Springer Nature for use of this material in this dissertation. D.B.K. and E.G.B. aided in the collection and analysis of the data in the chapter.

stiffness are of particular interest, as matrix modulation remains a tunable parameter of *in vitro* model design, and because vascular stiffening is associated with cardiovascular injury, disease and stroke [160,235–237]. Most *in vitro* BBB modeling is still performed on Transwell inserts, tissue culture plastic, and glass, with the approximate stiffness in the MPa-GPa range. This is much stiffer than the *in vivo* brain extracellular matrix (~1 kPa) and peripheral subendothelial matrices (~3-7 kPa) [92,238]. As ZO-1 has been a suggested regulator of cell-cell tension and junctional assembly via actomyosin organization,[14] and actin reorganization is involved in the cellular response to substrate stiffness,[76] here we aimed to use the JAnaP to quantify ZO-1 presentation in response to biochemical and physical cues associated with altered states of contractility.

6.2 Materials and Methods

6.2.1 Cell Culture and Treatments

Ethics approval for all studies were obtained from the University of Maryland, Institutional Biosafety Committee (Protocol Number ESSR #15-06). HBMECs were purchased from Cell Systems and cultured as previously described [214]. Cells (passage 7-10; 5e5 per coverslip) were seeded onto collagen-coated glass coverslips or polyacrylamide gels (as described below) and grown for two days. For conditions with cAMP supplements, 250 μM 8-(4-chlorophenylthio) adenosine-3',5'-cyclic monophosphate sodium salt (CPT-cAMP) (Abcam) and 17.5 μM 4-(3-butoxy-4-methoxybenzyl) imidazolidin-2-one (RO-20-1724) (Tocris Bioscience) were added to culture medium 24 hours after cells were plated. These concentrations were selected

because they are routinely used for culturing brain endothelial cells and are cited in many several previous studies [217–219,239]. Myosin II was inhibited with 50 μM (-)-blebbistatin (Sigma-Aldrich) for 1 hour at 37°C after 48 hours of culture (with or without cAMP supplements). The vehicle control consisted of medium containing 0.6% DMSO (Sigma-Aldrich). Alternatively, after 48-hour culture, protein phosphatases were inhibited via 0.1 nM calyculin A (Santa Cruz) treatment for 30 minutes at 37°C. The vehicle control consisted of DMSO at an equal volume to that used in the calyculin conditions (0.1% final concentration). These concentrations were selected for blebbistatin and calyculin A because we have previously measured lower and higher cell traction forces, respectively, for these inhibitors, while still maintaining cell viability [98]. All experiments were repeated two to four times.

6.2.2 Polyacrylamide Gel Preparation

Thin polyacrylamide gels were synthesized on glass coverslips as first described by Wang and Pelham [240], and used in our previous publications [76,157,192,241]. Here, gels were composed of acrylamide and bisacrylamide (bis) (BIO RAD) at the following concentrations: 15% acrylamide + 1.2% bis, 8% acrylamide + 0.2% bis, 8% acrylamide + 0.07% bis, and 3% acrylamide + 0.2% bis. Gels were activated using sulfo-SANPAH (Thermo Fisher) and then coated with 100 μg/mL collagen type 1 (Sigma-Aldrich) for 4 hours at room temperature (RT). For glass experiments, cells were plated on unactivated coverslips (22x22 mm, Fisher Scientific) that had been exposed to UV for 20 minutes and coated in 100 μg/mL collagen for 1-4 hours.

6.2.3 Atomic Force Microscopy

Atomic force microscopy (AFM) was used to measure the Young's modulus of each polyacrylamide gel composition. Following polymerization of the polyacrylamide, unactivated gels were rinsed with PBS and the coverslip was adhered to the bottom of a 50 x 9 mm petri dish. The dish was then filled with PBS and atomic force microscopy (AFM) was performed using an Asylum MFP-3D-BIO Atomic Force Microscope with TR400PB(L) probes from Asylum Research. Asylum's "Get Real" procedure was used to measure the spring constant of the cantilevers via the Sader method, as well as the inverse optical lever sensitivity via the thermal noise method. The spring constant of TR400PB(L) cantilevers was measured to be in the range 0.026-0.032 N/m, which was within a factor of 1.62 to Asylum's nominal value of 0.02 N/m. Three 100-curve force maps covering a 10 μm x 10 μm area were collected for each sample using a 1 μm force distance, a 1 V trigger point (~1.75 nN), and a scan rate of 0.99 Hz. Force curves were fit to the Hertz model within Asylum's Igor Pro-based software, using the equation $F = \frac{4}{3} \cdot \frac{E}{1-\upsilon^2} \cdot \sqrt{r} \cdot \delta^{3/2}$, with δ as the measured indentation of the sample and Young's modulus E as the fitting parameter. The Poisson's ratio υ of the sample was assumed to be 0.45 and the tip radius of curvature r was approximately 30 nm.

6.2.4 Immunostaining

HBMECs were rinsed with warm PBS, fixed with 1% formaldehyde (Fisher Scientific) for 10 minutes, and permeabilized in 0.25% TritonX-100 (Sigma-Aldrich) for 5 minutes. Cells were washed with PBS three times between each step, and then

blocked in 2% goat serum (Abcam) for 1 hour at RT. Primary antibody (rabbit polyclonal IgG to ZO-1, Santa Cruz Biotechnology, sc-10804) was then added to cells at a 1:50 dilution in 2% goat serum and incubated overnight at 4°C. The next day, samples were washed with PBS, then blocked again with 2% goat serum for 1 hour at RT. Cells were then incubated in 1:100 secondary antibody (goat anti-rabbit Alexa Fluor 488, Abcam) and 1:2500 Hoechst (ThermoFisher Scientific), in PBS, for 1 hour at RT, then rinsed with PBS.

6.2.5 Microscopy

All samples were imaged on an Olympus IX83 inverted microscope using a 60x oil objective and Olympus cellSens Software. Images were collected to maximize the monolayer coverage within that image. Image analysis was performed on raw images such that the pixel intensities were comparable between groups; however, the images presented in this manuscript have been adjusted to improve visibility.

6.2.6 Junction Analysis

Junctions were analyzed using the JAnaP described in Chapter 4. A threshold of 15 was used to isolate the ZO-1 junctions from the background noise.

6.2.7 Monolayer Coverage Quantification

ImageJ (National Institutes of Health, Bethesda, MD) was used to quantify monolayer coverage of each image. Visible holes in the monolayer were manually traced and quantified in ImageJ, and the total void area was summed per image. Monolayer coverage was expressed as a percentage by multiplying the fraction of the

total uncovered area divided by the total image area by 100 and then subtracting it from 100%. When monolayer coverage was less than the void area, the covered area was traced instead, and the void area was calculated by subtracting the sum of the covered area from the total image area. While all other data presented is on a per-cell basis, this measure is presented on a per-image basis. Note that this parameter is the only variable in this manuscript that was not quantified using the JAnaP.

6.2.8 Statistical Analysis

For instances where two groups of data are compared (i.e., Figure 2), statistical analyses were completed used an unpaired t-test. For other shape factor group calculations, a one-way ANOVA with a post-hoc Tukey test for multiple comparisons was used. For grouped junction analysis, a two-way ANOVA with a post-hoc Tukey test for multiple comparisons was used. Outliers were identified using the Grubbs' method with alpha = 0.0001 to remove only definite outliers. Measurements stated in this paper are presented in the format mean ± SEM. Note that only ***$p \leq 0.001$ and ****$p \leq 0.0001$ have been included within the graphs due to the large cell numbers included in analysis, however the full statistical data has been included separately in tables following the figures. Unless otherwise marked with brackets, significance is with respect to the control within the same treatment group (e.g., control with cAMP versus experimental with cAMP).

6.3 Results

6.3.1 cAMP supplements increase ZO-1 edge-coverage in HBMECs on glass

Several previous studies, including our own (Chapter 5), have shown that CPT-cAMP and RO-20-1724 increase tight junctions in various EC types [48,212]. Therefore, we first quantified the effects of these supplements in HBMECs on collagen-coated glass, to probe the changes in junction architecture on an extremely stiff substrate routinely used in cell culture. Representative images of cells immunostained for ZO-1 comparing the use of cAMP supplements are shown in Figure 6.1.A, and an example cell analyzed by the JAnaP is presented in Figure 6.1.B. The addition of cAMP supplements decreased the average cell perimeter and area from 195.0 ± 6.1 to 156.5 ± 3.6 μm and from 1185.0 ± 66.2 to 938.8 ± 37.0 μm^2, respectively, but increased solidity and circularity, leading to smaller but more rounded cells (Figure 6.1.C-F). Monolayer coverage was approximately 47 ± 3% and was unaffected by cAMP supplements (Figure 6.1.G). Note that the same initial seeding density was used throughout the manuscript, and while here, monolayer coverage was low, the same seeding density in subsequent conditions led to a significant increase in monolayer coverage. While cAMP supplements did not influence monolayer coverage, the overall ZO-1 localization increased from 15.2 ± 0.9% to 27.6 ± 0.9%, resulting from increased continuous and punctate junction presentation from 4.6 ± 0.5% to 11.3 ± 0.7% and 9.7 ± 0.5% to 14.3 ± 0.4%, respectively (Figure 6.1.H). These results suggest that while elevating cAMP induces slight changes in cellular morphology, it significantly

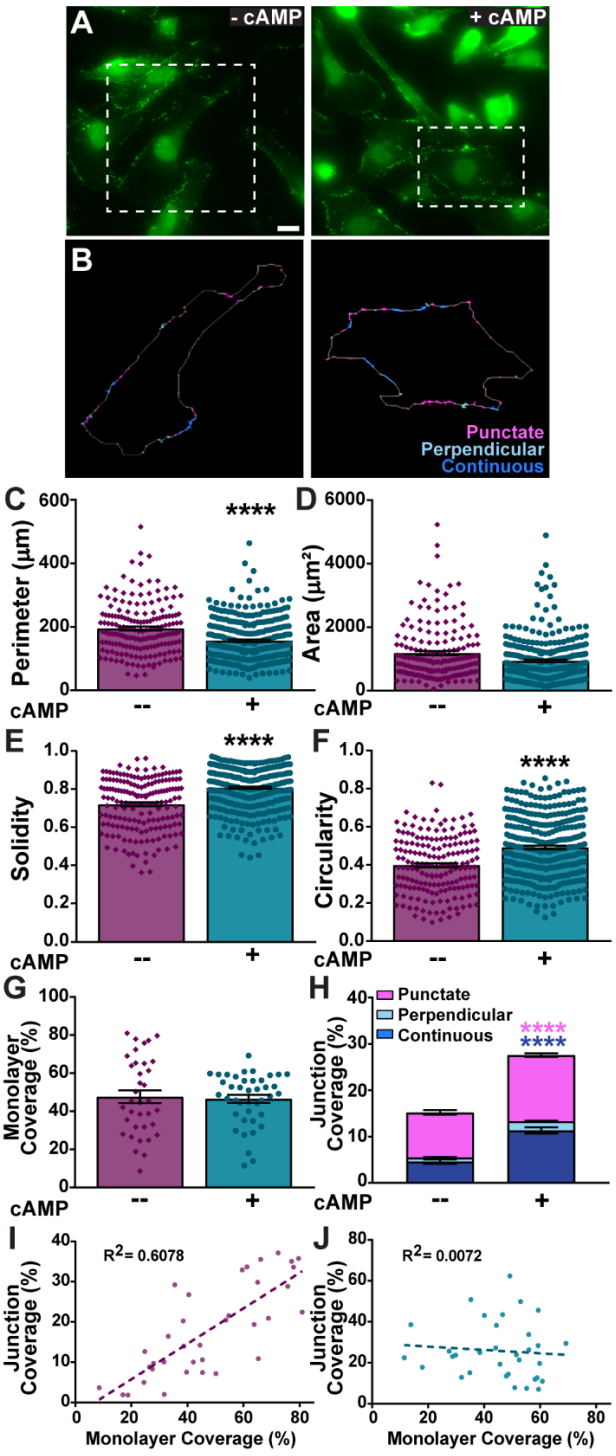

Figure 6.1 The effects of cAMP supplements on HBMECs on collagen-coated glass. (A) presents immunofluorescent images of ZO-1 in HBMECs with and without cAMP supplement (scale bar = 20 µm). An example cell of interest is denoted with the white hashed box and is presented in (B) with the junctions categorized by the JAnaP. (C-F) presents the average cell perimeter, area, solidity, circularity as calculated using the JAnaP. N = 177 cells without cAMP and N = 327 cells with cAMP. The coverage of the monolayer within each image is presented in (G) while the coverage of each junction per cell perimeter is presented in (H). For (G), N = 36 and 41 monolayer images for without and with cAMP, respectively. For (H), the bars represent the average results for N = 179 and 329 cells for without and with cAMP groups, respectively. Statistical analysis was performed using an unpaired t-test, ***$p \leq 0.001$ and ****$p \leq 0.0001$. The colors of the statistics in (H) indicate the differences with and without cAMP for each junction type. (I-J) present the relationship between total ZO-1 coverage and monolayer coverage (I) without and (J) with cAMP supplements, with each dot representing the average of all cells within each image. Full statistical information is included in Table 6.1.

increases the edge-localization of ZO-1. These quantified results are in line with the large body of qualitative evidence that cAMP agents improve junction architecture in EC barriers. Since edge-localization of junctional proteins typically requires

homophilic interactions with an adjacent binding partner in regions of cell-cell contact, we investigated the influence of monolayer coverage on total ZO-1 presentation. A positive correlation was found between monolayer and junction coverage (r-squared=0.6078) in the absence of supplements (Figure 6.1.I). However, this relationship was mitigated with the addition of supplements (Figure 6.1.J; r-squared=0.0078), suggesting that cAMP additives increase and stabilize the level of edge-localized ZO-1 at these confluency levels.

Adjusted P value	
Perimeter	<0.0001
Area	0.0005
Solidity	<0.0001
Circularity	<0.0001
Monolayer Coverage	0.7714
Continuous Junction Coverage	<0.0001
Punctate Junction Coverage	<0.0001
Perpendicular Junction Coverage	<0.0001

Table 6.1 Statistical p-values for Figure 6.1. Analysis via an unpaired t-test comparing HBMEC parameters for conditions with and without cAMP on collagen-coated. Note that significant values are highlighted in green and non-significant values ($P > 0.05$) are highlighted in red.

6.3.2 Biochemical inhibition of myosin II on stiff substrates increases continuous ZO-1

Despite the increase in junction localization with cAMP supplements on glass, the overall junction and monolayer coverage remained low. These cAMP supplements function to (1) inhibit myosin light chain phosphorylation which decreases EC contraction, and (2) activate Rac1 to increase cortical actin stabilization and decrease actin stress fiber formation [213]. Therefore, we investigated the interplay of blebbistatin, a myosin-II inhibitor, and cAMP supplements, to test the effects of further decreasing contractility on HBMEC barrier formation and junctional presentation. Representative immunostaining and JAnaP images are presented in Figure 6.2.A-B.

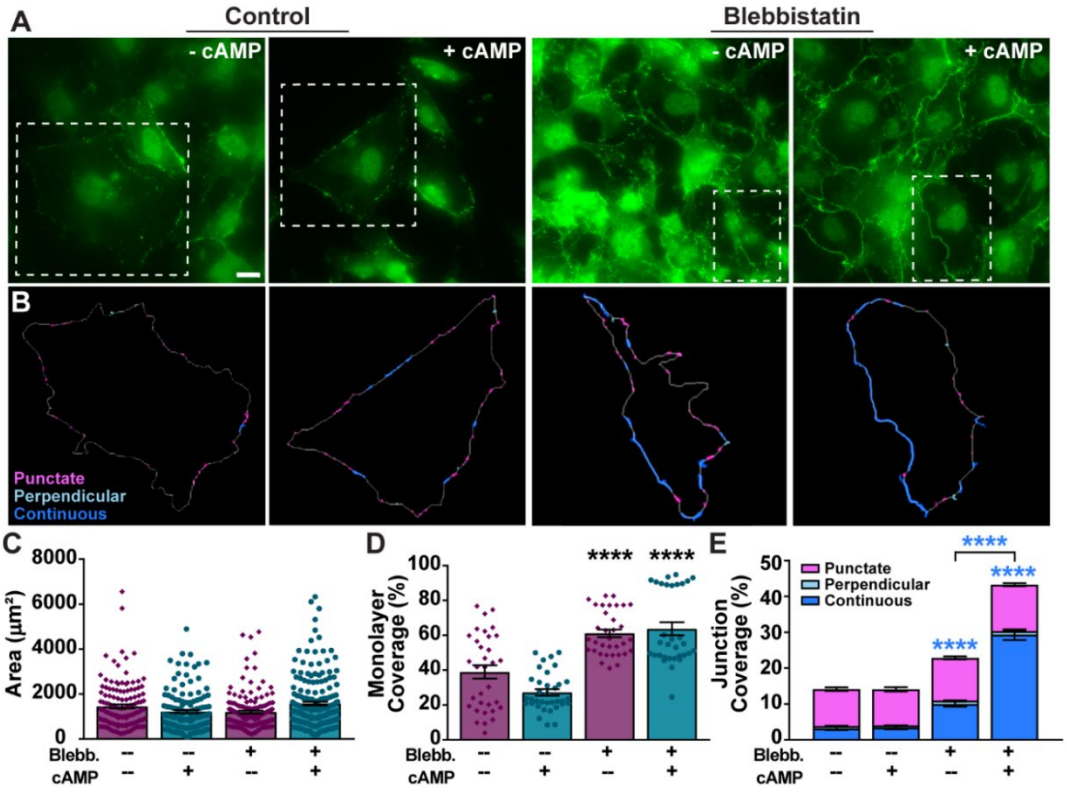

Figure 6.2 The effects of blebbistatin treatment with and without cAMP supplement on collagen-coated glass. (A) presents immunofluorescent images of ZO-1 in HBMECs for each treatment (scale bar = 20 μm). An example cell of interest is denoted with the white hashed box and is presented in (B) with the junctions categorized by the JAnaP. (C) presents the average cell area calculated using the JAnaP ($129 \leq N \leq 195$, where N is the number of cells) and (D) shows the coverage of the monolayer within each image ($32 \leq N \leq 35$, where N is the number of images). The coverage of each junction per cell perimeter is presented in (E) ($136 \leq N \leq 188$, where N is the number of cells). Statistical analysis was performed using a one-way ANOVA for (C-D) and a two-way ANOVA for (E), both with a post-hoc Tukey test for multiple comparisons, ****$p \leq 0.0001$. The statistics represent differences between the experimental group and the control with the same cAMP treatment unless otherwise marked with a bracket. The color of the statistics in (E) indicate the differences for the corresponding junction type. Full statistical information is included in Table 6.2.

The average cell area ranged from 1201 ± 64 to 1579 ± 83 μm^2 and was unchanged with blebbistatin or cAMP treatment (Figure 6.2.C). Other morphological parameters can be found in Figure 6.3, with statistical comparisons presented in Table 5.2. Monolayer coverage, however, increased over 20% when cells were treated with blebbistatin (irrespective of cAMP supplement) (Figure 6.2.D). Total ZO-1 edge-

coverage also increased from 14.2 ± 0.8% to 22.9 ± 1.0% with blebbistatin, and further to 43.3 ± 1.7% when treated with both blebbistatin and cAMP supplements (Figure 6.2.E). This increase was driven by significant increases in continuous junctions, as no change was observed in punctate or perpendicular junctions. The increase in both monolayer coverage and continuous junctions indicate improved barrier formation with decreased myosin II-mediated contractility, especially when HBMECs were supplemented with cAMP.

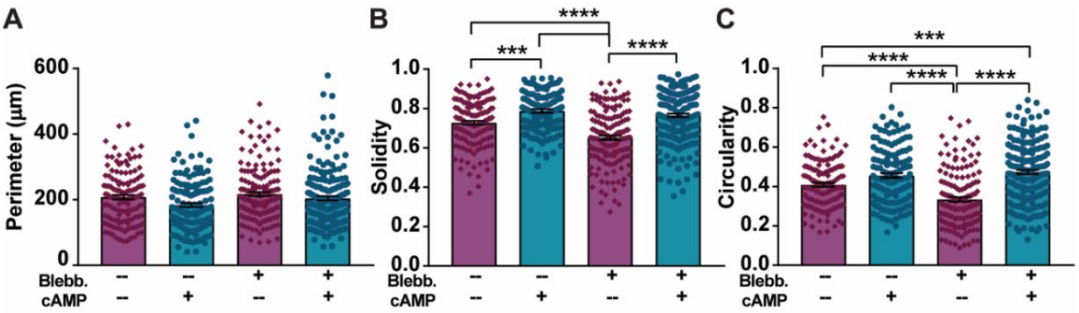

Figure 6.3 The effects of blebbistatin treatment on HBMEC morphology on collagen-coated glass with and without cAMP supplement. (A-C) presents the average cell perimeter, solidity, and circularity, respectively, calculated using the JAnaP ($129 \leq N \leq 195$, where N is the number of cells). Statistical analysis was performed using a one-way ANOVA with a post-hoc Tukey test for multiple comparisons, ***$p \leq 0.001$ and ****$p \leq 0.0001$.

	Adjusted P value							
	Perimeter	Area	Solidity	Circularity	Monolayer Coverage	Continuous Junction Coverage	Punctate Junction Coverage	Perpendicular Junction Coverage
Control vs. Control + cAMP	0.066	0.1586	0.0005	0.033	0.0291	0.9993	0.9922	0.9576
Control vs. 50 µM Blebb	0.7822	0.0499	<0.0001	<0.0001	<0.0001	<0.0001	0.0909	0.0039
Control vs. 50 µM Blebb + cAMP	0.9769	0.9898	0.0449	0.0003	<0.0001	<0.0001	0.0005	0.0002
Control + cAMP vs. 50 µM Blebb	0.003	0.9754	<0.0001	<0.0001	<0.0001	<0.0001	0.0442	0.0006
Control + cAMP vs. 50 µM Blebb + cAMP	0.1108	0.0532	0.3561	0.683	<0.0001	<0.0001	0.0001	<0.0001
50 µM Blebb vs. 50 µM Blebb + cAMP	0.4723	0.0106	<0.0001	<0.0001	0.9307	<0.0001	0.3924	0.9148

Table 6.2. Statistical p-values for Figures 6.2 and 6.3. A one-way ANOVA with a post-hoc Tukey test was used for multiple comparisons for HBMEC morphology and junction parameters on collagen-coated glass following blebbistatin treatment with and without cAMP (corresponds to data in Figure 3). Note that significant values are highlighted in green and non-significant values ($P > 0.05$) are highlighted in red.

6.3.3 Decreasing matrix stiffness increases continuous ZO-1 coverage

Previous results suggest that substrate stiffness modulates myosin II-mediated EC contractility [76] and monolayer traction forces [242]. Given the monolayer and junctional alterations observed with myosin II inhibition (Figure 6.2), we next investigated the mechanobiological effects of substrate stiffness on barrier formation. HBMECs were plated on collagen-coated polyacrylamide gels and immunostained for ZO-1 (Figure 6.4.A-B). The specific gel compositions were selected to span a wide range of physiologically- and pathologically- relevant stiffness. The brain extracellular matrix is approximately 1 kPa and peripheral subendothelial matrices range from 3-7 kPa,[76] and hence our lower gel stiffnesses represent physiologically "healthy" matrices in terms of mechanical properties. Blood vessel stiffening is associated with vascular injury, and thus the 15 and 194 kPa gels represent a "diseased" stiffness range, as evidenced by previous studies where atomic force microscopy was used to quantify the mechanical properties of endothelial cell substrates in peripheral arteries ex vivo and found diseased models to increase in stiffness from 3-5 kPa to 10-15 kPa [243,244].

The Young's modulus of each gel composition was previously determined [241] and confirmed again in our lab using AFM (Figure 6.5). Because our previous results suggested barrier improvement with cAMP, the results in Figure 6.4 present only conditions with cAMP supplement (see Figure 6.6 for results without supplement and full shape factor analysis). Note that the results on collagen-coated glass from Figure 6.1 are also included here for comparison.

Interestingly, cell area was consistent on all gels, despite the large stiffness range, and was roughly double the size of the cells cultured on glass (Figure 6.4.C). Monolayer coverage ranged from 92.2 ± 1.0 to 95.2 ± 0.6% on the gels, which was roughly 50% higher than the average monolayer coverage on glass (Figure 6.4.D). Total ZO-1 edge-localization increased on gels versus glass, with the greatest (55.8 ± 1.3%) observed on 1 kPa gels. This resulted from increased continuous presentation on 1 kPa, covering 35.5 ± 1.5% of the cell perimeter (at least 12% more than any other condition) (Figure 6.4.E). Without cAMP supplement, HBMECs also demonstrated higher junctional coverage on gels versus glass; however, the amplified enhancement of these parameters on 1 kPa gels was absent (Figure 6.6.C). No change in perpendicular junction coverage was observed, but punctate junctions increased between selective substrates. Overall, this suggests that while HBMEC morphological parameters are insensitive to matrix stiffness within a physiological (1 and 8 kPa) and even pathological (15 and 194 kPa) [76] range, they are affected by the orders of magnitude difference between polyacrylamide gels (kPa range) and glass (GPa). However, ZO-1 presentation seems to be more mechanosensitive, as more mature junctions were observed on 1 kPa compared to stiffer gels.

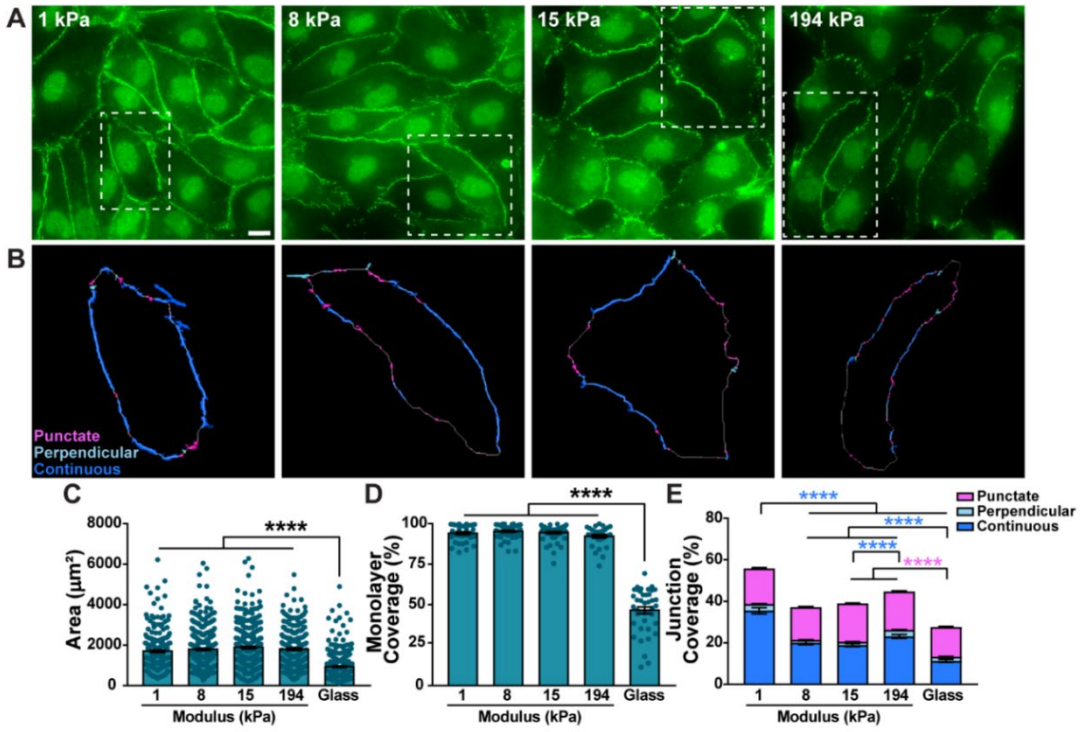

Figure 6.4. HBMECs on collagen-coated polyacrylamide gels of varying stiffness. (A) presents immunofluorescent images of ZO-1 in HBMECs with cAMP supplement on each gel stiffness (scale bar = 20 μm). An example cell of interest is denoted with the white hashed box and is presented in (B) with the junctions categorized by the JAnaP for each condition. (C) presents the average cell area calculated using the JAnaP ($167 \leq N \leq 327$, where N is the number of cells) and (D) shows the coverage of the monolayer within each image ($31 \leq N \leq 50$, where N is the number of images). The coverage of each junction per cell perimeter is presented in (E) ($228 \leq N \leq 343$, where N is the number of cells). Statistical analysis was performed using a one-way ANOVA for (C-D) and a two-way ANOVA for (E), both with a post-hoc Tukey test for multiple comparisons, ****$p \leq 0.0001$. The color of the statistics in (E) indicate the differences for the corresponding junction type. Full statistical information is included in Table 6.3.

	Adjusted P value							
	Perimeter	Area	Solidity	Circularity	Monolayer Coverage	Continuous Junction	Punctate Junction	Perpendicular Junction
1 kPa vs. 1 kPa + cAMP	<0.0001	0.0002	<0.0001	<0.0001	<0.0001	<0.0001	0.1716	<0.0001
1 kPa vs. 8 kPa	>0.9999	>0.9999	0.0068	0.0401	<0.0001	0.0003	>0.9999	0.3863
1 kPa vs. 8 kPa + cAMP	<0.0001	0.0016	<0.0001	<0.0001	<0.0001	<0.0001	>0.9999	0.4781
1 kPa vs. 15 kPa	0.9745	0.1943	0.0076	0.0438	<0.0001	0.9128	0.0005	0.998
1 kPa vs. 15 kPa + cAMP	<0.0001	0.0331	<0.0001	<0.0001	<0.0001	0.0024	<0.0001	0.9645
1 kPa vs. 194 kPa	0.968	0.7513	0.6783	0.7705	<0.0001	0.9901	0.0027	0.465
1 kPa vs. 194 kPa + cAMP	0.0004	0.0071	<0.0001	<0.0001	<0.0001	<0.0001	0.0008	<0.0001
1 kPa vs. Glass	<0.0001	<0.0001	<0.0001	0.0167	<0.0001	<0.0001	<0.0001	<0.0001
1 kPa vs. Glass + cAMP	<0.0001	<0.0001	0.1655	0.0195	<0.0001	0.4999	0.5196	0.6431
1 kPa + cAMP vs. 8 kPa	<0.0001	<0.0001	0.0108	0.0485	0.947	<0.0001	0.5029	<0.0001
1 kPa + cAMP vs. 8 kPa + cAMP	>0.9999	0.9971	0.9881	0.9239	>0.9999	<0.0001	0.2147	<0.0001
1 kPa + cAMP vs. 15 kPa	<0.0001	<0.0001	0.0051	0.0275	>0.9999	<0.0001	0.7742	<0.0001
1 kPa + cAMP vs. 15 kPa + cAMP	0.9998	0.7738	0.9814	0.5808	>0.9999	<0.0001	0.1609	<0.0001
1 kPa + cAMP vs. 194 kPa	<0.0001	0.0652	<0.0001	<0.0001	0.8972	<0.0001	0.9369	<0.0001
1 kPa + cAMP vs. 194 kPa + cAMP	0.9598	0.9972	0.8233	0.9216	0.9998	<0.0001	0.789	>0.9999
1 kPa + cAMP vs. Glass	>0.9999	0.0008	<0.0001	<0.0001	<0.0001	<0.0001	<0.0001	<0.0001
1 kPa + cAMP vs. Glass + cAMP	<0.0001	<0.0001	<0.0001	0.0048	<0.0001	<0.0001	<0.0001	<0.0001
8 kPa vs. 8 kPa + cAMP	<0.0001	0.0003	<0.0001	<0.0001	0.7214	<0.0001	>0.9999	>0.9999
8 kPa vs. 15 kPa	0.7519	0.2744	>0.9999	>0.9999	0.9942	0.0213	0.0053	0.0269
8 kPa vs. 15 kPa + cAMP	<0.0001	0.0093	<0.0001	<0.0001	0.8655	<0.0001	<0.0001	0.9375
8 kPa vs. 194 kPa	0.9996	0.5472	0.4933	0.7774	>0.9999	<0.0001	0.0214	0.0001
8 kPa vs. 194 kPa + cAMP	0.0024	0.0018	0.557	0.7187	0.9997	<0.0001	0.0073	<0.0001
8 kPa vs. Glass	<0.0001	<0.0001	<0.0001	<0.0001	<0.0001	0.4288	<0.0001	0.1344
8 kPa vs. Glass + cAMP	<0.0001	<0.0001	0.8726	>0.9999	<0.0001	0.0924	0.1404	0.0002
8 kPa + cAMP vs. 15 kPa	<0.0001	<0.0001	<0.0001	<0.0001	0.9952	<0.0001	0.0002	0.0216
8 kPa + cAMP vs. 15 kPa + cAMP	>0.9999	0.9939	>0.9999	0.9995	>0.9999	0.985	<0.0001	0.9858
8 kPa + cAMP vs. 194 kPa	<0.0001	0.2758	<0.0001	<0.0001	0.5944	0.001	0.0016	<0.0001
8 kPa + cAMP vs. 194 kPa + cAMP	0.9798	>0.9999	0.118	0.0921	0.9905	0.1857	0.0004	<0.0001
8 kPa + cAMP vs. Glass	0.9998	<0.0001	<0.0001	<0.0001	<0.0001	<0.0001	<0.0001	0.0104
8 kPa + cAMP vs. Glass + cAMP	<0.0001	<0.0001	<0.0001	<0.0001	<0.0001	<0.0001	0.0497	<0.0001
15 kPa vs. 15 kPa + cAMP	<0.0001	<0.0001	<0.0001	<0.0001	0.9997	<0.0001	0.9951	0.3393
15 kPa vs. 194 kPa	0.2216	<0.0001	0.5387	0.8123	0.9816	0.1686	>0.9999	0.8858
15 kPa vs. 194 kPa + cAMP	<0.0001	<0.0001	0.4404	0.6185	>0.9999	<0.0001	>0.9999	<0.0001
15 kPa vs. Glass	<0.0001	<0.0001	<0.0001	<0.0001	<0.0001	<0.0001	<0.0001	<0.0001
15 kPa vs. Glass + cAMP	<0.0001	<0.0001	0.9053	>0.9999	<0.0001	0.9995	<0.0001	0.9728
15 kPa + cAMP vs. 194 kPa	0.0002	0.8577	<0.0001	<0.0001	0.7697	0.0459	0.96	0.0038
15 kPa + cAMP vs. 194 kPa + cAMP	0.9992	0.9988	0.1043	0.0146	0.9989	0.0108	0.9973	<0.0001
15 kPa + cAMP vs. Glass	0.9926	<0.0001	<0.0001	<0.0001	<0.0001	<0.0001	<0.0001	0.0003
15 kPa + cAMP vs. Glass + cAMP	<0.0001	<0.0001	<0.0001	<0.0001	<0.0001	<0.0001	<0.0001	0.0059
194 kPa vs. 194 kPa + cAMP	0.0134	0.4698	0.0003	0.0062	0.9986	<0.0001	>0.9999	<0.0001
194 kPa vs. Glass	<0.0001	<0.0001	<0.0001	<0.0001	<0.0001	<0.0001	<0.0001	<0.0001
194 kPa vs. Glass + cAMP	<0.0001	<0.0001	0.9986	0.7367	<0.0001	0.0146	<0.0001	>0.9999
194 kPa + cAMP vs. Glass	0.8653	<0.0001	<0.0001	<0.0001	<0.0001	<0.0001	<0.0001	<0.0001
194 kPa + cAMP vs. Glass + cAMP	<0.0001	<0.0001	0.0025	0.3969	<0.0001	<0.0001	<0.0001	<0.0001
Glass vs. Glass + cAMP	<0.0001	0.47	<0.0001	<0.0001	>0.9999	<0.0001	<0.0001	<0.0001

Table 6.3 Statistical p-values for Figures 6.4 and 6.6. A one-way ANOVA with a post-hoc Tukey test was used for multiple comparisons for HBMEC parameters on collagen-coated polyacrylamide gels or glass with and without cAMP.

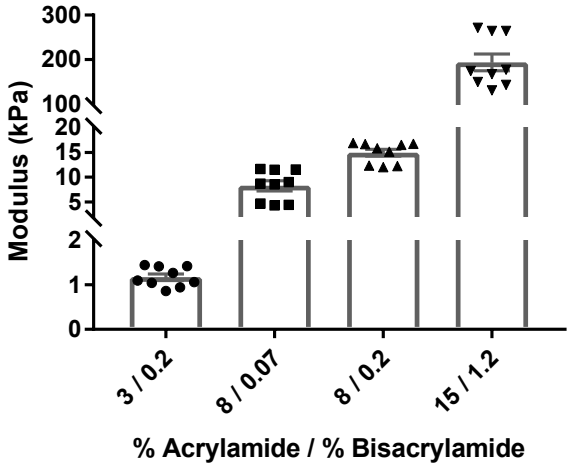

Figure 6.5. Young's modulus measurements of polyacrylamide gels as a function of acrylamide and bis acrylamide concentration. Each point represents the average Young's modulus of a 100-curve force map covering a 10 µm x 10 µm area. Three measurements were taken across 3 different samples for each gel composition (N=9, where N is the number of force maps).

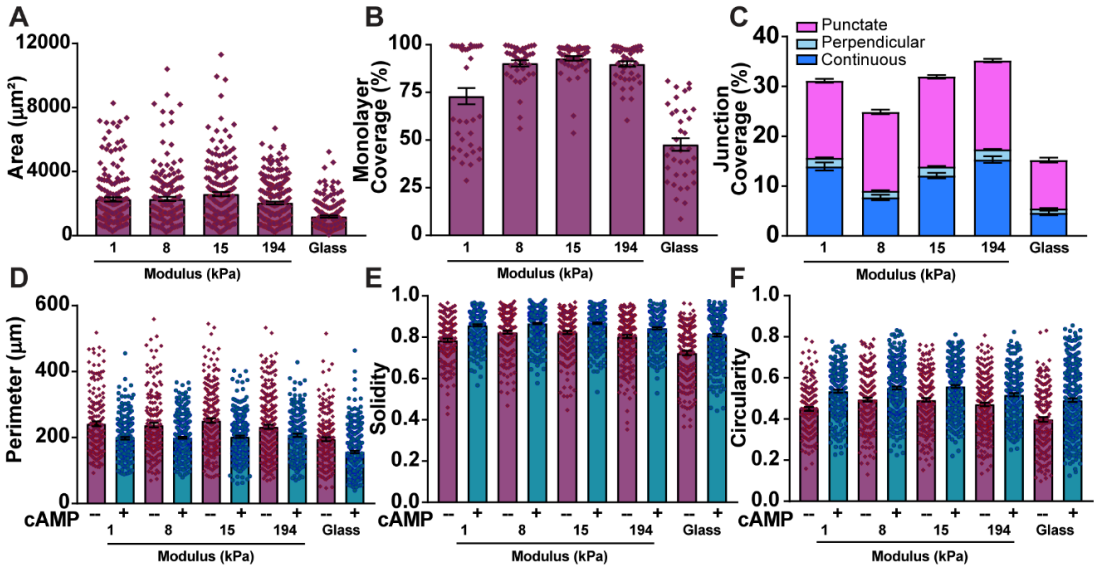

Figure 6.6. HBMECs on collagen-coated polyacrylamide gels of varying stiffness. (A-B) present the average cell area and monolayer coverage without cAMP supplement. For (A), $167 \leq N \leq 238$, where N is the number of cells. For (B), $36 \leq N \leq 50$, where N is the number of images. The coverage of each junction per cell perimeter without cAMP supplement is presented in (C). (D-F) presents the average cell perimeter, solidity, and circularity, respectively, with and without cAMP calculated using the JAnaP ($167 \leq N \leq 347$, where N is the number of cells). See Table 6.3 for statistical analysis.

6.3.4 Inhibition of protein phosphatases on soft substrates decreases ZO-1 junction coverage

Given the improved monolayer coverage and ZO-1 localization in conditions associated with decreased cell contractility (i.e., via blebbistatin treatment and soft substrate stiffness), we next investigated whether the opposite effect would be observed with increased contractility. HBMECs on collagen-coated 1 kPa gels or glass were treated with calyculin-A, a protein phosphatase inhibitor linked with increased cellular contractility,[245,246] immunostained for ZO-1, and analyzed via the JAnaP (Figure 6.7). In line with the section 6.3.3 results, cells were smaller and exhibited lower monolayer coverage on glass versus 1 kPa gels (Figure 6.7.B-C; see Figure 6.8 for additional morphological parameters). While calyculin treatment had no effect on cell area on the respective substrates, this treatment decreased monolayer coverage from 89.5 ± 3.5% to 70.0 ± 3.3% on 1 kPa gels. Notably, this effect was not observed on glass. Similarly, total ZO-1 localization decreased from 30.8 ± 1.0% to 13.7 ± 0.9% with calyculin treatment on 1 kPa gels, while junctional coverage on glass remained at ~19-20% for both conditions (Figure 6.7.D). This calyculin-induced decrease in ZO-1 on 1 kPa resulted from a decrease in both continuous and punctate junction presentation compared to the 1 kPa control.

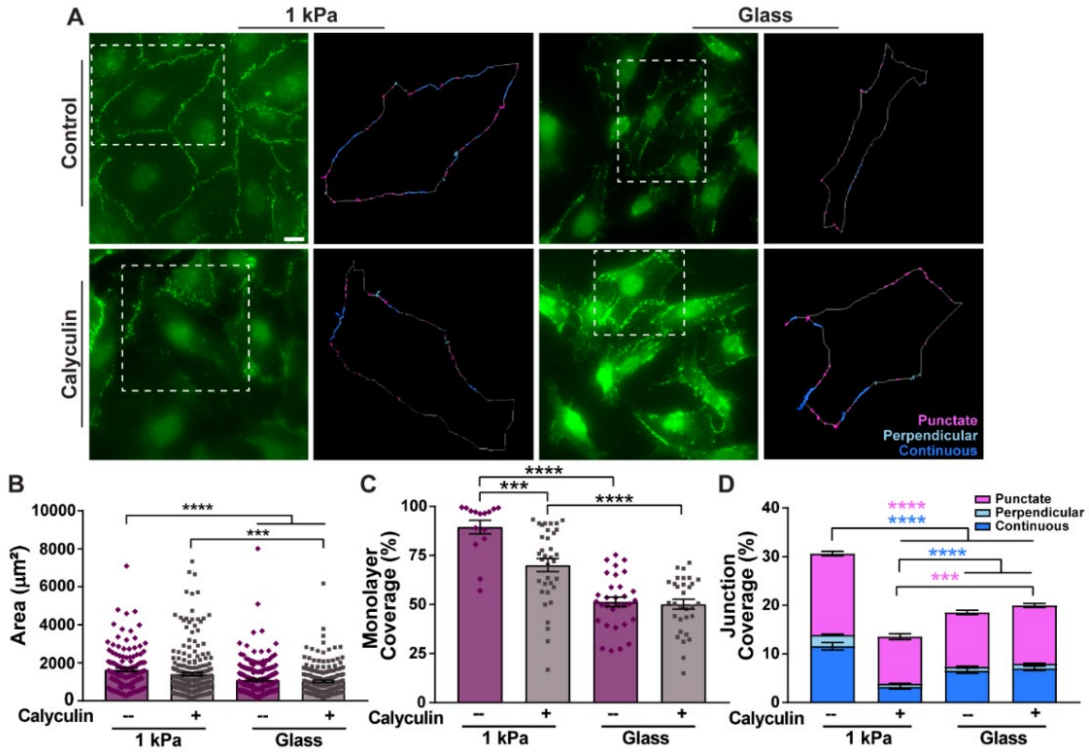

Figure 6.7. HBMECs treated with calyculin on 1 kPa collagen-coated polyacrylamide gels or glass. (A) presents immunofluorescent images of ZO-1 in HBMECs on each gel with cAMP supplement and an example cell of interest (denoted with the white hashed box) with the junctions categorized by the JAnaP for each condition (scale bar = 20 µm). (B) presents the average cell area calculated using the JAnaP ($131 \leq N \leq 236$, where N is the number of cells) and (C) shows the coverage of the monolayer within each image ($15 \leq N \leq 35$, where N is the number of images). The coverage of each junction per cell perimeter is presented in (D) ($131 \leq N \leq 215$, where N is the number of cells). Statistical analysis was performed using a one-way ANOVA for (C-D) and a two-way ANOVA for (E), both with a post-hoc Tukey test for multiple comparisons, ***$p \leq 0.001$ and ****$p \leq 0.0001$. The color of the statistics in (E) indicate the differences for the corresponding junction type. Full statistical information is included in Table 6.4.

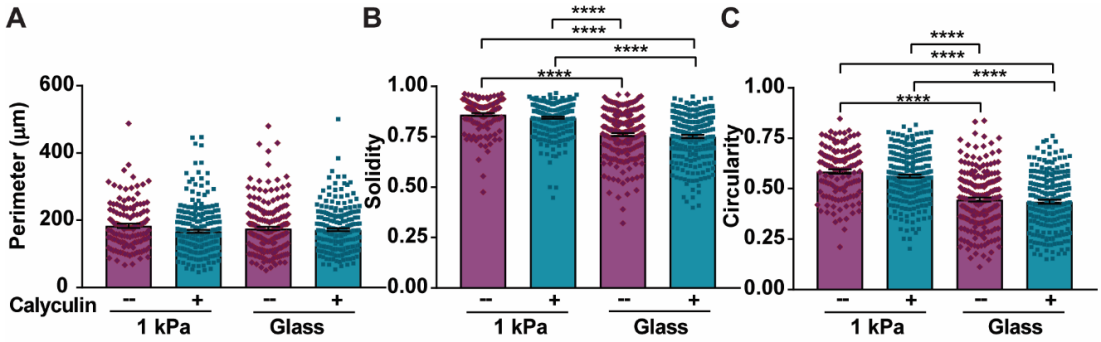

Figure 6.8 The effect of calyculin treatment on cell morphology on collagen-coated 1 kPa polyacrylamide gels versus glass. (A-C) presents the average cell perimeter, solidity, and circularity, respectively, calculated using the JAnaP ($131 \leq N \leq 236$, where N is the number of cells). Statistical analysis was performed using a one-way ANOVA with a post-hoc Tukey test for multiple comparisons, ***$p \leq 0.001$ and ****$p \leq 0.0001$.

	Adjusted P value							
	Perimeter	Area	Solidity	Circularity	Monolayer Coverage	Continuous Junction Coverage	Punctate Junction Coverage	Perpendicular Junction Coverage
1 kPa Control vs. 1 kPa Calyculin	0.1668	0.512	0.3579	0.0007	<0.0001	<0.0001	<0.0001	0.1668
1 kPa Control vs. Glass Control	<0.0001	<0.0001	<0.0001	<0.0001	<0.0001	<0.0001	<0.0001	<0.0001
1 kPa Control vs. Glass Calyculin	<0.0001	<0.0001	<0.0001	<0.0001	<0.0001	<0.0001	<0.0001	<0.0001
1 kPa Calyculin vs. Glass Control	0.01	<0.0001	<0.0001	<0.0001	0.0002	0.1487	0.2659	0.01
1 kPa Calyculin vs. Glass Calyculin	0.0005	<0.0001	<0.0001	<0.0001	<0.0001	0.004	0.0525	0.0005
Glass Control vs. Glass Calyculin	0.8803	0.7804	0.8325	0.991	0.8963	0.5199	0.863	0.8803

Table 6.4 Statistical p-values for Figures 6.7 and 6.8. A one-way ANOVA with a post-hoc Tukey test was used for multiple comparisons for HBMEC parameters with calyculin treatment.

6.4 Discussion

Since cell contractility has been previously been linked with barrier function and junction localizations, [15,53,77] our novel JAnaP was used to quantify the role of this phenomenon on junction presentation in HBMECs. First, the effect of cAMP supplements and substrate stiffness on ZO-1 presentation in HBMEC monolayers was investigated. The addition of cAMP supplements increased continuous junctions in every condition and also increased punctate and perpendicular junctions on glass. This was not surprising, based on our results in Chapter 5, and the significant evidence showing improvements in barrier properties with cAMP supplements. In ECs, cAMP reportedly blocks myosin light chain phosphorylation through Rho/ROCK signaling inhibition,[247] which has been linked with increased linear VE-cadherin formation,[14] and Beese et al. reported the supplements to improve continuous junction development in human umbilical vein ECs due to actin cytoskeleton reorganization [48]. Our results further support these points, since continuous ZO-1 presentation was further increased when myosin II was inhibited via blebbistatin.

Onken et al., previously observed increased actin stress fibers in HBMECs on polyacrylamide gels of increasing stiffness and a correlation between decreased substrate stiffness and increased linear VE-cadherin junctions as measured manually [15]. This aligns with our data since we found increased continuous ZO-1 on all gels (versus glass), with the highest continuous presentation on the softest 1 kPa gels with cAMP supplements. In fact, total junctional coverage was lowest on glass, which increased with blebbistatin and further increased on 1 kPa gels. Consistent with this trend was the overall monolayer coverage with cAMP, which was lowest on glass, increased with blebbistatin, and further increased on hydrogels. Overall, this indicates improved barrier formation in cells cultured on gels of biologically-relevant stiffness. Importantly, however, monolayer coverage could be influencing the overall ZO-1 presentation results, since junctional proteins typically localize to sites of cell-cell contact. We therefore investigated the relationship between total junction coverage and monolayer coverage for all conditions tested in this manuscript (Figure 6.9). Only a slight positive correlation emerged (r-squared=0.3007), suggesting that while

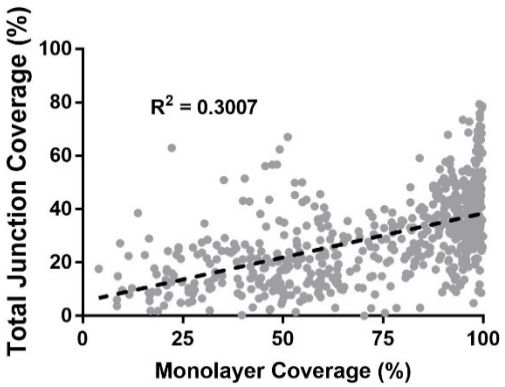

Figure 6.9. The effect of monolayer coverage on total ZO-1 junction coverage. This graph represents the average cellular junction coverage for each image, including all experimental groups presented in the manuscript (N=610 images). Linear regression was performed to determine an r-squared value of 0.3007.

monolayer coverage (and therefore, cell-cell contacts) play a role, it is not the only driving force regulating ZO-1 edge-localization.

Given our previous result that substrate stiffness modulates EC contractility,[76] it is likely that cells on glass are highly contractile, inducing the poorest barrier properties of the conditions tested. Meanwhile, decreasing contractility on glass, via blebbistatin, led to improved barrier properties, though not to the extent that resulted from decreased substrate stiffness. This suggests that mechanical modulation of the cell's microenvironment may adjust cellular contractility to a more optimal level. This was further supported by the final study, where calyculin significantly disrupted linear ZO-1 and increased discontinuous ZO-1 on 1 kPa gels. On 1 kPa, cells are likely minimally contracted such that calyculin treatment induced contraction, leading to disrupted junctional presentation. On glass, however, calyculin treatment did not affect ZO-1 edge-localization, likely because cells are already highly contractile, rendering calyculin ineffective in further enhancing contractility.

Overall, these results indicated improved junctional ZO-1 localization, with a more mature, linear phenotype in conditions driving lowered states of cell contractility. Specifically, biomimetic substrate stiffness was shown to improve barrier formation, decreasing contraction via mechanotransduction. This motivates the use of matrices of physiological stiffness *in vitro* modelling of the BBB and provides insight into potential therapeutic targeting of cell contractility for enhanced barrier function in disease.

6.5 Conclusion

In summary, we investigated the role of matrix stiffness and myosin II-mediated contractility on ZO-1 junction presentation in HBMECs using the JAnaP to provide

quantitative measures of cell-cell junction morphologies. Interestingly, the highest percentage of mature junctions was observed on the 1 kPa gels, which was the most physiologically relevant to the brain microenvironment and within the range of reported values for subendothelial matrix stiffness in vasculature. This further suggests that mimicking the mechanical environment of the *in vivo* system may be an effective approach to optimizing endothelial barrier properties for *in vitro* study; however, further investigation into the effects of these parameters on other tight junction proteins (e.g. claudins, occludins) is needed to fully understand the effects on barrier phenotype. Furthermore, additional experiments are needed to understand the physiological role (e.g., local permeability to molecules and cells) of each junction presentation type. Expanded use of the JAnaP could provide insight into the role of tight and adherens junction presentation in BBB physiology and pathology and possibly enable the study of junctional protein presentation in peripheral endothelial and epithelial cell monolayers. Understanding what conditions (e.g., contractility states) influence specific junction presentation and how that affects barrier properties could lead to the development of therapeutics capable of traversing the BBB for delivery to the brain or for diseases associated with BBB dysfunction.

Chapter 7 - Effects of Breast Cancer Cell Secreted Factors†

7.1 Introduction

Cancer metastasis occurs in approximately 20% of all cancer cases [248,249] and remains a devastating prognosis due to limited treatment options. Evidence in the literature, including *in vivo* imaging, has shown that tumor cells are capable of metastasizing to the brain through the circulatory and lymphatic systems [250], and that metastasis occurring through the circulatory system requires the tumor cells to traverse the BBB in order to reach the brain parenchyma [251]. The mechanisms governing how tumor cells cross the BBB, however, are not well understood.

In one study, close physical contact with the abluminal surface of the blood vessel was crucial for the spread of tumor cells, which actively transmigrated through gaps in the vascular wall, but also engaged in vascular remodeling during extravasation [252]. Unique to the BBB, tight junction proteins (e.g., claudins, occludins) are overexpressed, and act in conjunction with adherens junctions (e.g., VE-cadherin) to regulate barrier integrity and permeability [253]. These junctional proteins link to the actin cytoskeleton through ZO-1, which has been shown to regulate cell and junctional tension, cellular migration, barrier formation, and angiogenesis [14]. Disruption of these junctions is linked with increased permeability of the BBB to cells and molecules and is implicated in several diseases [2], including cancer metastasis [254] and glioblastoma, where microvascular leakiness correlates with histological tumor grade [255]. Metastatic breast tumor cells reportedly secrete factors that promote increased tumor cell-BBB

---

† This chapter was adapted from M.A. Pranda*, K.M. Gray*, A.J.L. DeCastro, G.M. Dawson, J.W. Jung, K.M Stroka. "Tumor cell mechanosensing during incorporation into the brain microvascular endothelium". *Cellular and Molecular Bioengineering* 12(5): 455-480 (2019) (*, equal contribution). Reproduced with permission of Springer in the format of Thesis/Dissertation via Copyright Clearance Center. M.A.P. co-wrote several sections in this chapter, and performed and analyzed the experiments for Figures 7.1, 7.2, and 7.8, with the help of A.J.L.D. and G.M.D. J.W.J aided in the analysis of all other figures.

adhesion and disrupt or rearrange junctions, weakening the barrier and leading to tumor cell transmigration [256,257]. Junction disruption can be considered a decrease of junctional proteins present at the cell boundary, while junctional rearrangement is a change in the boundary presentation (e.g., phenotype or morphology) of the specific junctional protein. As described above in chapters 2, 4, and 5, junctional phenotype is thought to be linked with the stability and maturity of the cell-cell junction. For instance, a linear, continuous junction parallel to the cell boundary is reported as a stable junction, exhibited by cells with low tension [15,258]. On the other hand, increased levels of cellular tension or contractility is linked with unstable, discontinuous junctions, which can take the form of punctate (e.g., dotted) or perpendicular (e.g., serrated) morphologies. Use of the JAnaP allows us to quantitatively phenotype these cell-cell junctions in a healthy BBB and in disease-associated states.

Tumor cell-derived biochemical cues and physical interaction with brain endothelial cells can alter brain endothelial cell-cell junctions in such a way that directs the mode of trans-endothelial migration. For instance, melanoma cells are reported to disrupt junctions, presumably through protease secretion, and induce endothelial cell apoptosis leading to paracellular transmigration [259]. Other studies have shown that breast tumor cells can cross endothelial barriers utilizing both transcellular and paracellular pathways [260]. Tumor cells also secrete endothelial-altering substances that can lead to an influx of calcium [261], glycocalyx degradation [260], and increased contractility [77,262], of the targeted endothelial cells, all of which are associated with enhanced tumor cell transmigration at cell-cell junctions [77,260–262]. Furthermore, we and others have demonstrated that tumor cells can even physically displace endothelial cells and “incorporate” or “intercalate” into the endothelium [263–265]. We hypothesized that this process may also represent a distinct step in the extravasation of tumor cells through the brain endothelium. Hence, we aimed to quantify how breast tumor cell biochemical factors and physical contact with the brain endothelial cells affect cell-cell junction organization, and ultimately, tumor cell incorporation into the endothelium.

In addition to cell-secreted factors, cell functionality is profoundly influenced by its surrounding extracellular matrix (ECM) [266]. However, it is not yet well understood which aspects of the brain microenvironment play a role in cancer progression [267]. Hyaluronic acid (HA) is a glycosaminoglycan that serves as a major building block of the brain ECM, which, unlike other parts of the body, is not highly organized and consists mainly of loosely crosslinked networks [268]. HA in the brain is linked with small glycoproteins, as well as tenasins, the density of which plays a large role in the function of various neural processes. Thus, the disruption of these linkages [268] as well as ECM rearrangement [269] could play a large role in disease progression. Indeed, for other ECM models such as collagen gels, crosslinking (e.g., via lysyl oxidase) has been shown to increase ECM stiffness, making it more conducive to the progression of tumors and other diseases [270–273]. While HA has important biological functions related to joint lubrication and wound healing, it also plays a role in the invasion of tumor cells, and, in the case of primary glioma tumors, HA is highly upregulated in the surrounding ECM [266].

Because ECM structure (e.g., arrangement, stiffness, etc.) is known to play a significant role in healthy and diseased states of the brain, here we have investigated how the crosslinking of a brain-like ECM affects brain endothelial cells, tumor cells, and the interaction between the two cell types. We have used an HA/gelatin-based system with varying degrees of crosslinking to mimic the brain ECM and used live-cell microscopy and immunofluorescence imaging to quantify cellular migration, morphology, cell-cell junction presentation, and tumor cell incorporation into brain endothelial monolayers, thus providing insight into the interplay of ECM crosslinking and bi-cellular systems on breast cancer metastasis across the BBB.

7.2 Materials and Methods

7.2.1 Cell Culture

Human breast adenocarcinoma cells, MDA-MB-231s (American Type Culture Collection, Manassas, VA, USA) were cultured in Dulbecco's Modified Eagle's Medium (DMEM) with high glucose and L-glutamine supplemented with 1% Penicillin/Streptomycin 10,000 U ml^{-1} (Pen/Strep) and 10% Fetal Bovine Serum (FBS) (Thermo Fisher Scientific, Waltham, MA, USA) and used below passage 20 after purchase. HBMECs were purchased from Cell Systems and cultured as previously described,[214] and used below passage 12.

7.2.2 HA/Gelatin film formation

HA/gelatin films were formed using the HyStem-C kit (ESIBIO, Alameda, CA, USA). The kit contained four components: DG water, Glycosil (thiolated HA), Gelin (thiolated Gelatin), and Extralink (thiol-reactive PEGDA crosslinker). Instructions from the kit were followed and were also described previously by Prestwich [274]. Briefly, all components were thawed for 30 - 60 minutes. Glycosil, Gelin, and DG water were then briefly heated at 37°C in a water bath to increase solubility. Glycosil and Gelin were then dissolved in 1 mL DG water, rocked for 1 hour at room temperature, then briefly re-heated in the water bath. Extralink was dissolved in DG water to 10%, then was further diluted into aliquots of 6, 4, and 1%. 24-well glass bottom plates (13 mm glass diameter) or 35 mm glass bottom dishes (14 mm glass diameter) (MatTek, Ashland, MA, USA) were plasma treated using a plasma cleaner with a 5 minute pumping step to create a vacuum and a 2.5 minute treatment on the

"High" RF power setting (Harrick Plasma, Ithaca, NY, USA, PDC-001-HP (115 V)) to increase hydrophilicity. The plates were then treated with ultraviolet light for 5 - 10 minutes for sterilization. Gelin and Glycosil were mixed in a 1:1 ratio and then the Glycosil/Gelin solution was combined in a 4:1 ratio with the appropriate concentration of Extralink. The final concentration of Extralink within the films were 0.2, 0.8, 1.2, and 2%. Twenty microliters of solution were plated in each well, spread, and covered for gelation, the time of which varied by Extralink concentration (2%: 2 - 5 minutes, 1.2%: 3-6 minutes, 0.8%: 4 - 7 minutes, 0.2%: 6 - 9 minutes). Once crosslinked, medium was added, and the films were incubated at 37°C for at least 30 minutes or until cells were ready to plate.

7.2.3 Atomic Force Microscopy

To measure the stiffness of the HA/gelatin, films were formed on 50 x 9 mm petri dishes. After the films had polymerized, the dishes were filled with PBS and an Asylum MFP-3D-BIO Atomic Force Microscope was used to perform AFM. The "Get Real" approach provided by Asylum Research was used to calculate the inverse optical lever sensitivity and the cantilever spring constant of the TR400PB(L) probes used for measurement. The cantilever spring constants were within the nominal range of 0.01 to 0.05 N m^{-1} (measured range: 0.026 to 0.028 N m^{-1}) and within a factor of 1.37 to Asylum's nominal value of 0.02 N m^{-1}. Four film samples of each composition were measured via five 100-curve force maps each (20 force maps in total). The force map specifications were as follows: 10 μm x 10 μm area, 2 μm force distance, 1 V trigger point (~1.57 nN), and a 0.99 Hz scan rate. The Hertz model was used to fit the data within Asylum's Igor Pro-based software using the equation $F = \frac{4}{3} \cdot (\frac{E}{1-\nu 2}) \cdot \sqrt{r} \cdot$

$\delta^{3/2}$ where the fitting parameter, E, is the Young's modulus, and δ, is the measured indentation of the sample. The Poisson's ratio, ν, and tip radius of curvature, r, were assumed to be 0.45 and 30 nm, respectively.

7.2.4 Tumor cell morphology and migration assays

Written, performed and analyzed by Marina Pranda, with the help of Ariana DeCastro and Greg Dawson (Stroka Lab).

HA/gelatin films were prepared as described above in 24-well glass bottom plates. After soaking with medium in the incubator, $5x10^4$ MDA-MB-231 cells were plated on top of the films and set-up to image as soon as the cells settled to the bottom of the plate. Images were collected via time-lapse phase-contrast microscopy and analyzed as described below in the data analysis section.

Tumor cell morphology was analyzed using ImageJ by manually tracing phase contrast images of live cells captured during or after time-lapse experiments in ImageJ. Cell circularity, solidity, and inverse aspect ratio were calculated as we have previously described [275]. To track tumor cell migration on bare films, phase-contrast time-lapse images were acquired in 5-minute intervals. The ImageJ Manual Tracking plugin was used to track the approximate centroid of each cell starting 5-6 hours post-plating and analyzed for up to the next 8-9 hours. Cells were not tracked if they went out of frame, divided during the tracking time, or were otherwise obstructed or hard to track. A custom Matlab (MathWorks, Natick, MA, USA) code was used to calculate cell speed, mean square displacement, and diffusion coefficient of the migrating cells, as we have previously described in detail [275]. Approximately 8 hours (495 frames) of data were

used for speed calculation, while approximately 7 hours (80-90 frames) were used for MSD calculation.

7.2.5 Tumor cell immunofluorescence staining

Written, performed and analyzed by Marina Pranda, with the help of Ariana DeCastro and Greg Dawson (Stroka Lab).

For CD44 staining, $2x10^4$ MDA-MB-231 cells were plated on HA/gelatin films formed with 0.2, 0.8, 1.2, and 2% Extralink in glass bottom dishes, or on dishes incubated with 20 μg ml^{-1} type I collagen for at least 1 hour at 37°C then washed three times with PBS. The next day, the cells were fixed in 3.7% formaldehyde (Millipore Sigma) for 10 minutes at room temperature, washed three times with PBS for 5 minutes each with rocking, and permeabilized with 0.5% Triton-X 100 (Millipore Sigma) for 5 minutes. The samples were then washed again three times in PBS for 5 minutes each and blocked in 2% Bovine Serum Albumin (BSA) (Millipore Sigma) for 1 hour at room temperature. Cells were then incubated at 4°C overnight with CD44 antibody (monoclonal CD44 antibody (156 3C11) Mouse mAb #3570, Cell Signaling Technologies, Danvers, MA, USA), which was dissolved in 2% BSA at a 1:100 ratio. Next, cells were rinsed with PBS and again blocked with 2% BSA for one hour at room temperature and washed with PBS. Cells were then incubated with 1:500 Phalloidin - Alexa Fluor 488 (Thermo Fisher Scientific), 1:100 of secondary antibody (Goat anti-Mouse IgG (H+L) Cross-Adsorbed Secondary Antibody Alexa Fluor 568, Thermo Fisher Scientific, A-11004), and 1:2500 of Hoechst 33342 (Thermo Fisher Scientific) diluted in PBS for 1 hour at room temperature. HBMECs transfected with the VE-cadherin-GFP adenovirus and tumor cells stained with Cell Tracker (described below)

were also fixed for 10 minutes in 3.7% formaldehyde, washed with PBS, and stained with 1:2500 of Hoechst 33342 for one hour at room temperature. Finally, all samples were washed with PBS and stored at 4°C until imaging via confocal microscopy.

7.2.6 Tumor-conditioned medium (TCM) preparation

To prepare TCM, MDA-MB-231 cells were seeded at 25% confluency in a T-75 flask and cultured in HBMEC medium for 72 hours. The medium was then collected, centrifuged at 300 x g for 10 minutes and the supernatant was filtered through a 40 μm cell strainer to remove any debris. This post-strained solution was then mixed at a 1:1 ratio with control HBMEC medium and designated as TCM. The TCM-free conditions consisted of HBMEC medium that was spun down and strained to the same degree as that collected from the MDA-MB-231 cells and mixed at a 1:1 ratio with fresh HBMEC medium.

7.2.7 HBMEC immunofluorescence staining

HA/gelatin films were prepared as described above in 24-well glass bottom plates. After soaking in medium at 37°C, $5x10^4$ HBMECs were plated onto each film. Approximately 24 hours later, the cells were treated with TCM or TCM-free (Control) medium and cultured for an additional 24 hours. For the VEGF studies, HBMECs were treated with TCM containing 0.12 μg/ml VEGF monoclonal antibody (Thermo Fisher Scientific #26503) or mouse IgG2b isotype control (Thermo Fisher Scientific), or TCM-free medium 24 hours after cell-seeding and cultured for an additional 24 hours. For immunofluorescence staining, HBMECs were rinsed with warm PBS and fixed with 1% formaldehyde (Millipore Sigma) for 10 minutes at room temperature. After

three subsequent 5-minute washes with PBS, the fixed HBMECs were then permeabilized with 0.25% Triton-X 100 (Millipore Sigma) for 5 minutes at room temperature. The samples were then washed again with PBS three times for 5 minutes each, then blocked for 1 hour at room temperature with 2% goat serum (Abcam, Cambridge, MA, USA). Primary antibodies (rabbit polyclonal IgG to ZO-1 antibody (H-300) and mouse monoclonal IgG to VE-cadherin antibody (F-8); Santa Cruz Biotechnology, Dallas, TX, USA, sc-10804 and sc-9989, respectively) were diluted 1:50 in 2% goat serum and added to the cells overnight at 4°C. Samples were rinsed the next day with PBS, blocked again for 1 hour at room temperature with 2% goat serum and then treated with secondary antibody (goat anti-rabbit Alexa Fluor 488, Abcam, ab150077; and goat anti-mouse Alexa Fluor 568, ThermoFisher Scientific) at a 1:100 dilution and 1:2500 Hoechst 33342 (ThermoFisher Scientific), in PBS, for 1 hour at room temperature. Samples were then rinsed with PBS and fresh PBS was added for imaging via fluorescence microscopy and analyzed as described below in the data analysis section.

7.2.8 ELISA assay for VEGF detection

To quantify the concentration of VEGF in TCM and TCM-free conditions, a Human VEGF Quantikine ELISA Kit (R&D Systems, Minneapolis, MN, USA) was used per the manufacturer's instructions. The medium samples were collected as stated in the "TCM Preparation" method above and quantified immediately following medium preparation.

7.2.9 Tumor cell incorporation assay and analysis

Written, performed and analyzed by Marina Pranda, with the help of Ariana DeCastro and Greg Dawson (Stroka Lab).

HA/gelatin films were prepared as described above in 24-well, glass bottom plates with 0.2, 0.8, 1.2, and 2% Extralink as well as a 1:1 mixture of gelatin and HA without Extralink (0%). $5x10^4$ - $1x10^5$ HBMECs were plated on the HA/gelatin films. To investigate the percent incorporation of metastatic breast tumor cells into HBMEC monolayers, live MDA-MB-231 cells were first stained with CellTracker Orange CMRA Dye (Thermo Fisher Scientific) per the manufacturer's instructions. Briefly, MDA-MB-231 cells were cultured in 6 well plates and equilibrated in HBMEC medium for two hours. The cells were washed with PBS and then incubated with 2 mL of 0.5 μM CellTracker Orange dye in RPMI-1640 and 1% Pen/Strep for 15 minutes. Cells were then washed again with PBS and incubated for 30 minutes in full HBMEC medium. The stained cells were then trypsinized and $1x10^4$ - $2.5x10^4$ MDA-MB-231 cells were plated on top of HBMECs that had been cultured to monolayer on HA/gelatin films for two days prior to MDA-MB-231 cell seeding. These samples were imaged using time-lapse phase-contrast and fluorescence microscopy as described below.

To quantify the time that tumor cells take to incorporate into HBMEC monolayers, and the percent of the tumor cells that incorporate into the monolayers, CellTracker-stained MDA-MB-231 cells were tracked on HMBEC monolayers by capturing images in 15-minute intervals. First, the total number of tumor cells per frame was recorded at the start of each time-lapse sequence. Tracking was carried out for 40

frames (585 minutes). Cells that went out of frame before frame 40 were excluded from analysis, as well as cells deemed "untrackable" due to clumping, visual obstructions, or migration to areas of large gaps in the monolayer. An incorporating cell was subjectively identified based on the disappearance of a white halo surrounding the cell and transition to a 2D-flattened morphology in phase contrast images. If a cell was spread, but retained a halo and 3D appearance, it was counted as not incorporating and instead was likely spreading on top of the monolayer. Percent incorporation was calculated by dividing the total cells that incorporated into the monolayer by the total number of cells tracked in each frame. The start time for a cell to incorporate was marked as the first frame where the cell appeared to be spreading into the monolayer, or the very first frame if it was already spread. If cells incorporated and then exited the monolayer, only the first instance of incorporation was counted. If a cell divided before incorporating or before frame 40, it was counted as two separate cells. If cells divided after incorporation, it was counted as one cell. Cumulative percent incorporation was calculated by averaging the total percent of cells that had incorporated at each 15-minute timepoint out of the total number of analyzable cells.

7.2.10 Microscopy

Confocal and live-cell microscopy performed by Marina Pranda (Stroka Lab).

Immunostained HBMECs were imaged on an Olympus IX83 inverted microscope using a 60x oil objective and Olympus cellSens Software. Images were collected in a manner that maximized monolayer coverage within the respective image. HBMEC images were collected at the same exposure times for consistent analysis and

have been enhanced via ImageJ, to the same extent for each channel, for improved visualization within this manuscript.

A PerkinElmer confocal spinning disk microscope (PerkinElmer, Waltham, MA) was used to obtain 3D images of fixed cells using a 40x water immersion objective. Vertical z-stacks were taken using appropriate filters using the Volocity 3D Image Analysis software. All acquisition settings were kept consistent between images within each experiment for CD44 imaging and slightly adjusted for best visualization for transmigration imaging. The ImageJ software (NIH; https://imagej.nih.gov) was used to reconstruct individual z-stack images into 3D, maximum-intensity and interpolated projections. Brightness of each channel in images of MDA-MB-231 cells stained for CD44 was adjusted separately but identically between each image to ensure that intensities could be compared. Brightness of each channel in images of MDA-MB-231 cells incorporating into HBMEC monolayers were adjusted separately for best visibility of appropriate parts of the cells; thus, intensities cannot be directly compared for these images.

Live-cell phase contrast and fluorescence images were captured using an IX83 microscope (Olympus, Center Valley, PA, USA) with a 10x objective for tumor cell migration assays on bare films, and 20x objective for tumor cell morphology assays on bare films, and incorporation assays with HBMECs and CellTracker-stained tumor cells. The Olympus cellSens Software (Olympus) was used to acquire the images. Phase contrast images of tumor cells on bare films were collected every 5 to 15 minutes for migration analysis, and additional images were captured at the end of the time-lapse on the second day for morphological analysis. The imaging regions for transmigration

experiments were selected based on best monolayer coverage and the presence of MDA-MB-231 cells. The live-cell imaging chamber was maintained at 37°C, 50% humidity, and 5% CO_2:95% air surrounding the microscope stage.

7.2.11 HBMEC morphology and junction analysis

To quantitatively analyze HBMEC morphology and cell-cell junction presentation, we utilized the JAnaP described in Chapter 3. Here, we utilized the ability to quantify an additional junction protein on the same cell. In addition to ZO-1, we co-stained the HBMECs for VE-cadherin. The waypoints generated on the ZO-1 image were projected to the VE-cadherin-tagged image, but the path between each waypoint was generated based on the intensities of the VE-cadherin image. A threshold value of 15 was used to isolate ZO-1 junctions while a threshold of 5 was used to isolate VE-cadherin junctions. Continuous junctions are junction pieces coinciding with the cell edge for at least 15 consecutive pixels. Junctions coinciding with the cell edge for less than 15 pixels are categorized as perpendicular, if they have a relative aspect ratio greater than 1.2, or punctate, if they have a relative aspect ratio less than 1.2. The relative aspect ratio is calculated by dividing the tip-to-tip distance (Tip Dist.), or maximum thickness, by the length of the junction coinciding with the cell edge, termed "path length". In this chapter, the percent of the junction coverage (calculated by dividing the cumulative sum of the path length of each junction type by the cell perimeter), as well as the tip-to-tip distance, are presented. The average tip-to-tip distance per cell for each junction type was calculated, providing a measure of the average maximum thickness of the continuous, perpendicular, and punctate junctions for each cell. The program-generated variables were calculated on a per cell basis, with

all cells from every trial pooled together (n is approximately 200 cells). The percent difference, however, was calculated based on the average of each junction type for every trial (n=3). The percent difference was calculated by taking the $(\%Junction_{TCM} - \%Junction_{Control}) \cdot ((\%Junction_{TCM} + \%Junction_{Control})/2)^{-1}$ for each junction type, for both ZO-1 and VE-cadherin.

7.2.12 Statistical Analysis

GraphPad Prism 8 (GraphPad, La Jolla, CA, USA) was used for all statistical analysis and graph preparation. Data was tested for normality using a D'Agostino-Pearson normality test, and some data within the same set did not follow a normal distribution. Thus, non-parametric tests were used for statistical analysis. If there were not sufficient values for a D'Agostino-Pearson test, a non-parametric test was used for consistency. If data was normally distributed in all comparison groups, a one-way analysis of variance (ANOVA) without assumed equal variances was used. For data that was not all normally distributed, a non-parametric Kruskal-Wallis ANOVA test with a Dunn's multiple comparison post-hoc test was used and for data that was all normally distributed a Brown-Forsythe and Welch ANOVA with Games-Howell post-hoc test was used. All tests were carried out with $P > 0.05$ indicating not statistically different, * $P \leq 0.05$, ** $P \leq 0.01$, *** $P \leq 0.001$, **** $P \leq 0.0001$. A linear regression was used to compare the number of tumor cells at the start versus monolayer quality, the percent difference in HBMEC junction presentation between TCM and control treatments, and the effect of Extralink concentration on junction tip-to-tip distance. A Mann-Whitney test was used to compare the TCM versus TCM-free conditions for each junction type at each Extralink concentration. A t-test was used to compare the

VEGF concentration in TCM versus TCM-free conditions. Errors bars represent standard error of the mean. All data represents pooled values from three independent trials unless otherwise noted in the figure captions.

7.3 Results

7.3.1 MDA-MB-231 cells become smaller and slower with increased HA/gelatin crosslinking

ECM crosslinking has been shown to alter tumor cell phenotype and invasiveness, and HA is known to be one of the primary components of the brain's ECM [268,270,271,273]. Hence, we aimed to evaluate the migration and morphology response of MDA-MB-231 tumor cells to varying degrees of HA/gelatin film crosslinking by altering the concentration of Extralink, a PEGDA-based crosslinker, during film formation [276,277]. We found that with increased Extralink concentration from 0.2% to 2%, MDA-MB-231 cells became significantly smaller (Figure 7.1.A,B) and more circular (Figure 7.1.A,C) and increased in inverse aspect ratio, circularity, and solidity (Figure 7.1.A,C). Furthermore, MDA-MB-231 cells plated on HA/gelatin films with increased Extralink concentrations demonstrated more homogeneous morphologies as evidenced by a decreased spread of the data with higher Extralink concentrations (Figure 7.1.B,C). Additionally, MDA-MB-231 cell speed decreased with increased crosslinking of HA/gelatin films (Figure 7.1.D). Plots of mean squared displacement vs. time indicated that MDA-MB-231 cells explored smaller areas with increased crosslinking of HA/gelatin films (Figure 7.1.E). Because a mesenchymal, metastatic phenotype is typically associated with highly migratory, elongated cells

[278,279], these changes in cell morphology and migration could be relevant to the cells' functionality.

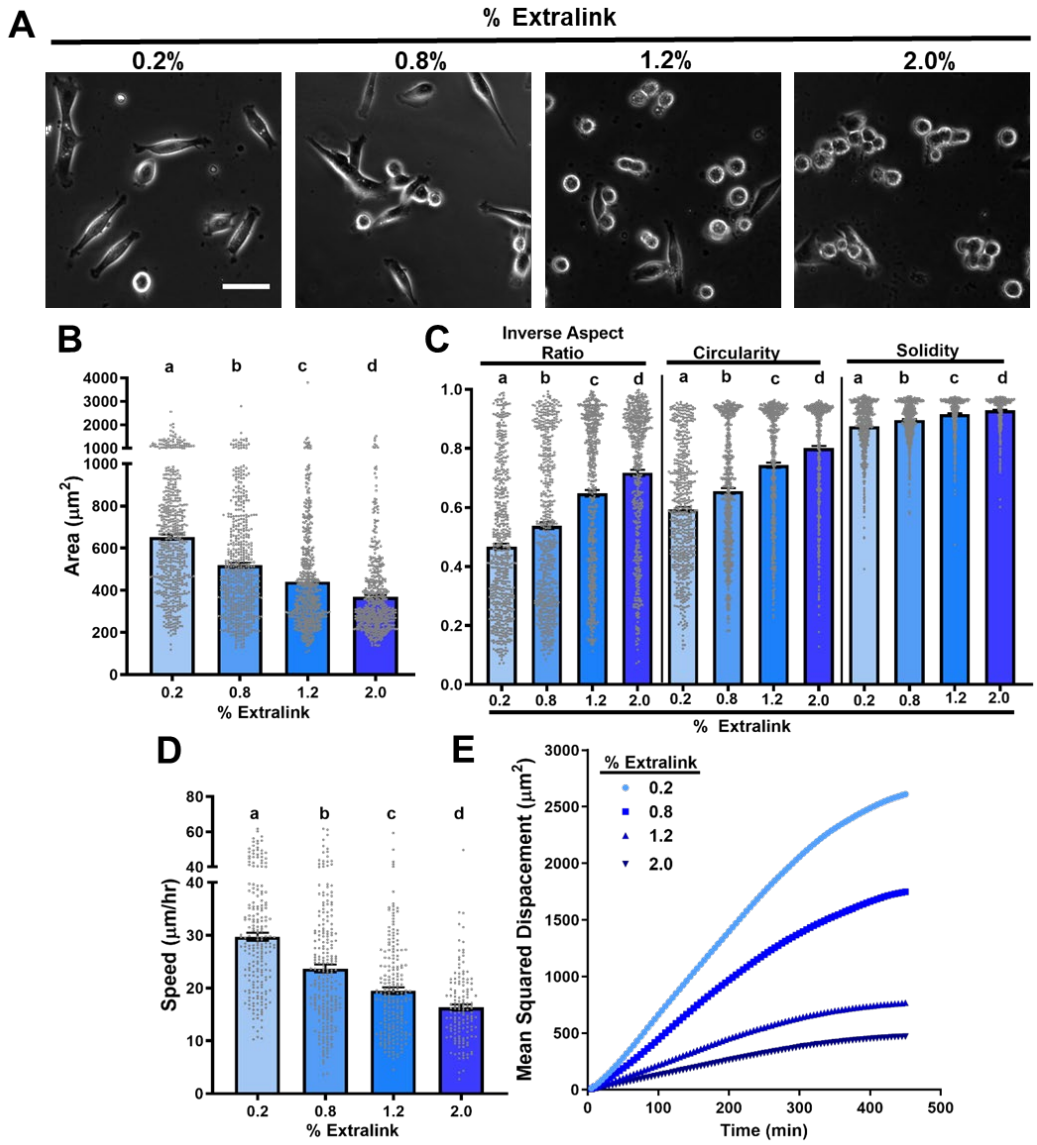

Figure 7.1 MDA-MB-231 morphology and migration parameters on HA/gelatin films with varying degrees of crosslinking. A) Phase contrast images of MDA-MB-231 cells on HA/gelatin films with 0.2, 0.8, 1.2, and 2% Extralink. Scale bar is 50 μm and applies to all images. B) Areas, C) inverse aspect ratio, circularity, and solidity, D) speed, E) mean squared displacement of MDA-MB-231 cells on HA/gelatin films with 0.2, 0.8, 1.2, and 2% Extralink. Means of columns that do not share a lower-case letter are significantly different with $P < 0.05$ via a non-parametric Kruskal-Wallis ANOVA test with a Dunn's multiple comparison post-hoc test. B,C: $529 \leq N \leq 582$, D: $142 \leq N \leq 228$ where N is the number of cells. E: $N = 3$, where N is the number of trials. All error bars represent standard error of the mean. All values are pooled from three independent trials. Data collection, analysis, and figure preparation was performed by Marina A. Pranda, with the help of Ariana DeCastro and Greg Dawson (Stroka Lab).

Cell attachment to HA is mediated by CD44, which also has been implicated in transducing HA stiffness cues and associated with brain tumor progression and invasion [266,280–282]. For breast tumor cells, CD44 increases tumor cell adhesion to and invasion of the endothelium, increasing the efficiency of distant metastasis [283]. Hence, we explored whether the morphological and migratory behavior with altered HA/gelatin film crosslinking were also associated with differences in CD44 binding. Interestingly, MDA-MB-231 cells immunostained for CD44 on HA/gelatin films with varying degrees of crosslinking, as well as type I collagen-coated glass, did not present observable differences in CD44 expression (Figure 7.2).

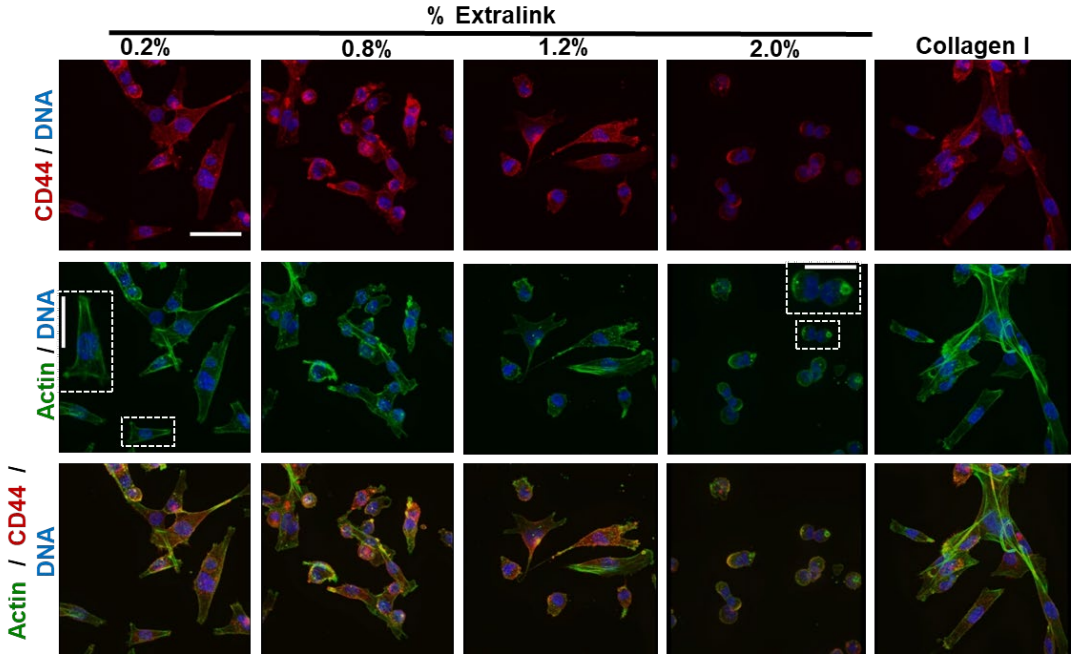

Figure 7.2 CD44 and actin staining in MDA-MB-231 cells. Reconstructed confocal z-stacks of MDA-MB-231 cells immunostained for CD44 (red) and stained for actin (green) on HA/gelatin films with 0.2, 0.8, 1.2, and 2% Extralink, as well as on glass coated with type I collagen. Scale bar on first image is 50 μm and applies to all images. Scale bar in the zoomed in inserts is 25 μm. Green: actin; red: CD44, blue: DNA. All images were reconstructed from a z-stack in ImageJ and intensities were adjusted equally for each channel and image. Data collection, analysis, and figure preparation was performed by Marina A. Pranda, with the help of Ariana DeCastro and Greg Dawson (Stroka Lab).

Meanwhile, actin arrangement was altered, with MDA-MB-231 cells on type I collagen and HA/gelatin films with 0.2% Extralink displaying a somewhat fibrous actin arrangement (Figure 7.2) which became more diffuse with increased film crosslinking, especially on the films with 2% Extralink (Figure 7.2). Increased cell spreading and mesenchymal migration are typically correlated with a more stress fiber-rich actin arrangement [284], which is indeed in line with our observations. A stress fiber-rich actin cytoskeleton is also often linked with a high degree of cellular contractility, which also correlates with the stiffness of the underlying cellular matrix [285]. Since increased crosslinking typically results in increased material stiffness, changes in film stiffness could drive alterations in tumor cell contractility and actin filament arrangement. Hence, we used atomic force microscopy to probe the effect of Extralink concentration on the Young's modulus of HA/gelatin films. The average modulus of the films formed with 0.2, 0.8, 1.2, and 2% Extralink were measured to be 0.85, 1.1, 1.5, and 3.8 kPa, respectively (Figure 7.3). Interestingly, only the Young's modulus of the film formed using 2% Extralink was statistically different from the Young's modulus of the other film compositions. Despite this, we still found significant differences in MDA-MB-231 cell phenotype and behavior on those film compositions (Figure 7.1).

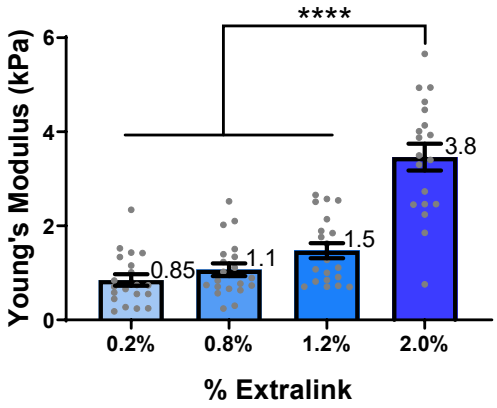

Figure 7.3: Atomic force microscopy measurements of HA/gelatin film stiffness. Young's modulus measurements of HA/gelatin films as a function of film crosslinking. Each point represents the average Young's modulus of a 100-curve force map covering a 10 μm x 10 μm area. The pooled results represent five measurements taken across 4 different samples for each film composition. The ROUT method (Q=1%) was used to identify and remove 1 outlier. The numbers next to each bar represent the average Young's Modulus (in kPa) for that film composition. Statistical analysis was performed using a one-way ANOVA with a post-hoc Tukey test for multiple comparisons, **** $P \leq 0.0001$.

7.3.2 HA/gelatin crosslinking does not affect HBMEC morphology or junction presentation

Metastasis across the BBB requires that tumor cells not only overcome the endothelial cell barrier, but also the underlying basement membrane. Tumor cells are reported to actively degrade the basement membrane by secreting matrix metalloproteinases (MMPs) [286]. Disruption of the basement membrane could lead to direct endothelial cell interaction with the brain ECM, and possibly abluminal HA-binding. Given the significant differences in MDA-MB-231 behavior on HA/gelatin films of varying crosslink density, we next wanted to understand how these differences in film composition might affect HBMEC monolayers. After two days of static culture on each film composition, HBMECs were fixed and immunostained for ZO-1 and VE-cadherin (Figure 7.4.A). In general, the percent of Extralink crosslinker did not affect the area (Figure 7.4.B), solidity (Figure 7.4.C), circularity (Figure 7.4.C), or perimeter

(Figure 7.5) of individual HBMECs within a monolayer. To assess how crosslinking affects cell-cell junctions, we used the JAnaP to quantify the percent of the cell perimeters presenting different junction types for ZO-1 and VE-cadherin (Figure 7.4.D-E). HBMECs on HA/gelatin films with 0.8% Extralink presented the highest amounts of continuous, punctate, and perpendicular ZO-1 (Figure 7.4.D). For VE-cadherin, no difference in continuous or perpendicular junction presentation was observed across the different film compositions, but punctate junctions were highest on HA/gelatin films with 0.8% and 2.0% Extralink (Figure 7.4.E). We note that these results, and the results described below, were obtained for our cell culture models under static conditions and in the absence of other BBB cells such as astrocytes and pericytes; we discuss these limitations further in the Discussion section below.

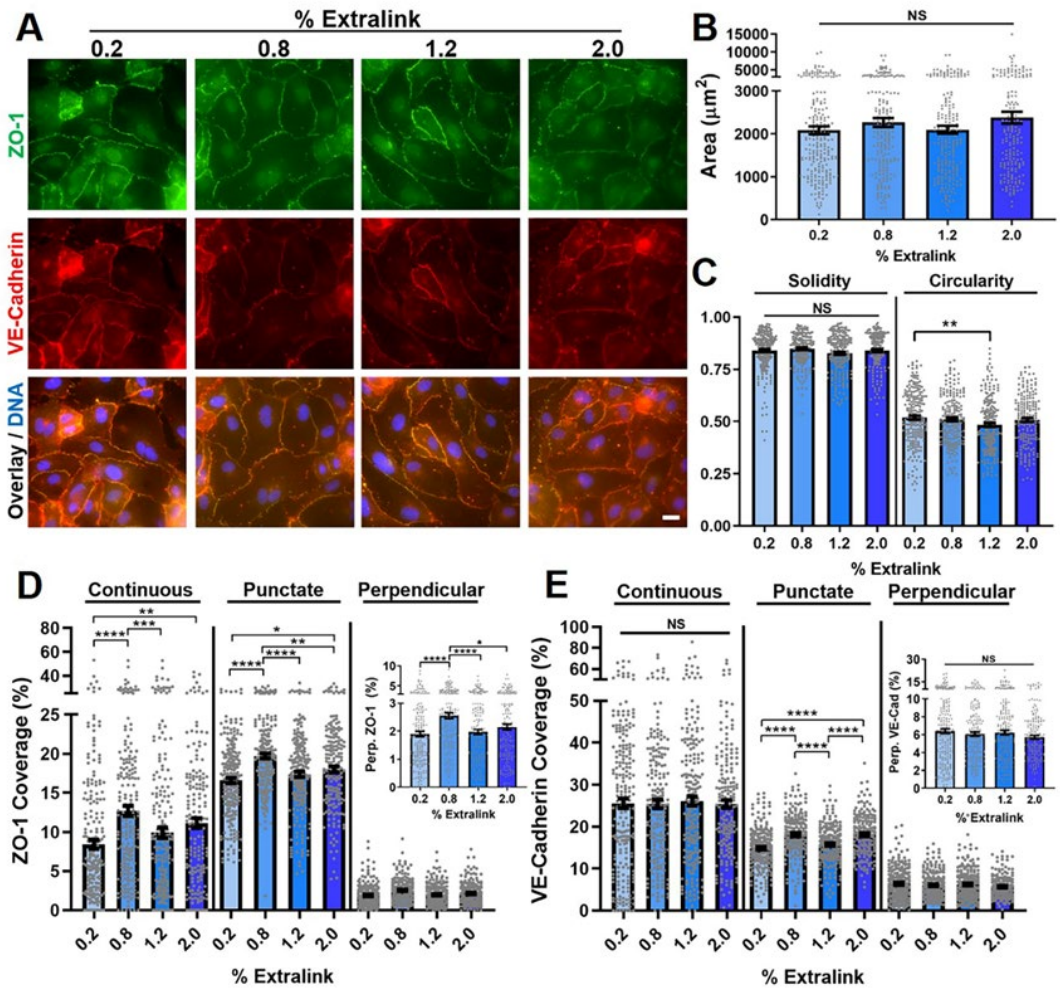

Figure 7.4: HBMEC morphology and junction presentation on HA/gelatin films with varying degrees of crosslinking. A) Immunofluorescence images of HBMECs immunostained for ZO-1 (green) and VE-cadherin (red) on HA/gelatin films with 0.2, 0.8, 1.2, and 2% Extralink. Scale bar on bottom right image is 20 μm and applies to all images in this panel. B) Area and C) solidity and circularity on HA/gelatin films with varying Extralink. The percent of the cell edge presenting continuous, punctate, and perpendicular junction for D) ZO-1 and E) VE-cadherin. The inset graphs depict the same perpendicular results, zoomed in to improve visibility. B-E: $182 \leq N \leq 223$, where N is the number of cells. A non-parametric Kruskal-Wallis ANOVA with a Dunn's multiple comparisons test was used for statistical analysis to compare results within each morphological parameter or junction type (*$P \leq 0.05$, **$P \leq 0.01$, ***$P \leq 0.001$, ****$P \leq 0.0001$, NS $P > 0.05$). All error bars represent standard error of the mean and dots for panels B-E represent values for individual cells.

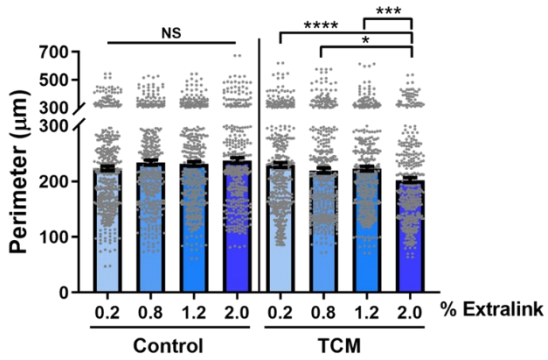

Figure 7.5: Effect of Extralink concentration and TCM treatment on HBMEC perimeter. HBMEC perimeters on HA/gelatin films with 0.2, 0.8, 1.2, and 2% Extralink treated with control medium or TCM. A non-parametric Kruskal-Wallis ANOVA with a Dunn's multiple comparisons test was used for statistical analysis to compare results within each treatment group (**P ≤ 0.01, NS P > 0.05)). All error bars represent standard error of the mean and dots represent values for individual cells.

7.3.3 Tumor conditioned medium alters HBMEC junction presentation

To understand the effects of biochemical signaling between HBMECs and metastatic tumor cells, and how these signaling effects may be modulated by HA/gelatin matrix crosslinking, we treated HBMECs with TCM. TCM-treated HBMECs presented visually thick, continuously connected junctions with a largely jagged morphology (Figure 7.6.A). The cells were smallest on HA/gelatin films made with 2.0% Extralink (Figures 7.4.B, 7.5 and 7.6.B) and were significantly smaller than HBMECs not treated with TCM on 0.8% and 2.0% Extralink. However, no changes in circularity or solidity were observed between Extralink concentrations or due to TCM treatment (Figures 7.4.C and 7.6.C). While no apparent trend was observed for VE-cadherin junctions on varying Extralink films in response to TCM, ZO-1 junctions generally decreased with increased Extralink, except continuous junctions on 0.2% (Figure 7.6.D,E).

Figure 7.6 (Next Page): TCM-treated HBMEC morphology and junction presentation on HA/gelatin films with varying degrees of crosslinking. A) Immunofluorescence images of HBMECs treated with TCM on HA/gelatin films with 0.2, 0.8, 1.2, and 2% Extralink. Scale bar on bottom right image is 20 μm and applies to all images in this panel. B) Area and C) solidity and circularity on HA/gelatin films with varying Extralink. The percent of the cell edge presenting continuous, punctate, and perpendicular junction for D) ZO-1 and E) VE-cadherin. The inset graphs depict the same perpendicular junction results but zoomed in to improve visibility. B-E: $195 \leq N \leq 224$, where N is the number of cells. The percent difference of F) ZO-1 and G) VE-cadherin between TCM (Fig. 7.6.D,E) and TCM-free (Fig. 7.4.D,E) for each junction type. F-G: N=3, where N is the number of trials. Legend in panel G applies to panels F and G. The colored dotted lines represent the linear regression (Lin. Reg.) of each respective junction type. The tip-to-tip distance (TipDist.) of H) ZO-1 and I) VE-cadherin, where the dotted and solid lines represent the linear regression of the TCM-free and TCM conditions, respectively. H-I: $86 \leq N \leq 129$, where N is the number of cells. Legend in panel I applies to panels H and I. A non-parametric Kruskal-Wallis ANOVA with a Dunn's multiple comparisons test was used for statistical analysis to compare results within each morphological parameter or junction type (*$P \leq 0.05$, **$P \leq 0.01$, ***$P \leq 0.001$, ****$P \leq 0.0001$, NS $P > 0.05$). For F-G, statistics represent the difference between TCM and TCM-free conditions presented in Fig 5D-E and Fig 4D-E, respectively, calculated using a Mann-Whitney test for each condition. For H-I, statistics represent the difference between TCM versus TCM-free results for each junction type at the respective Extralink concentration within the respective graph. All error bars represent standard error of the mean and dots for panels B-E represent values for individual cells. Linear regression statistical analysis rendered all fits non-significantly non-zero.

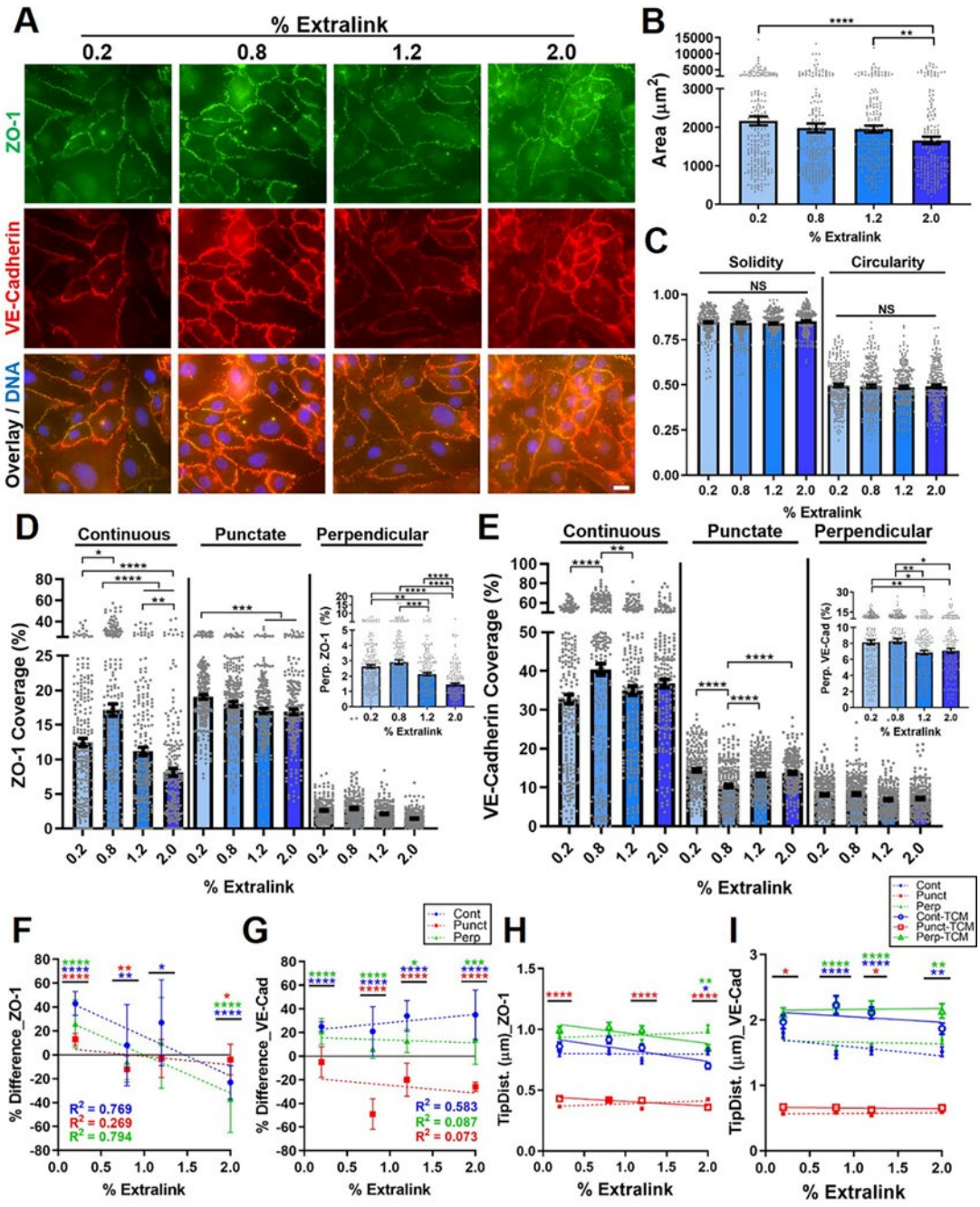

To investigate the specific effects of TCM treatment on HBMEC junctional protein presentation, we calculated the percent difference between the TCM (Figure 7.6.D,E) and TCM-free conditions (Figure 7.4.D,E) for each HBMEC junction type and film composition. For ZO-1, TCM treatment increased continuous junction

presentation on all films except on the film with the highest Extralink concentration. A linear fit (slope = -33.0 % Difference / % Extralink, $R^2 = 0.769$) suggests a decreasing trend with increasing Extralink concentration, though the slope was not significantly non-zero (Figure 7.6.F). While perpendicular junctions responded with a similar trend (slope = -31.7 % Difference / % Extralink, $R^2 = 0.794$, non-significant non-zero slope), punctate ZO-1 was much less sensitive to TCM (slope = -7.2 % Difference / % Extralink, $R^2 = 0.269$, non-significant non-zero slope). For VE-cadherin, both continuous and perpendicular junctions increased with TCM for all film compositions, while punctate junctions generally decreased. The response of VE-cadherin junction presentation to TCM was even less affected by the Extralink concentration compared to ZO-1, as the slope of the continuous, perpendicular, and punctate linear regressions were -3.1, 6.7, and -2.8 % Difference / % Extralink, respectively, and all were non-significantly non-zero (Figure 7.6.G).

Though quantification of junction coverage provides insight into the localization of each junctional protein, it does not provide an explicit measure of junction thickness or "protrusion". We therefore analyzed the average tip-to-tip distance of each junction type to quantify the maximum distance the junction protruded from the cell edge for ZO-1 (Figure 7.6.H) and VE-cadherin (Figure 7.6.I). As expected, the punctate junctions (presented in red in Figure 7.6.H,I) had the smallest tip-to-tip distance compared to continuous and perpendicular junctions. For ZO-1 (Figure 7.6.H), the perpendicular junctions had the largest tip-to-tip distance. This is in line with our expectations, since by definition, perpendicular junctions protrude radially outward from the cell edge [258]. Minimal change in ZO-1 tip distance was

observed, except for punctate junctions which increased with TCM on all films except the 2.0% Extralink film. On the other hand, TCM increased the protrusion thickness of VE-cadherin junctions in nearly every condition. Interestingly, the continuous and perpendicular junctions were nearly the same width, suggesting that the continuous junctions did not take the form of linear, mature junctions parallel to the cell border [15], rather protrusive perpendicular-like junctions that continuously presented themselves around the cell edge. Notably, the tip-to-tip distance of VE-cadherin was always greater than ZO-1 for each respective junction type. These results were in line with previous studies that reported manual width measurements of tight junctions (specifically, claudin-5) to be approximately 1 to 1.5 μm wide [83] and VE-cadherin junctions to be approximately 1 to 3 μm wide [161]. Overall, Extralink concentration did not affect the tip-to-tip distance results, since all the linear regression fits returned non-significantly non-zero slopes, though some significant differences did emerge between groups (Table 7.1).

ZO-1				
Continuous	0.15 kPa TCM	vs	2.1 kPa TCM	**
	0.75 kPa TCM	vs	2.1 kPa TCM	****
	1.4 kPa TCM	vs	2.1 kPa TCM	**
Punctate	0.15 kPa TCM	vs	2.1 kPa TCM	****
	0.75 kPa TCM	vs	2.1 kPa TCM	***
	1.4 kPa TCM	vs	2.1 kPa TCM	**
	0.15 kPa TCM-Free	vs	0.75 kPa TCM-Free	***
	0.15 kPa TCM-Free	vs	2.1 kPa TCM-Free	****
	0.75 kPa TCM-Free	vs	1.4 kPa TCM-Free	****
	1.4 kPa TCM-Free	vs	2.1 kPa TCM-Free	****
Perpendicular	0.15 kPa TCM	vs	2.1 kPa TCM	**
	0.75 kPa TCM	vs	2.1 kPa TCM	**
	1.4 kPa TCM	vs	2.1 kPa TCM	**
VE-cadherin				
Continuous	0.15 kPa TCM-Free	vs	0.75 kPa TCM-Free	*
	0.15 kPa TCM-Free	vs	2.1 kPa TCM-Free	*

Table 7.1: Statistical summary comparing the effect of Extralink concentration on junction tip-to-tip distance. A non-parametric Kruskal-Wallis ANOVA with a Dunn's multiple comparisons test was used for statistical analysis to compare results within each treatment group (****P ≤ 0.0001, ***P ≤ 0.001, *P ≤ 0.01, *P ≤ 0.05). Only groups with statistical differences are presented here.

Metastatic breast tumor cells secrete Vascular Endothelial Growth Factor (VEGF) which can disrupt or rearrange cell-cell junctions [256,257], or induce elevated expression of Angiopoietin-2 by endothelial cells, further weakening the monolayer [257]. To probe whether VEGF was playing a role in the junctional changes observed with TCM treatment, we first checked to see if VEGF was in fact present in the TCM produced by MDA-MB-231 cells. Using an ELISA, we found that VEGF was present in TCM at approximately 9000 pg/ml, a concentration significantly greater than the TCM-free control medium (approximately 3 pg/ml) (Figure 7.7.A). We therefore investigated the effects of inhibiting VEGF in TCM on junction presentation. To do this, we seeded HBMECs on HA/gelatin films composed of 0.8% Extralink. As expected, the HBMECs treated with the TCM control presented thick, jagged junctions (Figure 7.7.B), similar to those observed with TCM treatment (Figure 7.7.A). When VEGF was blocked, however, the junctions lost this perpendicular phenotype, and instead presented junctions resembling the TCM-free condition. Junction quantification showed a significant decrease in perpendicular junction coverage and thickness (Tip Dist.) for both ZO-1 (Figure 7.7.C,E) and VE-cadherin (Figure 7.7.D,F) with VEGF inhibition, but little to no significant difference between the anti-VEGF and TCM-free conditions. Furthermore, VEGF inhibition not only decreased continuous VE-cadherin coverage, but it also decreased the thickness of both continuous ZO-1 (Figure 7.7.E) and continuous VE-cadherin (Figure 7.7.F), verifying a shift from jagged junctions to the more linear phenotype observed in the absence of

TCM. Overall, these studies implicate tumor cell-secreted VEGF in the observed alterations in junctional appearance with TCM treatment.

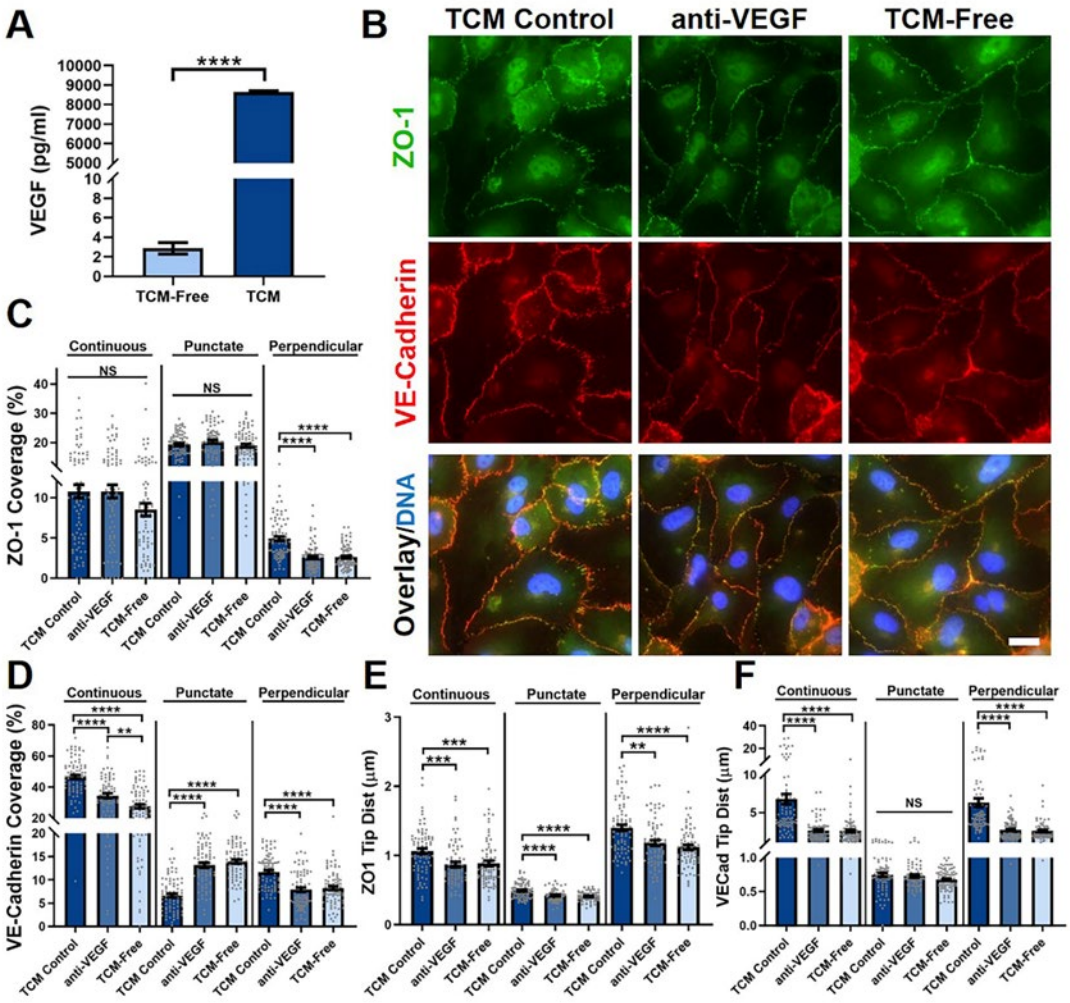

Figure 7.7: Role of tumor cell-secreted VEGF in HBMEC junction presentation. A) ELISA quantification of VEGF in TCM versus TCM-free control (N=3 biological replicates). B) Immunofluorescence images of HBMECs treated with TCM Control (TCM + isotype antibody), anti-VEGF (TCM + VEGF antibody), and TCM-Free control on 0.8% Extralink film. Scale bar on bottom right image is 20 μm and applies to all images in this panel. The percent of the cell edge presenting continuous, punctate, and perpendicular junction for C) ZO-1 and D) VE-cadherin. The tip-to-tip distance (Tip Dist) of E) ZO-1 and F) VE-cadherin. C-D: $77 \leq N \leq 82$ and E-F: $71 \leq N \leq 82$, where N is the number of cells. A t-test was used for statistical comparison for panel A, while a non-parametric Kruskal-Wallis ANOVA with a Dunn's multiple comparisons test was used for panels C-F to compare results within each junction type (*$P \leq 0.05$, **$P \leq 0.01$, ***$P \leq 0.001$, ****$P \leq 0.0001$, NS $P > 0.05$). All error bars represent standard error of the mean and dots for panels C-F represent values for individual cells.

7.3.4 MDA-MB-231 cells incorporate into HBMEC monolayers independently of HA/gelatin crosslinking

Because we observed that tumor cell-derived biochemical cues from TCM can alter HBMEC junction morphology, we next examined the effect of HA/gelatin film crosslinking on breast tumor cell incorporation into HBMEC monolayers. Phase contrast and fluorescence microscopy were used to evaluate CellTracker-stained MDA-MB-231 incorporation into HBMEC monolayers (Figure 7.8.A). We found no statistically significant difference in the percent incorporation of MDA-MB-231 cells into HBMECs (Figure 7.8.B) or in the time from the start of the time-lapse to complete incorporation (Figure 7.8.C) as a function of Extralink concentration. This was not surprising, since the alterations in HBMEC cell-cell junction presentation due to TCM-treatment were mostly not affected by the Extralink concentration of the underlying HA/gelatin films (Fig. 7.8.F-I). The cumulative percent of MDA-MB-231 cell incorporation, or percent of incorporation at each time point, was generally similar for all films, regardless of Extralink concentration under static conditions (Figure 7.8.D). Furthermore, we found that the plot of percent MDA-MB-231 cell incorporation at ~10 hours versus the average number of MDA-MB-231 cells at the start of the time-lapse had a slope that was not significantly non-zero (Figure 7.8.E).

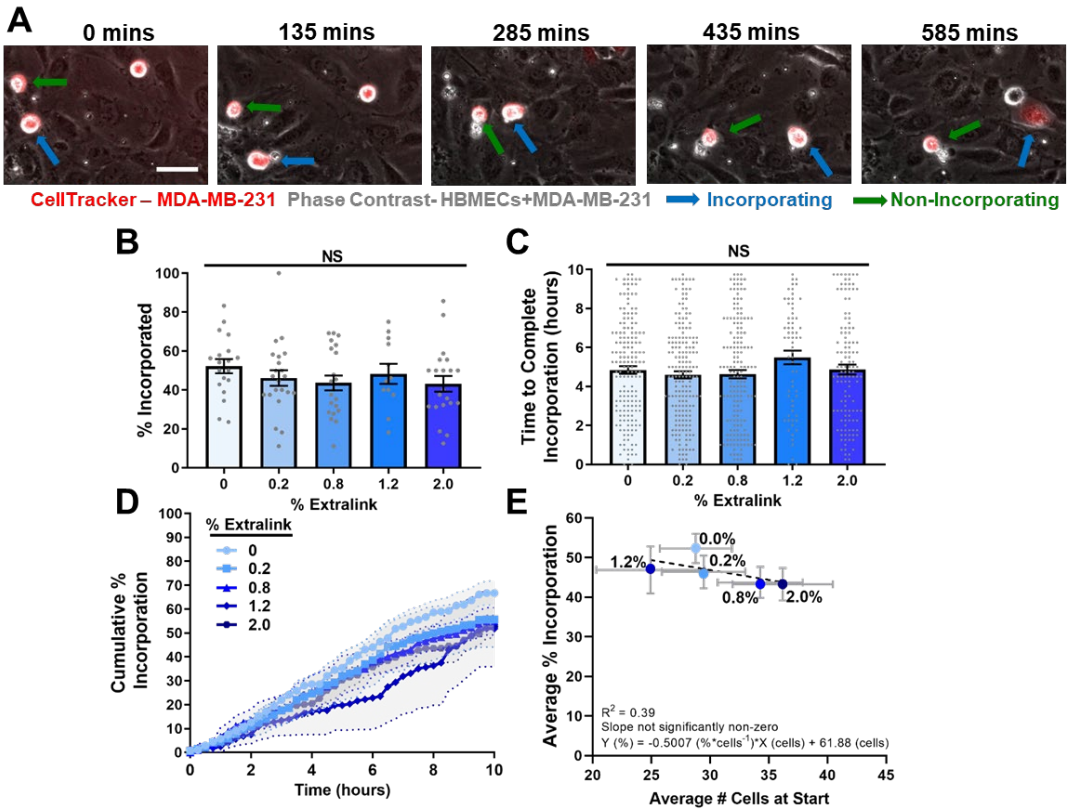

Figure 7.8: MDA-MB-231 cell incorporation into HBMEC monolayers on HA/gelatin films with varying degrees of crosslinking. A) Phase contrast images of an incorporating (blue arrow) and a non-incorporating (green arrow) CellTracker-stained MDA-MB-231 cell (red) on an HBMEC monolayer. B) Percent of MDA-MB-231 cells that incorporate ($12 \leq N \leq 22$, where N is the number of time-lapse sequences analyzed per condition), C) time from start of time-lapse to full incorporation of MDA-MB-231 cells, and D) the cumulative percent incorporation of MDA-MB-231 cells over time ($65 \leq N \leq 184$, where N is the number of incorporating cells) into HBMEC monolayers on HA/gelatin films with 0, 0.2, 0.8, 1.2, and 2% Extralink in a total time of 9.75 hours. E) Average percent incorporation as a function of the number of MDA-MB-231 cells in frame at the start of the time-lapse. For panels B and C, $P > 0.05$ via a non-parametric Kruskal-Wallis ANOVA test with a Dunn's multiple comparison post-hoc test between all groups. All error bars represent standard error of the mean. All data is pooled from three independent trials. Data collection, analysis, and figure preparation was performed by Marina A. Pranda, with the help of Ariana DeCastro and Greg Dawson (Stroka Lab).

7.4 Discussion

ECM crosslinking and stiffness are known regulators of many cellular functions in the context of physiologic and pathologic conditions. In this work, we explored the effects of HA crosslinking on metastatic breast tumor cell migration and incorporation into the human brain endothelium. Interestingly, our results showing reduced spreading area and more diffuse stress fibers for cells on more crosslinked and stiffer HA/gelatin films is contradictory to frequent reports in literature, including our own, where cells spread more on stiffer ECM-coated polyacrylamide gels [287–289]. Similarly, previous studies have shown that when utilizing HA-methacrylate gels crosslinked with dithiothreitol (DTT) and functionalized with Arg-Gly-Asp (RGD) peptides for cell adhesion, increasing HA weight percent and crosslinking density, thus increasing stiffness, increased the spreading area and speed of glioblastoma cells [290]. Also in opposition to our studies, Narkhede *et al.* found that increasing the concentration of DTT crosslinker in a methacrylated HA system coated with integrin binding proteins increased the cell area and speed of MDA-MB-231-BR cells, the brain-seeking clone of the parental MDA-MB-231 cells [291]. Notably, the work by Narkhede *et al.* was performed on HA gels formulated with different molecular weights, using a different mechanism of crosslinking, and with various coatings for cell adhesion, rather than gelatin incorporation as was used here. On the other hand, through chemical rather than mechanical signaling, soft HA gels can produce identical cellular responses to those on stiffer substrates [292]. Hence, mechanosensitivity in this context likely involves a delicate balance between sensing of multiple parameters of the ECM, including

stiffness, method and degree of crosslinking, method of adhesion molecule incorporation, and the specific composition of the matrix.

Our results suggest that HBMECs are less sensitive to the range of HA/gelatin crosslinking relative to MDA-MB-231 cells. This was not surprising, given that the measured Young's modulus of the films was in the relatively small range of 0.85 to 3.8 kPa. In Chapter 6, we showed that HBMEC morphology is sensitive to large differences in substrate stiffness (e.g., 194 kPa versus approximately 50 GPa) but not to smaller ranges of stiffness (e.g., 1-194 kPa) [215]. Thus, from a mechanobiological perspective, the result that HBMEC morphology was not altered as a function of the Extralink concentrations is consistent with our expectations. The increase in overall ZO-1 presentation on the film made with 0.8% Extralink, including increased continuous junctions, suggests that the tight junctions of monolayers on this film composition may be more mature than those on the other films tested.

Altogether, TCM minimally affected HBMEC size but altered ZO-1 and VE-cadherin junctional presentation to a more continuous and perpendicular morphology under static conditions. Importantly, this increase in continuous junctions with TCM took the form of a jagged, zipper-like phenotype rather than a linear, mature continuous junction. This junctional data suggests that TCM treatment results in a shift of the monolayers to a less mature state, which appears to occur independently of matrix crosslinking. This shift in monolayer maturity was not surprising, since many reports have shown that metastatic breast tumor cell-secreted biochemical factors, such as VEGF, are capable of altering endothelial cells [256,257]. Our results indicate that VEGF is in fact present in the TCM and that inhibiting its activity within TCM blocks

the shift in junction presentation from a linear morphology to more perpendicular phenotype observed with TCM treatment. This is consistent with previous reports that VEGF induces a serrated junction presentation in HBMECs [256]. Notably, most reports of junctional analysis rely on qualitative observation, fluorescence intensity image analysis, or quantification of the protein expression levels throughout the cells. An added benefit of using the JAnaP is the ability to simultaneously and semi-automatically quantify cell morphological parameters as well as the junctional proteins as they are presented at the cell-cell junction, providing a unique measurement capability to quantitatively compare between the TCM and TCM-free groups and assess heterogeneities in junctional morphology across the monolayer using statistical analysis. Together, these results suggest that the biochemical factors (e.g., VEGF) secreted by MDA-MB-231 cells alter HBMEC junction presentation in a manner unaffected by the extent of crosslinking of the underlying HA/gelatin film. It will be interesting to further examine this effect in the presence of physiologic flow conditions and in the presence of astrocytes and/or pericytes.

Our results suggest a lack of correlation between the number of tumor cells in the area of observation and propensity to incorporate. We note that if a tumor cell interacted directly with a gap between HBMECs in the monolayer, it was not included in the analysis. Therefore, once a monolayer of HBMECs was present in the system, breast tumor cells appeared to be less sensitive to HA/gelatin matrix crosslinking than when they were on bare films. These results suggest that HA/gelatin crosslinking does not significantly affect tumor cell incorporation into HMBEC monolayers, and that matrix mechanics might become more important post-extravasation, since tumor cells

on the bare gels without HBMECs showed such dramatic differences in morphology and migration. Our observations for MDA-MB-231 cells incorporating into HBMEC monolayers on HA/gelatin films are also consistent with our previous results, where percent tumor cell incorporation into HUVECs was independent of polyacrylamide gel stiffness [293].

An important note to make is that HBMECs may be remodeling the underlying matrix and/or depositing new ECM, therefore masking the original mechanical properties of the HA/gelatin films to the incorporating tumor cells and altering their interactions with the matrix post-incorporation. Indeed, previous studies have demonstrated that ECs are capable of low levels of ECM deposition after just one day of culture in favorable conditions [294], and thus HBMEC-matrix remodeling is plausible during the three-day culture period. It is also possible that cell adhesion molecules linking tumor cells and HBMECs could physically alter the migratory capacity of tumor cells within an HBMEC monolayer.

While our experiments have provided interesting insights into the biochemical and physical interactions between tumor cells, the HA matrix, and the brain endothelium, we acknowledge several important limitations of our system. First, our model lacks other cell types present at the *in vivo* BBB, including astrocytes and pericytes. There is a growing body of literature [295,296] to support the hypothesis that the presence of these cells, and/or their secreted biochemical factors, would likely influence tumor cell migration and incorporation into the brain endothelium, cell-cell junctions in the HBMECs, and possibly also the ECM. Indeed, our own previous work has shown that astrocyte conditioned media applied to MDA-MB-231 cells directly, or

to their ECM only, can result in increased cell migration [275]. Secondly, our models lack physiologic flow conditions. Shear stresses in the brain capillaries of rodent models have been measured to be in the range of 20-40 dyne cm^{-2} [297], which can influence endothelial barrier function, cell migration, tumor cell adhesion, and tumor cell proliferation [298–302]. The JAnaP can already calculate cell aspect ratios, and the next iteration of the program should include a feature that calculates alignment of endothelial cells to the direction of flow. Another limitation of our model is the lack of cylindrical geometry, which can influence EC elongation in the presence of shear stress [303]. Incorporation of these additional cells and mechanical cues will continue to be important as the field develops benchmarks for BBB models.

7.5 Conclusion

We have shown that MDA-MB-231 (but not HBMEC) morphology and migration parameters are sensitive to the crosslinking density of HA/gelatin films, with a trend that is opposite of that typically observed for varying stiffness of ECM-coated polyacrylamide gels. Meanwhile, our novel JAnaP was used to quantify modest alterations in HBMEC tight and adherens junctions as a function of HA/gelatin crosslinking density. In addition, we found that tumor cell-secreted factors (e.g., VEGF) led to increased presentation of immature adherens junctions, but minimally affected tight junction presentation. HA/gelatin crosslinking, however, did not seem to affect MDA-MB-231 cell incorporation into HBMEC monolayers. Overall, our quantitative results suggest that a combination of biochemical and physical factors promote tumor cell migration through the brain endothelium and suggest that ECM mechanics may become most significant once incorporation or transmigration is

complete. Future work will continue to build upon these results by incorporating more cellular components and mechanical cues into the experimental *in vitro* models.

Chapter 8 - Summary and Conclusions

The cell-cell junctions of the endothelium, and especially the BBB, play a major role in heath and disease progression. A vast amount of work has been dedicated to understanding EC barrier properties and their relation to junctional protein expression. However, these relationships have been based primarily on qualitative and correlative observations, with little quantitative data regarding the localized junctional protein patterns. Here, we developed a program to compute junction presentations within EC monolayers and used it to understand the influence of junction phenotype on barrier permeability. Furthermore, we assessed junction presentation in brain ECs, probing the role of substrate stiffness and cell contractility, as well as the effects of breast cancer cell secreted factors, highlighting examples of physiological and pathophysiological applications for which this tool could be valuable.

8.1 JAnaP Enables Junction Phenotyping

Here, we have established standardized junction phenotypes for continuous (linear and non-linear forms), perpendicular, and punctate patterns, and have developed and validated a user-friendly platform to semi-automate the analysis and quantification of these images (discussed in Chapter 4). Furthermore, the program has been made accessible to other researchers in the community via the Stroka Lab GitHub account (https://github.com/StrokaLab/JAnaP) for practitioners to download and use, accompanied by a thorough user guide for novice users to follow. The program is able to measure the percent coverage of each junction type on a full-cell and per-cell basis, as well as the length and thickness (or protrusion) for each individual junction piece

analyzed. This occurs in a semi-automated fashion, requiring only that the user (1) identify a threshold value for each junction protein to be studied and (2) seed waypoints on each image to identify the cells of interest. Conveniently, the JAnaP has been developed to allow for the generated waypoints to be applied to the same image of a different immuno-stain, enabling the analysis of at least two proteins without the need for repeat waypointing. Together, this program allows for the detailed calculation of cell-cell junction patterns in an efficient manner, enabling the analysis of junction phenotypes to study mechanistic changes in conjunction with the assessment of endothelial cell barrier properties.

8.2 Discontinuous Junctions Increase Barrier Permeability

Development of the JAnaP enabled a streamlined method for junction phenotyping, enabling the mechanistic study of alterations in junction architecture on the barrier function of the endothelium. Our work in Chapter 5 highlights the capabilities of combining junction phenotyping with the assessment of barrier function for the mechanistic study of the BBB, and possibly other EC and epithelial barriers. The influence of cell culture parameters such as matrix protein coating, culture time, and cAMP treatment on cell and junction morphology was investigated, showing only minor differences between the protein coatings studied. cAMP treatment significantly increased continuous junctions and increasing cell culture time required increased cAMP treatment for comparable protein coverage observed in shorter experiments. A local permeability assay was used to account for spatial heterogeneity within the ECs and the monolayer, which uncovered a correlation between the area of a permeated region and the number of gaps with no junction coverage or discontinuous junction

coverage at the cell edge. This suggests that increased continuous junction presentation is associated with a less permeable barrier. These results, however, are only indicative of the permeability of the specific probe used, and therefore future work is needed to unveil the role of junction presentation, especially the differentiation between punctate and perpendicular junctions, on permeability of molecules of different size and charge, and of different cell types known to traverse the endothelium.

8.3 Substrates of Biomimetic Stiffness Increase Continuous Junctions

Given the prior evidence that cell contractility influences barrier function and junction protein localization, and that ECs can sense and respond to the mechanics of their underlying substrate through a contractility-mediated mechanism, we investigated the role of matrix stiffness and myosin II-mediated contractility on ZO-1 junction presentation in HBMECs in Chapter 6. Use of the JAnaP showed the highest percentage of mature junctions on the 1 kPa gels, which was the most physiologically relevant to the brain microenvironment and within the range of reported values for subendothelial matrix stiffness in the vasculature. This motivates the use of mechanical cues to mimic the mechanical environment of the *in vivo* system, suggesting it may be an effective approach to optimizing endothelial barrier properties for *in vitro* study. Future studies of the effects of these parameters on other tight junction proteins (e.g. claudins, occludins), however, is needed to fully understand the effects of substrate stiffness on barrier phenotype. Furthermore, additional experiments are needed to better understand the physiological role (e.g., local permeability to molecules and cells) of each junction presentation in the context of the BBB. Understanding what conditions (e.g., contractility states) influence specific junction presentation and how that affects barrier

properties could lead to the development of therapeutics capable of traversing the BBB for delivery to the brain or for diseases associated with BBB dysfunction.

8.4 Breast Cancer Cell-Secreted VEGF Increases Non-linear Junctions

Since breast cancer often metastasizes to the brain, and disruption of the BBB by cancer cells is associated with metastatic progression, the effects of breast cancer cell secreted factors on HBMEC junction presentation were investigated in Chapter 7. An HA/gelatin film of different crosslink density was used to mimic the brain microenvironment and probe the interplay of matrix crosslinking with tumor cell and HBMEC response. While tumor cells were found sensitive to the physical alterations of the matrix, HBMEC morphology and junction presentation remained unchanged. Interestingly, HA/gelatin crosslinking did not influence tumor incorporation into HBMEC monolayers, suggesting that matrix mechanics might become more important to the tumor cells post-extravasation. Analysis with the JAnaP revealed that tumor conditioned medium (TCM) increased presentation of immature adherens junctions, but minimally affected tight junction presentation, a response likely mediated through VEGF signaling. It will be interesting to further examine this effect in the presence of physiologic flow conditions and in the presence of astrocytes and/or pericytes. Overall, these results suggest that a combination of biochemical and physical factors promote tumor cell migration through the brain endothelium and highlight use of the JAnaP as a technique to probe junctional changes in a pathophysiological context, such as breast cancer metastasis to the brain.

8.5 Concluding Remarks

Overall, this dissertation advocates for the quantification of cell-cell junction phenotype within the endothelium and introduces a streamlined technique enabling the calculation of this parameter. Development of the JAnaP provides for the detailed measurement of junction patterns in an efficient manner, enabling the study of mechanistic changes in conjunction with the assessment of endothelial cell barrier properties. Results from its application in this dissertation have revealed insights into the effect of continuous versus discontinuous junction on barrier permeability, mechanobiology of brain ECs, and the response of brain ECs to biochemical cues involved in breast cancer metastasis. Future use of this program holds significant potential for physiological and pathophysiological study, and drug delivery applications.

8.6 Contributions to the field

8.6.1 Scientific Contributions

The work in this dissertation makes the following contributions to the understanding of brain endothelial function and cell-cell junction phenotype:

- Established criteria for junction categorization and developed the JAnaP program as a tool for junction quantification (Chapter 4);
- Disseminated JAnaP tool through GitHub site for public access, accompanied by a detailed user-guide for practitioners to follow (Appendix A);

- Established that HBMEC junction presentation is minimally affected by substrate protein coating but significantly affected by time in culture and treatment with cAMP supplements (Chapter 5);
- Adapted "XPerT" assay for fibronectin-based systems (Chapter 5);
- Established correlation between discontinuous VE-cadherin and ZO-1 junctions and barrier permeability (Chapter 5);
- Established quantifiable connection between HBMEC contractility and ZO-1 junction presentation (Chapter 6);
- Established that soft substrates of brain relevant stiffness induce the greatest continuous junction presentation relative to other gels of physiologically-relevant stiffness (Chapter 6);
- Established that while tumor cell migration is significantly affected by differences in the crosslinking of a brain-mimetic HA/Gtn matrix, HBMEC morphology and junction presentation are minimally influenced (Chapter 7);
- Established that MDA-MB-231 cells secrete biochemical factors that increase immature adherens junction presentation in HBMECs, likely mediated, at least in part, by VEGF-signaling pathways (Chapter 7);
- Established that the crosslinking of an HA/Gtn matrix underlying an HBMEC monolayer plays little role in the ability of tumor cells to incorporate into the cell layer – Result of Marina A. Pranda's work (Chapter 7).

8.6.2 Peer-Reviewed Journal Publications

Published manuscripts:

- M.A. Pranda+, **K.M. Gray+**, G.M. Dawson, A.J. Decastro, J.W. Jung, K.M. Stroka. Tumor cell mechanosensing during incorporation into a biomimetic blood-brain barrier microenvironment. *Cellular and Molecular Bioengineering* 12(5):455-480 (2019) (Invited Submission for Young Innovators Special Issue) (+, equal contribution)
- **K.M. Gray**, D. Katz, E.G. Brown, K.M. Stroka. Quantitative phenotyping of cell-cell junctions to evaluate ZO-1 presentation in brain endothelial cells. *Annals of Biomedical Engineering* 47(7):1675-1687 (2019) DOI: 10.1007/s10439-019-02266-5
- C. Conrad, **K.M. Gray,** K.M. Stroka, I. Rizvi, G. Scarcelli. Mechanical Characterization of 3D Ovarian Cancer Nodules using Brillouin Confocal Microscopy. *Cellular and Molecular Bioengineering* (2019) DOI: 10.1007/s12195-019-00570-7
- D.B. Patel+, **K.M. Gray+**, Y. Santharam, T.N. Lamichhane, K.M. Stroka, S.M. Jay. Impact of Cell Culture Parameters on Production and Vascularization Bioactivity of Mesenchymal Stem Cell-Derived Extracellular Vesicles. *Bioengineering & Translational Medicine 2:170-179* (2017) DOI: 10.1002/btm2.10065 **(**Ranked top 20 most downloaded article in journal 2017-2018) (+, equal contribution)
- **K.M. Gray**, K.M. Stroka. Vascular Endothelial Cell Mechanosensing via Biomimetic Microfluidic Models. *Seminars in Cell and Developmental Biology* 71:106-117 (2017) (Invited Review, Mechanosensing themed issue) DOI: 10.1016/j.semcdb.2017.06.002

Manuscripts in preparation:

- **K.M. Gray**, J.W. Jung, C. Inglut, H. Huang, K.M. Stroka. Relating brain endothelial cell-cell junction phenotype to global and local barrier properties under varied cell culture conditions. (In Preparation, 2019)

- C. Inglut, **K.M. Gray**, J.W. Jung, J. Stabile, K.M. Stroka, H. Huang. Effects of Photodynamic Therapy on Brain Endothelial Cell Junction Phenotype. (In Progress, 2019)
- J. Li, **K.M. Gray**, C. Conrad, G. Scarcelli, K.M. Stroka, G.F. Payne. Mediated Electrochemical Fabrication: Mimicking Oxidative Crosslinking in Matrix Assembly (In Preparation, 2019)

8.6.3 National and International Conference Presentations

(* indicates presenting author)

- **K.M. Gray***, J.W. Jung, K.M. Stroka. *Quantifying brain endothelial cell-cell junction presentation: Investigating the role of cyclic-AMP and substrate composition* (poster, Cerebral Vascular Biology 13th International, June 2019, Miami, FL)
- M.A. Pranda*, **K.M. Gray**, N. Girma, K.M. Stroka. *Phenotyping of Metastatic Breast Tumor Cell Clones Based on Metastatic Site* (poster, American Association for the Advancement of Research Annual Meeting, February 2019, Washington, DC)
- **K.M. Gray***, D.B. Katz, E.G. Brown, K.M. Stroka. *Quantifying the Presentation of Cell-Cell Junctions: Evaluating the Mechanobiology of Brain Endothelium* (talk, Biomedical Engineering Society Annual Meeting, October 2018, Atlanta, GA)
- M. Shumakovich Pranda*, **K.M. Gray**, G.M. Dawson, K.M. Stroka. *Effect of Extracellular Matrix Crosslinking on Tumor Cell Migration and Transmigration* (talk, Biomedical Engineering Annual Meeting, October 2018, Atlanta, GA)
- C. Conrad, **K.M. Gray*,** K.M. Stroka, I. Rizvi, G. Scarcelli. Mechanical Characterization of Ovarian Cancer Nodules using Brillouin Confocal Microscopy. (poster, Biomedical Engineering Society Annual Meeting, October 2018, Atlanta, GA)

- C. Conrad*, **K.M. Gray,** K.M. Stroka, I. Rizvi, G. Scarcelli. *Overcoming the Limitations of 3D Nodule Mechanical Analysis using Brillouin Confocal Microscopy.* (poster & spotlight talk, Goodbye Flat Biology Conference, September 2018, Berlin, Germany)
- C. Conrad*, **K.M. Gray,** K.M. Stroka, I. Rizvi, G. Scarcelli. *Evaluating Ovarian Cancer 3D Nodule Mechanical Properties Using Brillouin Confocal Microscopy*. (talk, Advances in Brillouin Light Scattering & BioBrillouin Meeting, September 2018, Perugia, IT)
- **K.M. Gray***, J. Li, G.F. Payne, K.M. Stroka. *Electrodeposition of PEG-Hyaluronan-Gelatin Hydrogels to Spatiotemporally Control Cell Matrices for Mechanobiological Study* (talk, Cellular and Molecular Bioengineering Annual Conference, January 2018, Key Largo, FL)
- M.A. Shumakovich*, G.M. Dawson, **K.M. Gray,** K.M. Stroka. *Engineered Hyaluronic Acid Matrices for Studying Unique Mechanobiology of Tumor Metastasis Across the Blood-Brain Barrier* (poster, Cellular and Molecular Bioengineering Annual Conference, January 2018, Key Largo, FL)
- **K.M. Gray***, S. Ghosh, K.M. Stroka. *One-step Clear Alginate Hydrogels Electrodeposited for Organ-on-chip Applications* (talk, Biomedical Engineering Society Annual Meeting, October 2017, Phoenix, AZ)
- D.B. Patel*, **K.M. Gray**, Y. Santharam, T.N. Lamichhane, Max J. Lerman, John P. Fisher, K.M. Stroka, S.M. Jay. *Enhanced Production of Therapeutic Mesenchymal Stem Cell Extracellular Vesicles via Control of Cell Culture Parameters (*poster, Biomedical Engineering Society Annual Meeting, October 2017, Phoenix, AZ)
- D.B. Patel*, **K.M. Gray**, Y. Santharam, T.N. Lamichhane, K.M. Stroka, S.M. Jay. *Assessing Cell Culture Parameters for Enhanced Bioactive Extracellular Vesicle*

Production (poster, International Society for Extracellular Vesicles, May 2017, Toronto, CA)

- **K.M. Gray***, E.G. Brown, S. Ghosh, K.M. Stroka. *Biomimetic Matrices for Blood-brain Barrier-on-chip: Potential for Microelectronics* (talk, Cellular and Molecular Bioengineering Annual Conference, January 2017, Big Island, HI)
- **K.M. Gray***, M.A. Shumakovich, E.G. Brown, K.M. Stroka. *Human Brain Endothelial Cells on Biomimetic substrates: Mechanobio-logical Response to Tumor Cells* (talk, American Society for Matrix Biology, November 2016, St. Petersburg, FL)
- **K.M. Gray**, M.A. Shumakovich, D.B. Katz, E.G. Brown, K.M. Stroka*. *Biomimetic Models to Study Cell Mechanobiology at the Blood-Brain Barrier* (talk, Biomedical Engineering Society Annual Meeting, October 2016, Minneapolis, MN)
- **K.M. Gray***, D.B. Katz, E.G. Brown, K.M. Stroka. *Mechanobiological Response of Human Brain Endothelium: Role of Cell Contractility in Tight Junction Expression* (talk, 19th International Symposium on Signal Transduction at the Blood-Brain Barriers, September 2016, Copenhagen, DK)
- Scheduled: J. Li*, **K.M. Gray**, K.M. Stroka, W.E. Bentley, G.F. Payne. *Mediated Electrochemical Biofabrication Mimicking Oxidative Matrix Assembly* (talk, International Conference on Biofabrication, October 2019, Columbus, OH)
- Scheduled: C. Inglut*, **K.M. Gray**, B. Gaitan, D. Najafali, J. Stabile, I. Lopez, J. Jung, N. Connolly, K.M. Stroka, G.H. Woodworth, Y. Chen, H.C. Huang. *Photodynamic Therapy for Brain Cancer: Tissue Penetration and Blood Brain Barrier Modulation* (talk, Biomedical Engineering Society Annual Meeting, October 2019, Philadelphia, PA)

Chapter 9 - Future Work and Outlook

The work in this dissertation has motivated several additional projects, many of which will contribute to a more comprehensive understanding of the functional role of junctional protein phenotypes in physiological and pathophysiological states of the endothelium. For example, this dissertation has only focused in the "snap shot" analysis of ZO-1, VE-cadherin, and claudin-5 in brain ECs within a static system. Analysis of several other junction proteins (e.g., Occludin, PECAM-1) could be performed to study the functional differences in presentation of each protein. Additionally, live-cell imaging could be used to study the dynamic changes of junction patterns in shear stress or co-culture systems (e.g., with astrocytes) as additional biomimetic parameters in our EC model. Several future projects that are motivated by the results presented in this dissertation are discussed below.

9.1 Other Endothelial or Epithelial Cells

As described in Chapter 2, most vascular (and lymphatic) endothelial cells express TJs and AJs. In this dissertation, we have focused on HBMECS, which over express these proteins. However, significant opportunity exists to expand the application of the JAnaP to study the junctions of ECs from other vascular or lymphatic beds. Several examples in the literature, including many references in this document, present different EC types with different junction patterns, such as HUVECs [27] and human lymphatic ECs (HLECs) [68]. Theoretically, the JAnaP could be expanded to any EC type to quantify their edge-localized junctions to study their basal presentation levels or changes resulting from diseases associated with their respective vascular bed.

Additionally, while epithelial cells do not express VE-cadherin or claudin-5, they do express many other junction proteins. Therefore, the application of the JAnaP to quantify epithelial junctions also hold significant promise. One example in which changes in junction architecture plays a significant role in epithelial cells is in the context of cancer [304]. Decreased expression of cell-cell adhesion molecules, and the switch of cadherin protein expression from epithelial cadherin (E-cadherin) to neural cadherin (N-cadherin), are two signs of epithelial-to-mesenchymal transition (EMT) [29,305]. EMT is the process by which epithelial cells gain a migratory and invasive phenotype and as such, is implicated in tumor progression. Therefore, understanding the changes in junction presentation of various proteins known to be upregulated or downregulated in the context of EMT could enable a more comprehensive understanding of the mechanisms implicated in cancer progression. Targeting the molecules and pathways associated with altered cell-cell junctions could provide the opportunity for therapeutic treatment, diagnosis and prognosis of different epithelial-derived cancer types [305].

9.2 Junction Dynamics

Cell-cell junctions are not static in nature. Instead, they are extremely dynamic structures that exhibit with a great level of plasticity, enabling their regulation of cellular response and function in various physiological and pathological processes [27]. Even in confluent and stable ECs, junction proteins exist in a state of dynamic equilibrium, consistently shutting between the plasma membrane and intracellular compartments [23,306]. While the JAnaP has provided key insights into the phenotypic presentation of junction protein at one point in time, providing helpful information

when comparing various experimental groups, expansion of this program to quantitatively capture the dynamic changes of junction patterns holds significant promise.

Preliminary studies of HBMEC junction dynamics have been performed using the JAnaP. Use of a VE-cadherin-GFP adenovirus (previously described [307], and generously gifted from Dr. William Luscinskas (Harvard Medical School)) in combination with fluorescence live-cell imaging (via 60x oil objective on an Olympus IX83 inverted microscope) has enabled the capture of time-lapse sequences of VE-cadherin junctions (Figure 9.1.A.top row). Analysis with the JAnaP provided the visualization (Figure 9.1.A.bottom row) and quantitation of the cell morphology (e.g., area, Figure 9.1.B) and junction coverage for each phenotype (Figure 9.1.C) per cell overtime. This enabled the analysis of junction dynamics such as the fluctuations in presentation, where coverage changes were calculated as the absolute value of the junction coverage at t2 minus the junction coverage at t1 (Figure 9.1.D). Preliminary analysis suggests that the total coverage and continuous junction coverage fluctuates about 4-5% every 5 minutes. Since continuous junctions covered more of the cell edge, we also quantified the coverage change with respect to the junction coverage for each category to gauge the relative changes (Figure 9.1.E). This was calculated as the absolute value of the junction coverage at t2 minus the junction coverage at t1, divided by the junction coverage at t1. This analysis indicated that while the edge coverage by punctate and perpendicular junctions was only changing about 2-3% every 5 minutes, these changes were reflecting about a 30% change in the presentation of these patterns, suggesting a more dynamic fluctuation. This makes sense since continuous junctions

are thought to be more stable and less dynamic than discontinuous junctions [15]. This example highlights the capabilities of using the JAnaP to study junctional protein dynamics. Expansion of this approach could enable further understanding of the dynamics associated with junction presentation at the basal level, and after exposure to various treatments that we have already shown to alter junction presentation in this dissertation (e.g., cAMP, blebbistatin, VEGF).

Future updates to the JAnaP could provide the opportunity for combination with other programs or tools to allow real-time multi-parametric data acquisition including junction phenotype. One such program could be the CellBorder Tracker (described in section 2.2.3), which currently tracks the edges of ECs within a monolayer over time for dynamic analysis [69]. Combining this capability with the JAnaP capability of phenotypic categorization and calculation could significantly streamline data collection and analysis. Additionally, use of the JAnaP in parallel with on-chip models with integrated TEER or permeability measurement, such as the systems described by Maherally et al., [205] and Genes et al., [59], could further permit not only real-time dynamic data acquisition, but also correlative evaluation of junction presentation and measurements of barrier integrity. Thus, the role of each junction presentation in barrier function could be more specifically deduced.

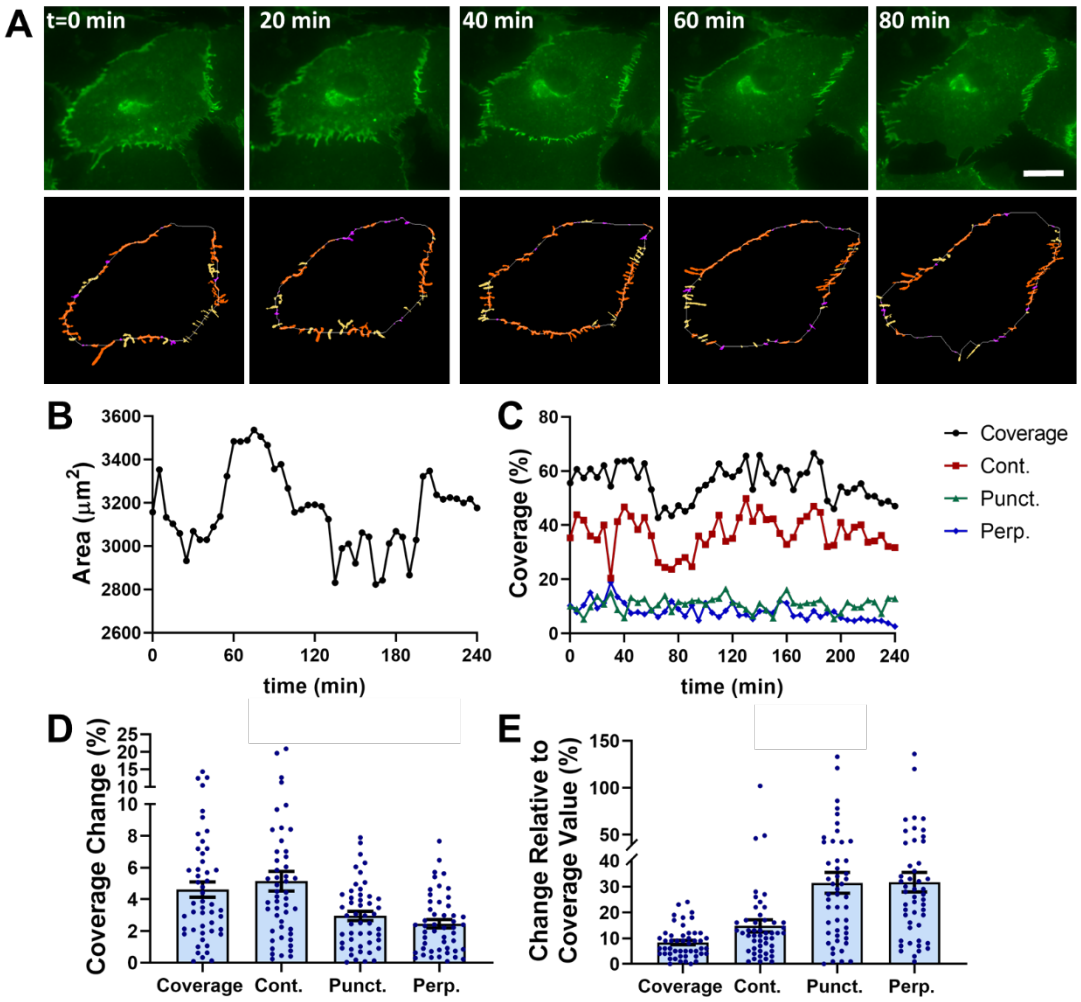

Figure 9.1 Dynamic VE-cadherin Junction Analysis. (A) The top row presents a few images from a time-lapse sequence of HBMECs transfected with VE-cadherin-GFP adenovirus. The bottom row depicts the corresponding image with the continuous (orange), punctate (purple) and perpendicular (yellow) junctions categorized by the JAnaP (scale bar = 20 μm). The cell area (B) and junction coverage (C) over time for the cell presented in (A). Images were collected every 5 minutes. (D) presents the change in junction coverage, taken as an absolute value for each junction category, while (E) presents the absolute junction change with respect to the junction presentation of that category. For D and E, N=49 where N is the number of time steps traced for the same cell presented in A-C.

9.3 Mechanical Cues

As described in Chapter 3, the mechanical cues of the cellular microenvironment can significantly affect EC behavior and function. As exemplified in Chapter 4, the alteration of junction protein presentation and localization can result from differences in subendothelial matrix stiffness. These, and most of the other experiments analyzed using the JAnaP, however, have been performed in static culture conditions. Thus, expanding the applications of the program to measure changes in junction patterning in response to various mechanical cues, especially those representing physiological and pathophysiological conditions, could provide further understanding of EC mechanobiology and mechanotransduction.

One example application for which the JAnaP could be used is to analyze images of ECs exposed to physiologic or pathological flow conditions using microfluidic devices such as those described in [139,225,308]. While increased junctional localization has been extensively previously described, the quantitative phenotypic analysis remains unknown. We would expect increased continuous junctions under physiological flows but that pathological shear would induce more discontinuous patterns. Particularly of interest would be the interplay of shear stress with additional cues such as substrate stiffness, [161] or astrocyte-conditioned medium, [308] which have been shown to alter EC behavior.

Another mechanical cue that would interesting to study is cellular stretching, which has been previously used to model traumatic brain injury [78,196] According to Wen et al., TBI is a major cause of mortality and disability in young people and as such, there is significant motivation to understand its side-effects [222]. Studies

involving TBI have shown decreased in junctional protein following the injury. As such, using the JAnaP to understand the time-course changes in junction presentation post-injury and how that affects the permeability and inflammatory responses could prove beneficial for mechanistic study to possibly inform therapies to combat this serious trauma.

Modification of the JAnaP to enable simultaneous analysis of cell angle (or chirality) [82] and junction angle [87] relative to flow would be another possibility for the future. These parameters have been described to influence junction presentation and barrier properties such as permeability. As such, correlating these parameters with junction patterns might help provide mechanistic insights into the mechanobiology influencing EC behavior under shear stress.

9.4 Force Transduction

Tissues in the body are continuously undergoing rearrangement, regulated by tightly balanced mechanical forces between cells [309]. This force transduction is mediated by cell-cell adhesions and plays an integral role in the development, maintenance, and adaptation of various tissues. ZO-1 is thought to be a central regulator of actomyosin organization influencing cell-cell tension, migration, angiogenesis, and barrier formation by regulating the tension acting on VE-cadherin [14]. Similarly, vinculin is thought to control force-dependent remodeling by associating with VE-cadherin in EC to modulate the pulling forces generated on focal adherens junctions via actomyosin contractility [54]. Several groups have therefore worked to quantify the force and tension across cell-cell junctions. Combination of these force-measuring

systems with the JAnaP could reveal the tension associated with each junction phenotype and the subsequent influence on cell behavior and function.

For example, Conway et al., developed tension sensors to measure the mechanical tension across VE-cadherin and PECAM-1 using förster resonance energy transfer (FRET) [310]. Use of these sensors in bovine ECs and HUVECs showed that junctional VE-cadherin experienced significant myosin-dependent tension in static conditions, but that shear stress triggered a decrease in VE-cadherin tension but an increase in junctional PECAM-1 tension. In other examples, groups used a combination of computational and experimental methods to quantify force transmission. In other examples using epithelial cells, cell proliferation was found to be regulated by forces across cell-cell junctions [309,311]. These studies used E-cadherin tension sensors in combination with traction force imbalance measurements (described in [312]) to show that at the sub-cellular level, basal force fluctuations were coupled with E-cadherin localization, but at the multi-cellular level, force exchange across the cell-cell junctions was dependent on the cell position. Furthermore, cells with lower E-cadherin force showed less proliferation, a phenomenon that was also found to be modulated by cell position (and substrate stiffness).

Therefore, it would be interesting to not only correlate junction presentation with tension measurement, but also integrate mechanical cues such as fluid shear to probe the interplay of these parameters. Combining these techniques with the JAnaP could enable sub-cellular and multi-cellular study with temporal and spatial resolution to systematically investigate the complex regulation of the homeostasis of mechanical stress in dynamic endothelial and epithelial tissues.

9.5 Transmigration of Cancer and Immune Cells

The infiltration of distal tissues by various cell types (e.g., cancer and immune cells) often requires the intravasation, and subsequent extravasation, of the vasculature. In Chapter 7, we described the incorporation of metastatic breast cancer cells into the brain endothelium; and the mechanisms used by different tumor cell types to cross various EC has previously been explored [228,265,313–316]. Additionally, the mechanisms involving neutrophil and leukocyte transendothelial migration have also been extensively studied [84,157,241,293,316–318]. Interestingly, many of the mechanisms implicated in the extravasation processes of the cells involved altered states of cellular contractility, where ECs become more contracted, and thus more permeable, in response to biochemical or biophysical cues exerted by the migratory cell type. In Chapter 6, we demonstrated the relation between cell contractility and junction presentation in HBMECs, showing increased discontinuous junctions in a contracted state. It would be interesting to perform live-cell imaging to visualize transmigration of different cell types across ECs with fluorescently-tagged junctions (e.g., via the VE-cadherin-GFP adenovirus described in section 9.2). Analysis of the captured images with the JAnaP could potentially provide information regarding junction presentation and transmigration location. It would be expected that the cells would permeate at sites of discontinuous junction, though in Chapter 5 we saw that not every discontinuous junction piece necessarily correlated with a permeable region. Therefore, performing these studies in conjunction with junction protein dynamics (section 9.2) to compare the rate-of-change of the junction patterns with the transmigration site might provide more mechanistic insight. Since we observed

junctional changes in response to cancer cell conditioned medium in Chapter 7, it would also be interesting to study junctions and transmigration after pre-exposure to biochemical cues secreted by the transmigrating cells. Combination of these transmigration studies with other biologically relevant biochemical cues (e.g., astrocytes at the BBB) and/or mechanical cues (section 9.3) could help to understand the mechanisms and mechanobiology involved transendothelial migration in both health and disease.

9.6 Quantitative Assessment for Drug Delivery

As explained in Chapters 1 and 2, the uniquely tight architecture of the BBB provides for tightly regulated transport control of substances into and out of the central nervous system. While this acts as a protective mechanism for the brain, it also acts as a barrier to the targeted delivery of therapeutics into the brain [199]. As such, significant effort has focused on the development of techniques to "open" the BBB for therapeutic delivery, including ultrasound,[197–199] photodynamic therapy,[200] and photothermal therapy [201]. Many of the methods in that literature describe disruption of the junctional protein structures to penetrate the barrier. Therefore, application of the JAnaP to compute a quantitative measure of the extent of junction disruption holds significant promise. For example, it could enable the development of dose-curves to understand the result of different doses of the respective treatment or penetration-technique on the junctional changes regulating the extent of therapeutic delivery.

As one example, we have worked in collaboration with Dr. Huang Chiao Huang's (University of Maryland) to study the effects of photodynamic therapy (PDT) as a method to modulate the junctions of the BBB to improve drug delivery for the

treatment of glioblastoma. Glioblastoma is a brain cancer that remains extremely hard to treat, leading to an unfortunate median patient survival rate of less than 18 months [319]. PDT is a method that uses light-activated photosensitizers (PS) to induce tissue injury or cell death. This technique has shown great promise for BBB-disruption and as a treatment for glioblastoma, extending the survival time up to 3-18 months longer in patients suffering from this disease [320]. Light activation of the PS generates reactive oxygen species (ROS) which can inflict damage on subcellular organelles such as mitochondria and the endoplasmic reticulum, motivating its use in conjunction with current cancer treatments such as chemotherapy, radiation, and thermal ablation [321]. Importantly, there is significant potential for the translation of this approach, since the photosensitizers, which emit a fluorescent signal, are currently used clinically as an imaging agent for the fluorescence-guided resection of high-grade gliomas [322].

Here, we investigated the effect of PDT with benzoporphyrin derivative (BPD) as a PS on HBMEC junctions. BPD has shown promise in pancreatic tumor mouse models, [323] and has been shown to decrease the expression of claudin-5 and VE-cadherin in peripheral ECs [324]. As expected, we observed decreased continuous VE-cadherin and ZO-1 with increased PDT treatment time, corresponding to 0, 0.006, 0.305, 0.61, and 1.22 J/cm^2, respectively (Figure 9.2). This was accompanied by an increase in perpendicular junctions while punctate junctions remained unaffected. Increased PDT treatment was also shown to increase permeability of HBMECs to 70 kDa dextran and liposomes (data not shown), likely due to the altered junction presentations observed. Future studies will focus on the ability of PDT to modulate paracellular permeability to increase the diffusion of chemotherapeutic-loaded

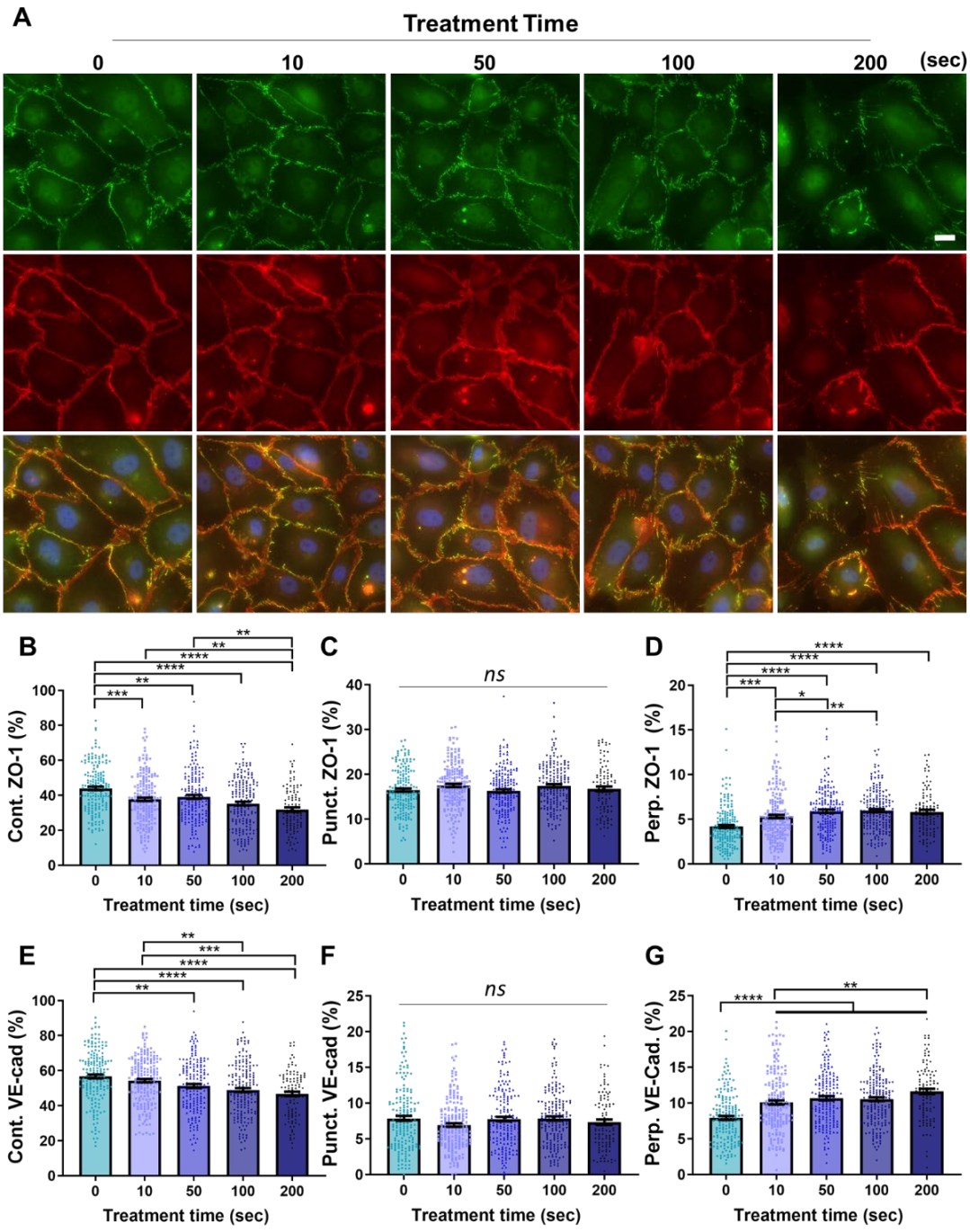

Figure 9.2 Photodynamic Therapy (PDT) of HBMEC Junctions. (A) Immunofluorescence images of HBMECs exposed to increasing PDT treatment (time, in seconds) stained for ZO-1 (green), VE-cadherin (red), and DNA (blue). Edge presentation of continuous, punctate, and perpendicular ZO-1 (B-D, respectively) and VE-cadherin (E-G, respectively). $105 \leq N \leq 195$, where N is the number of cells collected over 3 trials. The Kruskal-Wallis test with a Dunn's multiple comparison test was used to calculate significant differences for each parameter, where * $p < 0.05$, ** $p < 0.01$, *** $p < 0.001$, and **** $p < 0.0001$. (scale bar = 20 μm) The PDT treatment in this experiment was performed by Collin Inglut (Huang Lab).

liposomes across the HBMEC barrier for delivery to glioma cells in the bottom well of a Transwell setup. The JAnaP provides useful information into the junctional changes in response to PDT treatment and can inform the doses selected for efficient drug delivery. The above example illustrates just one application of the JAnaP and highlights the potential for evaluating numerous other drug delivery systems involving BBB- (and other EC-barrier) penetration by junction modulation.

9.7 *In Vivo* Study

While the applications of the JAnaP in this dissertation provide examples of the significant impact this program could have on the study of vascular endothelial cell-cell junctions, these studies have been confined to *in vitro* lab cultures. To confirm the significance of different junction protein presentations and their impact on disease progression, it is imperative that we also perform studies *in vivo*. The two most commonly used *in vivo* models to study the vascular system are rodents and zebrafish. While both systems provide dynamic, real-time imaging capabilities, zebrafish offer the added benefits of being optically transparent and available at a low cost for high-throughput studies [325]. Although both rodent and zebrafish models present varied homology for human application and require expertise for the respective animal/fish handling and maintenance, they do provide accurate evaluation of the complexity of vascular networks *in vivo*.

To visualize endothelial cells and their cell-cell junctions in mice and rats, fluorescence images of post-mortem extracted tissue is a common approach. Additionally, the isolation and reperfusion of vessels is also useful to study the endothelium and their associated transport/permeability properties [326]. This

approach enables treatment of the *ex vivo* vessels with various substances of interest, then subsequent assay or imaging to quantify or visualize changes in the barrier. JAnaP analysis could easily be integrated into this approach. While various live-imaging techniques such as positron emission tomography (PET), single-photon emission computed tomography (SPECT), and magnetic resonance imaging (MRI) enable the study of barrier transport properties, [325] their resolution for junction presentation visualization remains limited without invasive measures such as window placements. Nevertheless, thin window placement in conjunction with two-photon imaging has enabled the study of vascular permeability and transport properties, as well as the interaction of vessels with surrounding cell types. This approach offers the opportunity to visualize structural vascular parameters such as length and turnover of capillary segments, vascular network branch points, etc., [325,327,328].

In zebrafish, the inherent optical transparency enables easy visualization without the need for intrusive techniques. Additionally, these fish can be transgenically modified to uniformly express fluorescently-labeled vasculature [329]. Because adult zebrafish possess a BBB that is surprisingly similar to humans, including tight junction protein (e.g., ZO-1, claudin-5) expressing ECs,[330] this model has been especially useful for *in vivo* study of the BBB. Furthermore, zebrafish have been used to study the extravasation dynamics of metastatic tumor cells [329], and more recently, junctional tension across VE-cadherin junctions using tension sensors [87]. Interestingly, use of the tension sensors indicated decreased tension and increased junction linearity in maturing junctions, determined by the age of the zebrafish. This study specifically highlights the potential for combining these measurements with JAnaP quantification

of junction presentation to correlate junction patterns *in vivo.* Together these examples highlight the *in vivo* measurement capabilities associated with vascular structure and motivate the future evaluation of *in vivo* junction patterns using the JAnaP to confirm conclusions drawn from *in vitro* study.

9.8 Outlook

It is seemingly clear that the cell-cell junctions of the endothelial and epithelial cells lining the structures of the human body play a significant role in health and disease by modulating several aspects of cellular function. Combining many of the current quantification techniques to measure cell function and junction presentation hold significant promise for the study of the mechanisms underpinning these processes. Future understanding of the molecules and pathways involved offers important potential for therapeutic targets to correct the dysregulation implicated in disease progression. Furthermore, the expanded study of junction phenotyping could possibly provide predictive capabilities for disease, in cases of, for example, melanoma where subtypes of cancer cells are distinguished by their intercellular contacts [331]. The work in this dissertation has motivated the quantification of junction patterns, developed a tool to perform this measurement, and applied this approach to study EC physiology and pathophysiology. The field will benefit from future evaluation of junction phenotypes for different junction proteins, in other EC systems, and in various disease contexts.

Appendices

Appendix A. JAnaP User Guide

USER-GUIDE for the
Junction Analyzer Program (JAnaP)

Guide Author: Kelsey Gray, Cell and Microenvironment Engineering Lab,
University of Maryland
Version 1.2: 06/25/2019

Please refer to the following article for more information and/or cite
when using the JAnaP for published works:
Gray, K.M., Katz, D.B., Brown, E.G. et al. *Ann Biomed Eng* 47(7): 1675-1687(2019).
https://doi.org/10.1007/s10439-019-02266-5

For questions and feedback, please contact:

Dr. Kimberly Stroka
kstroka@umd.edu
Fischell Department of Bioengineering
University of Maryland, College Park

Image Requirements:

1) Image resolution must be 1024 x 1024 pixels or 2048 x 2048 pixels. Record the resolution of your images.

2) Record the image scale (i.e. pixels to µm conversion). This will be required in the "parameter" section for correct result calculations.

3) Images must be in tiff format.

4) When saving your images, consider naming the files in a consistent manner that includes the experimental conditions, the stain or fluorescence channel, the date, etc. These are all helpful as unique identifiers (i.e. "variants" or "dimensions") for processing and organization via the JAnaP.

5) Note that this program has been used and validated on images collected using a 60x oil objective. Ensure your images are taken with enough magnification to clearly see the edge-localized junctions.

Computer Requirements:

1) This current version of the user guide is for use on PCs.

Download Instructions:

1) Navigate to the JAnaP repository on GitHub at https://github.com/StrokaLab/JAnaP
2) Click "Clone or download" and select "Download ZIP"
3) Unzip the contents of the repository:
    - Right click on the downloaded zip file and select "Extract All."
    - Create Documents/GitHub folder on your PC and extract files to this location.
4) On Windows, run the "setup.bat" file located in the bin folder. This will install Python 2.7 and all of the required packages.
    - If you use virtualenv you can find the requirements.txt file in the bin folder
5) Run web application.py as described below

Program Instructions:

1) Open command prompt:
    - Click on windows/start icon (in bottom left corner of screen)

- Type “cmd” and select the “Command Prompt”

2) Within command prompt, navigate to folder containing “JAnaP-master”:
   - Within the command prompt type: cd Documents\GitHub\ JAnaP-master
   - Hit “Enter” then type: python web\application.py
   - Note: To stop the program, type “Ctrl+C” in the command prompt

3) Open web browser and type “127.0.0.1:5000”. The following screen should load:

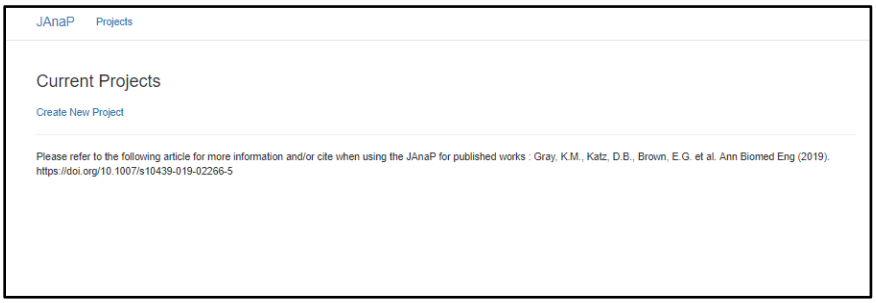

4) Click “Create New Project” and when the following screen appears, type in the name of the new project (e.g., Example Project) you would like to create and click “Save”

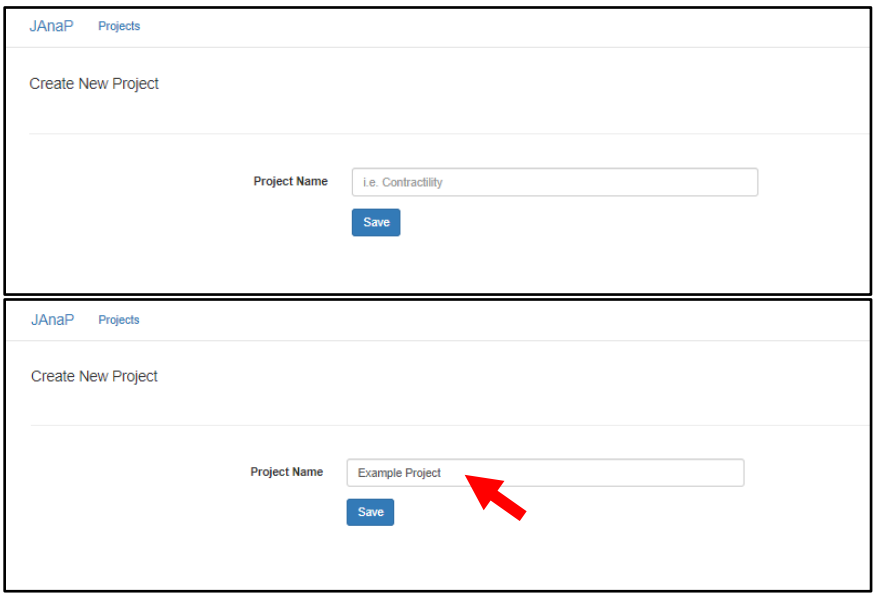

5) The following screen should load:

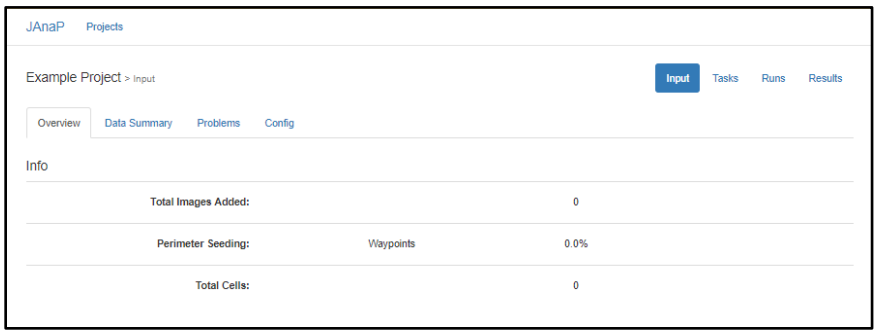

- NOTE: If you click on “JAnaP” the home page will re-appear, and your project will now be listed in the “Current Projects” list. Click on the link to your project to return to the screen above.

6) To load images into your project:
   - Navigate to the “projects” folder within the “JAnaP-master” folder on your computer
     - Documents > GitHub > JAnaP-master > data > projects

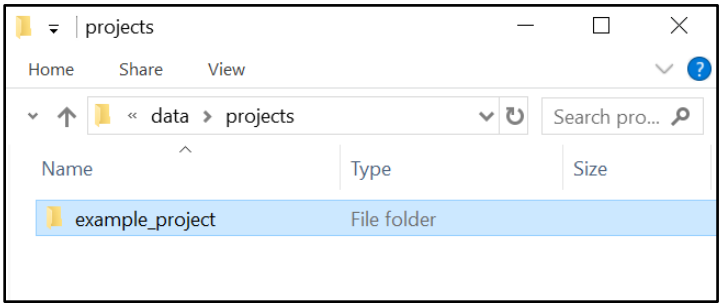

   - Select your project folder (e.g., “example_project”) and navigate to the “images” folder
     - example_project > input > images

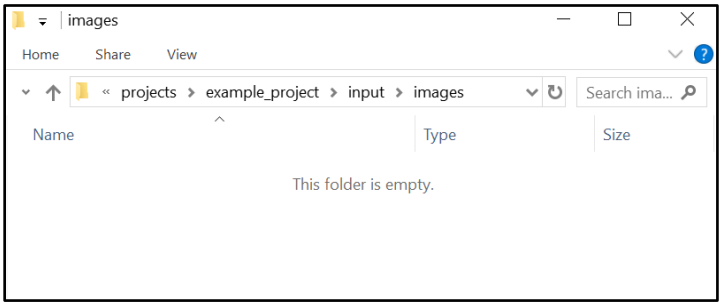

   - Drag and drop the images you would like included in your analysis into this folder. When you refresh your browser, your project should then reflect the total number of images added.
     - Here, 6 images were added into the example_project>input>images folder
     - Note: only tiff files should be uploaded

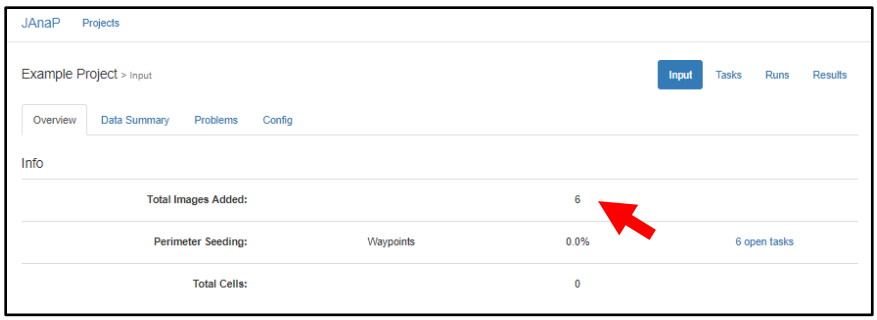

7) To select the cells of interest to be "waypointed" and analyzed, click "6 open task":
   - Note: This "6" value will change depending on the number of images in the "Total Images Added" section, the total number of "open" versus "done" tasks, and the "Variants" identified (described below).

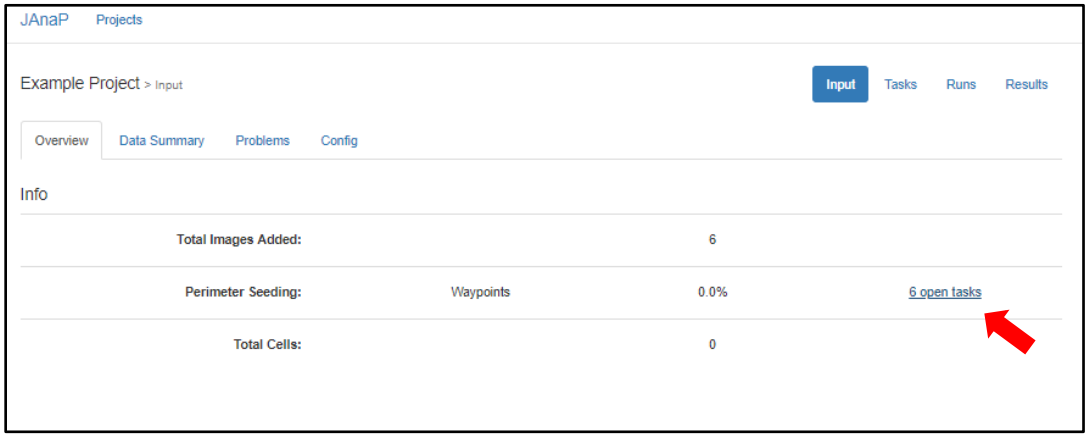

8) The following screen should appear, where the tab selected is "Open" tasks and the number of images listed should reflect the "# open tasks" listed on the previous screen:

9) Select "View Task" next to the image you would like to view and/or waypoint cells, and the following screen should appear presenting the image you selected:

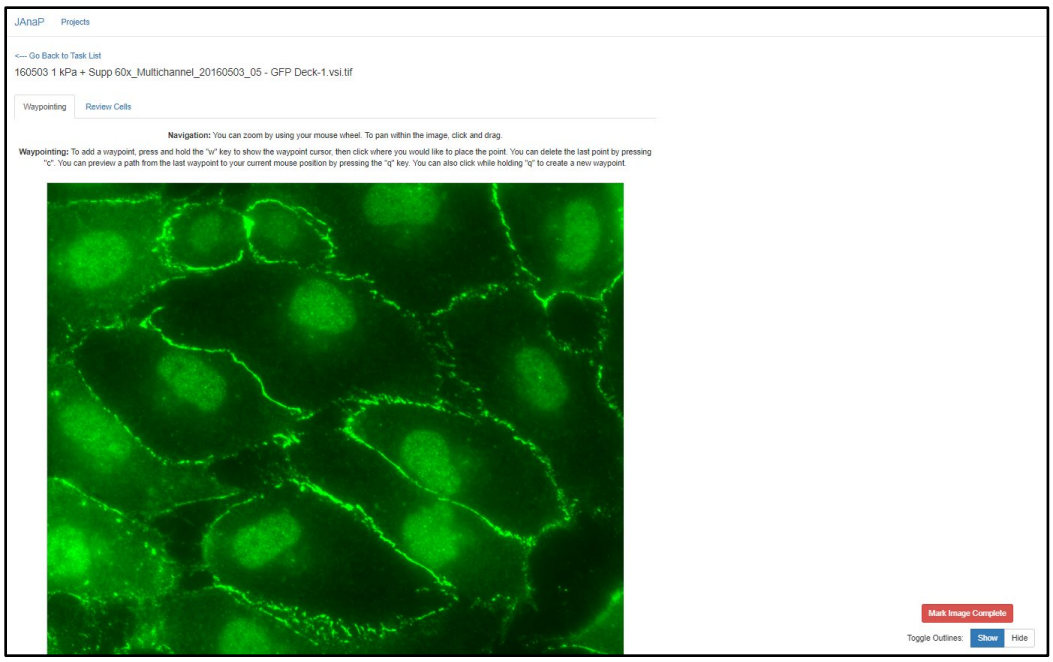

10) Under the "Waypointing" tab, you can begin waypointing each cell using the instructions on the page.
    - NOTE: A mouse should be used for waypointing (i.e., a laptop trackpad will likely not work)
    - Hold "q" and click on a spot in the perimeter of a cell.
    - Move your cursor to another spot on the perimeter while holding "q" and the connecting path should appear. If you agree with the connecting path, click on that spot to add it as a waypoint. Otherwise, move your cursor around the cell perimeter until you agree with the automated path.
    - Continue seeding waypoints until the entire cell perimeter is traced.
        - Number of waypoints – This depends on the cell, the amount of junction presentation, and the quality of staining. If a cell has mostly continuous junctions and/or the edge of the cell is very distinct relative the background, less waypoints are likely required. Try seeding a waypoint and then trace the edge with your mouse holding "q" for as long as the path accurately follows the cell edge. Once it begins to deviate, move your mouse back closer to the last waypoint to seed a waypoint where the path is accurate.
        - Use your best judgement when deciding the location of the cell perimeter when little to no stain is present around the cell edge. More waypoints will likely be required in this region.
    - If you misplace a waypoint, click "c" to remove the last waypoint seeded.

    In the following image, the circled cell has been fully waypointed. The cell path has been traced in white, and a zoomed-in cropped image has been added to help show the tracing (Note: this is for the user guide only, it will not appear this way in the GUI):

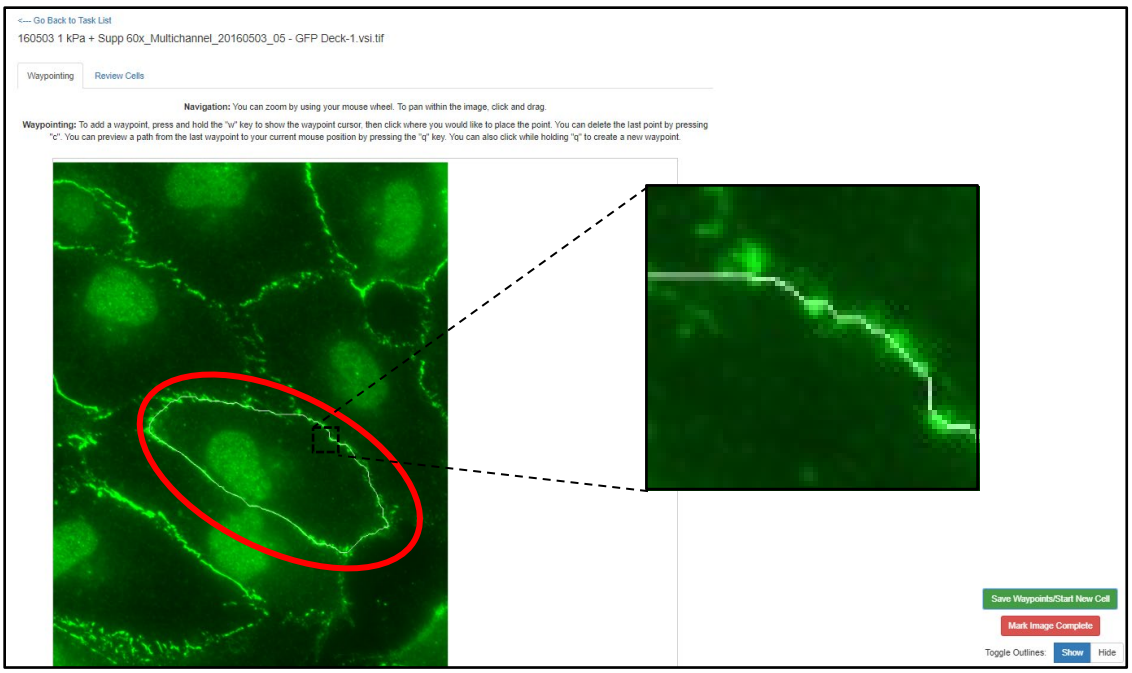

11) Click “Save Waypoints/Start New Cell” once the cell perimeter has been fully traced.

12) The image will reappear with a rough tracing (i.e. lines connecting the waypoints) of the waypointed cells in blue to indicate which have already been traced within that image.

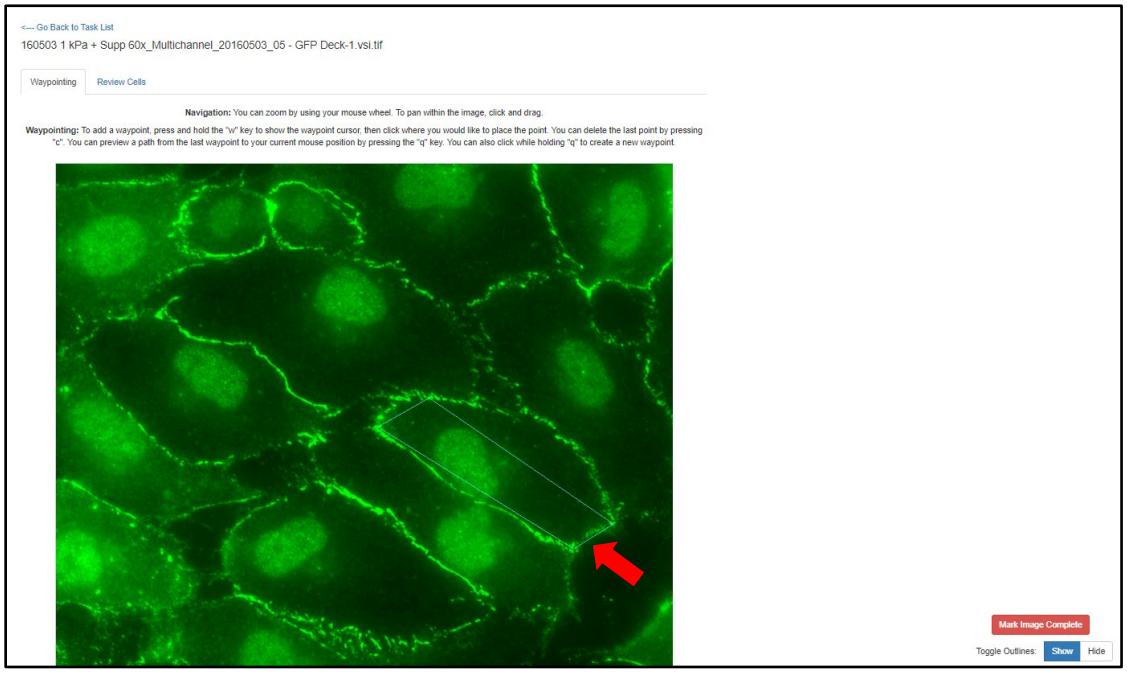

13) To view or remove previously waypointed cells, click the “Review Cells” tab. The list of traced cells will appear on the right side, designated by their center waypoints.

Here, you can click “show” to visualize the traced perimeter of each cell or click “Delete” to remove the waypoints associated with that cell.

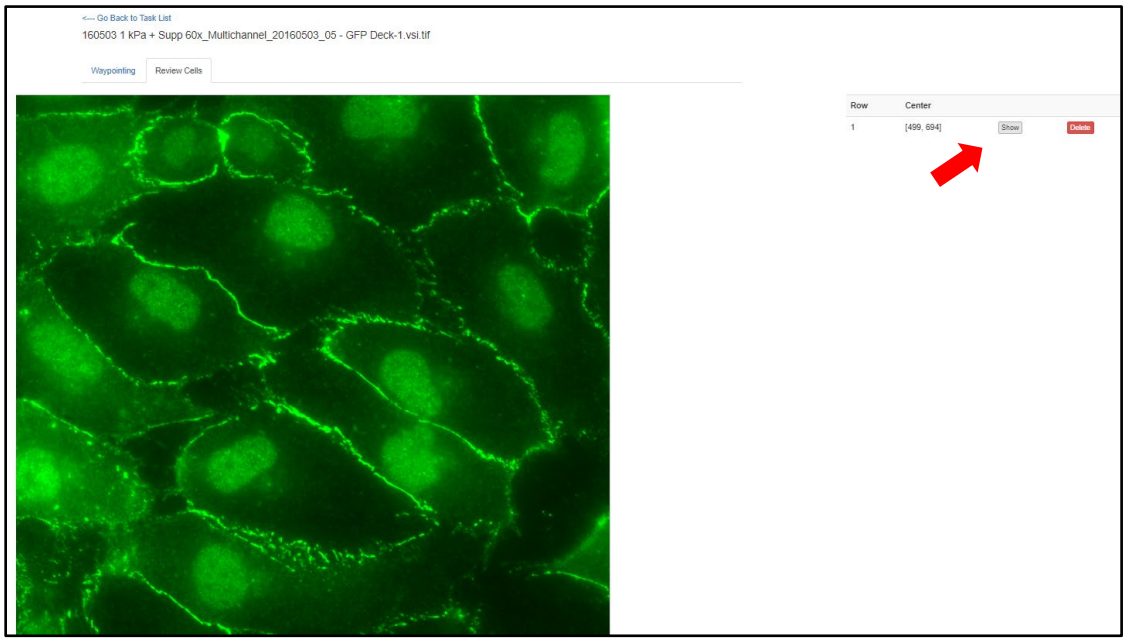

14) To navigate back to the “Tasks”, click “← Go Back to Task List” in the upper left corner. This will bring you to following screen:

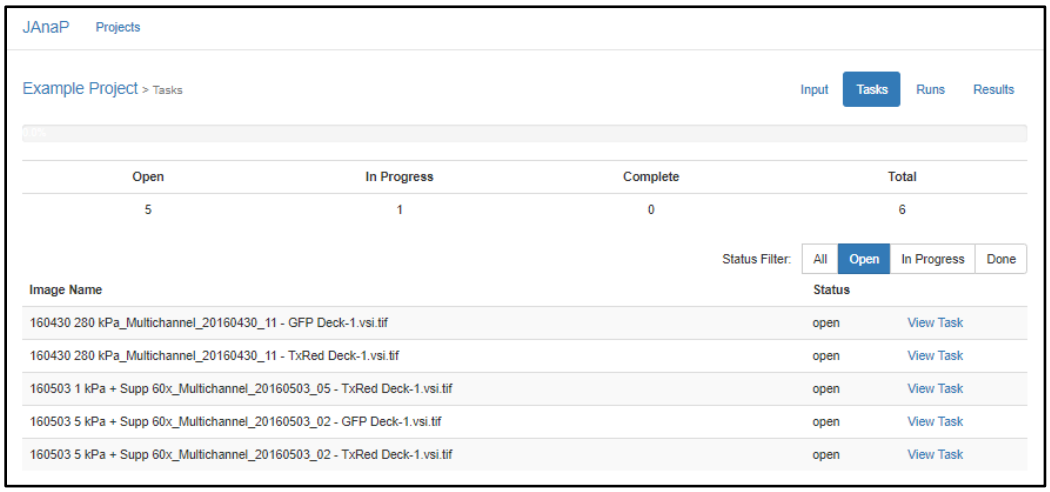

The remainder of the open tasks will be listed when the “Open” tab is selected, and the total tally should be reflected across the top of the page. Here, 5 images are still listed as open, but the one image that we have started is now listed as “In Progress”. When you click on the “In Progress” tab, all images that have been started will be listed:

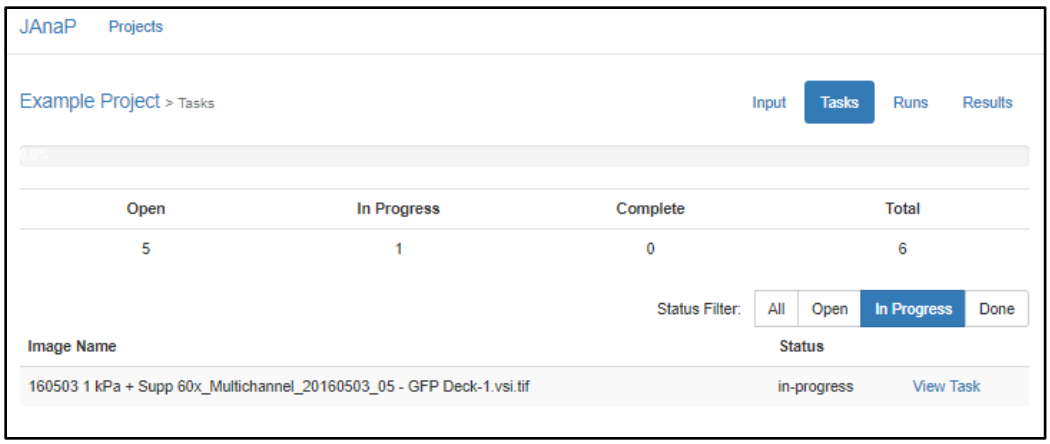

15) To continue waypointing the cells in any image in the "Open" or "In Progress" tab, click "View Task" and repeat steps 10-12.

- As an example, 3 cells have been traced here, each indicated by the blue outlines in the image below and listed in the "Review Cells" tab in the second image.

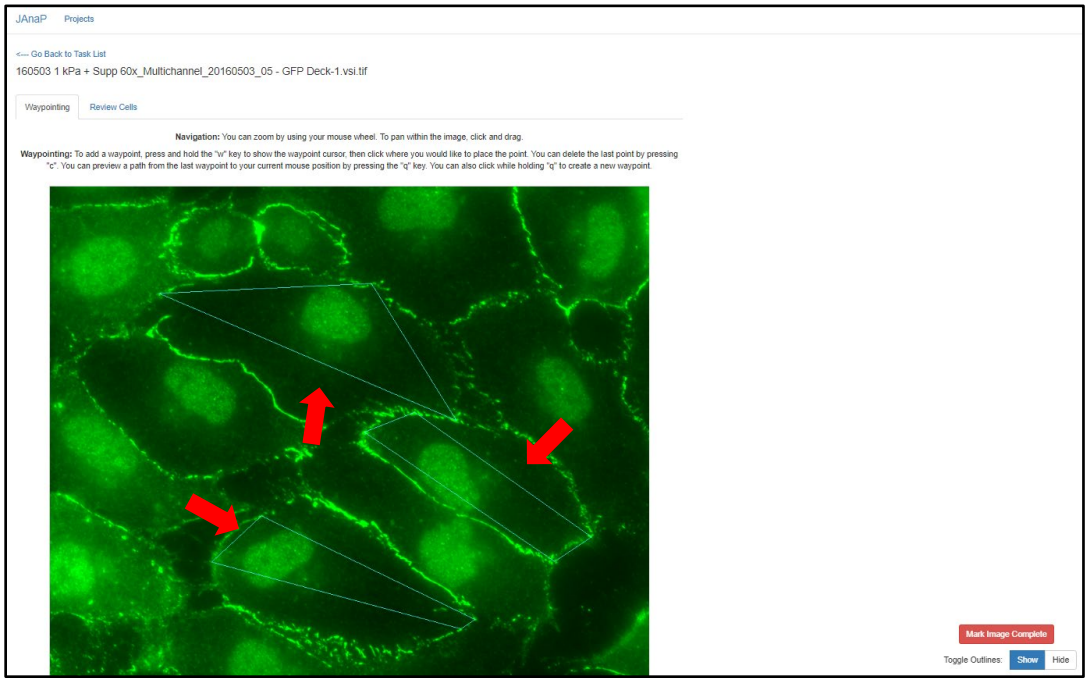

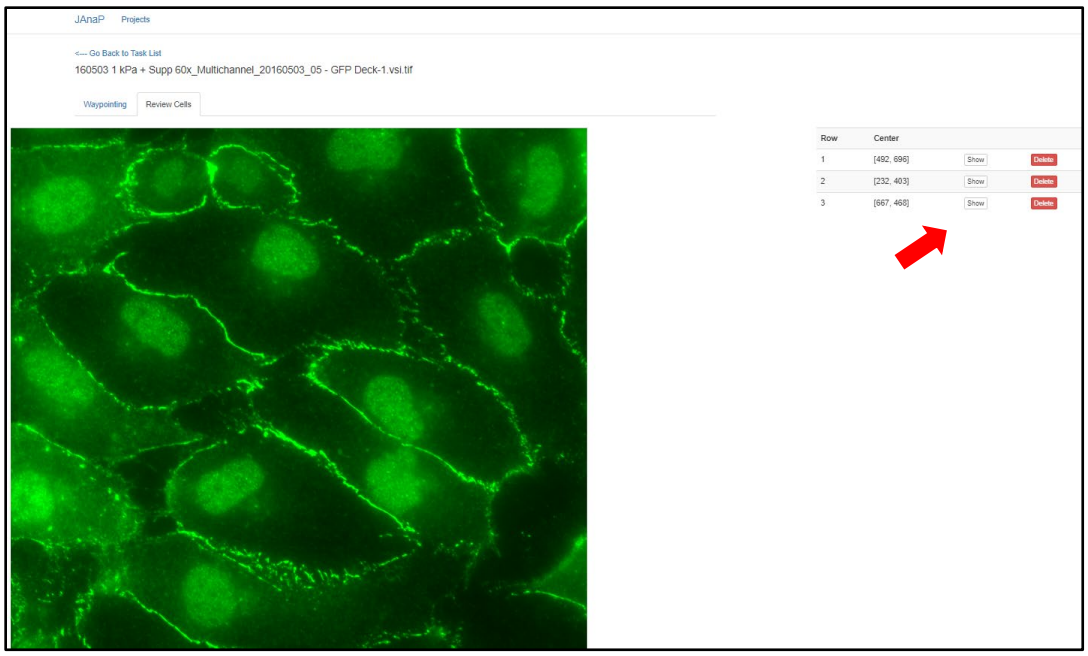

16) Once all cells of interest in the image have been traced, navigate back to the "Waypointing" tab and click "Mark Image Complete" in the bottom right corner. The following screen will appear:

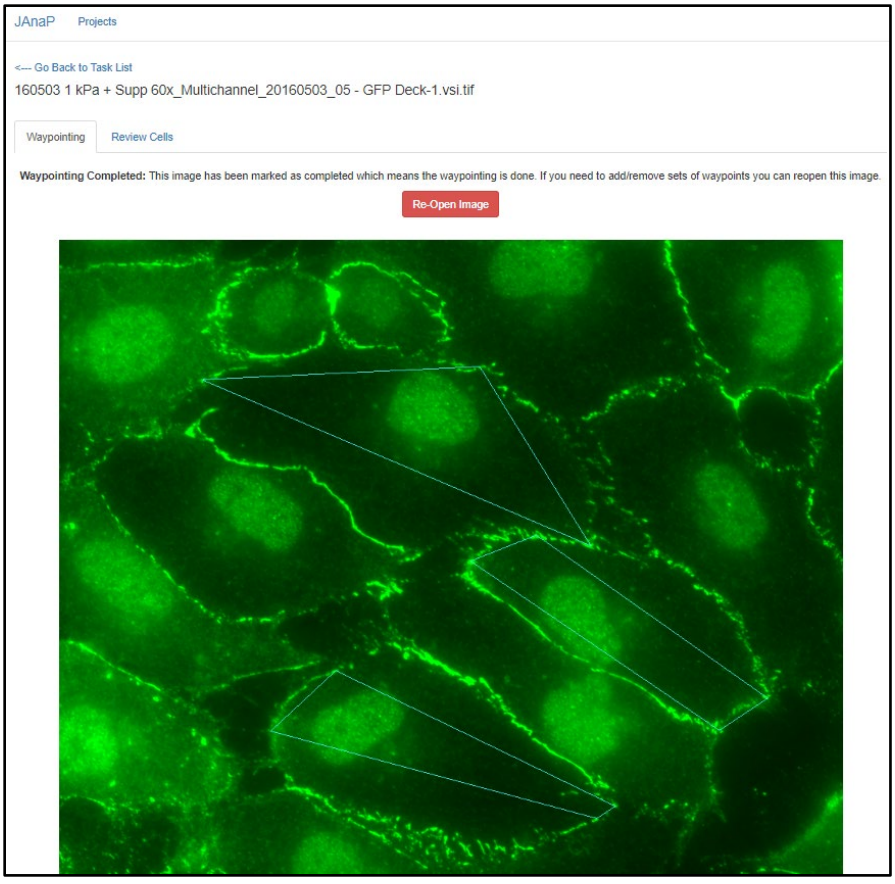

- The “Re-Open Image” button can be clicked if any adjustments are needed after the image has been marked as “complete”. “Re-opening” the image will allow you to continue waypointing new cells, or review or delete previously waypointed cells as described in step 14.
  - Note: If you re-open the image, be sure to “Mark Image Complete” once all changes have been made. “Open” images will not be processed, even if cells have been waypointed within that image.

17) Click on the “← Go Back to Task List” link in the top left of the screen to bring you back to the previous “Tasks” tab, where the “Status Filter” will be updated accordingly:

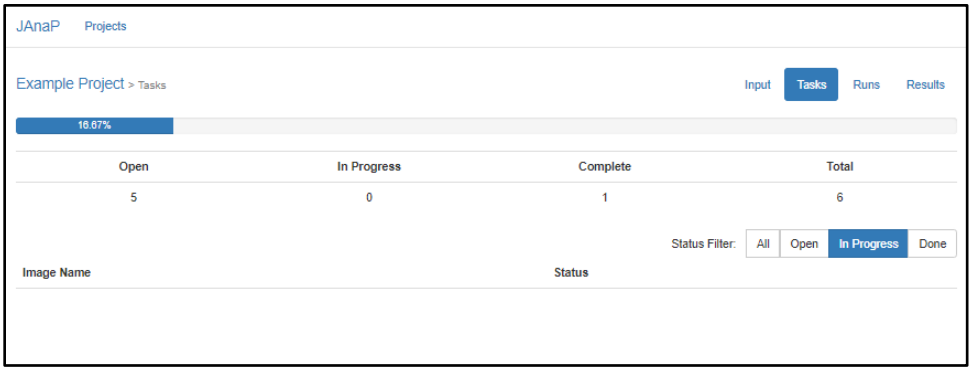

- In this example, the one image we have marked as complete is now registered as “Complete” and nothing is listed as “In Progress”. Select the “Done” tab to view the list of images marked as complete:

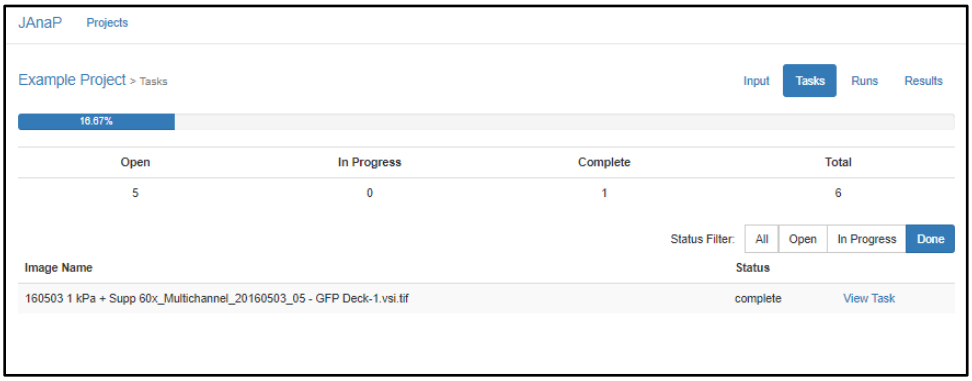

- NOTE: Clicking “View Task” next to the image in the “Done” tab will bring you back to the screen in step 17 and allow you to re-open the image if needed.

18) To navigate back to the project overview, click the “Input” button next to “Tasks” in the upper right corner. The “Overview” tab will appear and provide an updated count of the total images added, the percentage of the images marked as “Done”, and the total number of waypointed cells at that time:

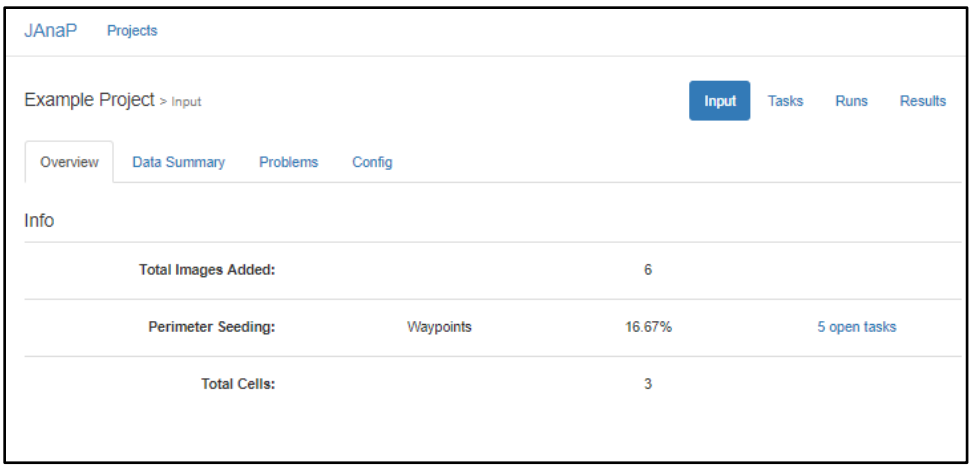

19) Click the "Config" tab to add in the user-designated and project-specific input. The follow screen will appear:

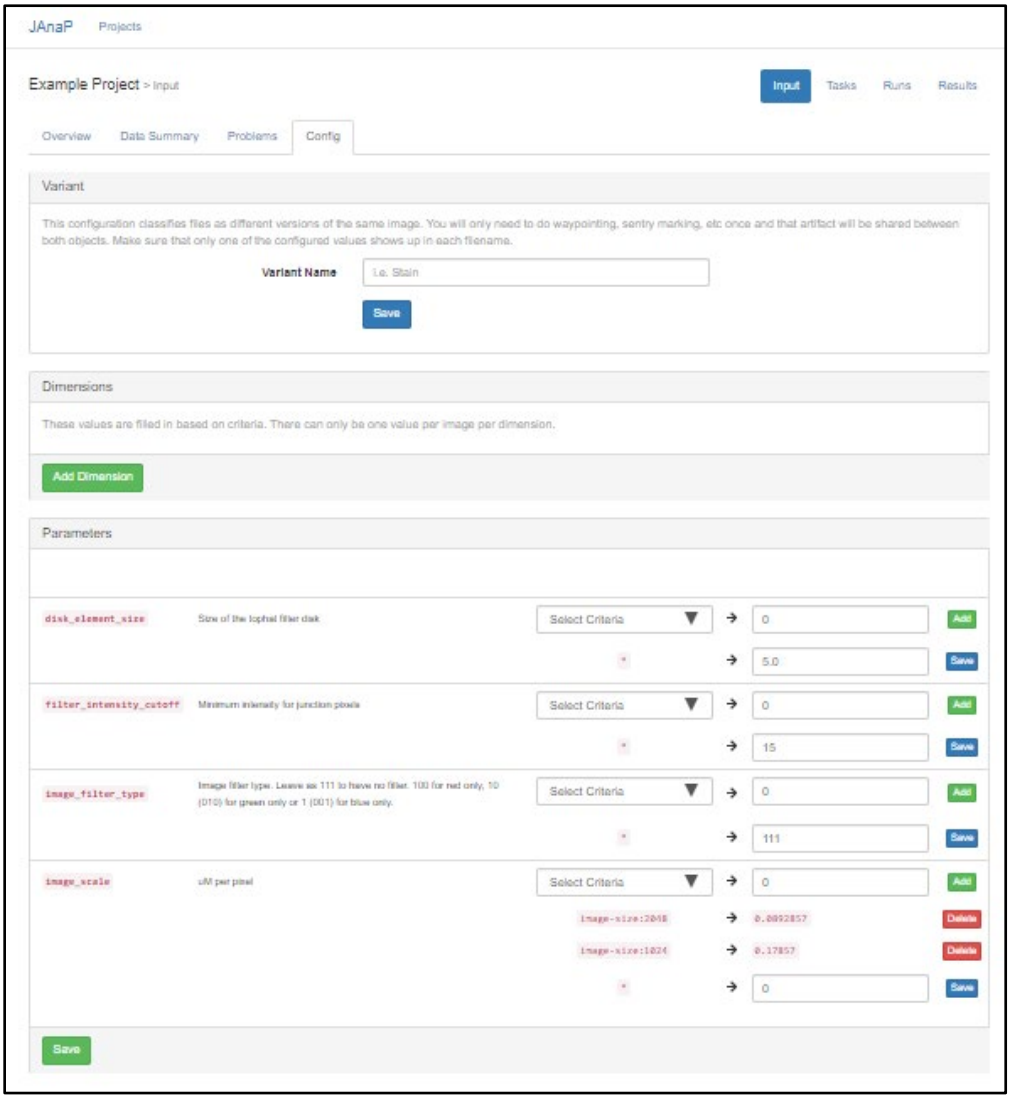

- **Variant -** The first option is to designate a "Variant Name". Typically, this is used if you include more than one stain/channel of the same image. This allows you to waypoint a cell one time but analyze the junctions immunostained for different proteins using different secondary fluorophores. It requires that the same image name is used for the different filters/channels except for the specific designation of the different filter/channel. Note that the variant values must be written out within the image name.
  - In this case, the "Variant Name" could be something like "Stain" or "Filter".
  - Each value of the variant (e.g., type of stain or filter, like GFP or TxRed) would then be typed in the "Add Value" field and "Add" would be clicked. These must be the specific designations that differentiate between the same images that otherwise have the same name. Be sure to check how it is written within the image filenames (e.g., TxRed versus TexasRed) and include each value.

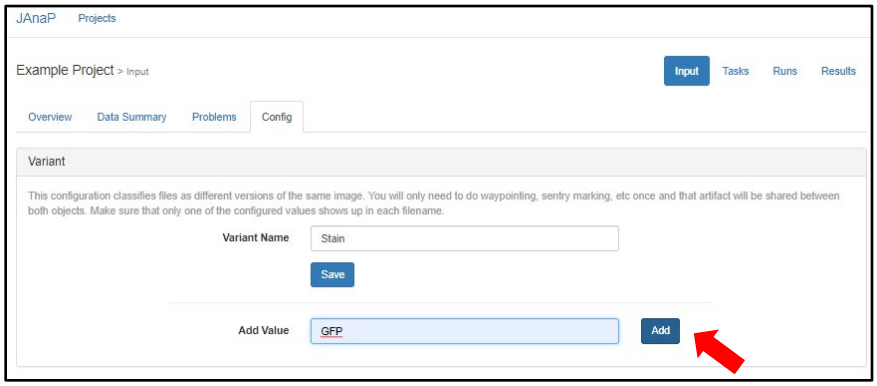

- The added values will appear under the "Primary Value" field and can be deleted via the "Delete Value" selection field:

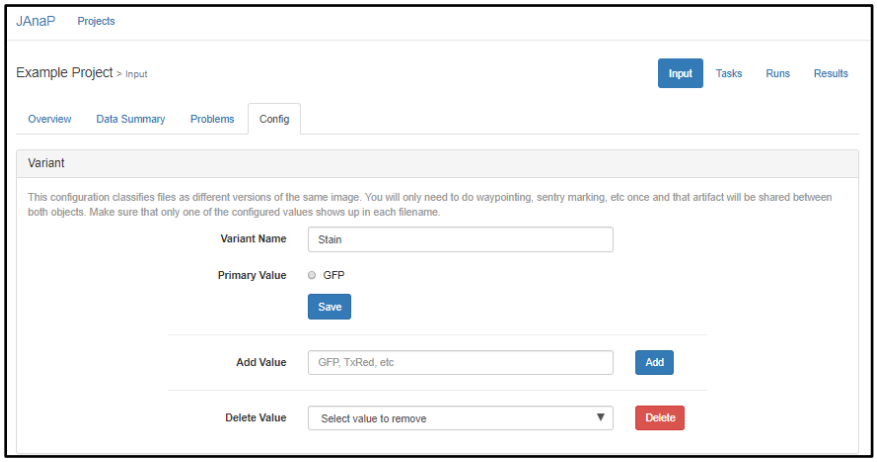

- Once you've added all variant values, you can then select a "Primary Value" which designates the channel you will perform the waypointing on. Then click "Save." This will remove the other channels/stains/variant values from the "Tasks" lists, since the waypoints are only identified on the "Primary Value"

images and will be applied to the other channels/values automatically for processing.

I. Here, GFP has been selected as the “Primary Value”:

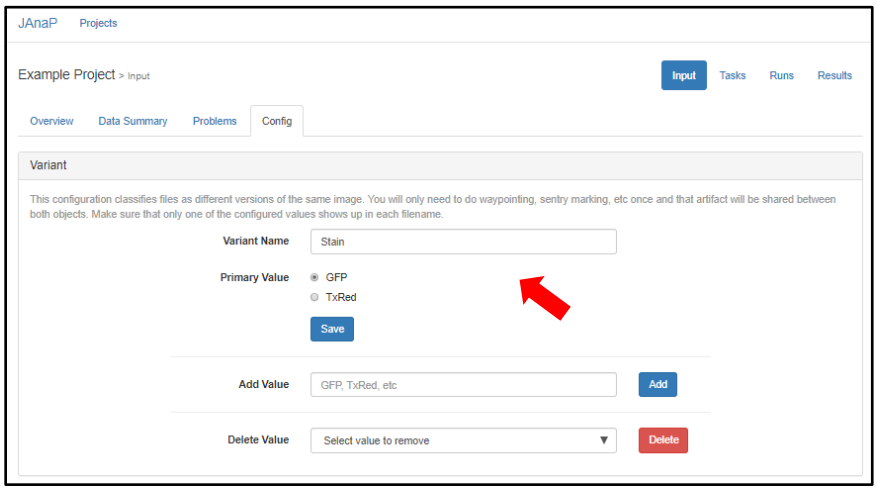

- Once variants have been added, they will be included in the “Data Summary” tab along with the breakdown of image and cell counts within each variant value.

  In this example we have included 3 GFP images and 3 TxRed images, which is reflected in the “Image Count”. At this point, we have waypointed 3 cells in one GFP image. Those 3 cells are reflected in the “Cell Count” column. Since we added GFP and TxRed as variants, and selected GFP as the primary value, however, those 3 waypoints were also transferred to the TxRed counterparts of those GFP images, thus 3 cells are listed in the “Cell Count” column for that variant as well:

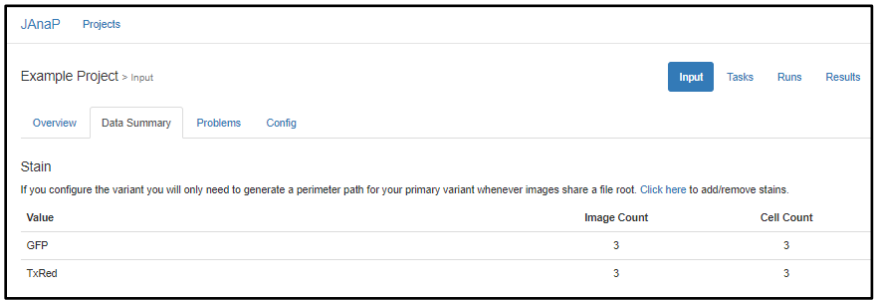

- **Dimension -** The next option is to designate “Dimensions” located in the “Config” tab under the “Variant” section. This allows you to designate different conditions, experiments, trial dates, etc. within this one project based on the image filenames, that will help ease data filtering/sorting for post-processing data analysis. To do this, click the green “Add Dimension” button:

- The following screen will appear and allow you to identify the name and type of dimension. Then click "Create".
  - **I.** The **Dimension Name** should be a descriptive title for the category you are sorting, for example, the name could be "Treatment Group" or "Date", etc.
  - **II.** The two options for the **Dimension Type** are:

- "Date Parse" - uses date within the filename or associated with the file to sort cells/files by date. If this is selected, click "create" and then select "Config" tab (clicking "create" auto-saves the Dimension)
- "String Match" - uses character strings within the filename to sort cells/files into the specific dimension category. If this is selected, click "create", and the following screen will appear.
  - This is where the different groups within the specified category can be defined. Click "Add Row" to input each category sub-type.

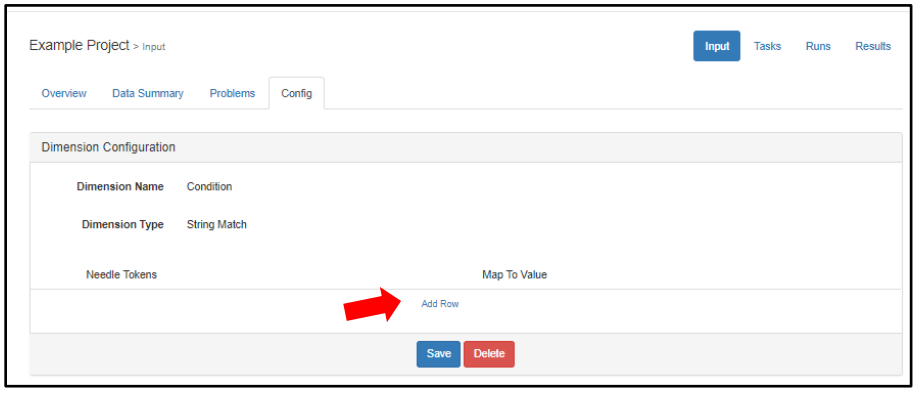

- The follow screen will appear:

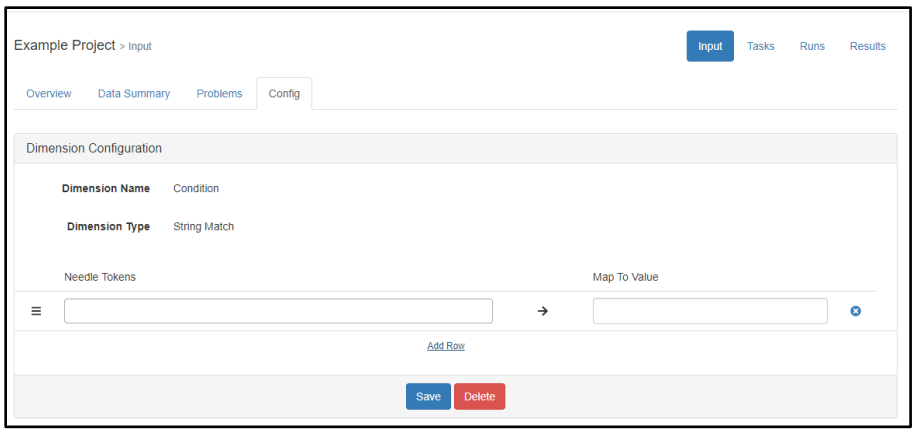

- Here, a "Needle Token" is a phrase within the image title that will be used to sub-categorize the image and the "Map to Value" is the sub-category to which you would like it assigned.
    - Needle Tokens:
        - Type in the phrase and then hit "Enter" or "Shift + Enter" to register it in the needle token field
        - Several needle tokens can be associated with one "Map to Value". This is particularly helpful if there are differences in naming schemes between different dates or trials.
        - Note that the Needle Tokens are case and space sensitive so they must exactly match the phrase within the image title.
        - Importantly, the algorithm cycles through the list of needle tokens and assigns the filename to the "Map to Value" associated with the first "Needle Token" found within the filename. Therefore, start with the most specific "Needle Tokens" first on the list.
    - Map to Value:
        - This will be the sub-category listed next to the cells/images in the output, so use something that allows for easy "filtering" or "sorting" in the spreadsheet
        - This phrase must be at least 5 characters long, so if needed, add spaces between each letter to increase the total phrase character length
    - Click "Save"
    - To add more sub-categories, click "Add Row" and repeat the above steps to enter in each sub-category needed

- As an example, here the filename is:

160503 1 kPa + Supp 60x_Multichannel_20160503_05 - GFP Deck-1.vsi.tif

- We want to group this image into a sub-category called “1 kPa Supp” so we assign the “Needle Token” as “1 kPa + Supp” and the “Map to Value” as “1 kPa Supp” as below:

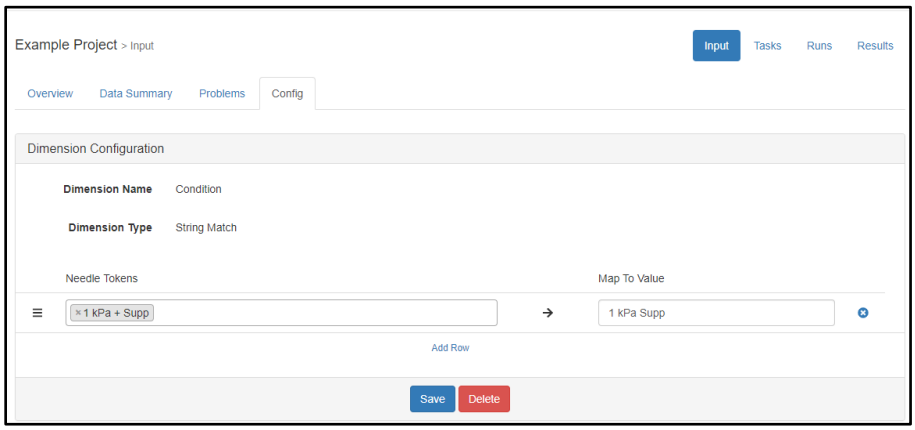

- Now, all images with “1 kPa + Supp” in the filename will be sub-categorized to “1 kPa Supp” in the output excel spreadsheet.
- Say, though, that for some of the images, the naming scheme was altered such that some of the files were instead missing a space between a few or all the phrases in the needle token (e.g., 160503 1kPa+Supp 60x_Multichannel_20160503_05 – GFP Deck-1.vsi.tif, or 160503 1kPa +Supp 60x_Multichannel_20160503_05 – GFP Deck-1.vsi.tif). You still want them to be sub-categorized as “1 kPa Supp” since they are the same condition, but the needle tokens don’t exactly match the phrases in the filename to be accurately sub-categorized. Therefore, you would add each different naming structure in as a needle token, all to the same “Map to Value” as below:

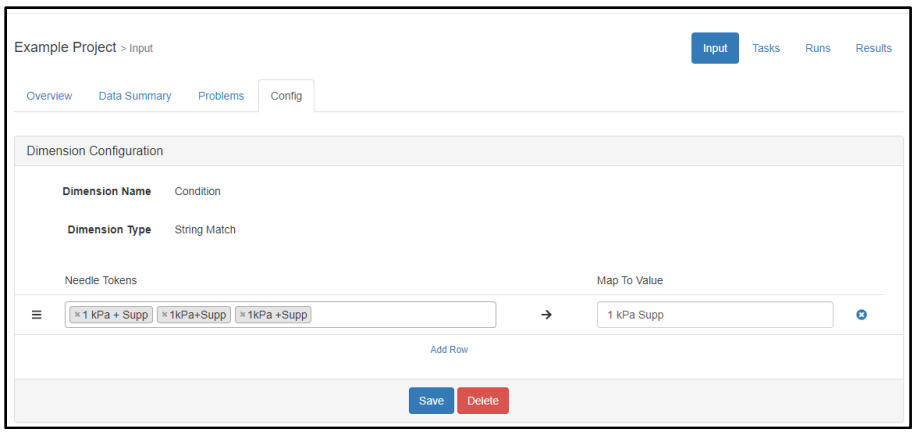

- Now, in this example, we also have a condition on 1 kPa without supplement. So, we click “Add Row” so another box appears as below:

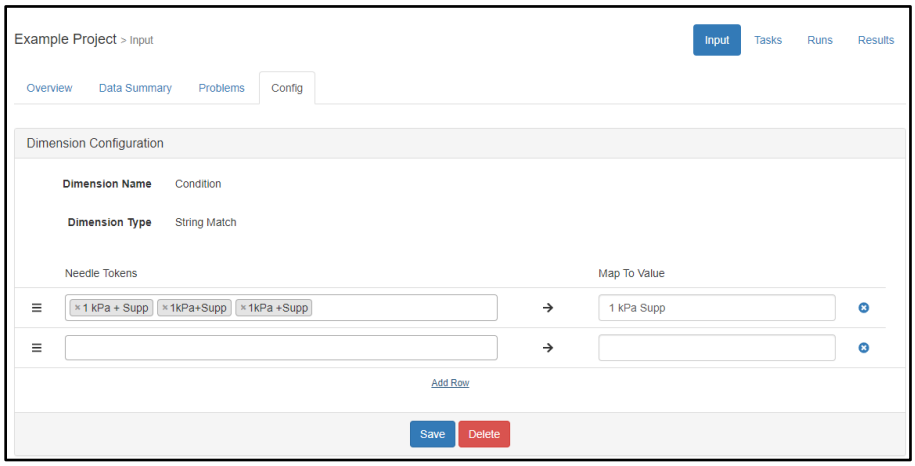

- We type in “1 kPa” as a “Needle Token” and as a “Map to Value”. Since perhaps the naming scheme was also an issue here, we also include “1kPa” as an additional “Needle Token” as below, and hit “save”:

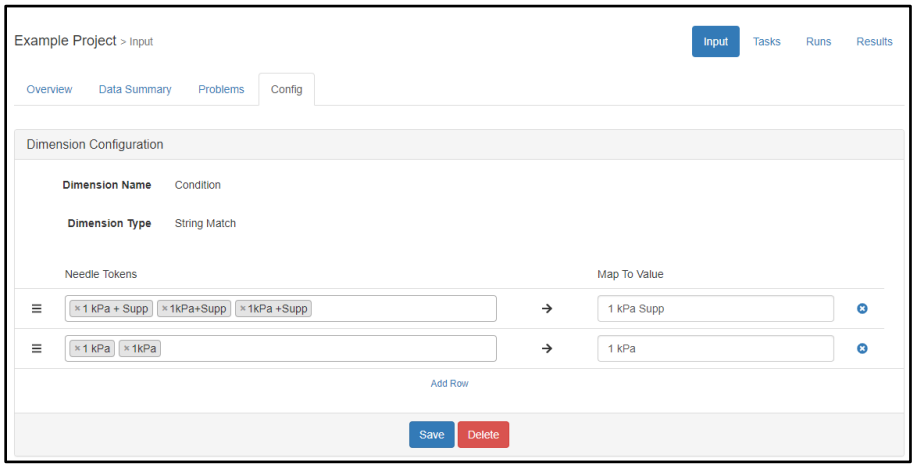

- Importantly: We added 1 kPa + Supp first before 1 kPa since the program cycles through the list of needle tokens in order and assigned the image to the first sub-category to which it fits. Since “1 kPa” is included in the image names containing “1 kPa + Supp”, all images would have been assigned to the “1 kPa” Map to Value if it were listed first. As written, the image name must meet the first criteria (e.g., include 1 kPa + Supp) otherwise it will be grouped a “1 kPa”.

---------- End Example

- Once all Dimensions have been put in and saved, you can navigate to the “Data Summary” tab. This section should now be populated to reflect the

"Variants" and the "Dimensions" and the respective Image and Cell Counts associated with each categorization:

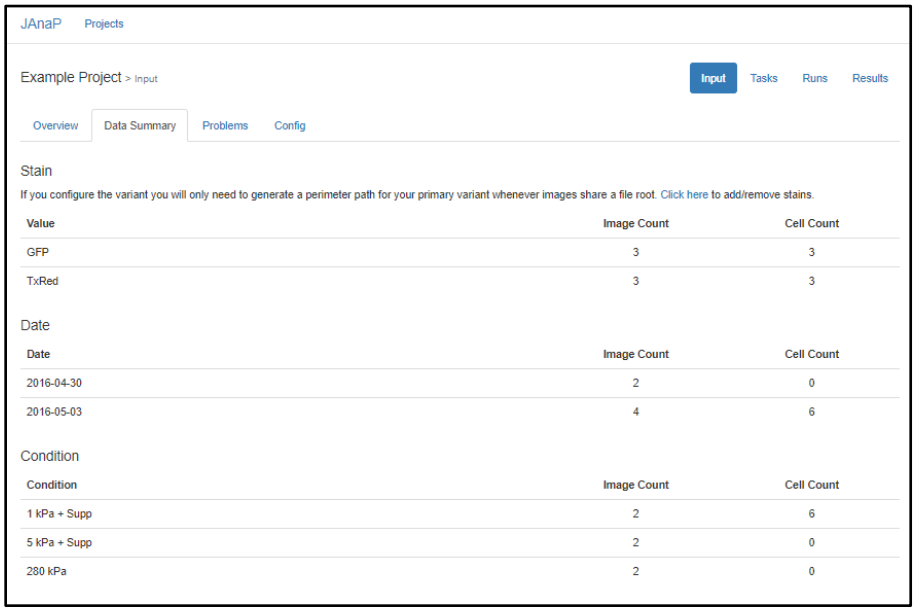

- Here, the counts still reflect the 3 cells in the 1 image that has been marked complete plus the TxRed counterpart based on the variants identified.

- **Parameters -** The next option on the "Config" tab (below "Variant" and "Dimension") is to designate "Parameters":

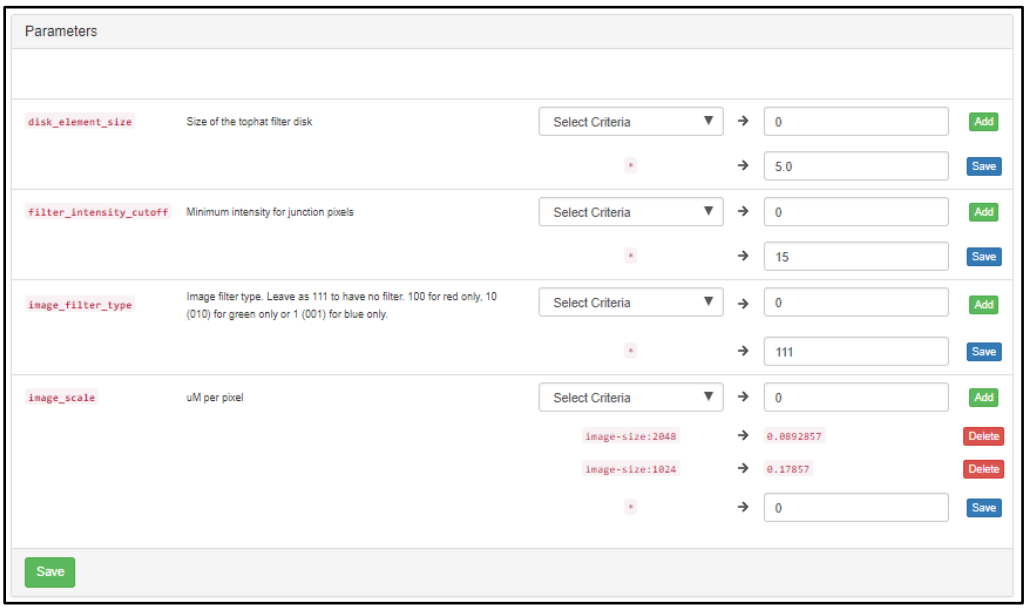

- This section allows you to adjust the following:

I. disk_element_size – this allows the user to define the size of the disk used for the tophat filter. The default is a disk size of 5 and should only be changed in specific circumstances.

II. filter_intensity_cutoff – this defines the intensity threshold value used to differentiate between regions of junction and no junction. This value should be determined for each project (using the python notebook described below) but a good starting point is 15 for GFP images and 5 for TxRed images with low levels of background. See the bottom section "Jupyter Notebook" for how to check the appropriate threshold values for your project.

III. image_filter_type – this defines which color channels are included in the analysis where the three numbers represent RGB. The default is 111 which keeps full RGB images in the analysis and should only be changed in specific circumstances.

IV. image_scale – this defines the conversion from pixel to microns so that the results are reported in terms of microns. The input values are based on image size and put in units of micron per pixel. This value should be changed for each project depending on the objective and camera used for image collection and the resolution of the images.
    - NOTE: The default values reflect the Stroka Lab IX83 microscope using the 60x oil objective for 1024 x 1024 and 2048 x 2048-pixel images

Note that a * indicates the default value applied to all images. There is a dropdown menu next to each variable that allows the user the designate a specific variable for each type/category of image. The "Delete", "Add", "Save" buttons can be used to adjust all inputs as necessary.

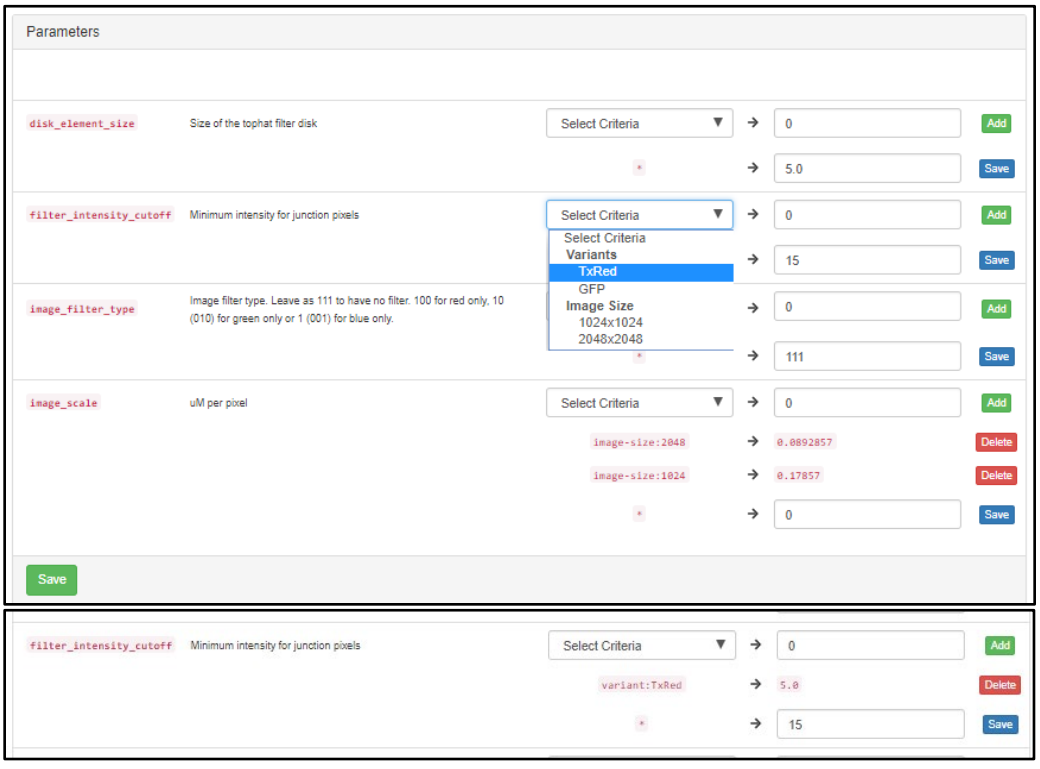

20) Click save in the bottom left hand corner of the Config tab to save any changes

21) To check if there are any issues with the uploaded images based on the configurations set up in the Config tab, scroll up to the top of the "Input" screen and click on the "Problems Tab" indicated below

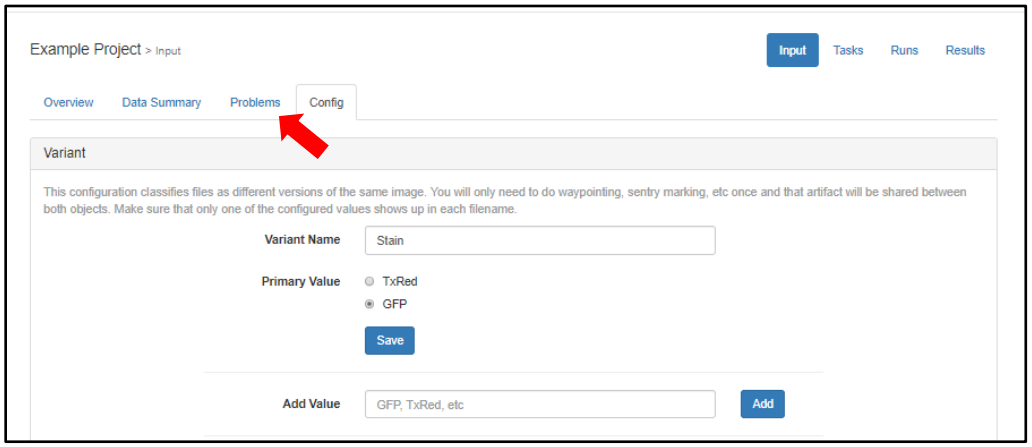

If no problems exist, the "Problems" tab will be blank as below:

If a problem is present, it will be listed under "Summary" with an explanation of the problem. Below is an example of this situation:

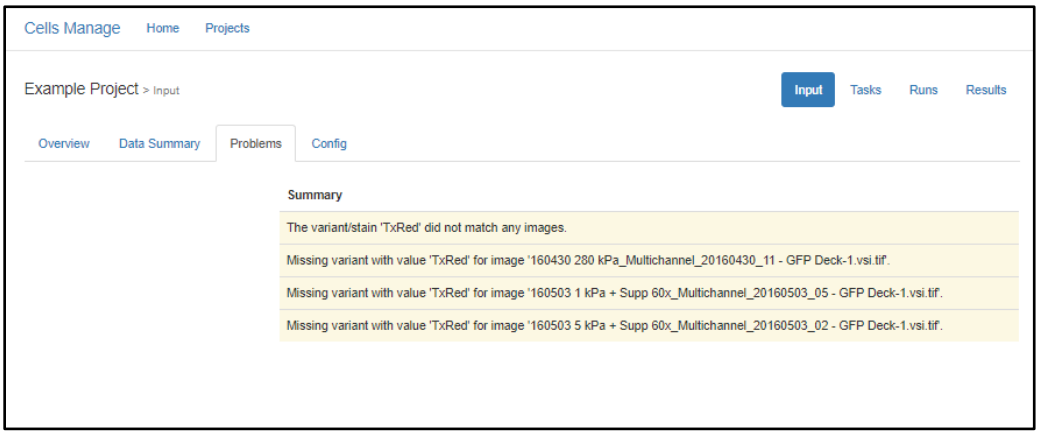

- Here, two variants were added to the configuration (i.e., GFP and TxRed) but no images with TxRed in the filename were uploaded into the program. This could be because those images were accidentally skipped when uploading the images or because the files do not have TxRed in the

filenames. Note: variants must be an exact match to the filename (e.g., Texas Red in the filename will not be included with the TxRed variant).

As problems are fixed, they will be removed from this list on the Problems tab.

22) Click on the Tasks tab button in the top right of the project to check your waypointing progress on based on any changes to your configuration. Note that the number of images requiring waypoints will decrease depending on the number of variants you include (e.g., only half of the images will be listed, if two variants are included).

Complete the waypointing process for all images in the "Open" and "In Progress" tabs until the counters read "0" for each and the "Complete" count matches the "Total" count as below:

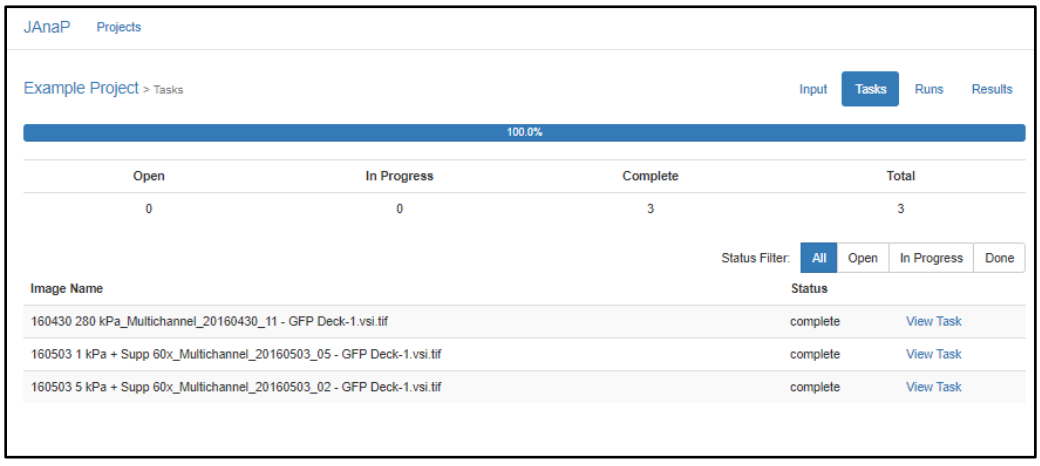

23) The program is now ready to be run. To do this, click on the "Runs" tab in the top right corner:

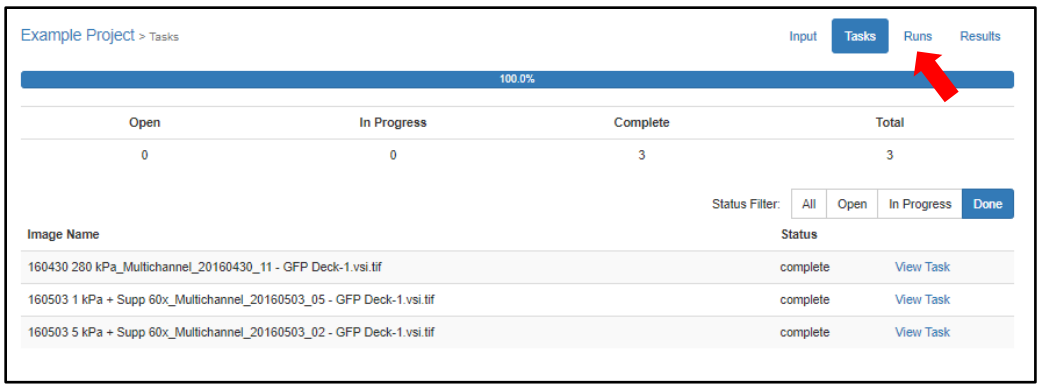

24) The “Overview” page will load as below:

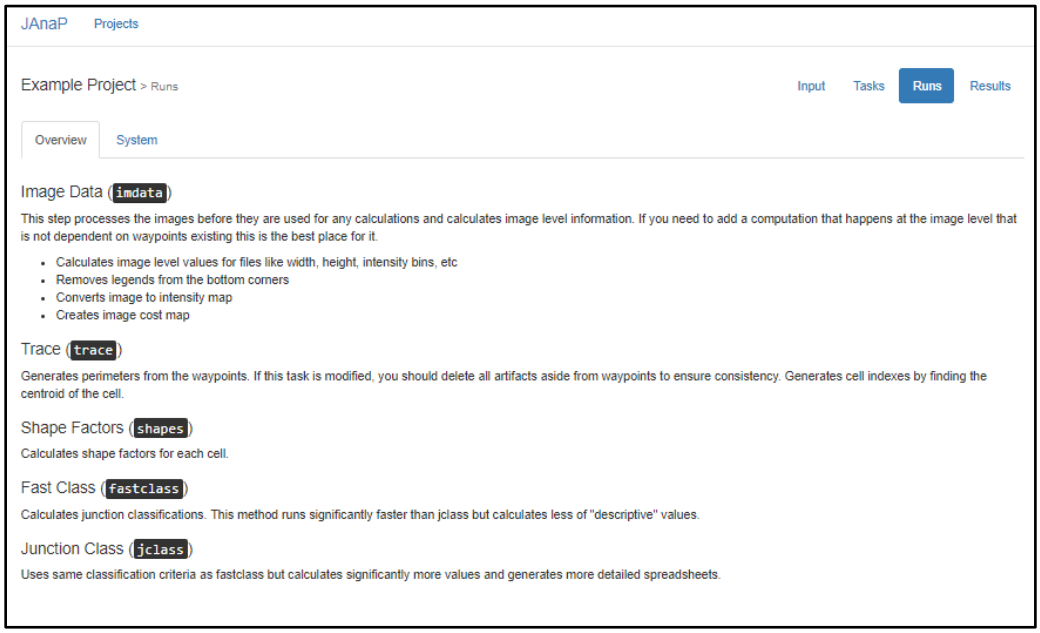

- The categories listed on this tab indicate each group of calculations to be processed by the program:
  - Image Data: processes the images as described
  - Trace: traces the outline of each cell to generate the cell path & perimeter
  - Shape Factor: uses trace data to calculate shape factors of each cell (e.g., area, circularity, solidity)
    - Note: a variant must be included for the shape factors to process. If a variant is not needed for your specific application, simply add something that is included in every image title as a placeholder variant and select it as the primary value.
  - Fast Class: categorizes junctions into continuous, punctate and perpendicular
  - Junction Class: generates more detailed calculations for the junctions in Fast Class, such as the start and end index, length, aspect ratio, tip-to-tip distance, etc. for each junction feature coinciding with the cell path.

25) To process the images, navigate to the “System” page by clicking on the “System” tab:

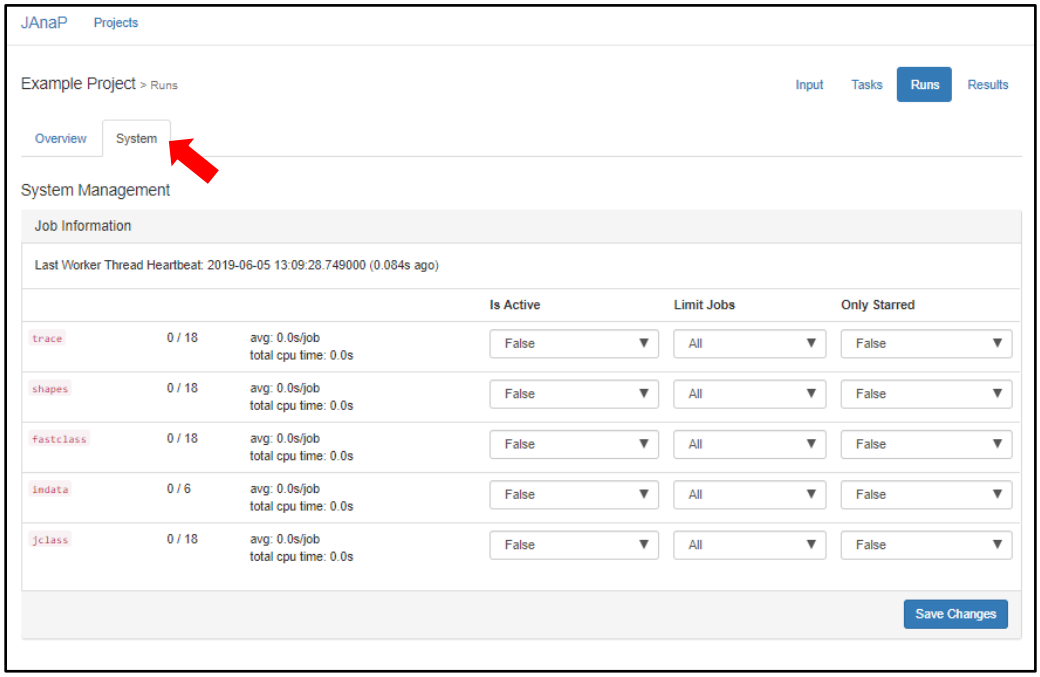

- Here, you will find the categories described on the “Overview” page listed to control which groups are being processed at any time.

- Note: The denominator of the counters (e.g., 0/18) indicates the total number of cells to be analyzed except for “imdata” which indicates the total number of images to be analyzed. Here, we have 6 total images (3 GFP and 3 TxRed) which included 18 total cells (9 from GFP and 9 from TxRed).

26) To begin processing the cells, change the “Is Active” column to “True” using the drop-down menu for each category you would like to process and click “Save Changes”. See below as an example:

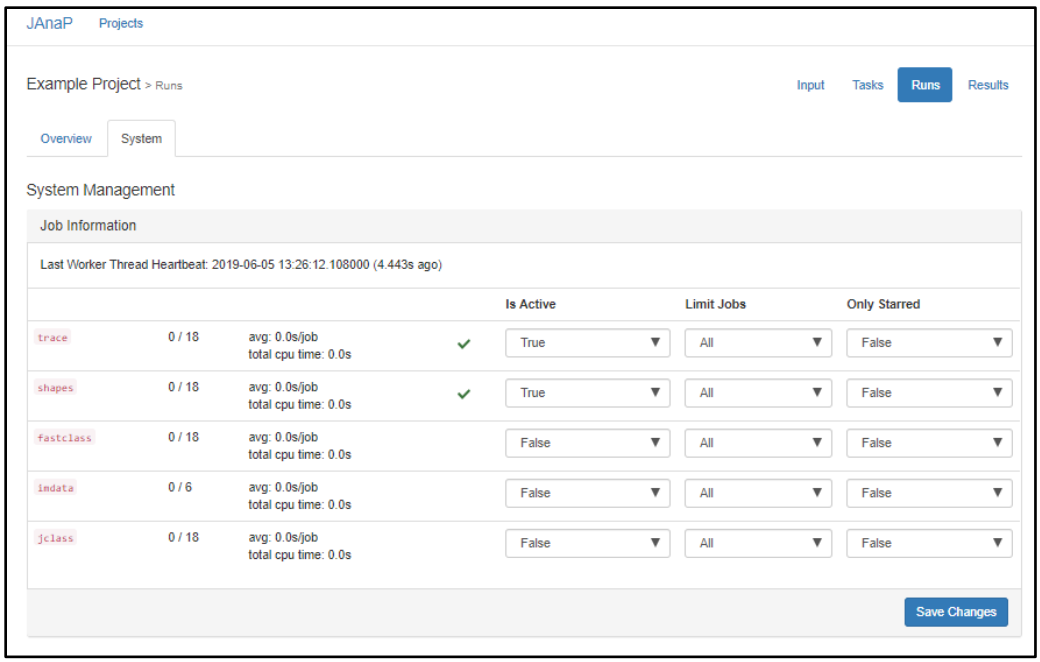

- To speed up the processing time, open a new command prompt and navigate to the project folder (as in step 1).
    - Within the command prompt, type cd Documents\GitHub\JAnaP-master
    - Hit “Enter” then type: python web\fast-worker.py
    - Note: To stop the fast worker application, type “Ctrl+C” in the command prompt

- Reload the window in your browser at any time to check the progress of the run. The counter will update to show how many images/cells have been processed out of the total. Below is an example where all the cells have been processed for the first category:

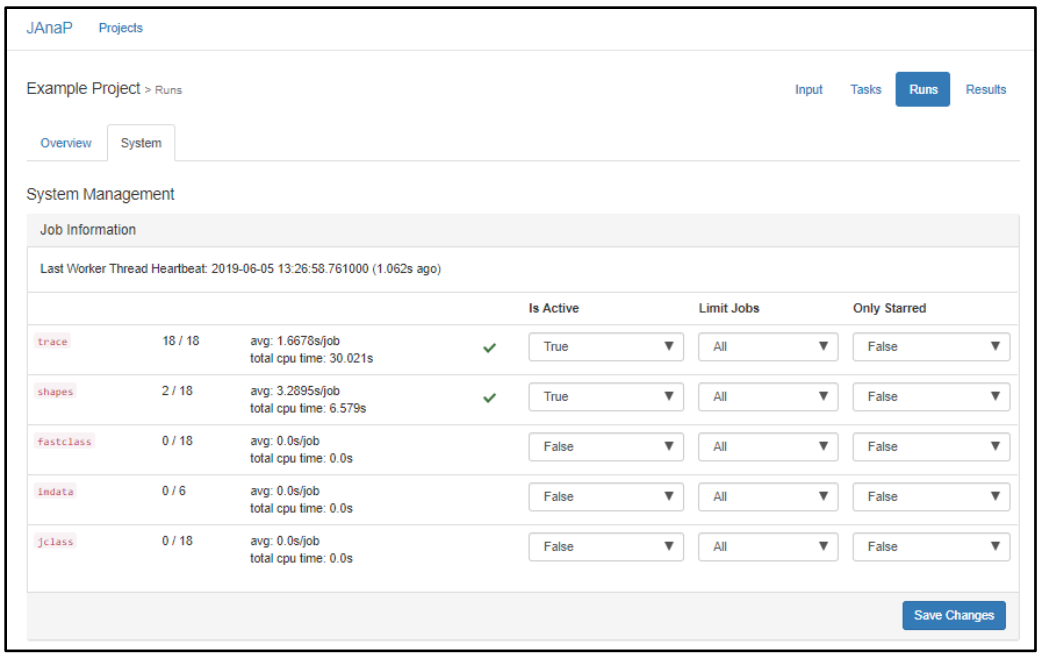

- To continue processing the other categories, change the “Is Active” status to “True” for the other categories. Since the run is complete for the “trace” and “shape” categories, the status can now be switched to “False”.

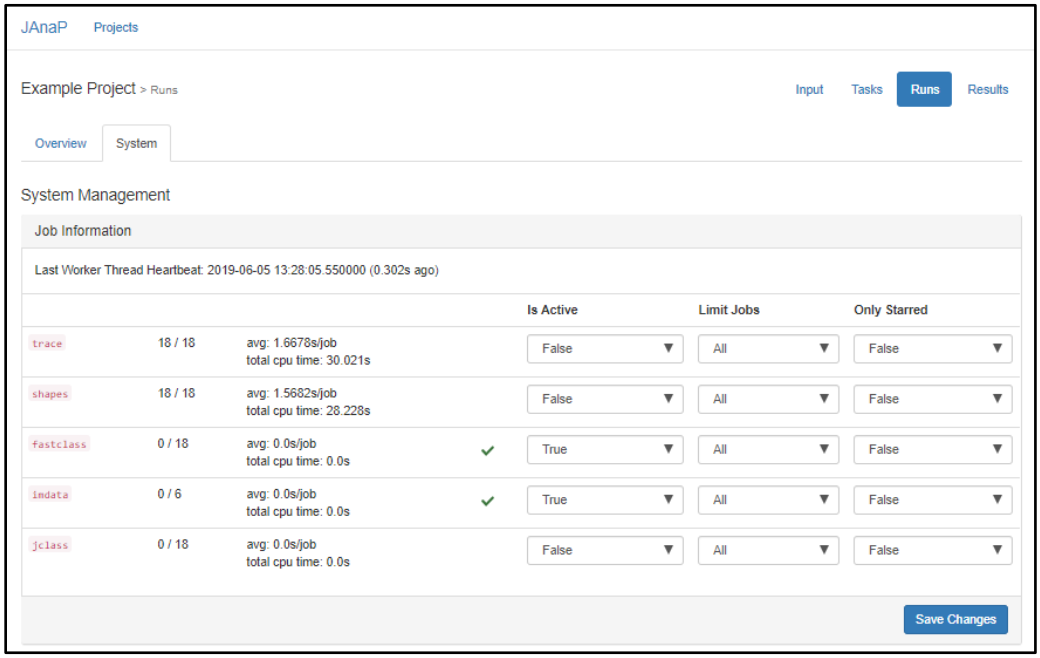

- Note that you can switch all columns to “True” if you would like to leave the program alone to run for a long period of time (e.g., overnight). The first four categories are all required to generate the categorization spreadsheet which includes the shape factors and the junction analysis.

The jclass takes much longer to process, so only switch this to “True” if you specifically need the data generated in that separate spreadsheet.

Once everything is finished, make sure all “Is Active” columns are set to “False”:

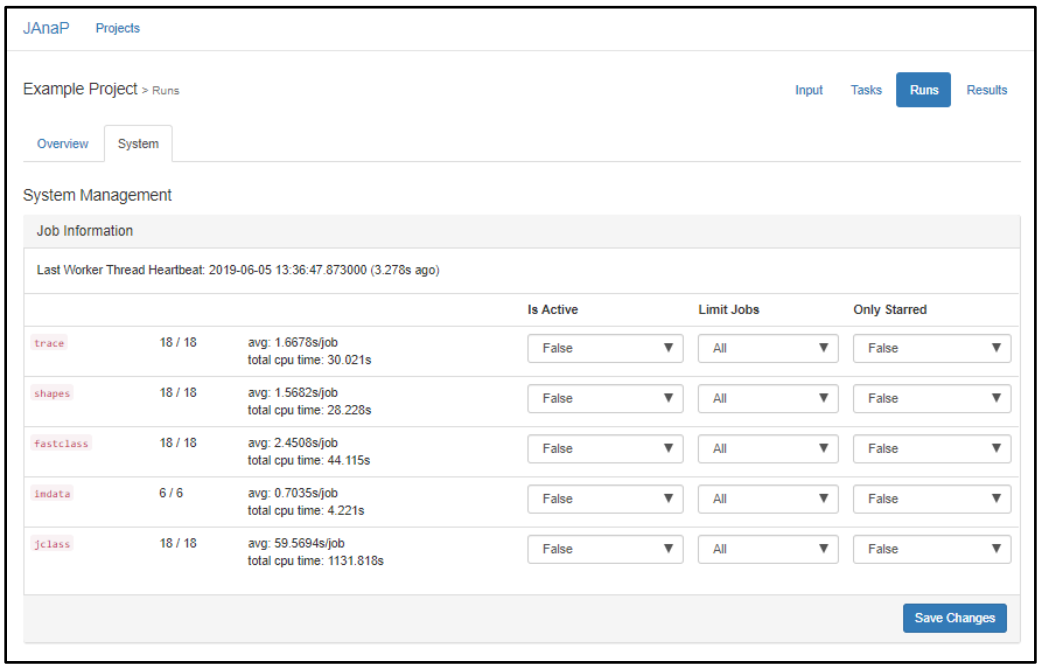

27) Click on the “Results” button in the top right corner of the project page to generate the excel files for export. The following screen will load:

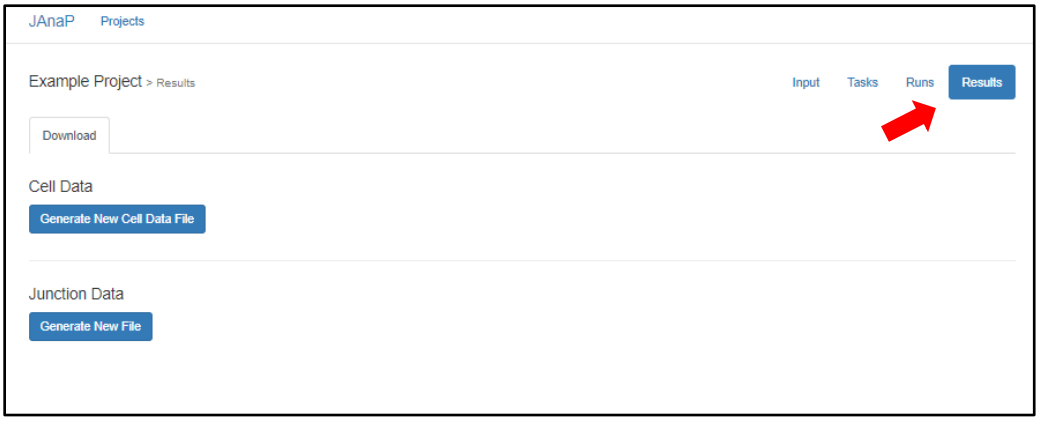

28) Click on “Generate New File” for any of the files types to generate that spreadsheet at any point in the processing period. The details of each category are discussed in the next step.
- Once the button has been pushed, the page will read “File processing is scheduled” under that category, as below under “Cell Data”:

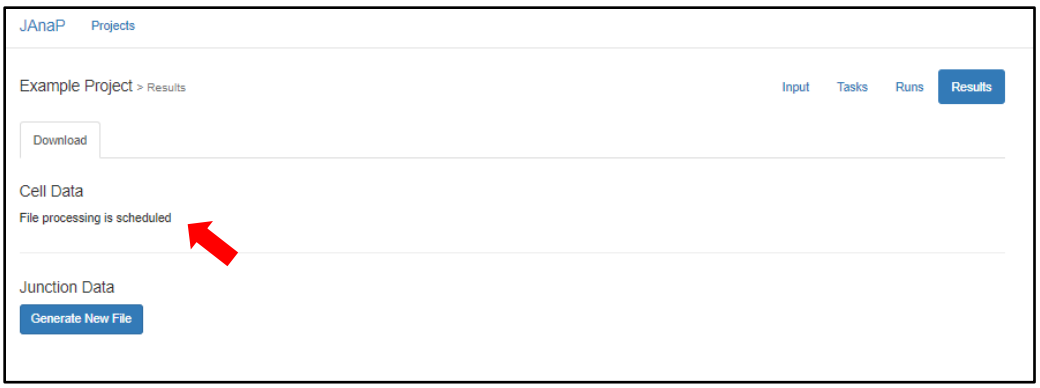

- After a few minutes, the file link will appear under the category header or the page can be re-loaded to load the file link.
    - Clicking on the link will download the file which will be opened as an excel spreadsheet.
    - Note that the name indicates the category of the file (e.g., "cell_data_v2), and the numbers indicated the date and time when the file was generated (e.g., 20190606071019 means the file was generated on June 06, 2019 at 07:10.19).

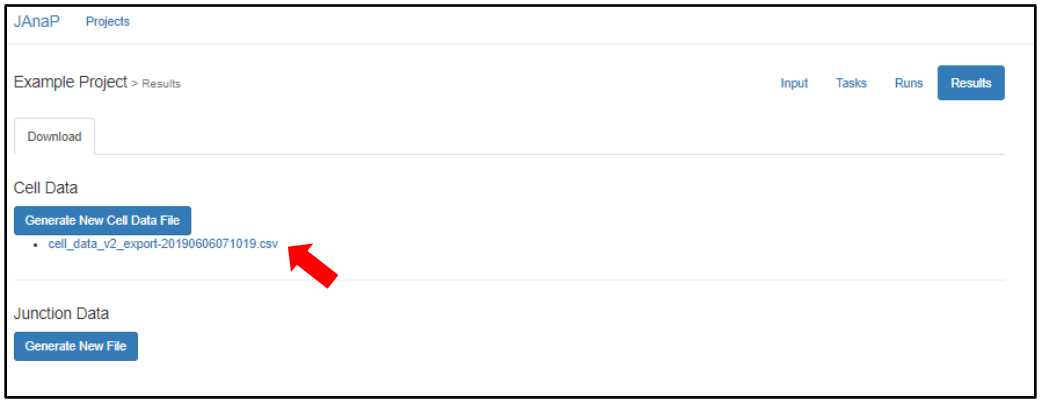

- A new file can be generated at any point by re-clicking on the blue "Generate New File" button. If so, a new file will appear with the appropriate date/time reflected in the filename:

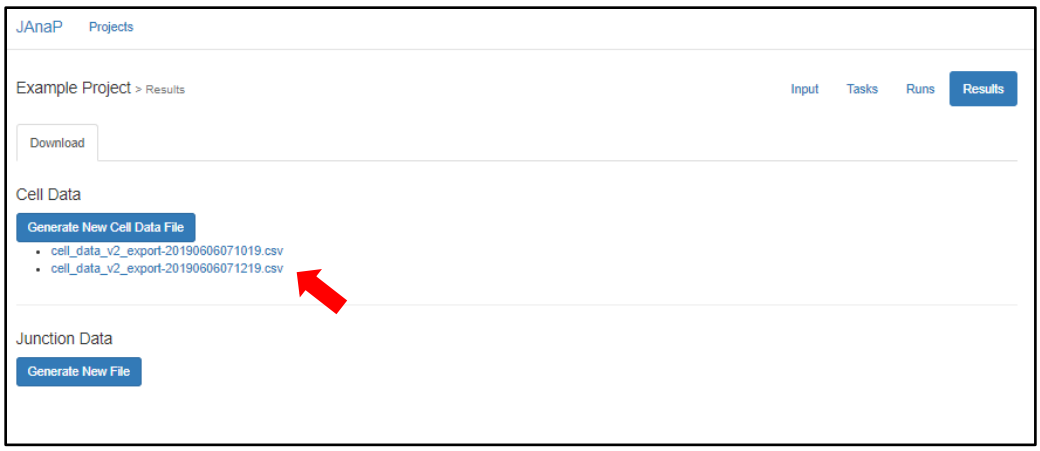

29) The spreadsheet categories are as follows:

- **Cell data:** This provides the shape factors and junction presentation percentages for every cell waypointed within the project
  - File Name: The name of the image in which the specific cell is located in
  - File Root: The base name of the image (e.g., TxRed or GFP identifier removed)
  - Variant Columns: A column will be generated for each variant and dimension added in the configurations tab. Here, stain: GFP or TxRed, was added as the variant and date and Condition: 1 kPa + Supp, 5 kPa + Supp, and 280 kPa, were added as dimensions. This allows for easy filtering within the spreadsheet to groups results by the various sub-dimensions.
  - Cell ID & Cell Number: This is the unique identifier assigned to each cell. It consists of the file/image name and the center coordinates of the waypoints. The center coordinates will be the same for every cell sharing the same waypoints (i.e., the same cell with more than one variant or stain) such that the difference in the Cell ID only lies in the image name differentiating it between variants.
  - Image Height: The height of the image in pixels calculated by the "Image Data"
  - Image Width : The width of the image in pixels calculated by the "Image Data"
  - Perimeter Count: The perimeter of the cell based on counted pixels
  - Perimeter Calc: The perimeter of the cell that accounts for pixel diagonals since cells are round objects not solely composed of linear edges
  - Perimeter (µm): The perimeter calc value converted to µm based on the conversion designated in the configuration tab for that image size
  - Area: The cell area (pixels^2) calculated using the same correction for pixel diagonals as in perimeter calc
  - Area (µm^2): The cell area converted to µm based on the conversion designated in the configuration tab for that image size

- Solidity: Calculated using the formula: $(cell\ area)/(convex\ hull\ area)$ as a measure of how solid the cell is. A value of 1 indicates a completely solid shape while a lower value indicates more protrusive features.
- Circularity: Calculated using the formula: $4\pi(area)/perimeter^2$ as a measure of how close the cell is to a perfect circle. A value of 1 indicates a perfect circle while a lower value indicates a more oblong or protrusive shape.
- Convex Area: Calculated using the Shoelace Method through the Scipy library and used to calculate solidity.
- Hull Aspect Ratio: The inverse aspect ratio of the cell calculated by taking the minor axis of the cell divided by the major axis of the cell. The axes are determined based on an ellipse fit to the convex hull.
- Coverage (%): The percent of the cell perimeter presenting junction.
- Continuous (%): The percent of the cell perimeter presenting continuous junction.
- Punct (%): The percent of the cell perimeter presenting punctate junction.
- Perp (%): The percent of the cell perimeter presenting perpendicular junction.
- Discontinuous (%): The percent of the cell perimeter presenting punctate and perpendicular junction.

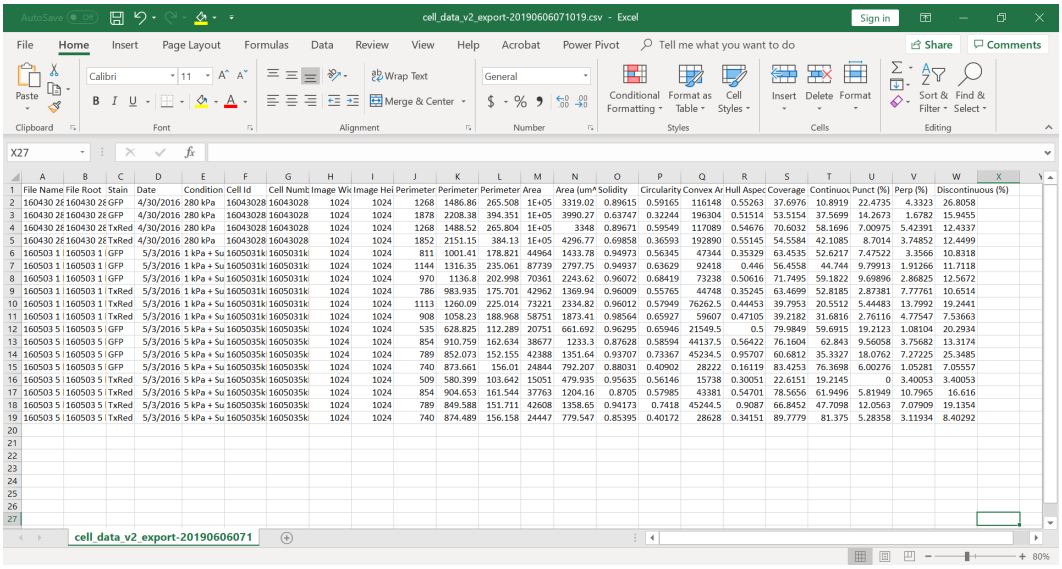

- **Junction Data:** This provides additional junction detail for that calculated in "Cell Data" generated in spreadsheets by variant (Here, one for GFP and one for TxRed).
  - Note that if you do not "run" the "jclass" job, the spreadsheets will either not generate, or will still be generated but will not contain any information.

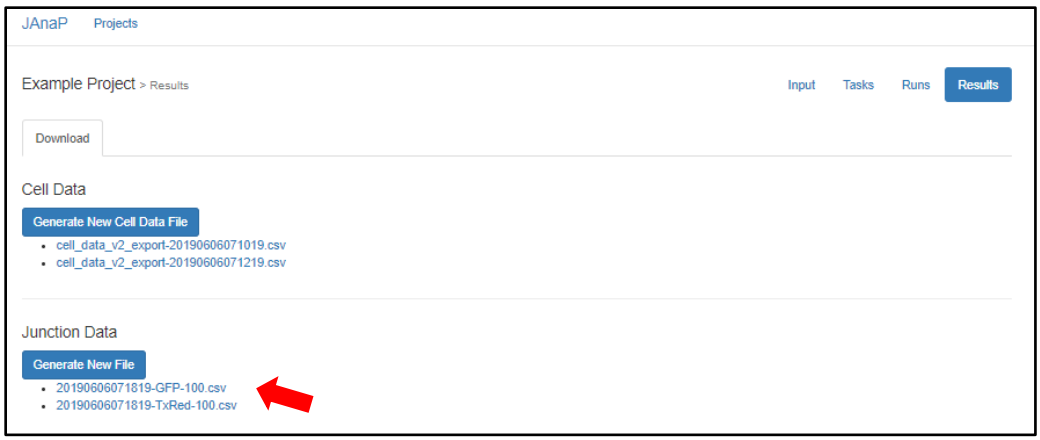

- File Name, Variant Columns, Cell ID: All the same as in "Cell Data" spreadsheet
- Path Start: Counter around the cell path indicating where junction piece begins, determined by the first waypoint seeded and continues in the direction of waypoint seeding around the cell
- Path End: Counter around the cell path indicating where junction piece ends
- Segment Length: Length (in pixels) that the junction piece coincides with the cell path
- Path AR Length: Length of the segment taking into account square-roots for pixel diagonals since the segments are not solely composed of linear edges (similar to perimeter count versus perimeter calc as described in the above section).
- Abs Tip Dist: Measure of junction thickness or maximum protrusion radially from cell path.
- Relative Path AR: Calculated by dividing "Abs Tip Dist" by "Path AR Length", used to determine whether a discontinuous junction is perpendicular or punctate
- Classification: Category to which junction piece is designated – Continuous, Perpendicular or Punctate
- Classification Simple: Simplified category to which junction piece is designated – Continuous or Discontinuous

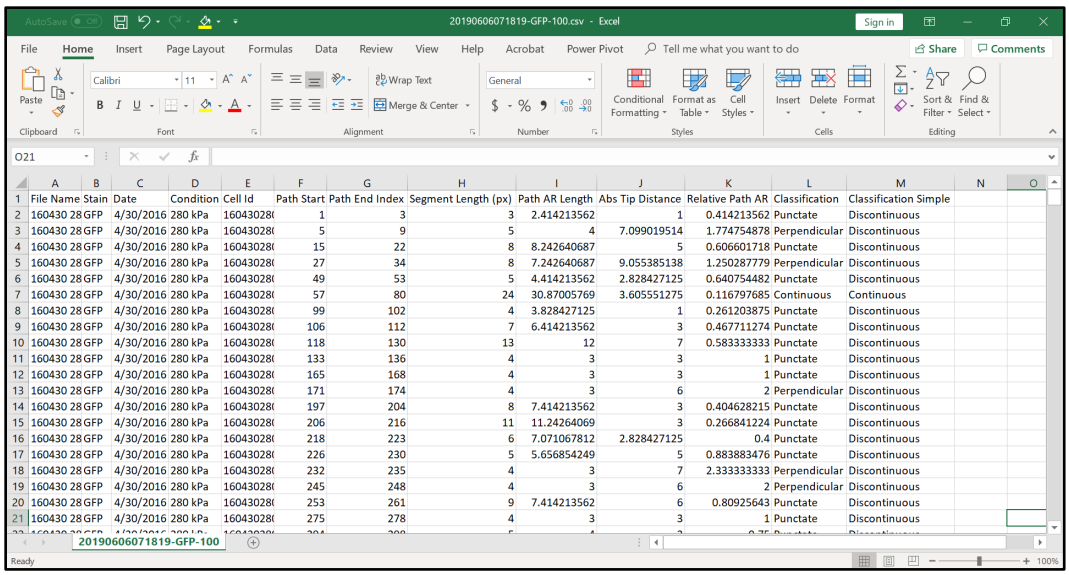

	A	B	C	D	E	F	G	H	I	J	K	L	M	N	O
1	File Name Stain		Date	Condition	Cell Id	Path Start	Path End Index	Segment Length (px)	Path AR Length	Abs Tip Distance	Relative Path AR	Classification	Classification Simple		
2	160430 28 GFP		4/30/2016	280 kPa	16043028(	1	3	3	2.414213562	1	0.414213562	Punctate	Discontinuous		
3	160430 28 GFP		4/30/2016	280 kPa	16043028(	5	9	5	4	7.099019514	1.774754878	Perpendicular	Discontinuous		
4	160430 28 GFP		4/30/2016	280 kPa	16043028(	15	22	8	8.242640687	5	0.606601718	Punctate	Discontinuous		
5	160430 28 GFP		4/30/2016	280 kPa	16043028(	27	34	8	7.242640687	9.055385138	1.250287779	Perpendicular	Discontinuous		
6	160430 28 GFP		4/30/2016	280 kPa	16043028(	49	53	5	4.414213562	2.828427125	0.640754482	Punctate	Discontinuous		
7	160430 28 GFP		4/30/2016	280 kPa	16043028(	57	80	24	30.87005769	3.605551275	0.116797685	Continuous	Continuous		
8	160430 28 GFP		4/30/2016	280 kPa	16043028(	99	102	4	3.828427125	1	0.261203875	Punctate	Discontinuous		
9	160430 28 GFP		4/30/2016	280 kPa	16043028(	106	112	7	6.414213562	3	0.467711274	Punctate	Discontinuous		
10	160430 28 GFP		4/30/2016	280 kPa	16043028(	118	130	13	12	7	0.583333333	Punctate	Discontinuous		
11	160430 28 GFP		4/30/2016	280 kPa	16043028(	133	136	4	3	3	1	Punctate	Discontinuous		
12	160430 28 GFP		4/30/2016	280 kPa	16043028(	165	168	4	3	3	1	Punctate	Discontinuous		
13	160430 28 GFP		4/30/2016	280 kPa	16043028(	171	174	4	3	6	2	Perpendicular	Discontinuous		
14	160430 28 GFP		4/30/2016	280 kPa	16043028(	197	204	8	7.414213562	3	0.404628215	Punctate	Discontinuous		
15	160430 28 GFP		4/30/2016	280 kPa	16043028(	206	216	11	11.24264069	3	0.266841224	Punctate	Discontinuous		
16	160430 28 GFP		4/30/2016	280 kPa	16043028(	218	223	6	7.071067812	2.828427125	0.4	Punctate	Discontinuous		
17	160430 28 GFP		4/30/2016	280 kPa	16043028(	226	230	5	5.656854249	5	0.883883476	Punctate	Discontinuous		
18	160430 28 GFP		4/30/2016	280 kPa	16043028(	232	235	4	3	7	2.333333333	Perpendicular	Discontinuous		
19	160430 28 GFP		4/30/2016	280 kPa	16043028(	245	248	4	3	6	2	Perpendicular	Discontinuous		
20	160430 28 GFP		4/30/2016	280 kPa	16043028(	253	261	9	7.414213562	6	0.80925643	Punctate	Discontinuous		
21	160430 28 GFP		4/30/2016	280 kPa	16043028(	275	278	4	3	3	1	Punctate	Discontinuous		

30) All the data generated using the GUI is saved in the GitHub project folder:
- Documents > GitHub > JAnaP-master > data > projects > *your project*:
  - Artifacts – This includes all the raw files generated for each cell during the waypointing process and the information calculated during the run process.
  - Input – input images of the cells you placed here in step 6
  - Output – this is where all the excel spreadsheets that you generate in step 28 & 29 are stored
  - System – this stores the system information and logs of any problems during processing

31) The program can be re-run (e.g., with different parameters) at any time:
- To do this, the artifacts need to be deleted from the individual folders within the artifacts folder described above. This will register in the GUI and reset the counters in step 26 to “0”.
  - *Important* DO NOT DELETE THE WAYPOINTS FOLDER (unless the waypoints specifically need to be re-done for the project). This will remove the saved waypoint information and require the entire waypoint process to be performed again. If you leave the waypoints, the cell IDs will remain, and the calculations will be re-calculated based on the parameters in the configurations tab at that time.
  - Be sure you save the original artifacts folders and/or excel spreadsheets of the original data in case you need to reference back, as well as the configuration data used to generate them (saved in the _project.config.json file within the project folder). The results will be saved over and the excel files generated do not save the configuration data within them.

Jupyter Notebook:

This notebook allows you to identify threshold values for use in JAnaP processing and generate figures based on the calculated data. The following instructions provide guidance on how to work through the notebook as it is currently written. Note that at any time, the notebook can be copied and re-saved using a different name for future reference or to make changes to the graphing or calculations themselves.

A. First time use/install:
   1. Open a command prompt
   2. Right click and select "Run as Admin."
   3. Type in "Pip install jupyter"

B. Subsequent Usage:
   1. In a new command prompt, navigate to folder containing "JAnaP-master" then type jupyter notebook. For example:
      - cmd > cd Documents\GitHub\ JAnaP-master\
      - cmd > jupyter notebook

   2. The web page will open and look like the following:

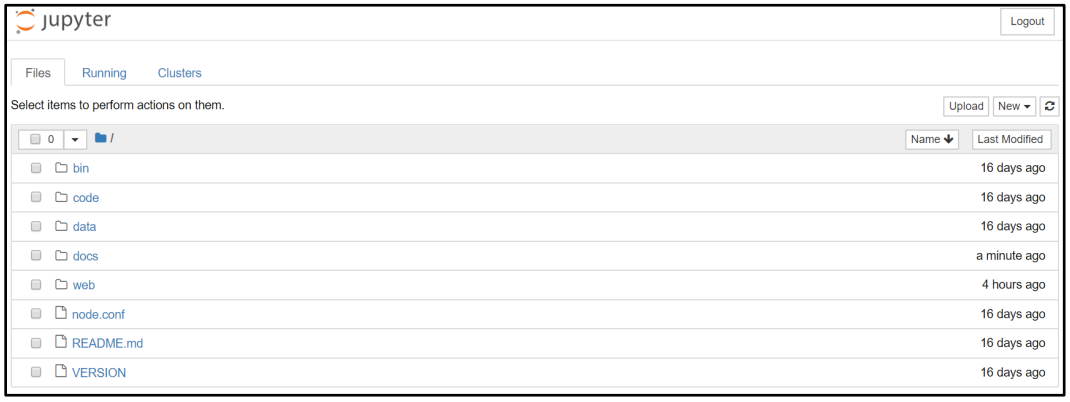

   3. Click on the "docs" folder then select the link to the "Thresholding":

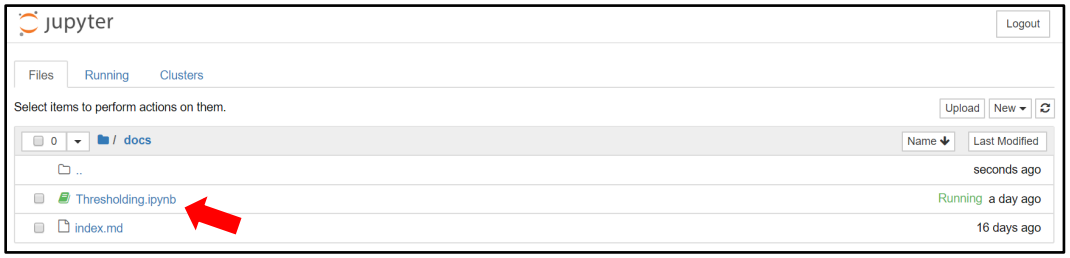

   4. The following page will appear in a new window:

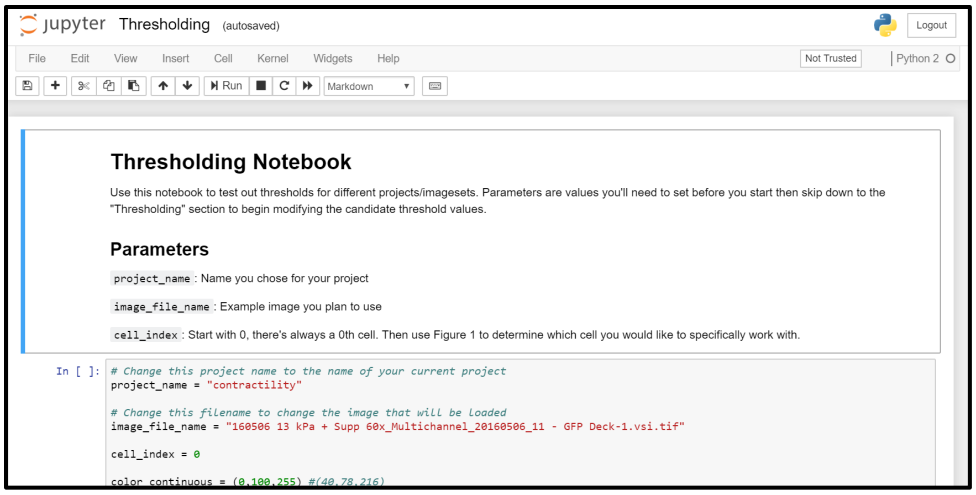

5. Click on the first box and type in the specified parameters (e.g., project name, image name, and cell_index) as follows, then hit Ctrl+Enter to run:

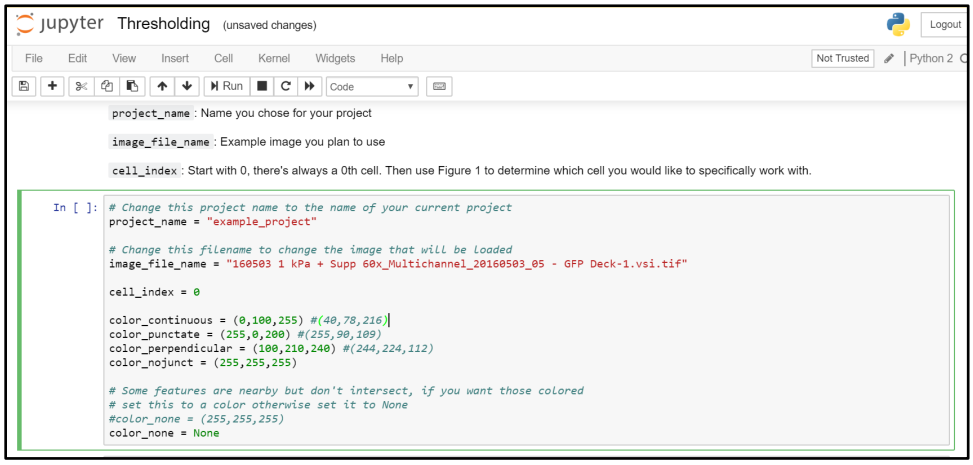

- Note: If you don't know the cell index, you can continue through step 6 to view an annotated image of the waypointed cells to help identify which cell you would like to view moving forward. If you decide to change the cell index in box 1, simply rerun that box and subsequent boxes by selecting them and hitting Ctrl+Enter.
- Note: If you change any parameters in any box after Ctrl+Enter has been hit, you must re-run box 2 prior to re-running the box of interest for the modified image to appear.
- Note: What you type for "project_name" in the Thresholding notebook must exactly match the project name created in the JAnaP web interface.

6. Click on the next two boxes and hit Ctrl+Enter to run each. After the 3rd box, your annotated image will appear as follows:

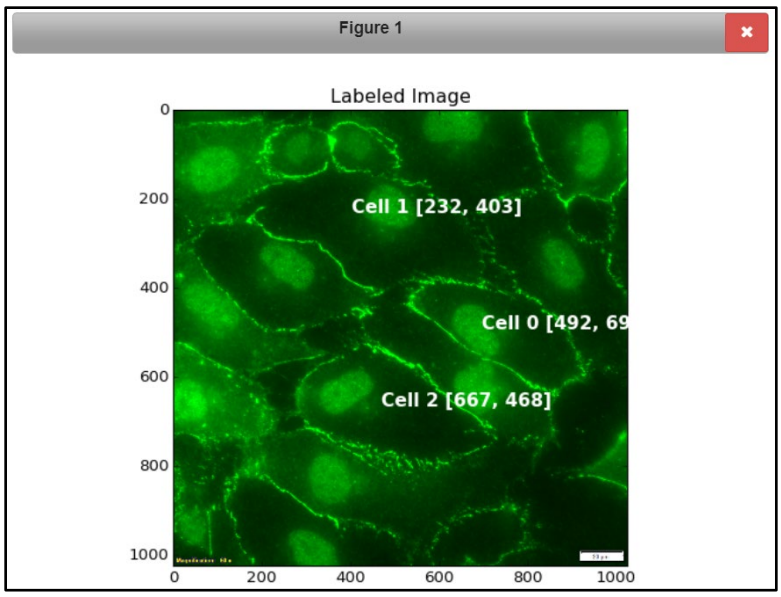

- Note: the following tool bar will appear below each image.
    - Selecting the square button will allow you to select an area within the image to zoom-in on

    - Click the "home" button to return to the original image at any point

    - The save button will **NOT** save the image.

    - To save the image, you must insert the following line at the bottom of the cell that generated the image:

cv2.imwrite(output_prefix + 'TitleYouWantImageSavedAs.png', input_image)

- input_image is the plot generated in this box. This can be substituted in subsequent cells for the plot generated within that cell (e.g., in the 6th box it would be "plotter").
- Adding a # symbol in front of this line will comment out the command if you would like to run the cell without saving the image but keeping the command there for future use.

7. Click Ctrl+Enter in the 4th box for the center coordinates of the specified cell index to appear. Here, this is for Cell 2:

```
In [5]: print "Cell Center: ", image_waypoints[cell_index].get("geometric_center")
        Cell Center:  [492, 696]
```

8. Click Ctrl+Enter in the 5th box for a cropped image of the cell of interest to be generated:

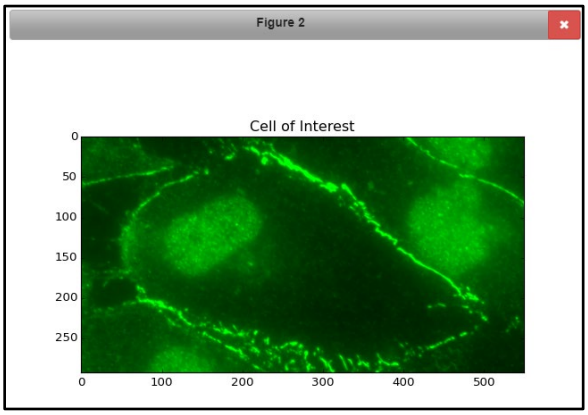

- The crop level of the image can be adjusted by changing the following values (decreasing the number provides a "tighter" crop). Note that this can be changed throughout the notebook for any of the cropped images.

```
waypoints = numpy.asarray(image_waypoints[cell_index].get("waypoints"))

r_cell_min, r_cell_max = numpy.min(waypoints[:, 0]), numpy.max(waypoints[:, 0])
c_cell_min, c_cell_max = numpy.min(waypoints[:, 1]), numpy.max(waypoints[:, 1])

i_r_max, i_c_max, depth = input_image.shape
frame_r_min, frame_r_max = max([r_cell_min - 50, 0]), min([r_cell_max + 50, i_r_max])
frame_c_min, frame_c_max = max([c_cell_min - 50, 0]), min([c_cell_max + 50, i_c_max])

pyplot.figure(2)
pyplot.title('Cell of Interest')
pyplot.imshow(input_image[frame_r_min:frame_r_max, frame_c_min:frame_c_max])
pyplot.show()
```

9. To identify the optimal threshold value, enter a value next to "Threshold" and click Ctrl+Enter in the 6th box. Repeat this process, adjusting the threshold as necessary to reflect the isolated junctions as you would expect. Note that increasing the threshold isolates less junction while decreasing the threshold isolates more junction.

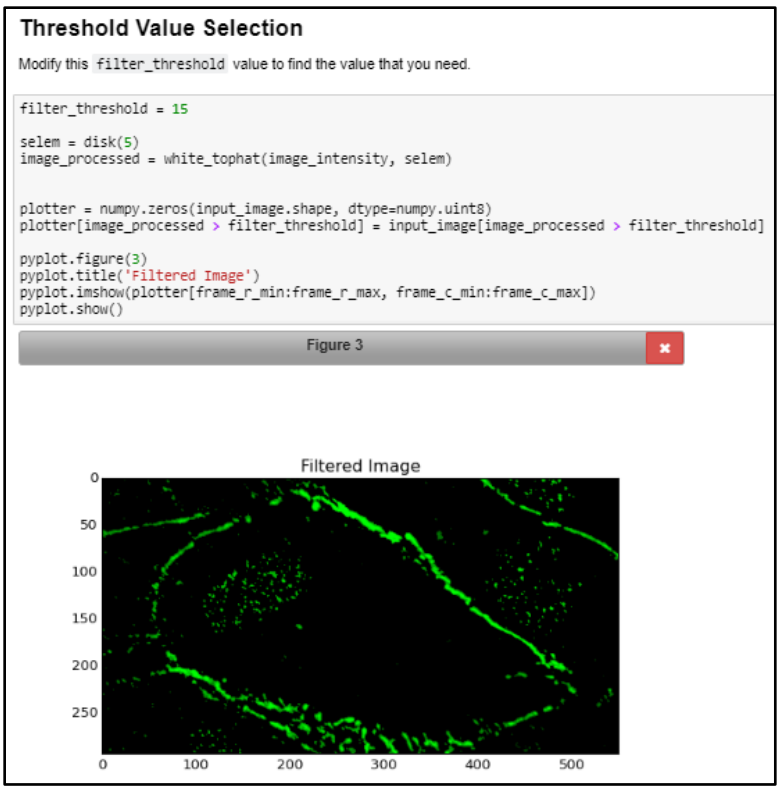

- NOTE: Repeat this step for several cells to determine the optimal threshold value for the images within your experiment. Be sure to determine the optimal threshold level for each variant (e.g., GFP and TxRed stain).
- The optimal threshold value(s) can now be used as parameter inputs in the "Config" tab of the GUI prior to processing the code in step 25.

10. Click Ctrl+Enter in Box 7 to generate images of the cell perimeter:

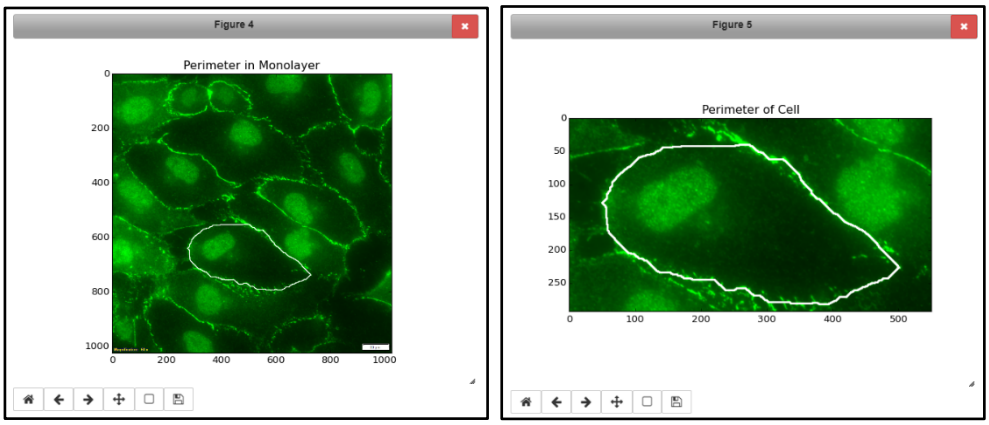

11. Clicking Ctrl+Enter in the next two boxes will generate the following images presenting the junction detail:

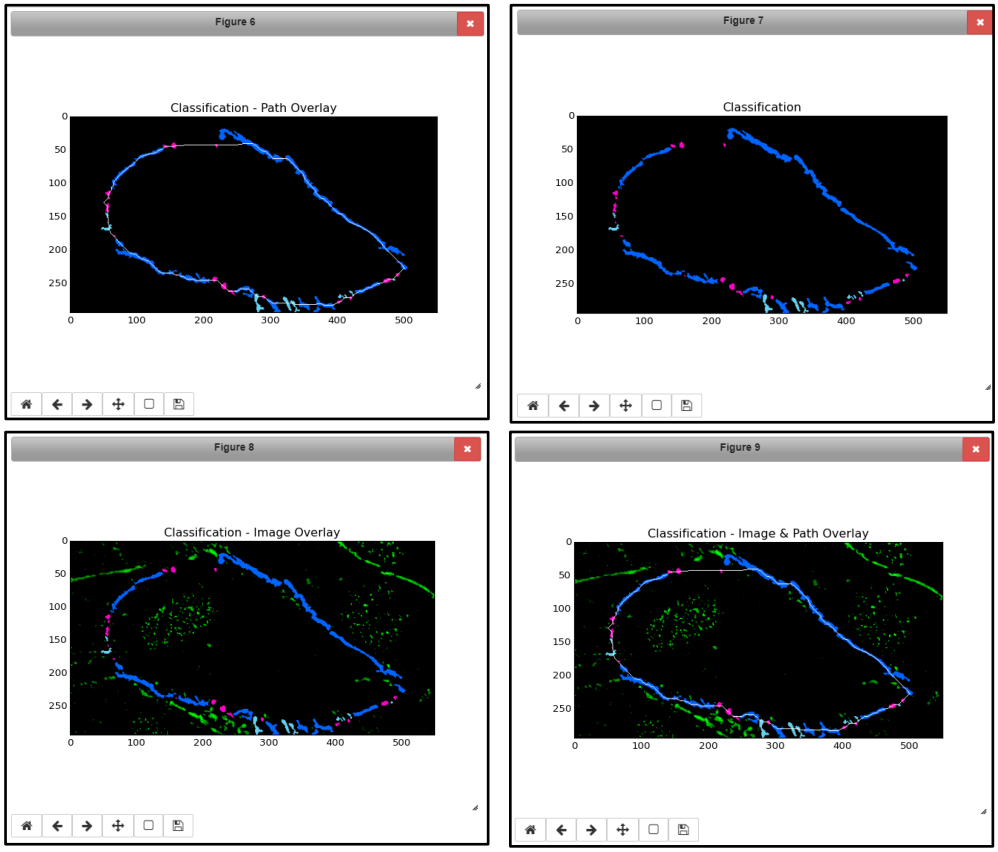

- Here, the continuous junctions are colored in blue, the punctate junctions are colored in magenta, and the perpendicular junctions are colored in light blue. These colors can be changed by modifying the RBG values specified in following section in the 1st box:

```
# Change this project name to the name of your current project
project_name = "example_project"

# Change this filename to change the image that will be loaded
image_file_name = "160503 1 kPa + Supp 60x_Multichannel_20160503_05 - GFP Deck-1.vsi.tif"

cell_index = 2

color_continuous = (0,100,255)
color_punctate = (255,0,200)
color_perpendicular = (100,210,240)
color_nojunct = (255,255,255)

# Some features are nearby but don't intersect, if you want those colored
# set this to a color otherwise set it to None
#color_none = (255,255,255)
color_none = None
```

- To save these images, remove the # symbol from the code above and re-run:

```
## Uncommenting these lines will save the generated images

#cv2.imwrite(output_prefix + ' junctions.png', plotter)
#cv2.imwrite(output_prefix + ' junctions no path.png', plotter_class)
#cv2.imwrite(output_prefix + " junctions-alpha.png", blended_plotter)
```

```
## Uncommenting these lines will save the generated images

cv2.imwrite(output_prefix + ' junctions.png', plotter)
cv2.imwrite(output_prefix + ' junctions no path.png', plotter_class)
cv2.imwrite(output_prefix + " junctions-alpha.png", blended_plotter)
```

- The images will be saved in the project docs folder: Documents\GitHub\JAnaP-master\docs
- Adding the # back in as shown on the left will prevent further images from being saved. This allows you to save only the images you are interested in.

Bibliography

1. Hawkins, B. T. & Davis, T. P. The Blood-Brain Barrier/Neurovascular Unit in Health and Disease. Pharmacol. Rev. 57: 173–185, 2005.
2. Grammas, P., Martinez, J. & Miller, B. Cerebral microvascular endothelium and the pathogenesis of neurodegenerative diseases. Expert Rev. Mol. Med. 13: 2011.
3. Palmer, A. M. The Role of the Blood Brain Barrier in Neurodegenerative Disorders and their Treatment. J. Alzheimer's Dis. 24: 643–656, 2011.
4. Abbott, N. J. & Friedman, A. Overview and introduction: the blood-brain barrier in health and disease. Epilepsia 53 Suppl 6: 1–6, 2012.
5. Weiss, N., Miller, F., Cazaubon, S. & Couraud, P. O. The blood-brain barrier in brain homeostasis and neurological diseases. Biochim. Biophys. Acta - Biomembr. 1788: 842–857, 2009.
6. Wood, M. J., O'Loughlin, A. J. & Lakhal, S. Exosomes and the blood–brain barrier: implications for neurological diseases. Ther. Deliv. 2: 1095–1099, 2011.
7. Abbott, N. J., Patabendige, A. A. K., Dolman, D. E. M., Yusof, S. R. & Begley, D. J. Structure and function of the blood-brain barrier. Neurobiol. Dis. 37: 13–25, 2010.
8. Wong, A. D., Ye, M., Levy, A. F., Rothstein, J. D., Bergles, D. E. & Searson, P. C. The blood-brain barrier: an engineering perspective. Front. Neuroeng. 6: 2013.
9. Abbott, N. J., Patabendige, A. A. K., Dolman, D. E. M., Yusof, S. R. &

Begley, D. J. Structure and function of the blood–brain barrier. Neurobiol. Dis. 37: 13–25, 2010.

10. Cardoso, F. L., Brites, D. & Brito, M. A. Looking at the blood-brain barrier: molecular anatomy and possible investigation approaches. Brain Res. Rev. 64: 328–63, 2010.

11. Fanning, A. S., Jameson, B. J., Jesaitis, L. A. & Anderson, J. M. The Tight Junction Protein ZO-1 Establishes a Link between the Transmembrane Protein Occludin and the Actin Cytoskeleton. J. Biol. Chem. 273: 29745–29753, 1998.

12. Dejana, E., Orsenigo, F. & Lampugnani, M. G. The role of adherens junctions and VE-cadherin in the control of vascular permeability. J. Cell Sci. 121: 2008.

13. Abbott, N. J., Rönnbäck, L. & Hansson, E. Astrocyte–endothelial interactions at the blood–brain barrier. Nat. Rev. Neurosci. 7: 41–53, 2006.

14. Tornavaca, O., Chia, M., Dufton, N., Almagro, L. O., Conway, D. E., Randi, A. M., Schwartz, M. A., Matter, K. & Balda, M. S. ZO-1 controls endothelial adherens junctions, cell-cell tension, angiogenesis, and barrier formation. J. Cell Biol. 208: 821–838, 2015.

15. Onken, M. D., Mooren, O. L., Mukherjee, S., Shahan, S. T., Li, J. & Cooper, J. A. Endothelial monolayers and transendothelial migration depend on mechanical properties of the substrate. Cytoskeleton 71: 695–706, 2014.

16. Sakolish, C. M., Esch, M. B., Hickman, J. J., Shuler, M. L. & Mahler, G. J. Modeling Barrier Tissues In Vitro: Methods, Achievements, and Challenges. EBioMedicine 5: 30–39, 2016.

17. Potente, M. & Mäkinen, T. Vascular heterogeneity and specialization in

development and disease. Nat. Rev. Mol. Cell Biol. 18: 477–494, 2017.

18. Aird, W. C. Phenotypic heterogeneity of the endothelium: II. Representative vascular beds. Circ. Res. 100: 174–190, 2007.

19. Aird, W. C. Phenotypic heterogeneity of the endothelium: I. Structure, function, and mechanisms. Circ. Res. 100: 158–173, 2007.

20. Cerutti, C. & Ridley, A. J. Endothelial cell-cell adhesion and signaling. Exp. Cell Res. 358: 31–38, 2017.

21. Dejana, E., Orsenigo, F., Molendini, C., Baluk, P. & Mcdonald, D. M. Organization and signaling of endothelial cell-to-cell junctions in various regions of the blood and lymphatic vascular trees. Cell Tissue Res. 335: 17–25, 2009.

22. Liebner, S., Cavallaro, U. & Dejana, E. The Multiple Languages of Endothelial Cell-to-Cell Communication. Arter. Thromb Vasc Biol. 26: 1431–1438, 2006.

23. Dejana, E., Tournier-Lasserve, E. & Weinstein, B. M. The Control of Vascular Integrity by Endothelial Cell Junctions: Molecular Basis and Pathological Implications. Dev. Cell 16: 209–221, 2009.

24. Wahl-Jensen, V. M., Afanasieva, T. A., Seebach, J., Ströher, U., Feldmann, H. & Schnittler, H.-J. Effects of Ebola Virus Glycoproteins on Endothelial Cell Activation and Barrier Function. J. Virol. 79: 10442–10450, 2005.

25. Aird, W. C. The role of the endothelium in severe sepsis and multiple organ dysfunction syndrome. Blood 101: 3765–3777, 2003.

26. Clark, P. R., Kim, R. K., Pober, J. S. & Kluger, M. S. Tumor necrosis factor disrupts claudin-5 endothelial tight junction barriers in two distinct NF-KB-

dependent phases. PLoS One 10: 1–21, 2015.

27. Seebach, J., Cao, J. & Schnittler, H. J. Quantitative dynamics of VE-cadherin at endothelial cell junctions at a glance: basic requirements and current concepts. Discoveries 4: e63, 2016.

28. Ferreri, D. M., Minnear, F. L., Yin, T., Kowalczyk, A. P. & Vincent, P. A. N-Cadherin Levels in Endothelial Cells Are Regulated by Monolayer Maturity and p120 Availability. Cell Commun. Adhes. 15: 333–349, 2009.

29. Rai, H. & Ahmed, J. *N-Cadherin: A Marker Of Epithelial To Mesenchymal Transition In Tumor Progression*. *The Internet Journal of Oncology* 10: (2014).

30. Taddei, A., Giampietro, C., Conti, A., Orsenigo, F., Breviario, F., Pirazzoli, V., Potente, M., Daly, C., Dimmeler, S. & Dejana, E. Endothelial adherens junctions control tight junctions by VE-cadherin-mediated upregulation of claudin-5. Nat. Cell Biol. 10: 923–934, 2008.

31. Giampietro, C., Taddei, A., Corada, M., Sarra-Ferraris, G. M., Alcalay, M., Cavallaro, U., Orsenigo, F., Lampugnani, M. G. & Dejana, E. Overlapping and divergent signaling pathways of N-cadherin and VE-cadherin in endothelial cells. 2012. doi:10.1182/blood-2011-09

32. Bazzoni, G. & Dejana, E. Endothelial Cell-to-Cell Junctions: Molecular Organization and Role in Vascular Homeostasis. Physiol. Rev. 84: 869–901, 2004.

33. Hatanaka, K., Simons, M. & Murakami, M. Phosphorylation of VE-cadherin controls endothelial phenotypes via p120-catenin coupling and Rac1

activation. Am J Physiol Hear. Circ Physiol 300: 162–172, 2011.

34. Stockton, R. A., Schaefer, E. & Schwartz, M. A. p21-activated Kinase Regulates Endothelial Permeability through Modulation of Contractility*. 2004. doi:10.1074/jbc.M408877200

35. Bazzoni, G. Endothelial tight junctions: permeable barriers of the vesselwall. ThrombHaemost 95: 36–42, 2006.

36. Lampugnani, M. G., Orsenigo, F., Gagliani, M. C., Tacchetti, C. & Dejana, E. Vascular endothelial cadherin controls VEGFR-2 internalization and signaling from intracellular compartments. J. Cell Biol. 174: 593–604, 2006.

37. Furuse, M. & Tsukita, S. Claudins in occluding junctions of humans and flies. Trends Cell Biol. 16: 181–8, 2006.

38. Gavard, J. & Gutkind, J. S. VE-cadherin and claudin-5: it takes two to tango. Nat Cell Biol 10: 883–885, 2008.

39. Colegio, O. R., Van Itallie, C. M., Mccrea, H. J., Rahner, C., Anderson, J. M. & Melvin, J. Claudins create charge-selective channels in the paracellular pathway between epithelial cells. Am J Physiol Cell Physiol 283: 142–147, 2002.

40. Yeung, D., Manias, J. L., Stewart, D. J. & Nag, S. Decreased junctional adhesion molecule-A expression during blood-brain barrier breakdown. Acta Neuropathol 115: 635–642, 2008.

41. Balda, M. S., Gonzalez-Mariscal, L., Matter, K., Cereijido, M. & Anderson, J. M. Assembly of the tight junction: the role of diacylglycerol. J. Cell Biol. 123: 293–302, 1993.

42. Andreeva, A. Y., Krause, E., Müller, E. C., Blasig, I. E. & Utepbergenov, D. I. Protein kinase C regulates the phosphorylation and cellular localization of occludin. J. Biol. Chem. 276: 38480–6, 2001.

43. Wolburg, H., Neuhaus, J., Kniesel, U., Krauss, B., Schmid, E. M., Ocalan, M., Farrell, C. & Risau, W. Modulation of tight junction structure in blood-brain barrier endothelial cells. Effects of tissue culture, second messengers and cocultured astrocytes. J. Cell Sci. 107: 1994.

44. Turner, J. R., Angle, J. M., Black, E. D., Joyal, J. L., Sacks, D. B. & Madara, J. L. PKC-dependent regulation of transepithelial resistance: roles of MLC and MLC kinase. Am. J. Physiol. Physiol. 277: C554–C562, 1999.

45. Meyer, T. N., Schwesinger, C., Ye, J., Denker, B. M. & Nigam, S. K. Reassembly of the Tight Junction after Oxidative Stress Depends on Tyrosine Kinase Activity*. 2001. doi:10.1074/jbc.M011477200

46. Staddon, J. M., Herrenknecht, K., Smales, C. & Rubin, L. L. Evidence that tyrosine phosphorylation may increase tight junction permeability. J. Cell Sci. 108: 609–619, 1995.

47. Kevil, C. G., Oshima, T., Alexander, B., Coe, L. L., Steven Alexander, J., Alex-ander, B. & Steven Alexander, J. H. H2O2-mediated permeability: role of MAPK and occludin. Am. J. Physiol. - Cell Physioloigy 279: C21–C30, 2000.

48. Beese, M., Wyss, K., Haubitz, M. & Kirsch, T. Effect of cAMP derivates on assembly and maintenance of tight junctions in human umbilical vein endothelial cells. BMC Cell Biol. 11: 68, 2010.

49. Patterson, C. E., Lum, H., Schaphorst, K. L., Verin, A. D. & Garcia, J. G. Regulation of endothelial barrier function by the cAMP-dependent protein kinase. Endothelium 7: 287–308, 2000.

50. Cullere, X., Shaw, S. K., Andersson, L., Hirahashi, J., Luscinskas, F. W. & Mayadas, T. N. Regulation of vascular endothelial barrier function by Epac, a cAMP-activated exchange factor for Rap GTPase. Blood 105: 1950–5, 2005.

51. Sporbert, A., Mertsch, K., Smolenski, A., Haseloff, R. F., Schonfelder, G., Paul, M., Ruth, P., Walter, U. & Blasig, I. E. *Phosphorylation of vasodilator-stimulated phosphoprotein: a consequence of nitric oxide-and cGMP-mediated signal transduction in brain capillary endothelial cells and astrocytes*. *Molecular Brain Research* 67: (1999).

52. Mayhan, W. G. VEGF increases permeability of the blood-brain barrier via a nitric oxide synthase/cGMP-dependent pathway. Am. J. Physiol. - Cell Physiol. C1148–C1153, 1999.

53. Nieuw Amerongen, V. G. P., Beckers, C. M. L., Achekar, I. D., Zeeman, S., Musters, R. J. P. & Van Hinsbergh, V. W. M. Involvement of Rho Kinase in Endothelial Barrier Maintenance. Arterioscler. Thromb. Vasc. Biol. 27: 2332–2339, 2007.

54. Huveneers, S., Oldenburg, J., Spanjaard, E., van der Krogt, G., Grigoriev, I., Akhmanova, A., Rehmann, H. & de Rooij, J. Vinculin associates with endothelial VE-cadherin junctions to control force-dependent remodeling. J. Cell Biol. 196: 641–52, 2012.

55. Baluk, P., Fuxe, J., Hashizume, H., Romano, T., Lashnits, E., Butz, S.,

Vestweber, D., Corada, M., Molendini, C., Dejana, E. & McDonald, D. M. Functionally specialized junctions between endothelial cells of lymphatic vessels. J. Exp. Med. 204: 2349–2362, 2007.

56. Wegener, J. & Seebach, J. Experimental tools to monitor the dynamics of endothelial barrier function: A survey of in vitro approaches. Cell Tissue Res. 355: 485–514, 2014.

57. Bates, D. O. Vascular endothelial growth factors and vascular permeability. Cardiovasc. Res. 87: 262–271, 2010.

58. Jo, H., Dull, R. 0, Hollis, T. M. & Tarbell, J. M. Endothelial albumin permeability is shear dependent, time dependent, and reversible. Am. J. Physiol. - Hear. Circ. Physiol. 260: H1992–H1996, 1991.

59. Genes, L. I. et al. Technique for Real-Time Measurements of Endothelial Permeability in a Microfluidic Membrane Chip Using Laser-Induced Fluorescence Detection. Anal. Chem. 77: 808–816, 2005.

60. Phelps, J. E. & Depaola, N. *Spatial variations in endothelial barrier function in disturbed flows in vitro*. (2000).

61. Michaelis, S., Rommel, C. E., Endell, J., Göring, P., Wehrspohn, R., Steinem, C., Janshoff, A., Galla, H.-J. & Wegener, J. Macroporous silicon chips for laterally resolved, multi-parametric analysis of epithelial barrier function. Lab Chip 12: 2329–2336, 2012.

62. Dubrovskyi, O., Birukova, A. A. & Birukov, K. G. Measurement of local permeability at subcellular level in cell models of agonist- and ventilator-induced lung injury. Lab. Investig. 93: 254–263, 2013.

63. Bergner, S., Vatsyayan, P. & Matysik, F.-M. Recent advances in high resolution scanning electrochemical microscopy of living cells-A review. Anal. Chim. Acta 775: 1–13, 2013.

64. Rothermal, A., Nieber, M., Muler, J., Wolf, P., Schmidt, M. & Robitzki, A. Real-time measurement of PMA-induced cellular alterations by microelectrode array-based impedance spectroscopy. Biotechniques 41: 445–450, 2006.

65. Gitter, A. H., Bertog, M., Schulzke, J.-D. & Fromm, M. Measurement of paracellular epithelial conductivity by conductance scanning. Eur. J. Physiol. 434: 830–840, 1997.

66. Claude, P. *Morphological Factors Influencing Transepithelial Permeability" A Model for the Resistance of the Zonula Occludens*. *J. Membrane Biol* 39: (1978).

67. Seebach, J., Donnert, G., Kronstein, R., Werth, S., Wojciak-Stothard, B., Falzarano, D., Mrowietz, C., Hell, S. W. & Schnittler, H.-J. Regulation of endothelial barrier function during flow-induced conversion to an arterial phenotype. Cardiovasc. Res. 75: 596–607, 2007.

68. Kakei, Y., Akashi, M., Shigeta, T., Hasegawa, T. & Komori, T. Alteration of Cell-Cell Junctions in Cultured Human Lymphatic Endothelial Cells with Inflammatory Cytokine Stimulation. Lymphat. Res. Biol. 12: 136–143, 2014.

69. Seebach, J., Abdallah, A. T., Lenk, J., Lindemann, N., Jiang, X., Brinkmann, K., Bogdan, S. & Schnittler, H.-J. The CellBorderTracker, a novel tool to quantitatively analyze spatiotemporal endothelial junction dynamics at the subcellular level. Histochem. Cell Biol. 144: 517–532, 2015.

70. Adamson, R. H., Curry, F. E., Adamson, G., Liu, B., Jiang, Y., Aktories, K., Barth, H., Daigeler, A., Golenhofen, N., Ness, W. & Drenckhahn, D. Rho and rho kinase modulation of barrier properties: cultured endothelial cells and intact microvessels of rats and mice. J. Physiol. 539: 295–308, 2002.

71. Taha, A. A., Taha, M., Seebach, J. & Schnittler, H.-J. ARP2/3-mediated junction-associated lamellipodia control VE-cadherin–based cell junction dynamics and maintain monolayer integrity. Mol. Biol. Cell 25: 245–256, 2014.

72. Furihata, T., Kawamatsu, S., Ito, R., Saito, K., Suzuki, S., Kishida, S., Saito, Y., Kamiichi, A. & Chiba, K. Hydrocortisone enhances the barrier properties of HBMEC/ciβ, a brain microvascular endothelial cell line, through mesenchymal-to-endothelial transition-like effects. Fluids Barriers CNS 12: 1–15, 2015.

73. Mckenzie, J. A. G. & Ridley, A. J. Roles of Rho/ROCK and MLCK in TNF-a-Induced Changes in Endothelial Morphology and Permeability. J. Cell. Physiol 213: 221–228, 2007.

74. Millán, J., Cain, R. J., Reglero-Real, N., Bigarella, C., Marcos-Ramiro, B., Fernández-Martín, L., Correas, I. & Ridley, A. J. Adherens junctions connect stress fibres between adjacent endothelial cells. BMC Biol. 8: 11, 2010.

75. Dorland, Y. L. & Huveneers, S. Cell–cell junctional mechanotransduction in endothelial remodeling. Cell. Mol. Life Sci. 74: 279–292, 2017.

76. Stroka, K. M. & Aranda-Espinoza, H. Endothelial cell substrate stiffness influences neutrophil transmigration via myosin light chain kinase-dependent

cell contraction. Blood 118: 1632–1640, 2011.

77. Li, B., Zhao, W.-D., Tan, Z.-M., Fang, W.-G., Zhu, L. & Chen, Y.-H. Involvement of Rho/ROCK signalling in small cell lung cancer migration through human brain microvascular endothelial cells. FEBS Lett. 580: 4252–60, 2006.

78. Andrews, A. M., Lutton, E. M., Merkel, S. F., Razmpour, R. & Ramirez, S. H. Mechanical Injury Induces Brain Endothelial-Derived Microvesicle Release: Implications for Cerebral Vascular Injury during Traumatic Brain Injury. Front. Cell. Neurosci. 10: 43, 2016.

79. Lippmann, E. S., Al-Ahmad, A., Azarin, S. M., Palecek, S. P. & Shusta, E. V. A retinoic acid-enhanced, multicellular human blood-brain barrier model derived from stem cell sources. Sci. Transl. Med. 4: 2014.

80. Hoelzle, M. K. & Svitkina, T. The cytoskeletal mechanisms of cell-cell junction formation in endothelial cells. Mol. Biol. Cell 23: 310–23, 2012.

81. Adamson, R. H., Liu, B., Fry, G. N., Rubin, L. L. & Curry, F. E. Microvascular permeability and number of tight junctions are modulated by cAMP. Am. Physiol. Soc. 274: H1885–H1894, 1998.

82. Fan, J., Ray, P., Lu, Y. W., Kaur, G., Schwarz, J. J. & Wan, L. Q. Cell chirality regulates intercellular junctions and endothelial permeability. Sci. Adv. 4: eaat2111, 2018.

83. Katt, M. E., Linville, R. M., Mayo, L. N., Xu, Z. S. & Searson, P. C. Functional brain-specific microvessels from iPSC-derived human brain microvascular endothelial cells: the role of matrix composition on monolayer

formation. Fluids Barriers CNS 15: 7, 2018.

84. Huynh, J., Nishimura, N., Rana, K., Peloquin, J. M., Califano, J. P., Montague, C. R., King, M. R., Schaffer, C. B. & Reinhart-King, C. A. Age-Related Intimal Stiffening Enhances Endothelial Permeability and Leukocyte Transmigration. Sci. Transl. Med. 3: 112ra122-112ra122, 2011.

85. Wu, Y., Kanchanawong, P. & Zaidel-Bar, R. Actin-Delimited Adhesion-Independent Clustering of E-Cadherin Forms the Nanoscale Building Blocks of Adherens Junctions. Dev. Cell 32: 139–154, 2015.

86. Ting, L. H., Jahn, J. R., Jung, J. I., Shuman, B. R., Feghhi, S., Han, S. J., Rodriguez, M. L. & Sniadecki, N. J. Flow mechanotransduction regulates traction forces, intercellular forces, and adherens junctions. Am J Physiol Hear. Circ Physiol 302: 2220–2229, 2012.

87. Lagendijk, A. K., Gomez, G. A., Baek, S., Hesselson, D., Hughes, W. E., Paterson, S., Conway, D. E., Belting, H. G., Affolter, M., Smith, K. A., Schwartz, M. A., Yap, A. S. & Hogan, B. M. Live imaging molecular changes in junctional tension upon VE-cadherin in zebrafish. Nat. Commun. 8: 2017.

88. Canfield, S. G., Stebbins, M. J., Morales, B. S., Asai, S. W., Vatine, G. D., Svendsen, C. N., Palecek, S. P. & Shusta, E. V. An isogenic blood-brain barrier model comprising brain endothelial cells, astrocytes, and neurons derived from human induced pluripotent stem cells. J. Neurochem. 140: 874–888, 2017.

89. Kim, B. J., Bee, O. B., Mcdonagh, M. A., Stebbins, M. J., Palecek, S. P., Doran, K. S. & Shusta, E. V. Modeling Group B Streptococcus and Blood-

Brain Barrier Interaction by Using Induced Pluripotent Stem Cell-Derived Brain Endothelial Cells. mSphere 2: e00398-17, 2017.

90. Barrett, W. A. & Mortensen, E. N. *Interactive live-wire boundary extraction*. *Medical Image Analysis* 1: (1996).

91. AIRD, W. C. Spatial and temporal dynamics of the endothelium. J. Thromb. Haemost. 3: 1392–1406, 2005.

92. Peloquin, J., Huynh, J., Williams, R. M. & Reinhart-King, C. A. Indentation measurements of the subendothelial matrix in bovine carotid arteries. J. Biomech. 44: 815–821, 2011.

93. Morrison, T. M., Choi, G., Zarins, C. K. & Taylor, C. A. Circumferential and longitudinal cyclic strain of the human thoracic aorta: age-related changes. J. Vasc. Surg. 49: 1029–1036, 2009.

94. Lam, R. H. W., Sun, Y., Chen, W. & Fu, J. Elastomeric microposts integrated into microfluidics for flow-mediated endothelial mechanotransduction analysis. Lab Chip 12: 1865–1873, 2012.

95. Polacheck, W. J., Li, R., Uzel, S. G. M. & Kamm, R. D. Microfluidic platforms for mechanobiology. Lab Chip 13: 2252–2267, 2013.

96. Nge, P. N., Rogers, C. I. & Woolley, A. T. Advances in Microfluidic Materials, Functions, Integration, and Applications. Chem. Rev. 113: 2550–2583, 2013.

97. Vickers, D. A. L., Chory, E. J., Harless, M. C. & Murthy, S. K. p38 Signaling and Receptor Recycling Events in a Microfluidic Endothelial Cell Adhesion Assay. PLoS One 8: e65828, 2013.

98. Raman, P. S., Paul, C. D., Stroka, K. M. & Konstantopoulos, K. Probing cell traction forces in confined microenvironments. Lab Chip 13: 4599–4607, 2013.

99. Shemesh, J., Jalilian, I., Shi, A., Heng Yeoh, G., Knothe Tate, M. L. & Ebrahimi Warkiani, M. Flow-induced stress on adherent cells in microfluidic devices. Lab Chip 15: 4114–4127, 2015.

100. Freund, J. B., Goetz, J. G., Hill, K. L. & Vermot, J. Fluid flows and forces in development: functions, features and biophysical principles. Development 139: 1229–1245, 2012.

101. Young, E. W. K. Advances in microfluidic cell culture systems for studying angiogenesis. J. Lab. Autom. 18: 427–436, 2013.

102. Bersini, S., Yazdi, I. K., Talò, G., Shin, S. R., Moretti, M. & Khademhosseini, A. Cell-microenvironment interactions and architectures in microvascular systems. Biotechnol. Adv. 34: 1113–1130, 2016.

103. Koutsiaris, A. G. Wall shear stress in the human eye microcirculation in vivo, segmental heterogeneity and performance of in vitro cerebrovascular models. Clin. Hemorheol. Microcirc. 63: 15–33, 2016.

104. Wong, K. H. K., Chan, J. M., Kamm, R. D. & Tien, J. Microfluidic Models of Vascular Functions. Annu. Rev. Biomed. Eng. 14: 205–230, 2012.

105. Bianchi, E., Molteni, R., Pardi, R. & Dubini, G. Microfluidics for in vitro biomimetic shear stress-dependent leukocyte adhesion assays. J. Biomech. 46: 276–283, 2013.

106. Samatov, T. R., Shkurnikov, M. U., Tonevitskaya, S. A. & Tonevitsky, A. G. Modelling the metastatic cascade by in vitro microfluidic platforms. Prog.

Histochem. Cytochem. 49: 21–29, 2015.

107. Bersini, S., Jeon, J. S., Moretti, M. & Kamm, R. D. In vitro models of the metastatic cascade: from local invasion to extravasation. Drug Discov. Today 19: 735–742, 2014.

108. Chen, Y., Chan, H. N., Michael, S. A., Shen, Y., Chen, Y., Tian, Q., Huang, L. & Wu, H. A microfluidic circulatory system integrated with capillary-assisted pressure sensors. Lab Chip 17: 653–662, 2017.

109. Liu, M.-C., Shih, H.-C., Wu, J.-G., Weng, T.-W., Wu, C.-Y., Lu, J.-C. & Tung, Y.-C. Electrofluidic pressure sensor embedded microfluidic device: a study of endothelial cells under hydrostatic pressure and shear stress combinations. Lab Chip 13: 1743–1753, 2013.

110. Hattori, K., Munehira, Y., Kobayashi, H., Satoh, T., Sugiura, S. & Kanamori, T. Microfluidic perfusion culture chip providing different strengths of shear stress for analysis of vascular endothelial function. J. Biosci. Bioeng. 118: 327–332, 2014.

111. Abaci, H. E., Devendra, R., Soman, R., Drazer, G. & Gerecht, S. Microbioreactors to manipulate oxygen tension and shear stress in the microenvironment of vascular stem and progenitor cells. Biotechnol. Appl. Biochem. 59: 97–105, 2012.

112. Rotenberg, M. Y., Ruvinov, E., Armoza, A. & Cohen, S. A multi-shear perfusion bioreactor for investigating shear stress effects in endothelial cell constructs. Lab Chip 12: 2696–2703, 2012.

113. Voyvodic, P. L., Min, D. & Baker, A. B. A multichannel dampened flow

system for studies on shear stress-mediated mechanotransduction. Lab Chip 12: 3322–3330, 2012.

114. Zhou, M., Zhang, X., Wen, X., Wu, T., Wang, W., Yang, M., Wang, J., Fang, M., Lin, B. & Lin, H. Development of a Functional Glomerulus at the Organ Level on a Chip to Mimic Hypertensive Nephropathy. Sci. Rep. 6: 31771, 2016.

115. Zheng, F., Fu, F., Cheng, Y., Wang, C., Zhao, Y. & Gu, Z. Organ-on-a-Chip Systems: Microengineering to Biomimic Living Systems. Small 12: 2253–2282, 2016.

116. Verhulsel, M., Vignes, M., Descroix, S., Malaquin, L., Vignjevic, D. M. & Viovy, J.-L. A review of microfabrication and hydrogel engineering for micro-organs on chips. Biomaterials 35: 1816–1832, 2014.

117. Yum, K., Hong, S. G. & Lee, L. P. Physiologically relevant organs on chips. Biotechnol. J. 9: 16–27, 2014.

118. Kim, D., Wu, X., Young, A. T. & Haynes, C. L. Microfluidics-based in vivo mimetic systems for the study of cellular biology. Acc. Chem. Res. 47: 1165–1173, 2014.

119. Tkachenko, E., Gutierrez, E., Saikin, S. K., Fogelstrand, P., Kim, C., Groisman, A. & Ginsberg, M. H. The nucleus of endothelial cell as a sensor of blood flow direction. Biol. Open 0: 1–6, 2013.

120. Reinitz, A., DeStefano, J., Ye, M., Wong, A. D. & Searson, P. C. Human brain microvascular endothelial cells resist elongation due to shear stress. Microvasc. Res. 99: 8–18, 2015.

121. Helms, H. C., Abbott, N. J., Burek, M., Cecchelli, R., Couraud, P.-O., Deli, M. A., Förster, C., Galla, H. J., Romero, I. A., Shusta, E. V, Stebbins, M. J., Vandenhaute, E., Weksler, B. & Brodin, B. In vitro models of the blood-brain barrier: An overview of commonly used brain endothelial cell culture models and guidelines for their use. J. Cereb. blood flow Metab. 36: 862–90, 2016.

122. van der Helm, M. W., van der Meer, A. D., Eijkel, J. C. T., van den Berg, A. & Segerink, L. I. Microfluidic organ-on-chip technology for blood-brain barrier research. Tissue barriers 4: e1142493, 2016.

123. Carafoli, E. Intracellular Calcium Homeostasis. Ann. Rev. Biochem 56: 395–433, 1987.

124. Chen, Z.-Z., Gao, Z.-M., Zeng, D.-P., Liu, B., Luan, Y. & Qin, K.-R. A Y-Shaped Microfluidic Device to Study the Combined Effect of Wall Shear Stress and ATP Signals on Intracellular Calcium Dynamics in Vascular Endothelial Cells. Micromachines 7: 213, 2016.

125. Lafaurie-Janvore, J., Antoine, E. E., Perkins, S. J., Babataheri, A. & Barakat, A. I. A simple microfluidic device to study cell-scale endothelial mechanotransduction. Biomed. Microdevices 18: 63, 2016.

126. Yamamoto, K., Furuya, K., Nakamura, M., Kobatake, E., Sokabe, M. & Ando, J. Visualization of flow-induced ATP release and triggering of Ca2+ waves at caveolae in vascular endothelial cells. J. Cell Sci. 124: 3477–3483, 2011.

127. Richter, T., Floetenmeyer, M., Ferguson, C., Galea, J., Goh, J., Lindsay, M. R., Morgan, G. P., Marsh, B. J. & Parton, R. G. High-Resolution 3D Quantitative Analysis of Caveolar Ultrastructure and Caveola–Cytoskeleton Interactions.

Traffic 9: 893–909, 2008.

128. Parton, R. G. & del Pozo, M. A. Caveolae as plasma membrane sensors, protectors and organizers. Nat. Rev. Mol. Cell Biol. 14: 98–112, 2013.

129. Baratchi, S., Tovar-Lopez, F. J., Khoshmanesh, K., Grace, M. S., Darby, W., Almazi, J., Mitchell, A. & McIntyre, P. Examination of the role of transient receptor potential vanilloid type 4 in endothelial responses to shear forces. Biomicrofluidics 8: 044117, 2014.

130. B. Nilius, J. Vriens, J. Prenen, G. Droogmans, T. V. TRPV4 calcium entry channel: a paradigm for gating diversity. Am. J. Physiol. Cell Physiol. 286: C195–C205, 2004.

131. Soffe, R., Baratchi, S., Tang, S.-Y., Mitchell, A., Mcintyre, P. & Khoshmanesh, K. Concurrent shear stress and chemical stimulation of mechano-sensitive cells by discontinuous dielectrophoresis. Biomicrofluidics 10: 024117, 2016.

132. Compton, J. L., Luo, J. C., Ma, H., Botvinick, E. & Venugopalan, V. High-throughput optical screening of cellular mechanotransduction. Nat. Photonics 8: 710–715, 2014.

133. Marin, T., Gongol, B., Chen, Z., Woo, B., Subramaniam, S., Chien, S. & Shyy, J. Y.-J. Mechanosensitive microRNAs—role in endothelial responses to shear stress and redox state. Free Radic. Biol. Med. 64: 61–68, 2013.

134. Raasch, M., Rennert, K., Jahn, T., Peters, S., Henkel, T., Huber, O., Schulz, I., Becker, H., Lorkowski, S., Funke, H. & Mosig, A. Microfluidically supported biochip design for culture of endothelial cell layers with improved perfusion

conditions. Biofabrication 7: 015013, 2015.

135. Mina, S. G., Wang, W., Cao, Q., Huang, P., Murray, B. T. & Mahler, G. J. Shear stress magnitude and transforming growth factor-βeta 1 regulate endothelial to mesenchymal transformation in a three-dimensional culture microfluidic device. RSC Adv. 6: 85457–85467, 2016.

136. Mahler, G. J., Frendl, C. M., Cao, Q. & Butcher, J. T. Effects of shear stress pattern and magnitude on mesenchymal transformation and invasion of aortic valve endothelial cells. Biotechnol. Bioeng. 111: 2326–2337, 2014.

137. Thomas, A., Daniel Ou-Yang, H., Lowe-Krentz, L., Muzykantov, V. R. & Liu, Y. Biomimetic channel modeling local vascular dynamics of pro-inflammatory endothelial changes. Biomicrofluidics 10: 014101, 2016.

138. Fontijn, R. D., Volger, O. L., Van Der Pouw-Kraan, T. C., Doddaballapur, A., Leyen, T., Baggen, J. M., Boon, R. A. & Horrevoets, A. J. G. Expression of Nitric Oxide-Transporting Aquaporin-1 Is Controlled by KLF2 and Marks Non-Activated Endothelium In Vivo. PLoS One 10: e0145777, 2015.

139. Pfenniger, A., Wong, C., Sutter, E., Cuhlmann, S., Dunoyer-Geindre, S., Mach, F., Horrevoets, A. J., Evans, P. C., Krams, R. & Kwak, B. R. Shear stress modulates the expression of the atheroprotective protein Cx37 in endothelial cells. J. Mol. Cell. Cardiol. 53: 299–309, 2012.

140. Huang, R.-T., Wu, D., Meliton, A., Oh, M.-J., Krause, M., Lloyd, J. A., Nigdelioglu, R., Hamanaka, R. B., Jain, M. K., Birukova, A., Kress, J. P., Birukov, K. G., Mutlu, G. M. & Fang, Y. Experimental Lung Injury Reduces KLF2 to Increase Endothelial Permeability via Regulation of RAPGEF3-Rac1

Signaling. Am. J. Respir. Crit. Care Med. 195: 639–651, 2017.

141. Liu, X. F., Yu, J. Q., Dalan, R., Liu, A. Q. & Luo, K. Q. Biological factors in plasma from diabetes mellitus patients enhance hyperglycaemia and pulsatile shear stress-induced endothelial cell apoptosis. Integr. Biol. 6: 511–522, 2014.

142. DeVerse, J. S., Sandhu, A. S., Mendoza, N., Edwards, C. M., Sun, C., Simon, S. I. & Passerini, A. G. Shear stress modulates VCAM-1 expression in response to TNF-α and dietary lipids via interferon regulatory factor-1 in cultured endothelium. Am. J. Physiol. - Hear. Circ. Physiol. 305: H1149-1157, 2013.

143. Alonzo, L. F., Moya, M. L., Shirure, V. S. & George, S. C. Microfluidic device to control interstitial flow-mediated homotypic and heterotypic cellular communication. Lab Chip 15: 3521–3529, 2015.

144. Boldock, L., Wittkowske, C. & Perrault, C. M. Microfluidic traction force microscopy to study mechanotransduction in angiogenesis. Microcirculation 2017. doi:10.1111/micc.12361

145. Du, Y., Herath, S. C. B., Wang, Q., Wang, D., Asada, H. H. & Chen, P. C. Y. Three-Dimensional Characterization of Mechanical Interactions between Endothelial Cells and Extracellular Matrix during Angiogenic Sprouting. Sci. Rep. 6: 21362, 2016.

146. Galie, P. A., Nguyen, D.-H. T., Choi, C. K., Cohen, D. M., Janmey, P. A. & Chen, C. S. Fluid shear stress threshold regulates angiogenic sprouting. Proc. Natl. Acad. Sci. U. S. A. 111: 7968–7973, 2014.

147. Vickerman, V. & Kamm, R. D. Mechanism of a flow-gated angiogenesis

switch: early signaling events at cell–matrix and cell–cell junctions. Integr. Biol. Integr. Biol 4: 863–874, 2012.

148. Kim, S., Chung, M., Ahn, J., Lee, S. & Jeon, N. L. Interstitial flow regulates the angiogenic response and phenotype of endothelial cells in a 3D culture model. Lab Chip 16: 4189–4199, 2016.

149. Kim, S., Chung, M. & Jeon, N. L. Three-dimensional biomimetic model to reconstitute sprouting lymphangiogenesis in vitro. Biomaterials 78: 115–128, 2016.

150. Song, J. W., Daubriac, J., Tse, J. M., Bazou, D. & Munn, L. L. RhoA mediates flow-induced endothelial sprouting in a 3-D tissue analogue of angiogenesis. Lab Chip 12: 5000–5006, 2012.

151. Shamloo, A., Xu, H. & Heilshorn, S. Mechanisms of Vascular Endothelial Growth Factor-Induced Pathfinding by Endothelial Sprouts in Biomaterials. Tissue Eng. Part A 18: 320–330, 2012.

152. Shamloo, A., Mohammadaliha, N., Heilshorn, S. C. & Bauer, A. L. A Comparative Study of Collagen Matrix Density Effect on Endothelial Sprout Formation Using Experimental and Computational Approaches. Ann. Biomed. Eng. 44: 929–941, 2016.

153. Chan, K. L. S., Khankhel, A. H., Thompson, R. L., Coisman, B. J., Wong, K. H. K., Truslow, J. G. & Tien, J. Crosslinking of collagen scaffolds promotes blood and lymphatic vascular stability. J. Biomed. Mater. Res. Part A 102: 3186–3195, 2014.

154. Park, Y. K., Tu, T.-Y., Lim, S. H., Clement, I. J. M., Yang, S. Y. & Kamm, R.

D. In Vitro Microvessel Growth and Remodeling within a Three-Dimensional Microfluidic Environment. Cell. Mol. Bioeng. 7: 15–25, 2014.

155. Whisler, J. A., Chen, M. B. & Kamm, R. D. Control of Perfusable Microvascular Network Morphology Using a Multiculture Microfluidic System. Tissue Eng. Part C Methods 20: 543–552, 2014.

156. Herath, S. C. B., Sharghi-Namini, S., Du, Y., Wang, D., Ge, R., Wang, Q.-G., Asada, H. & Chen, P. C. Y. A Magneto-Microfluidic System for Investigating the Influence of an Externally Induced Force Gradient in a Collagen Type I ECM on HMVEC Sprouting. SLAS Technol. 1–12, 2016. doi:10.1177/2211068216680078

157. Stroka, K. M., Levitan, I. & Aranda-Espinoza, H. OxLDL and substrate stiffness promote neutrophil transmigration by enhanced endothelial cell contractility and ICAM-1. J. Biomech. 45: 1828–34, 2012.

158. Lampi, M. C., Faber, C. J., Huynh, J., Bordeleau, F., Zanotelli, M. R. & Reinhart-King, C. A. Simvastatin Ameliorates Matrix Stiffness-Mediated Endothelial Monolayer Disruption. PLoS One 11: e0147033, 2016.

159. Grevesse, T., Versaevel, M., Circelli, G., Desprez, S. & Gabriele, S. A simple route to functionalize polyacrylamide hydrogels for the independent tuning of mechanotransduction cues. Lab Chip 13: 777–780, 2013.

160. Kohn, J. C., Lampi, M. C. & Reinhart-King, C. A. Age-related vascular stiffening: causes and consequences. Front. Genet. 6: 2015.

161. Kohn, J. C., Zhou, D. W., Bordeleau, F., Zhou, A. L., Mason, B. N., Mitchell, M. J., King, M. R. & Reinhart-King, C. A. Cooperative Effects of Matrix

Stiffness and Fluid Shear Stress on Endothelial Cell Behavior. Biophys. J. 108: 471–478, 2015.

162. Galie, P. A., van Oosten, A., Chen, C. S. & Janmey, P. A. Application of multiple levels of fluid shear stress to endothelial cells plated on polyacrylamide gels. Lab Chip 15: 1205–1212, 2015.

163. Franco, D., Milde, F., Klingauf, M., Orsenigo, F., Dejana, E., Poulikakos, D., Cecchini, M., Koumoutsakos, P., Ferrari, A. & Kurtcuoglu, V. Accelerated endothelial wound healing on microstructured substrates under flow. Biomaterials 34: 1488–1497, 2013.

164. Robotti, F., Franco, D., Bänninger, L., Wyler, J., Starck, C. T., Falk, V., Poulikakos, D. & Ferrari, A. The influence of surface micro-structure on endothelialization under supraphysiological wall shear stress. Biomaterials 35: 8479–8486, 2014.

165. Sundararaghavan, H. G., Saunders, R. L., Hammer, D. A. & Burdick, J. A. Fiber alignment directs cell motility over chemotactic gradients. Biotechnol. Bioeng. 110: 1249–1254, 2013.

166. Morgan, J. T., Wood, J. A., Shah, N. M., Hughbanks, M. L., Russell, P., Barakat, A. I. & Murphy, C. J. Integration of basal topographic cues and apical shear stress in vascular endothelial cells. Biomaterials 33: 4126–4135, 2012.

167. Han, S., Shin, Y., Jeong, H. E., Jeon, J. S., Kamm, R. D., Huh, D., Sohn, L. L. & Chung, S. Constructive remodeling of a synthetic endothelial extracellular matrix. Sci. Rep. 5: 18290, 2015.

168. Spuul, P., Chi, P.-Y., Billottet, C., Chou, C.-F. & Génot, E. Microfluidic

devices for the study of actin cytoskeleton in constricted environments: Evidence for podosome formation in endothelial cells exposed to a confined slit. Methods 94: 65–74, 2016.

169. Zuo, Y., He, X., Yang, Y., Wei, D., Sun, J., Zhong, M., Xie, R., Fan, H. & Zhang, X. Microfluidic-based generation of functional microfibers for biomimetic complex tissue construction. Acta Biomater. 38: 153–162, 2016.

170. Wei, D., Sun, J., Bolderson, J., Zhong, M., Dalby, M. J., Cusack, M., Yin, H., Fan, H. & Zhang, X. Continuous Fabrication and Assembly of Spatial Cell-Laden Fibers for a Tissue-Like Construct via a Photolithographic-Based Microfluidic Chip. Appl. Mater. Interfaces 9: 14606–14617, 2017.

171. Ye, M., Sanchez, H. M., Hultz, M., Yang, Z., Bogorad, M., Wong, A. D. & Searson, P. C. Brain microvascular endothelial cells resist elongation due to curvature and shear stress. Sci. Rep. 4: 1–6, 2014.

172. Verbridge, S. S., Chakrabarti, A., DelNero, P., Kwee, B., Varner, J. D., Stroock, A. D. & Fischbach, C. Physicochemical regulation of endothelial sprouting in a 3D microfluidic angiogenesis model. J. Biomed. Mater. Res. Part A 101: 2948–2956, 2013.

173. Mannino, R. G., Myers, D. R., Ahn, B., Wang, Y., Rollins, M., Gole, H., Lin, A. S., Guldberg, R. E., Giddens, D. P., Timmins, L. H. & Lam, W. A. “Do-it-yourself in vitro vasculature that recapitulates in vivo geometries for investigating endothelial-blood cell interactions”. Sci. Rep. 5: 12401, 2015.

174. Westein, E., van der Meer, A. D., Kuijpers, M. J. E., Frimat, J.-P., van den Berg, A. & Heemskerk, J. W. M. Atherosclerotic geometries exacerbate

pathological thrombus formation poststenosis in a von Willebrand factor-dependent manner. Proc. Natl. Acad. Sci. U. S. A. 110: 1357–1362, 2013.

175. Simmons, C. S., Ribeiro, A. J. S. & Pruitt, B. L. Formation of composite polyacrylamide and silicone substrates for independent control of stiffness and strain. Lab Chip 13: 646–649, 2013.

176. Zheng, W., Jiang, B., Wang, D., Zhang, W., Wang, Z. & Jiang, X. A microfluidic flow-stretch chip for investigating blood vessel biomechanics. Lab Chip 12: 3441–3450, 2012.

177. Sinha, R., Le Gac, S., Verdonschot, N., van den Berg, A., Koopman, B. & Rouwkema, J. Endothelial cell alignment as a result of anisotropic strain and flow induced shear stress combinations. Sci. Rep. 6: 2016.

178. Poulin, A., Saygili Demir, C., Rosset, S., Petrova, T. V. & Shea, H. Dielectric elastomer actuator for mechanical loading of 2D cell cultures. Lab Chip 16: 3788–3794, 2016.

179. Wang, J., Fan, B., Wei, Y., Suo, X. & Ding, Y. A simple multi-well stretching device to induce inflammatory responses of vascular endothelial cells. Lab Chip 16: 360–367, 2016.

180. Stucki, A. O., Stucki, J. D., Hall, S. R. R., Felder, M., Mermoud, Y., Schmid, R. A., Geiser, T. & Guenat, O. T. A lung-on-a-chip array with an integrated bio-inspired respiration mechanism. Lab Chip 15: 1302–1310, 2015.

181. Huh, D., Leslie, D. C., Matthews, B. D., Fraser, J. P., Jurek, S., Hamilton, G. A., Thorneloe, K. S., Mcalexander, M. A. & Ingber, D. E. A Human Disease Model of Drug Toxicity–Induced Pulmonary Edema in a Lung-on-a-Chip

Microdevice. Sci. Transl. Med. 4: 2012.

182. Fede, C., Fortunati, I., Weber, V., Rossetto, N., Bertasi, F., Petrelli, L., Guidolin, D., Signorini, R., De Caro, R., Albertin, G. & Ferrante, C. Evaluation of gold nanoparticles toxicity towards human endothelial cells under static and flow conditions. Microvasc. Res. 97: 147–155, 2015.

183. Strobl, F. G., Breyer, D., Link, P., Torrano, A. A., Bräuchle, C., Schneider, M. F. & Wixforth, A. A surface acoustic wave-driven micropump for particle uptake investigation under physiological flow conditions in very small volumes. Beilstein J. Nanotechnol. 6: 414–419, 2015.

184. Li, L., Lv, X., Ostrovidov, S., Shi, X., Zhang, N. & Liu, J. Biomimetic Microfluidic Device for in Vitro Antihypertensive Drug Evaluation. Mol. Pharm. 11: 2009–2015, 2014.

185. Lamberti, G., Soroush, F., Smith, A., Kiani, M. F., Prabhakarpandian, B. & Pant, K. Adhesion patterns in the microvasculature are dependent on bifurcation angle. Microvasc. Res. 99: 19–25, 2015.

186. Kang, T., Park, C., Choi, J.-S., Cui, J.-H. & Lee, B.-J. Effects of shear stress on the cellular distribution of polystyrene nanoparticles in a biomimetic microfluidic system. J. Drug Deliv. Sci. Technol. 31: 130–136, 2016.

187. Wang, X.-Y., Fillafer, C., Pichl, C., Deinhammer, S., Hofer-Warbinek, R., Wirth, M. & Gabor, F. A multichannel acoustically driven microfluidic chip to study particle-cell interactions. Biomicrofluidics 7: 2013.

188. Samuel, S. P., Jain, N., O'Dowd, F., Paul, T., Kashanin, D., Gerard, V. A., Gun'ko, Y. K., Prina-Mello, A. & Volkov, Y. Multifactorial determinants that

govern nanoparticle uptake by human endothelial cells under flow. Int. J. Nanomedicine 7: 2943, 2012.

189. Tissue Chip for Drug Screening | National Center for Advancing Translational Sciences. Available at: https://ncats.nih.gov/tissuechip. (Accessed: 7th May 2017)

190. Fitzpatrick, S. 'Organs-on-Chips' Technology: FDA Testing Groundbreaking Science | FDA Voice. *FDA Voice* 2017. Available at: https://blogs.fda.gov/fdavoice/index.php/2017/04/organs-on-chips-technology-fda-testing-groundbreaking-science/. (Accessed: 6th June 2017)

191. Wallez, Y. & Huber, P. Endothelial adherens and tight junctions in vascular homeostasis, inflammation and angiogenesis. Biochim. Biophys. Acta - Biomembr. 1778: 794–809, 2008.

192. Hamilla, S. M., Stroka, K. M. & Aranda-Espinoza, H. VE-Cadherin-Independent Cancer Cell Incorporation into the Vascular Endothelium Precedes Transmigration. PLoS One 9: e109748, 2014.

193. Escribano, J., Chen, M. B., Moeendarbary, E., Cao, X., Shenoy, V., Manuel Garcia-Aznar, J., Kamm, R. D. & Spill, F. Balance of Mechanical Forces Drives Endothelial Gap Formation and May Facilitate Cancer and Immune-Cell Extravasation. 2018. doi:10.1101/375931

194. Abdullahi, W., Tripathi, D. & Ronaldson, P. T. Blood-brain barrier dysfunction in ischemic stroke: targeting tight junctions and transporters for vascular protection. Am. J. Physiol. Physiol. 315: C343–C356, 2018.

195. Nitz, T., Eisenblatter, T., Psathaki, K. & Gaï, H.-J. Serum-derived factors

weaken the barrier properties of cultured porcine brain capillary endothelial cells in vitro. Brain Res. 981: 30–40, 2003.

196. Hemphill, M. A., Dauth, S., Yu, C. J., Dabiri, B. E. & Parker, K. K. Traumatic Brain Injury and the Neuronal Microenvironment: A Potential Role for Neuropathological Mechanotransduction. Neuron 85: 1177–1192, 2015.

197. Goutal, S., Gerstenmayer, M., Auvity, S., Caillé, F., Mériaux, S., Buvat, I., Larrat, B. & Tournier, N. Physical blood-brain barrier disruption induced by focused ultrasound does not overcome the transporter-mediated efflux of erlotinib. J. Control. Release 292: 210–220, 2018.

198. Mesiwala, A. H., Farrell, L., Wenzel, H. J., Silbergeld, D. L., Crum, L. A., Winn, H. R. & Mourad, P. D. High-intensity focused ultrasound selectively disrupts the blood-brain barrier in vivo. Ultrasound Med. Biol. 28: 389–400, 2002.

199. Sheikov, N., McDannold, N., Vykhodtseva, N., Jolesz, F. & Hynynen, K. Cellular mechanisms of the blood-brain barrier opening induced by ultrasound in presence of microbubbles. Ultrasound Med. Biol. 30: 979–989, 2004.

200. Semyachkina-Glushkovskaya, O., Kurths, J., Borisova, E., Sokolovski, S., Mantareva, V., Angelov, I., Shirokov, A., Navolokin, N., Shushunova, N., Khorovodov, A., Ulanova, M., Sagatova, M., Agranivich, I., Sindeeva, O., Gekalyuk, A., Bodrova, A. & Rafailov, E. Photodynamic opening of blood-brain barrier. Biomed. Opt. Express 8: 5040–5048, 2017.

201. Li, C.-H., Shyu, M.-K., Jhan, C., Cheng, Y.-W., Tsai, C.-H., Liu, C.-W., Lee, C.-C., Chen, R.-M. & Kang, J.-J. Gold Nanoparticles Increase Endothelial

Paracellular Permeability by Altering Components of Endothelial Tight Junctions, and Increase Blood-Brain Barrier Permeability in Mice. Toxicol. Sci. 148: 192–203, 2015.

202. Griep, L. M., Wolbers, F., de Wagenaar, B., ter Braak, P. M., Weksler, B. B., Romero, I. A., Couraud, P. O., Vermes, I., van der Meer, A. D. & van den Berg, A. BBB ON CHIP: microfluidic platform to mechanically and biochemically modulate blood-brain barrier function. Biomed. Microdevices 15: 145–150, 2013.

203. Siddharthan, V., Kim, Y. V, Liu, S. & Kim, K. S. Human astrocytes/astrocyte conditioned medium and shear stress enhance the barrier properties of human brain microvascular endothelial cells. Brain Res. 1147: 39–50, 2007.

204. Arthur, F. E., Shivers, R. R. & Bowman, P. D. Astrocyte-mediated induction of tight junctions in brain capillary endothelium: an efficient in vitro model. Brain Res. 433: 155–9, 1987.

205. Maherally, Z., Fillmore, H. L., Ling Tan, S., Fei Tan, S., Jassam, S. A., Quack, F. I., Hatherell, K. E. & Pilkington, G. J. Real-time acquisition of transendothelial electrical resistance in an all-human, in vitro, 3-dimensional, blood–brain barrier model exemplifies tight-junction integrity. FASEB J. 32: 168–182, 2018.

206. Tilling, T., Korte, D., Hoheisel, D. & Galla, H. J. Basement membrane proteins influence brain capillary endothelial barrier function in vitro. J. Neurochem. 71: 1151–1157, 1998.

207. Rahmanian, M., Kan Pertoft, H., Kanda, S., Christofferson, R., Claesson-

Welsh, L. & Heldin, P. Hyaluronan Oligosaccharides Induce Tube Formation of a Brain Endothelial Cell Line in Vitro. Exp. Cell Res. 237: 223–230, 1997.

208. Camci-Unal, G., Aubin, H., Ahari, A. F., Bae, H., Nichol, J. W., Khademhosseini*, A., Kim, I.-S., Hwang, S.-J., Li, H. D., Choi, J. H., Jeon, E. S. & Kim, D. K. Surface-modified hyaluronic acid hydrogels to capture endothelial progenitor cells. Soft Matter 6: 5120, 2010.

209. Partyka, P. P., Godsey, G. A., Galie, J. R., Kosciuk, M. C., Acharya, N. K., Nagele, R. G. & Galie, P. A. Mechanical stress regulates transport in a compliant 3D model of the blood-brain barrier. Biomaterials 115: 30–39, 2017.

210. Pranda, M. A., Gray, K. M., Dawson, G. M., DeCastro, A. J. L., Jung, J. W. & Stroka, K. M. Tumor cell mechanosensing during incorporation into the brain microvascular endothelium. Cell. Mol. Bioeng. In Press, 2019.

211. Qiao, J., Huang, F. & Lum, H. PKA inhibits RhoA activation: a protection mechanism against endothelial barrier dysfunction. Am. J. Physiol. Lung Cell. Mol. Physiol. 284: L972-80, 2003.

212. Wong, K. H. K., Truslow, J. G. & Tien, J. The role of cyclic AMP in normalizing the function of engineered human blood microvessels in microfluidic collagen gels. Biomaterials 31: 4706–4714, 2010.

213. Li, A. Q., Zhao, L., Zhou, T. F., Zhang, M. Q. & Qin, X. M. Exendin-4 promotes endothelial barrier enhancement via PKA- and Epac1-dependent Rac1 activation. Am. J. Physiol. Cell Physiol. 308: C164-75, 2015.

214. Hsu, J., Serrano, D., Bhowmick, T., Kumar, K., Shen, Y., Kuo, Y. C., Garnacho, C. & Muro, S. Enhanced endothelial delivery and biochemical

effects of α-galactosidase by ICAM-1-targeted nanocarriers for Fabry disease. J. Control. Release 149: 323–331, 2011.

215. Gray, K. M., Katz, D. B., Brown, E. G. & Stroka, K. M. Quantitative Phenotyping of Cell–Cell Junctions to Evaluate ZO-1 Presentation in Brain Endothelial Cells. Ann. Biomed. Eng. 47: 1675–1687, 2019.

216. Fazakas, C., Wilhelm, I., Nagyőszi, P., Farkas, A. E., Haskó, J., Molnár, J., Bauer, H., Bauer, H.-C., Ayaydin, F., Dung, N. T. K., Siklós, L. & Krizbai, I. A. Transmigration of Melanoma Cells through the Blood-Brain Barrier: Role of Endothelial Tight Junctions and Melanoma-Released Serine Proteases. PLoS One 6: e20758, 2011.

217. McRae, M. P., LaFratta, L. M., Nguyen, B. M., Paris, J. J., Hauser, K. F. & Conway, D. E. Characterization of cell-cell junction changes associated with the formation of a strong endothelial barrier. Tissue Barriers 6: 1–9, 2018.

218. Eigenmann, D. E., Xue, G., Kim, K. S., Moses, A. V, Hamburger, M. & Oufir, M. Comparative study of four immortalized human brain capillary endothelial cell lines, hCMEC/D3, hBMEC, TY10, and BB19, and optimization of culture conditions, for an in vitro blood-brain barrier model for drug permeability studies. Fluids Barriers CNS 10: 33, 2013.

219. Winger, R. C., Koblinski, J. E., Kanda, T., Ransohoff, R. M. & Muller, W. a. Rapid remodeling of tight junctions during paracellular diapedesis in a human model of the blood-brain barrier. J. Immunol. 193: 2427–37, 2014.

220. Tominaga, N., Kosaka, N., Ono, M., Katsuda, T., Yoshioka, Y., Tamura, K., Lötvall, J., Nakagama, H. & Ochiya, T. Brain metastatic cancer cells release

microRNA-181c-containing extracellular vesicles capable of destructing blood–brain barrier. Nat. Commun. 6: 6716, 2015.

221. Feng, S., Zou, L., Wang, H., He, R., Liu, K., Zhu, H., Feng, S., Zou, L., Wang, H., He, R., Liu, K. & Zhu, H. RhoA/ROCK-2 Pathway Inhibition and Tight Junction Protein Upregulation by Catalpol Suppresses Lipopolysaccaride-Induced Disruption of Blood-Brain Barrier Permeability. Molecules 23: 2371, 2018.

222. Wen, J., Qian, S., Yang, Q., Deng, L., Mo, Y. & Yu, Y. Overexpression of netrin-1 increases the expression of tight junction-associated proteins, claudin-5, occludin, and ZO-1, following traumatic brain injury in rats. Exp. Ther. Med. 8: 881–886, 2014.

223. Zheng, Y., Tang, Y., Liu, W., Mao, E., Li, L., Wu, J., Zhang, R. & Zhang, S. A Study on Increased Permeability and Morphological Changes in Actin Cytoskeleton and Tight Junction of Vascular Endothelial Cells Induced by Tumor Necrosis Factor-Alpha. Chinese Crit. Care Med. 21: 160–163, 2009.

224. Camci-Unal, G., Cuttica, D., Annabi, N., Demarchi, D. & Khademhosseini, A. Synthesis and Characterization of Hybrid Hyaluronic Acid-Gelatin Hydrogels. Biomacromolecules 14: 1085–1092, 2013.

225. Booth, R. & Kim, H. Characterization of a microfluidic in vitro model of the blood-brain barrier (μBBB). Lab Chip 12: 1784, 2012.

226. Hayashi, K., Nakao, S., Nakaoke, R., Nakagawa, S., Kitagawa, N. & Niwa, M. Effects of hypoxia on endothelial/pericytic co-culture model of the blood-brain barrier. 2004. doi:10.1016/j.regpep.2004.05.023

227. Daneman, R., Zhou, L., Kebede, A. A. & Barres, B. A. Pericytes are required for blood-brain barrier integrity during embryogenesis. 2010. doi:10.1038/nature09513

228. Aragon-Sanabria, V., Pohler, S. E., Eswar, V. J., Bierowski, M., Gomez, E. W. & Dong, C. VE-Cadherin Disassembly and Cell Contractility in the Endothelium are Necessary for Barrier Disruption Induced by Tumor Cells OPEN. Nat. Publ. Gr. 2017. doi:10.1038/srep45835

229. Fan, J. & Fu, B. M. Quantification of Malignant Breast Cancer Cell MDA-MB-231 Trans- migration Across Brain and Lung Microvascular Endothelium. Ann. Biomed. Eng. 44: 2189–2201, 2016.

230. Gray, K. M. & Stroka, K. M. Vascular endothelial cell mechanosensing: New insights gained from biomimetic microfluidic models. Semin. Cell Dev. Biol. 71: 106–117, 2017.

231. Birukova, A. A., Tian, X., Cokic, I., Beckham, Y., Gardel, M. L. & Birukov, K. G. Endothelial barrier disruption and recovery is controlled by substrate stiffness. Microvasc. Res. 87: 50–57, 2013.

232. Byfield, F. J., Reen, R. K., Shentu, T. P., Levitan, I. & Gooch, K. J. Endothelial actin and cell stiffness is modulated by substrate stiffness in 2D and 3D. J. Biomech. 42: 1114–1119, 2009.

233. Newell-Litwa, K. A., Horwitz, R. & Lamers, M. L. Non-muscle myosin II in disease: mechanisms and therapeutic opportunities. Dis. Model. Mech. 8: 1495–1515, 2015.

234. Cheney, R. E. Myosins in cell junctions. Bioarchitecture 2: 158–170, 2012.

235. Chen, Y., Shen, F., Liu, J. & Yang, G.-Y. Arterial stiffness and stroke: de-stiffening strategy, a therapeutic target for stroke. BMJ 2: 65–72, 2017.

236. Boutouyrie, P., Tropeano, A. I., Asmar, R., Gautier, I., Benetos, A., Lacolley, P. & Laurent, S. Aortic stiffness is an independent predictor of primary coronary events in hypertensive patients: a longitudinal study. Hypertens. (Dallas, Tex. 1979) 39: 10–5, 2002.

237. Zieman, S. J., Melenovsky, V. & Kass, D. A. Mechanisms, Pathophysiology, and Therapy of Arterial Stiffness. Arterioscler. Thromb. Vasc. Biol. 25: 932–943, 2005.

238. Mckee, C. T., Last, J. A., Russell, P. & Murphy, C. J. Indentation Versus Tensile Measurements of Young's Modulus for Soft Biological Tissues. Tissue Eng. Part B 17: 155–164, 2011.

239. Wilhelm, I., Fazakas, C. & Krizbai, I. a. In vitro models of the blood-brain barrier. Acta Neurobiol Exp 71: 113–128, 2011.

240. Wang, Y. L. & Pelham, R. J. Preparation of a flexible, porous polyacrylamide substrate for mechanical studies of cultured cells. Methods Enzymol. 298: 489–96, 1998.

241. Stroka, K. M. & Aranda-espinoza, H. Neutrophils Display Biphasic Relationship Between Migration and Substrate Stiffness. Cell Motil. Cytoskeleton 66: 328–341, 2009.

242. Krishnan, R., Klumpers, D. D., Park, C. Y., Rajendran, K., Trepat, X., van Bezu, J., M van Hinsbergh, V. W. M., Carman, C. V, Brain, J. D., Fredberg, J. J., Butler, J. P. & van Nieuw Amerongen, G. P. Substrate stiffening promotes

endothelial monolayer disruption through enhanced physical forces. Am J Physiol Cell Physiol 300: 146–154, 2011.

243. Kothapalli, D., Liu, S.-L., Bae, Y. H., Monslow, J., Xu, T., Hawthorne, E. A., Byfield, F. J., Castagnino, P., Rao, S., Rader, D. J., Puré, E., Phillips, M. C., Lund-Katz, S., Janmey, P. A. & Assoian, R. K. Cardiovascular Protection by ApoE and ApoE-HDL Linked to Suppression of ECM Gene Expression and Arterial Stiffening. Cell Rep. 2: 1259–1271, 2012.

244. Klein, E. A., Yin, L., Kothapalli, D., Castagnino, P., Byfield, F. J., Xu, T., Levental, I., Hawthorne, E., Janmey, P. A. & Assoian, R. K. Cell-Cycle Control by Physiological Matrix Elasticity and In Vivo Tissue Stiffening. Curr. Biol. 19: 1511–1518, 2009.

245. Mierke, C. T., Bretz, N. & Altevogt, P. Contractile Forces Contribute to Increased Glycosylphosphatidylinositol-anchored Receptor CD24-facilitated Cancer Cell Invasion. J. Biol. Chem. 286: 34858–34871, 2011.

246. Cho, Y.-E., Ahn, D.-S., Morgan, K. G. & Lee, Y.-H. Enhanced contractility and myosin phosphorylation induced by Ca 21-independent MLCK activity in hypertensive rats. Cardiovasc. Res. 91: 162–170, 2011.

247. Essler, M., Staddon, J. M., Weber, P. C. & Aepfelbacher, M. Cyclic AMP Blocks Bacterial Lipopolysaccharide-Induced Myosin Light Chain Phosphorylation in Endothelial Cells Through Inhibition of Rho/Rho Kinase Signaling. J Immunol 164: 6543–6549, 2000.

248. Achrol, A. S., Rennert, R. C., Anders, C., Soffietti, R., Ahluwalia, M. S., Nayak, L., Peters, S., Arvold, N. D., Harsh, G. R., Steeg, P. S. & Chang, S. D.

Brain metastases. Nat. Rev. 5: 2019.

249. Nayak, L., Lee, E. Q. & Wen, P. Y. Epidemiology of Brain Metastases. Curr. Oncol. Rep. 14: 48–54, 2012.

250. Achrol, A. S., Rennert, R. C., Anders, C., Soffietti, R., Ahluwalia, M. S., Nayak, L., Peters, S., Arvold, N. D., Harsh, G. R., Steeg, P. S. & Chang, S. D. Brain metastases. Nat. Rev. 5: 2019.

251. Arshad, F., Wang, L., Sy, C., Avraham, S. & Avraham, H. K. Blood-brain barrier integrity and breast cancer metastasis to the brain. Patholog. Res. Int. 2011: 1–12, 2010.

252. Kienast, Y., Von Baumgarten, L., Fuhrmann, M., Klinkert, W. E. F., Goldbrunner, R., Herms, J. & Winkler, F. Real-time imaging reveals the single steps of brain metastasis formation. Nat. Med. 16: 116–122, 2010.

253. Abbott, N. J. & Friedman, A. Overview and introduction: the blood-brain barrier in health and disease. Epilepsia 53 Suppl 6: 1–6, 2012.

254. Martin, T. A. & Jiang, W. G. Loss of tight junction barrier function and its role in cancer metastasis. Biochim. Biophys. Acta - Biomembr. 1788: 872–891, 2009.

255. Roberts, H. C., Roberts, T. P. L., Brasch, R. C. & Dillon, W. P. Quantitative Measurement of Microvascular Permeability in Human Brain Tumors Achieved Using Dynamic Contrast-enhanced MR Imaging: Correlation with Histologic Grade. AJNR Am J Neuroradiol 21: 891–899, 2000.

256. Lee, T.-H., Karsenty Avraham, H., Jiang, S. & Avraham, S. Vascular endothelial growth factor modulates the transendothelial migration of MDA-

MB-231 breast cancer cells through regulation of brain microvascular endothelial cell permeability. J. Biol. Chem. 278: 5277–5284, 2003.

257. Avraham, H. K., Jiang, S., Fu, Y., Nakshatri, H., Ovadia, H. & Avraham, S. Angiopoietin-2 mediates blood-brain barrier impairment and colonization of triple-negative breast cancer cells in brain. J. Pathol. 232: 369–381, 2014.

258. Dorland, Y. L. & Huveneers, S. Cell-cell junctional mechanotransduction in endothelial remodeling. Cell. Mol. Life Sci. 74: 279–292, 2017.

259. Fazakas, C., Wilhelm, I., Nagyoszi, P., Farkas, A. E., Haskó, J., Molnar, J., Bauer, H., Bauer, H.-C., Ayaydin, F., Dung, N. T. K., Siklós, L. & Krizbai, I. A. Transmigration of melanoma cells through the blood-brain barrier: role of endothelial tight junctions and melanoma-released serine proteases. PLoS One 6: e20758, 2011.

260. Fan, J. & Fu, B. M. Quantification of malignant breast cancer cell MDA-MB-231 transmigration across brain and lung microvascular endothelium. Ann. Biomed. Eng. 44: 2189–2201, 2016.

261. Rodriguez, P. L., Jiang, S., Fu, Y., Avraham, S. & Avraham, H. K. The proinflammatory peptide substance P promotes blood-brain barrier breaching by breast cancer cells through changes in microvascular endothelial cell tight junctions. Int. J. Cancer 134: 1034–1044, 2014.

262. Cai, J., Jiang, W. G. & Mansel, R. E. Phosphorylation and disorganization of vascular-endothelial cadherin in interaction between breast cancer and vascular endothelial cells. Int. J. Mol. Med. 4: 191–5, 1999.

263. Hamilla, S. M., Stroka, K. M. & Aranda-Espinoza, H. VE-Cadherin-

independent cancer cell incorporation into the vascular endothelium precedes transmigration. PLoS One 9: e109748, 2014.

264. Reymond, N., Riou, P. & Ridley, A. J. Rho GTPases and cancer cell transendothelial migration. Methods Mol. Biol. 827: 123–142, 2012.

265. Onken, M. D., Li, J. & Cooper, J. A. Uveal melanoma cells utilize a novel Route for transendothelial migration. PLoS One 9: e115472, 2014.

266. Novak, U. & Kaye, A. H. Extracellular matrix and the brain: components and function. J. Clin. Neurosci. 7: 280–290, 2000.

267. Eichler, A. F., Chung, E., Kodack, D. P., Loeffler, J. S., Fukumura, D. & Jain, R. K. The biology of brain metastases-translation to new therapies. Nat. Rev. Clin. Oncol. 8: 344–356, 2011.

268. Mouw, J. K., Ou, G. & Weaver, V. M. Extracellular matrix assembly: a multiscale deconstruction. Nat. Publ. Gr. 15: 771, 2014.

269. Barnes, J. M., Przybyla, L. & Weaver, V. M. Tissue mechanics regulate brain development, homeostasis and disease. J. Cell Sci. 130: 71–82, 2017.

270. Cox, T. R. & Erler, J. T. Remodeling and homeostasis of the extracellular matrix: implications for fibrotic diseases and cancer. Dis. Model. Mech. 4: 165–178, 2011.

271. Akiri, G., Sabo, E., Dafni, H., Vadasz, Z., Kartvelishvily, Y., Gan, N., Kessler, O., Cohen, T., Resnick, M., Neeman, M. & Neufeld, G. Lysyl oxidase-related protein-1 promotes tumor fibrosis and tumor progression in vivo. Cancer Res. 63: 1657–1666, 2003.

272. Kass, L., Erler, J. T., Dembo, M. & Weaver, V. M. Mammary epithelial cell:

Influence of extracellular matrix composition and organization during development and tumorigenesis. Int. J. Biochem. Cell Biol. 3 39: 1987–1994, 2007.

273. Levental, K. R., Yu, H., Kass, L., Lakins, J. N., Egeblad, M., Erler, J. T., Fong, S. F. T., Csiszar, K., Giaccia, A., Weninger, W., Yamauchi, M., Gasser, D. L. & Weaver, V. M. Matrix crosslinking forces tumor progression by enhancing integrin signaling. Cell 139: 891–906, 209AD.

274. Prestwich, G. D. & Spectus, C. O. N. Evaluating drug efficacy and toxicology in three dimensions: using synthetic extracellular matrices in drug discovery. Acc. Chem. Res. 41: 139–148, 2008.

275. Shumakovich, M. A., Mencio, C. P., Siglin, J. S., Moriarty, R. A., Geller, H. M. & Stroka, K. M. Astrocytes from the brain microenvironment alter migration and morphology of metastatic breast cancer cells. FASEB J. 31: 5049–5067, 2017.

276. Zheng Shu, X., Liu, Y., Palumbo, F. S., Luo, Y. & Prestwich, G. D. In situ crosslinkable hyaluronan hydrogels for tissue engineering. Biomaterials 25: 1339–1348, 2004.

277. Vanderhooft, J. L., Alcoutlabi, M., Magda, J. J. & Prestwich, G. D. Rheological Properties of Cross-Linked Hyaluronan-Gelatin Hydrogels for Tissue Engineering. doi:10.1002/mabi.200800141

278. Sarrió, D., Rodriguez-Pinilla, S. M., Hardisson, D., Cano, A., Moreno-Bueno, G. & Palacios, J. Epithelial-mesenchymal transition in breast cancer relates to the basal-like phenotype. Cancer Res. 68: 989–997, 2008.

279. Yankaskas, C. L., Thompson, K. N., Paul, C. D., Vitolo, M. I., Mistriotis, P., Mahendra, A., Bajpai, V. K., Shea, D. J., Manto, K. M., Chai, A. C., Varadarajan, N., Kontrogianni-Konstantopoulos, A., Martin, S. S. & Konstantopoulos, K. A microfluidic assay for the quantification of the metastatic propensity of breast cancer specimens. Nat. Biomed. Eng. 3: 452–465, 2019.

280. Kim, Y. & Kumar, S. CD44-mediated adhesion to hyaluronic acid contributes to mechanosensing and invasive motility. Mol. Cancer Res. 12: 1416–1429, 2014.

281. Zhang, P., Fu, C., Bai, H., Song, E. & Song, Y. CD44 variant, but not standard CD44 isoforms, mediate disassembly of endothelial VE-cadherin junction on metastatic melanoma cells. FEBS Lett. 588: 4573–4582, 2014.

282. Bellail, A. C., Hunter, S. B., Brat, D. J. & Van Meir, E. G. Microregional extracellular matrix heterogeneity in brain modulates glioma cell invasion. Int. J. Biochem. Cell Biol. 36: 1046–1069, 2004.

283. McFarlane, S., Coulter, J. A., Tibbits, P., O'Grady, A., McFarlane, C., Montgomery, N., Hill, A., McCarthy, H. O., Young, L. S., Kay, E. W., Isacke, C. M. & Waugh, D. J. J. CD44 increases the efficiency of distant metastasis of breast cancer. Oncotarget 6: 11465–76, 2015.

284. Vallenius, T. Actin stress fibre subtypes in mesenchymal-migrating cells. Open Biol. 3: 2013.

285. Discher, D. E., Janmey, P. & Wang, Y.-L. Tissue cells Ffeel and respond to the stiffness of their substrate. Science (80-.). 310: 1139–1143, 2005.

286. Wrobel, J. K. & Toborek, M. Blood–brain barrier remodeling during brain metastasis formation. Mol. Med. 22: 32–40, 2016.

287. Yeung, T., Georges, P. C., Flanagan, L. A., Marg, B., Ortiz, M., Funaki, M., Zahir, N., Ming, W., Weaver, V. & Janmey, P. A. Effects of substrate stiffness on cell morphology, cytoskeletal structure, and adhesion. Cell Motil. Cytoskeleton 60: 24–34, 2005.

288. Stroka, K. M. & Aranda-Espinoza, H. Neutrophils display biphasic relationship between migration and substrate stiffness. Cell Motil. Cytoskeleton 66: 328–341, 2009.

289. Stroka, K. M., Sheng Wong, B., Shriver, M., Phillip, J. M., Wirtz, D., Kontrogianni-Konstantopoulos, A. & Konstantopoulos, K. Loss of giant obscurins alters breast epithelial cell mechanosensing of matrix stiffness. Oncotarget 5: 2016.

290. Ananthanarayanan, B., Kim, Y. & Kumar, S. Elucidating the mechanobiology of malignant brain tumors using a brain matrix-mimetic hyaluronic acid hydrogel platform. Biomaterials 32: 7913–7923, 2011.

291. Narkhede, A. A., Crenshaw, J. H., Manning, R. M. & Rao, S. S. The influence of matrix stiffness on the behavior of brain metastatic breast cancer cells in a biomimetic hyaluronic acid hydrogel platform. J. Biomed. Mater. Res. - Part A 1–10, 2018.

292. Pogoda, K., Bucki, R., Byfield, F. J., Cruz, K., Lee, T., Marcinkiewicz, C. & Janmey, P. A. Soft substrates containing hyaluronan mimic the effects of increased stiffness on morphology, motility, and proliferation of glioma cells.

Biomacromolecules 18: 3040−3051, 2017.

293. Stroka, K. M., Hayenga, H. N. & Aranda-Espinoza, H. Human Neutrophil Cytoskeletal Dynamics and Contractility Actively Contribute to Trans-Endothelial Migration. PLoS One 8: 61377, 2013.

294. Hielscher, A., Ellis, K., Qiu, C., Porterfield, J. & Gerecht, S. Fibronectin deposition participates in extracellular matrix assembly and vascular morphogenesis. 2016.

295. Jamieson, J. J., Searson, P. C. & Gerecht, S. Engineering the human blood-brain barrier in vitro. J. Biol. Eng. 11: 2017.

296. Destefano, J. G., Jamieson, J. J., Linville, R. M. & Searson, P. C. Benchmarking in vitro tissue-engineered blood-brain barrier models. Fluids Barriers CNS 15: 32, 2018.

297. Turitto, V. T. Blood viscosity, mass transport, and thrombogenesis. Prog. Hemost. Thromb. 6: 139–77, 1982.

298. Baeyens, N., Bandyopadhyay, C., Coon, B. G., Yun, S. & Schwartz, M. A. Endothelial fluid shear stress sensing in vascular health and disease. J. Clin. Invest. 126: 821–828, 2016.

299. Northcott, J. M., Dean, I. S., Mouw, J. K. & Weaver, V. M. Feeling Stress: The Mechanics of Cancer Progression and Aggression. Front. Cell Dev. Biol. 6: 17, 2018.

300. Lee, H. J., Diaz, M. F., Price, K. M., Ozuna, J. A., Zhang, S., Sevick-Muraca, E. M., Hagan, J. P. & Wenzel, P. L. Fluid shear stress activates YAP1 to promote cancer cell motility. Nat. Commun. 8: 2017.

301. Ajami, N. E., Gupta, S., Maurya, M. R., Nguyen, P., Li, J. Y.-S., Shyy, J. Y.-J., Chen, Z., Chien, S. & Subramaniam, S. Systems biology analysis of longitudinal functional response of endothelial cells to shear stress. Proc. Natl. Acad. Sci. 114: 10990–10995, 2017.

302. DeStefano, J. G., Xu, Z. S., Williams, A. J., Yimam, N. & Searson, P. C. Effect of shear stress on iPSC-derived human brain microvascular endothelial cells (dhBMECs). Fluids Barriers CNS 14: 20, 2017.

303. Ye, M., Sanchez, H. M., Hultz, M., Yang, Z., Bogorad, M., Wong, A. D. & Searson, P. C. Brain microvascular endothelial cells resist elongation due to curvature and shear stress. Sci. Rep. 4: 4681, 2014.

304. Salvador, E., Burek, M. & Förster, C. Y. Tight Junctions and the Tumor Microenvironment. Curr. Pathobiol. Rep. 4: 135–145, 2016.

305. Knights, A. J., Funnell, A. P. W., Crossley, M. & Pearson, R. C. M. Holding Tight: Cell Junctions and Cancer Spread. Trends Cancer Res. 8: 61–69, 2012.

306. Shen, L., Weber, C. R. & Turner, J. R. The tight junction protein complex undergoes rapid and continuous molecular remodeling at steady state. J. Cell Biol. 181: 683–695, 2008.

307. Shaw, S. K., Bamba, P. S., Perkins, B. N. & Luscinskas, F. W. Real-time imaging of vascular endothelial-cadherin during leukocyte transmigration across endothelium. J. Immunol. 167: 2323–2330, 2001.

308. Prabhakarpandian, B., Shen, M.-C., Nichols, J. B., Mills, I. R., Sidoryk-Wegrzynowicz, M., Aschner, M. & Pant, K. SyM-BBB: a microfluidic blood brain barrier model. Lab Chip 13: 1093–1101, 2013.

309. Ng, M. R., Besser, A., Brugge, J. S. & Danuser, G. Mapping the dynamics of force transduction at cell-cell junctions of epithelial clusters. Elife 4: e03282, 2014.

310. Conway, D. E., Breckenridge, M. T., Hinde, E., Gratton, E., Chen, C. S. & Schwartz, M. A. Fluid Shear Stress on Endothelial Cells Modulates Mechanical Tension across VE-Cadherin and PECAM-1. Curr. Biol. 23: 1024–1030, 2013.

311. Mohan, A., Schlue, K. T., Kniffin, A. F., Mayer, C. R., Duke, A. A., Narayanan, V., Arsenovic, P. T., Bathula, K., Danielsson, B. E., Dumbali, S. P., Maruthamuthu, V. & Conway, D. E. Spatial Proliferation of Epithelial Cells Is Regulated by E-Cadherin Force. Biophys. J. 115: 853–864, 2018.

312. Maruthamuthu, V., Sabass, B., Schwarz, U. S. & Gardel, M. L. Cell-ECM traction force modulates endogenous tension at cell–cell contacts. PNAS 108: 4708–4713, 2011.

313. Lee, T.-H., Karsenty Avraham, H., Jiang, S. & Avraham, S. Vascular Endothelial Growth Factor Modulates the Transendothelial Migration of MDA-MB-231 Breast Cancer Cells through Regulation of Brain Microvascular Endothelial Cell Permeability*. J. Biol. Chem. 278: 5277–5284, 2003.

314. Molnár, J., Fazakas, C., Haskó, J., Sipos, O., Nagy, K., Nyúl-Tóth, Á., Farkas, A. E., Végh, A. G., Váró, G., Galajda, P., Krizbai, I. A. & Wilhelm, I. Transmigration characteristics of breast cancer and melanoma cells through the brain endothelium: Role of Rac and PI3K. Cell Adh. Migr. 10: 269–281, 2016.

315. Escribano, J., Chen, M. B., Moeendarbary, E., Cao, X., Shenoy, V., Garcia-

Aznar, J. M., Kamm, R. D. & Spill, F. Balance of Mechanical Forces Drives Endothelial Gap Formation and May Facilitate Cancer and Immune-Cell Extravasation. PLOS Comput. Biol. 1–21, 2018.

316. Yeh, Y.-T., Serrano, R., François, J., Chiu, J.-J., Julie Li, Y.-S., del Álamo, J. C., Chien, S. & Lasheras, J. C. Three-dimensional forces exerted by leukocytes and vascular endothelial cells dynamically facilitate diapedesis. PNAS 115: 133–138, 2018.

317. Stroka, K. M. & Aranda-Espinoza, H. Effects of Morphology vs. Cell–Cell Interactions on Endothelial Cell Stiffness. Cell. Mol. Bioeng. 4: 9–27, 2011.

318. Vanderburgh, J. A., Hotchkiss, H., Potharazu, A., Taufalele, P. V & Reinhart-King, C. A. Substrate stiffness heterogeneities disrupt endothelial barrier integrity in a micropillar model of heterogeneous vascular stiffening †. 2018. doi:10.1039/c8ib00124c

319. Ostrom, Q. T., Gittleman, H., Liao, P., Vecchione-Koval, T., Wolinsky, Y., Kruchko, C. & Barnholtz-Sloan, J. S. Neuro-Oncology CBTRUS Statistical Report: Primary brain and other central nervous system tumors diagnosed in the United Introduction. 1–88, 2017. doi:10.1093/neuonc/nox158

320. Kostron, H., Obwegeser, A. & Jakober, R. *Photodynamic therapy in neurosurgery: a review*. *Journal of Photochemistry and Photobiology B: Biology* 36: (1996).

321. Cancer, C. A. & Clin, J. Photodynamic Therapy of Cancer: An Update. Cancer J Clin 61: 250–281, 2012.

322. Hadjipanayis, C. G. & Stummer, · Walter. 5-ALA and FDA approval for

glioma surgery. J. Neurooncol. 141: 479–486, 2019.

323. Huang, H.-C., Rizvi, I., Liu, J., Anbil, S., Kalra, A., Lee, H., Baglo, Y., Paz, N., Hayden, D., Pereira, S., Pogue, B. W., Fitzgerald, J. & Hasan, T. Photodynamic Priming Mitigates Chemotherapeutic Selection Pressures and Improves Drug Delivery. Cancer Res. 78: 558–571, 2018.

324. Zhang, C., Feng, W., Vodovozova, E., Tretiakova, D., Boldyrevd, I., Li, Y., Kürths, J., Yu, T., Semyachkina-Glushkovskaya, O. & Zhu, D. Photodynamic opening of the blood-brain barrier to high weight molecules and liposomes through an optical clearing skull window. 2018. doi:10.1364/BOE.9.004850

325. Jackson, S., Meeks, C., Vézina, A., Robey, R. W., Tanner, K. & Gottesman, M. M. Model systems for studying the blood-brain barrier: Applications and challenges. Biomaterials 214: 119217, 2019.

326. Hoque, M. T., Shah, A., More, V., Miller, D. S. & Bendayan, R. In vivo and ex vivo regulation of breast cancer resistant protein (Bcrp) by peroxisome proliferator-activated receptor alpha (Pparα) at the blood-brain barrier. J. Neurochem. 135: 1113–1122, 2015.

327. Zuluaga-Ramirez, V., Rom, S. & Persidsky, Y. Craniula: A cranial window technique for prolonged imaging of brain surface vasculature with simultaneous adjacent intracerebral injection. Fluids Barriers CNS 12: 24, 2015.

328. Chen, C., Zhang, Y. P., Sun, Y., Xiong, W., Shields, L. B. E., Shields, C. B., Jin, X. & Xu, X.-M. An In Vivo; Duo-color Method for Imaging Vascular Dynamics Following Contusive Spinal Cord Injury. J. Vis. Exp. e56565, 2017.

doi:10.3791/56565

329. Stoletov, K., Kato, H., Zardouzian, E., Kelber, J., Yang, J., Shattil, S. & Klemke, R. Visualizing extravasation dynamics of metastatic tumor cells. J. Cell Sci. 123: 2332–2341, 2010.

330. Jeong, J.-Y., Kwon, H.-B., Ahn, J.-C., Kang, D., Kwon, S.-H., Park, J. A. & Kim, K.-W. Functional and developmental analysis of the blood-brain barrier in zebrafish. Brain Res. Bull. 75: 619–628, 2008.

331. Rickelt, S., Franke, W. W., Doerflinger, Y., Goerdt, S., Brandner, J. M. & Peitsch, W. K. Subtypes of melanocytes and melanoma cells distinguished by their intercellular contacts: heterotypic adherens junctions, adhesive associations, and dispersed desmoglein 2 glycoproteins. Cell Tissue Res. 334: 401–422, 2008.